

Department of Imaging and Applied Physics

Centre for Marine Science and Technology

**Acoustic observation of ice rifting and breaking events on the
Antarctic ice shelf using remote hydroacoustic listening stations**

Binghui Li

This thesis is presented for the Degree of

Doctor of Philosophy

of

Curtin University of Technology

February 2010

DECLARATION

To the best of my knowledge and belief this thesis contains no material previously published by any other person except where due acknowledgement has been made.

This thesis contains no material which has been accepted for the award of any other degree or diploma in any university.

Signature: _____

Date: _____

ABSTRACT

Long-term continuous monitoring of ice break-up on ice shelves and icebergs in Antarctica is essential for a global observation system of climate change and its consequences. While calving of massive pieces of ice from the Antarctic ice shelf is well observed from satellites, numerous ice breaks of smaller volume cannot be systematically monitored and statistically analysed by the existing means of remote sensing and local in-situ observations. This study aimed to investigate the feasibility of an alternative monitoring approach based on remote acoustic observations of ice rifting and breaking events on Antarctic ice shelves and icebergs using distant underwater acoustic listening stations in the ocean. This investigation was carried out using long-term continuous sea noise recordings made from 2002 to 2007 at two hydroacoustic stations deployed in the Indian Ocean as part of the International Monitoring System of the Comprehensive Nuclear-Test-Ban Treaty: off Cape Leeuwin in Western Australia (HA01) and off Chagos Archipelago (HA08).

Investigations of a number of scientific and technical issues relevant to the main objective were carried out in this study. They include: 1) processing of the CTBT hydroacoustic data from the two IMS stations with the aim of detecting and identifying signals received from Antarctic ice breaking events; 2) investigating the time-frequency arrival structure of the signals expected from ice events using experimental data and numerical modelling of acoustic propagation from Antarctica to the IMS stations in the Indian Ocean; 3) analysing the bearing accuracy of the IMS stations; 4) examining three different schemes for localization of ice events using either one or two IMS stations; 5) analysing the spatial distribution of Antarctic ice events observed over 6 years of data collection and its correlation with the major glacial features of the Eastern Antarctic coastal zone which are most likely sources of newly calved icebergs and underwater noise produced by ice break-up; 6) analysing long-term variations in the occurrence of ice events and their links with changes in climate related metocean characteristics of the Eastern Antarctic coastal zone.

A number of important findings and conclusions were made based on the results of this study. It was revealed that Antarctica is one of the major sources of low-frequency underwater noise at the two IMS stations in the Indian Ocean. The transient signals received at the IMS stations from Antarctic ice events consist mainly of a mode one arrival pulse with strong frequency dispersion, which is due to the acoustic propagation characteristics in the near-surface acoustic channel of the polar ocean environment south of the Antarctic Convergence Zone (ACZ). Both HA01 and H08S stations have bearing estimate accuracy for transient acoustic noise in Antarctica of about 0.2° RMS. The bearing error of HA01 also has a systematic component of around 0.8° clockwise. The bearing deviation induced by horizontal refraction of acoustic propagation across the ACZ polar frontal zone and over the continental slopes can be considerable, up to 1° for sources located in the easternmost and westernmost parts of the Eastern Antarctic coastal zone observed from the IMS stations. The localization of Antarctic ice events can be achieved either by triangulation using bearing estimates, if the same event can be detected at both stations, or by estimating the range to the noise source through inversion of mode 1 dispersion characteristic when the signal is detected only at one station. The location of ice events in the Antarctic coastal zone can also be coarsely estimated from the low cut-off frequency of mode 1 measured at the receive station. The majority of ice events observed at HA01 were located within a number of back-azimuth sectors which correspond to the directions to the ice shelves and iceberg tongues which are known as active zones of ice break-up in Eastern Antarctica. The temporal changes in the occurrence frequency of ice events detected at HA01 reveal strong seasonal variations but no significant interannual trend.

Based on the main results and findings, this study achieved its primary aim to demonstrate the feasibility of remote monitoring of ice rifting and breaking events on Antarctic ice shelves and icebergs using the IMS hydroacoustic listening stations deployed in the Indian Ocean.

ACKNOWLEDGEMENTS

First and foremost I would like to offer my sincerest gratitude to my principal supervisor Prof. Alexander (Sasha) Gavrilov for his tremendous support throughout all aspects of this study. Without his tireless supervision, inspirational encouragement, understanding and patience, this thesis would not have been completed and written. His wide knowledge in underwater acoustics and his logical way of thinking have been of great value for me.

I express my deep acknowledgement to my co-supervisor Dr. Alec Duncan for his excellent guidance, advice and insight throughout my work. He also provided detailed and constructive comments on my thesis writing.

This PhD project was mainly funded by Australian Research Council (Discovery Project DP0559994) and Australian Antarctic Division (Australian Antarctic Science Grant). Other sources of funding were from Australian Postgraduate Award scholarship from Australian government, Curtin Research Scholarship from Curtin University, Faculty Postgraduate Award from Faculty of Science and Engineering, Curtin University of Technology, and Curtin Completion Scholarship from Curtin University of Technology.

Special thanks to Dr. David Jepsen of Geoscience Australia for providing us with the copies of acoustic recordings from the HA01 station of the IMS hydroacoustic network. The copies of acoustic recordings from the H08S station are provided by Comprehensive Nuclear-Test-ban Treaty Organization and downloaded from the website of the U. S. Army Space and Missile Defence Command Monitoring Research Program (<http://www.rdss.info/>). Thanks also goes to Dr. Jason Gedamke from Australian Centre for Applied Marine Mammal Science in Australian Antarctic Division for providing us with the acoustic recordings from the noise loggers deployed near Australian Antarctic Casey station.

I would like to extend my acknowledgement to all staff and students at the Center for Marine Science and Technology (CMST) for their support and help during the last four years. They are the people who make CMST such a diverse, dynamic, supportive and fun team to work with.

Finally, I am forever indebted to my wife staying along with me in Australia, and my parents and my sisters back home in China, for their endless love, caring, support and encouragement.

TABLE OF CONTENTS

Abstract	i
Acknowledgements	iii
Table of contents	v
List of figures	x
List of tables	xxvii
Chapter 1. Introduction	1
1.1 Overview	1
1.2 Rationale of the study	1
1.2.1 <i>Ice disintegration as one of indicators of climate change</i>	1
1.2.2 <i>Conventional ice shelf monitoring methods</i>	2
1.2.3 <i>Remote Hydroacoustic Monitoring as an innovative approach to ice monitoring</i>	5
1.3 Aims of the study	8
1.4 Structure of the thesis	9
Chapter 2. CTBT hydroacoustic data processing and hydroacoustic event classification	11
2.1 Overview	11
2.2 Background	12
2.2.1 <i>IMS hydroacoustic network</i>	12
2.2.2 <i>Two hydroacoustic stations in the Indian Ocean and their Antarctic observation coverage</i>	14
2.3 CTBT hydroacoustic data collection from the HA01 and H08S station	16
2.4 Preliminary hydroacoustic data processing	18
2.4.1 <i>Hydrophone channel synchronization</i>	19
2.4.2 <i>Raw data conditioning</i>	20
2.4.3 <i>Cross correlation and the time difference of arrivals (TDOA)</i>	22
2.4.4 <i>Slowness and back-azimuth estimation of hydroacoustic events</i>	22
2.5 Coherent signal classifications based on waveform and spectrograms	23

2.5.1	<i>Whale calls</i>	24
2.5.2	<i>Man-made signals</i>	25
2.5.3	<i>Seismic signals</i>	27
2.5.4	<i>Harmonic tremor signals from Antarctica</i>	27
2.5.5	<i>Antarctic ice cracking or breaking signals (ice events)</i>	28
2.6	Temporal and spatial distributions of all coherent signals	30
2.7	Statistical analysis of the principle characteristics of ice events at the HA01 station	35
2.8	Concluding remarks	37
Chapter 3. Numerical modelling of acoustic propagation from Antarctica and experimental investigation of the origin of ice events		39
3.1	Overview	39
3.2	Background theory	40
3.2.1	<i>Acoustic wave equation and its normal mode solution</i>	40
3.2.2	<i>Normal modes in range-dependent environment</i>	43
3.2.3	<i>Acoustic propagation loss due to scattering from rough boundaries</i>	44
3.2.4	<i>Broadband modelling</i>	46
3.3	Numerical modelling of sound propagation from Antarctica to the IMS hydroacoustic stations	46
3.3.1	<i>Sound speed profiles from Antarctica to the IMS stations in the Indian Ocean</i>	46
3.3.2	<i>Transfer function of the ocean acoustic channel</i>	52
3.3.3	<i>The dependence of propagation loss on sea depth, source depth and frequency</i>	58
3.3.4	<i>Transmission loss</i>	62
3.3.5	<i>Mode coupling effect</i>	63
3.3.6	<i>Mode and frequency dispersion</i>	68
3.3.7	<i>Modelled arrival structure of the signal from ice events</i>	71
3.4	Simultaneous observation of ice breaking events from the IMS stations in the Indian Ocean and by other observational means in Antarctica	74

3.4.1 <i>Underwater acoustic signals from ice events observed in Antarctica</i>	74
3.4.2 <i>Signals from ice break off the Shackleton Ice Shelf</i>	78
3.5 Concluding remarks	82
Chapter 4. Bearing error analysis of HA01 and H08S hydroacoustic stations	83
4.1 Overview	83
4.2 Bearing errors from the differential travel times	84
4.3 Random bearing errors due to temporal horizontal motion of the hydrophones	86
4.3.1 <i>Numerical analysis of random bearing errors</i>	87
4.3.2 <i>Experimental estimation of random bearing error</i>	89
4.3.2.1 The HA01 station	89
4.3.2.2 The H08S station	91
4.4 Effect of horizontal refraction on bearing estimation	92
4.4.1 <i>Numerical solution for horizontal rays</i>	93
4.4.2 <i>Potential effect of horizontal refraction on bearing estimation</i>	95
4.4.2.1 In the Indian Ocean	95
4.4.2.2 In the Southern Ocean	98
4.4.3 <i>Deviation of bearing from the IMS hydroacoustic stations to detected hydroacoustic events due to horizontal refraction</i>	100
4.4.3.1 The HA01 station	101
4.4.3.2 The H08S station	101
4.4.4 <i>Experimental observation of the frequency dependence of horizontal refraction effect on bearing estimation of hydroacoustic events</i>	104
4.5 Systematic bearing error estimation and calibration	107
4.5.1 <i>A geometric model for bearing calibration of the IMS hydroacoustic station</i>	108
4.5.2 <i>Experimental estimation of the systematic bearing error and calibration of array geometry</i>	110
4.5.2.1 The HA01 station	111
4.5.2.2 The H08S station	116

4.5.3 Examination of the systematic bearing error from HA01 using acoustic and satellite observations of Antarctic icebergs	120
4.6 Conclusions	124
Chapter 5. The localization of Antarctic ice breaking event	126
5.1 Overview	126
5.2 Antarctic ice event localization by azimuthal intersection	127
5.3 Localization of Antarctic ice events based on modal frequency dispersion	134
5.3.1 The time-frequency structure of signals from ice events	135
5.3.2 The range estimation procedure	139
5.3.3 Case studies	140
5.3.4 The limitation of ice event localization based on modal frequency dispersion	144
5.4 Localization based on observed cut-off frequencies	144
5.5 Concluding remarks	148
Chapter 6. Spatial distribution analysis of Antarctic ice events	150
6.1 Overview	150
6.2 Spatial distribution of the ice events observed at HA01	151
6.3 Azimuth dependence of the propagation loss from Antarctica to HA01	156
6.4 concluding remarks	159
Chapter 7. Temporal variations of the occurrence of Antarctic ice events	161
7.1 Overview of the chapter	161
7.2 The Variations of occurrence of ice events	161
7.3 Correlation between the occurrence frequency of ice events and metocean characteristics of Eastern Antarctica	167
7.3.1 sea surface temperature	168
7.3.2 Air temperature	170
7.3.3 Wind speed	172
7.3.4 Antarctic sea ice extent	175
7.3.5 Signal level of ice events observed at HA01	177
7.3.6 Discussion	179

7.4 Concluding remarks	182
Chapter 8. Conclusions and recommendations	184
8.1 Overview	184
8.2 Conclusions	184
8.3 Recommendations for future work	189
References	191
Appendix A. An algorithm for recognising transient signals received from Antarctica	203

LIST OF FIGURES

- Figure 1.1. Satellite images of the rifting and calving process of a large iceberg from the Pine Island Glacier in the Amundsen Sea during the period from late 2000 to late 2001 [http://visibleearth.nasa.gov/view_rec.php?id=2319]. The red arrows point at the ice rift position. 3
- Figure 1.2. A network of seismo-acoustic stations across the fracture zone in the Amery ice shelf deployed in the joint Australian-US experiment (Bassis et al., 2005). L and T in the left panel represent longitudinal-to-flow rift and transverse-to-flow rift respectively. The right panel shows the photo of the tip of the rift T2 (bottom) and the location of the instruments around the tip (top). VC refers to seismic station and LTS and LTN refer to the GPS baselines. 4
- Figure 1.3. The global network of CTBT IMS hydroacoustic stations. Star signs indicate the locations of the IMS T-phase stations deployed on small islands and circle signs show the hydrophone stations in the ocean. 6
- Figure 2.1. General layout of the HA01 hydroacoustic station. Three hydrophones are deployed in a triangular shape with a separation of about 2 km. They are submerged in the SOFAR channel at a depth of around 1100 meters. The hydrophones are cabled to the data collection and communication facility on shore for real-time data transmission via satellite to the International Data Center in Vienna. 13
- Figure 2.2. Unblocked geodetic ray paths (yellow line) launched from the HA01 station to the Indian Ocean and part of Southern Ocean 14

plotted over the bathymetry map. The ray paths were assumed to be blocked if they cross an area with a sea depth of less than 300 meters.

- Figure 2.3. Unblocked geodetic ray paths (yellow line) launched from the H08S station to the Indian Ocean and part of Southern Ocean plotted over the bathymetry map. The ray paths were assumed to be blocked if they cross an area with a sea depth of less than 300 meters. 15
- Figure 2.4. Percentage of annual hydroacoustic data availability for the HA01 and H08S stations from 2001 to 2008. 16
- Figure 2.5. Percentage of monthly hydroacoustic data availability for the HA01 station from 2001 to 2008. 17
- Figure 2.6. Percentage of monthly data availability for the H08S station from 2002 to 2005. 18
- Figure 2.7. Basic flow chart of the preliminary processing of the hydroacoustic data from the IMS stations. TDOA stands for Time Difference of Arrivals. 19
- Figure 2.8. Waveforms (top) and spectrograms (bottom) of the detected event before (left) and after (right) low-frequency filtering. The transient seen in the spectrogram is a weak ice event. 21
- Figure 2.9. The waveform (top panels) and spectrogram (bottom panels) of Antarctic blue (left panels) and Pygmy (right panels) whale calls, received at one of the HA01 hydrophones in 2007. 24

Figure 2.10.	Left panels: the waveform (top) and spectrogram (bottom) of an air-gun signal from an offshore seismic survey near Cape Leeuwin received at HA01 on day 305 in year 2004; right panels: the waveform (top) and spectrogram (bottom) of an air-gun signal from an offshore seismic survey on the north west shelf of Australia, received at H08S hydroacoustic station with the arrival date of day 55 in 2005.	25
Figure 2.11.	The waveform (left panel) and spectrogram (right panel) of ship noise observed at HA01.	26
Figure 2.12.	The waveform (left panel) and spectrogram (right panel) of a seismic event detected at HA01 on day 306 in 2003.	27
Figure 2.13.	The waveform (top) and spectrogram (bottom) of noise fragments from two harmonic tremor events with (left) and without (right) higher frequency harmonics observed at the HA01 station on Day 4 in 2007. Back-azimuth to these events was 192.14° and 194.97° respectively.	28
Figure 2.14.	The waveform and spectrogram of a sea noise fragment which contains an ice event detected at HA01 on Day 9 in 2007. Back-azimuth to this event is 165.95° .	30
Figure 2.15.	Typical spectrograms of Antarctic ice events having one dominant arrival with a noise-like precursor (left panel) and two distinctive arrivals with a noisy precursor (right panel).	30
Figure 2.16.	Percentage of time when coherent low-frequency noise signals were observed at HA01, versus the day of observation and the back-azimuth to signals sources.	33

Figure 2.17.	Percentage of time when coherent low-frequency noise signals were observed at H08S, versus the day of observation and the back-azimuth to signals.	34
Figure 2.18.	Histogram of the signal level of ice events detected at HA01 over the six year period from 2002 to 2007. The resolution is in 0.05 dB sound level bin.	36
Figure 2.19.	Histogram of the Signal-to-noise ratios of ice events received at HA01. The resolution is in 0.5 dB SNR bin.	36
Figure 2.20.	Histogram of the frequencies of peak power spectral density calculated for the ice events received at HA01. The resolution is in 1 Hz bin.	37
Figure 3.1.	The temperature (top panel), salinity (middle panel) and sound speed (bottom panel) profiles along the path from Vincennes Bay, Antarctica (66.5°S, 109.5°E) to the HA01 hydroacoustic station (34.89°S, 114.15°E), with monthly climatology data for January.	49
Figure 3.2.	The temperature (top panel), salinity (middle panel) and sound speed (bottom panel) profiles along the path from Vincennes Bay, Antarctica (66.5°S, 109.5°E) to the H08S station (7.65°S, 72.47°E), with monthly climatology data for January.	51
Figure 3.3.	Amplitude (arbitrary unit) of the transfer function of modes 1 to 4 as a function of frequency numerically modelled using the adiabatic mode model for the propagation path from Vincennes Bay in Antarctica to HA01 (top panel) and to H08S (bottom panel), shown	55

disregarding cylindrical spreading.

- Figure 3.4. Variations of the attenuation coefficient (dB/km) of modes 1-4 56
along the initial 200-km section (over the Antarctic continental
shelf) of the propagation path from Vincennes Bay in Antarctica to
HA01 (shown in Figure 3.1).
- Figure 3.5. Variations of the amplitude (arbitrary unit) of the transfer function 57
of modes 1 to 4 at 30 Hz with along the propagation paths from
Vincennes Bay to HA01 (top panel) and to H08S (bottom panel)
numerically modelled using the adiabatic mode model, shown
disregarding cylindrical spreading.
- Figure 3.6. The attenuation (dB/km) as a function of sea depth and frequency 60
for mode one (left panel) and mode two (right panel). The sound
speed profile is taken from the region of Vincennes Bay, Antarctica
for winter season, and the sea depth parameters are from Table 3.1.
- Figure 3.7. Product $\psi_{ms}(z_s) \times \psi_{mr}(z_r)$ as a function of source depth and 61
frequency for mode 1 (top panel) and mode 2 (bottom panel).
 $\psi_{ms}(z_s)$ is the mode amplitude at the source position and
 $\psi_{mr}(z_r)$ is the mode amplitude at the HA01 hydrophone.
- Figure 3.8. Transmission loss (dB) at 10 Hz modelled along the path from 63
Vincennes Bay to HA01 (top panel) and to H08S (bottom panel) for
the source depth of 200 m.
- Figure 3.9. Absolute value of the amplitude $A_m(r, \omega)$ (arbitrary unit) (see 66
Equation (3.12)) of modes 1 to 4 at 20 Hz as a function of range
numerically modelled using the coupled-mode model for the

propagation path from Vincennes Bay to HA01 (top panel) and H08S (bottom panel).

- Figure 3.10. Absolute value of the amplitude (arbitrary unit) of modes 1 to 4 at the receivers of HA01 (top panel) and H08S (bottom panel) numerically modelled using the coupled-mode model. 67
- Figure 3.11. The sound speed profiles typical for the acoustic path sections in Southern Ocean south of ACZ (panel (a1)) and in the Indian Ocean (panel (b1)); the corresponding shapes of mode 1 at 2, 10 and 40 Hz (panels (a2) and (b2)), shapes of the first three modes at 10 Hz (panels (a3) and (b3)), and the group velocities of the first three modes (panels (a4) and (b4)) versus frequency. 69
- Figure 3.12. Variations of the group velocity (m/s) of modes 1 (top panel) and 2 (bottom panel) versus frequency and range along the modelled acoustic path from Vincennes Bay in Antarctica to the HA01 station. 70
- Figure 3.13. The waveform of a Gaussian pulse with a width of 20 ms and unity amplitude filtered in the frequency band of 3-50 Hz. 72
- Figure 3.14. Modelled waveform of the signal received on the HA01 hydrophone from an ice event in Vincennes Bay. The waveform of the emitted signal is shown in Figure 3.12. 73
- Figure 3.15. Spectrogram of the modelled signal shown in Figure 3.13. 73
- Figure 3.16. (a) Signals from the same series of transient noise events occurred on Day 117 in 2004 and recorded on the Casey sea noise logger in Antarctica (top) and at the HA01 station (bottom), and the 76

waveform (b) and spectrogram (c) of the first event in the series at the noise logger (top) and HA01 (bottom).

- Figure 3.17. The waveform of signal from an ice event recorded on Day 102 in 2004 on the Casey sea noise logger (top panel) and at HA01 (middle panel), and the spectrogram of the signal at HA01 (bottom panel). 77
- Figure 3.18. Three MODIS satellite images of the Shackleton Ice Shelf and the surrounding ocean taken on Days 276 (top panel), 282 (middle panel) and 288 (bottom panel) in 2007. The red circles indicate the new iceberg calved on Day 276. The red arrow shows the bearing direction from HA01 to the source of underwater noise. 80
- Figure 3.19. The waveform (top panel), spectrogram (middle panel) and measured back-azimuth of the signal from an ice calving event off Shackleton ice shelf observed at the HA01 station on Day 276 in 2007. 81
- Figure 4.1. RMS bearing errors for HA01 as a function of the back-azimuth to located sources and the standard deviation of the receivers' horizontal position. 88
- Figure 4.2. RMS bearing errors for H08S station as a function of the back-azimuth to located sources and the standard deviation of the receivers' horizontal position. 89
- Figure 4.3. The spatial variation of the mode 1 wavenumber at 20 Hz in the Indian and Southern Oceans. The sound speed is derived from the winter climatology data. The horizontal resolution is 0.1° . Two transects (red lines) across the Indian Ocean from $[45^\circ\text{S } 90^\circ\text{E}]$ to 94

[9°N 62.5°E] (line **A**) and the Southern Ocean [45°S 90°E] to [64.8°S 97.3°E] (line **B**) are also shown in the map.

- Figure 4.4. The sound speed profile in the month of August and the bathymetry along the transect across the Indian Ocean from [44°S 90°E] to [9°N 62.5°E]. 96
- Figure 4.5. The azimuth deviation rate of rays from the geodetic line due to the wavenumber gradient along the transect in the Indian Ocean from [44°S 90°E] to [9°N 62.5°E]. Left panel shows the azimuth deviation rate for modes 1-3 at 20 Hz and the right panel shows the deviation rate for mode 1 at different frequencies. 97
- Figure 4.6. The sound speed profile in the month of August and the bathymetry along the transect crossing the ACZ and the Southern Ocean from [45°S 90°E] to [64.8°S 97.3°E]. 98
- Figure 4.7. The azimuth deviation rate of rays from the geodetic line due to the horizontal wavenumber gradient along the transect in the southern Ocean from [45°S 90°E] to [64.8°S 97.3°E]. Left panel shows the deviation rate of the first three modes at 20 Hz and the right panel shows the same for mode 1 at different frequencies. 99
- Figure 4.8. Bearing deviation from the true azimuth observed at HA01 for noise sources located in the Indian and Southern Oceans. The deviation errors are due to horizontal refraction calculated for mode 1 at 20 Hz (left panel) and 50 Hz (right panel) for winter climatology data. 102
- Figure 4.9. Same as Figure 4.8, but for H08S. 103

- Figure 4.10. Bearing errors due to horizontal refraction numerically predicted 105
for mode 1 at frequencies of 4.5Hz, 7.5Hz and 10.5Hz. Climatology
data are taken for the winter season.
- Figure 4.11. Top panel: The 10-minute signal of the main-shock of the Great 106
Sumatra-Andaman Earthquake received at one channel of the HA01
station; Bottom panel: The back-azimuth estimates to the
earthquake made from HA01 station in three different 1/3-octave
frequency bands with the central frequencies of 4.5Hz, 7.5Hz and
10.5Hz.
- Figure 4.12. Track of the R/V Melville cruise in May/June 2003 overlain on 111
shaded bathymetry of the Indian Ocean. The IMS hydroacoustic
stations are shown by triangles and the locations of explosions are
shown by circles (Blackman et al., 2003).
- Figure 4.13. The patterns of the HA01 triplet in the Cartesian coordinate system 115
before and after correction. The blue line represents the pattern
based on the relative positions of the moorings determined during
deployment; the red line is the result obtained after correction of the
relative coordinate using Equation (4.16) and the seven explosive
signals. The coordinates of hydrophone 1 are fixed as a reference
position.
- Figure 4.14. Systematic bearing error as a function of back-azimuth from HA01 116
calculated for the original and corrected coordinates of the
HA01 moorings.
- Figure 4.15. The patterns of the H08S triplet in the Cartesian coordinate system 119
before (blue) and after (red) correction.

- Figure 4.16. Systematic bearing error as a function of back-azimuth from H08S 120
calculated for the original and corrected coordinates of the H08S
moorings.
- Figure 4.17. Back-azimuth to a series of harmonic tremor signals received at 121
HA01 as a function of signal arrival times. Blue and red dots show
the measurements made respectively before and after correction for
the systematic bearing error of about 0.9° .
- Figure 4.18. Bearing error along the path from HA01 to Dibble Glacier in 122
Antarctica due to horizontal refraction of mode 1 at 10 Hz in
summer. The launch angle at HA01 is 163.5° . The error is
calculated as a residual of the true back-azimuth to an acoustic
source located along the path at different distances from HA01 and
the launch angle of the path from HA01. For the source location in
the Antarctica ($R > 3500$ km), the error is expected to be about
 0.05° .
- Figure 4.19. Two MODIS satellite images taken on Julian days 256 (left panel) 123
and 268 (right panel) in 2003 showing the locations of iceberg
C008 drifting along the ice shelf off Victor Bay (highlighted by red
circles). The iceberg position on day 261 is shown in the right panel
by a blue colour iceberg contour (highlighted by a blue circle),
placed according to the AITD data. The blue and red bars in the
right panel show the directions from HA01 to the detected tremor
events measured before (blue) and after (red) correction of the
HA01 array geometry. The bar width indicates the standard
deviation of measurements.
- Figure 5.1. Localization of nine intense Antarctic ice events, observed at both 129

HA01 and H08S stations in 2003. Red dots indicate the locations of the events by triangulation from the two stations.

Figure 5.2. Waveforms (top panels) and spectrograms (bottom panels) of one 130
of the signals from the same Antarctic ice event recorded at HA01
(left panels) and H08S station (right panels).

Figure 5.3. Locations of four selected ice events detected at HA01 and HA08 131
and error ellipses of 95% confidence (red lines). The white lines
show the source locations that satisfy the travel time difference of
signals measured at both stations. The error ellipses were
calculated assuming that the random errors of back-azimuth
estimates are Gaussian distributed with a standard deviation of
0.5°.

Figure 5.4. The spectrogram of an ice event signal received at the HA01 station 138
(left panel) and its fine time-frequency structure measured with a
resolution of 0.5 Hz (right panel).

Figure 5.5. Fitting the theoretical (red lines) power spectrum of a signal 138
segment to the measured one (blue line) by shifting the theoretical
spectrum around the measured spectrum with the mode 1 frequency
of 11.2 Hz.

Figure 5.6. Ice event location (left panel) and a comparison of its errors (right 141
panel) estimated for the location by triangulation from the HA01
and H08S stations (red) and for the location using the mode 1
frequency dispersion of the signal received only at HA01.

Figure 5.7. Left panel: the typical monthly sound speed profile in the top 500- 142
m water layer in four different seasons in the Southern Ocean;

Right panel: the error variation of the range estimates to the ice event obtained through frequency dispersion inversion of the mode 1 arrival at HA01 resulting from using different monthly climatology data. The error is calculated relative to the range to the location found by the intersection of two back-azimuths from HA01 and H08S.

Figure 5.8. Comparison between the modelled (blue colour) and observed (red colour) relative arrival times of multipath arrivals (left panel) and the arrival time difference of adjacent arrival peaks (right panel). In the model, the distance from the sound source is assumed to be 180 km. 144

Figure 5.9. Histogram of the mode 1 cut-off frequency of the Antarctic ice events observed at HA01 over the period from late 2001 to 2005. The frequency bin size is 0.4 Hz. 145

Figure 5.10. Histograms of the mode 1 cut-off frequencies of the ice events observed at HA01 within different back-azimuth sectors (shown in each panel) over the period from late 2001 to 2005. The frequency bin size is 0.4 Hz. 146

Figure 5.11. Histograms of the minimum sea depth along acoustic paths from ice events to HA01 derived from the mode 1 cut-off frequency of the ice signals received at HA01 over the period from late 2001 to 2005. Sea depth estimates are made for the soft (top panel), intermediate (middle panel) and hard bottom acoustic models. The depth bin size is 20 m. 148

Figure 6.1. Histogram of the back-azimuth to the ice events observed at the HA01 station over the whole period from late 2001 to early 2008. 152

The histogram bin width is half a degree. The vertical bars with numbers superimposed on the histograms indicate the clusters of most numerous ice events.

- Figure 6.2. The spatial distribution of ice events along the Eastern Antarctic coastline represented by projecting the events back-azimuths shown in Figure 6.1 onto the Antarctic coastline. The number of events observed in half-degree azimuth bins is indicated by size and colour-coded dots. 153
- Figure 6.3. Histograms of the back-azimuths to the Antarctic ice events observed at the HA01 station in each year from 2002 (top panel) to 2007 (bottom panel). The azimuth bin width of the annual histograms is half a degree. The vertical bars of the event clusters are the same as those in Figure 6.1. 155
- Figure 6.4. Mean value and standard deviation of the signal level versus the back-azimuth of the Antarctic ice events observed at HA01 in summer (red) and winter (blue) over the six-year period from 2002 to 2007. The frequency band of measurements is 3-30 Hz. 159
- Figure 7.1. Unfiltered variations of the weekly occurrence frequency of ice events detected at the HA01 station over the 6-year period from late 2001 to early 2008. 162
- Figure 7.2. Median filtered variation of the weekly occurrence frequency of Antarctic ice events detected at HA01 over the 6-year period from late 2001 to early 2008. The window length of the median filter is 8 weeks. 163
- Figure 7.3. The principal basis function of the periodicity transform applied to 164

the occurrence frequency variation shown in Figure 7.1. The mean value of the whole time series is added to the basis function in the plot. The period of this function is 53 weeks.

- Figure 7.4. The residual variation of the occurrence frequency without the seasonal component (blue line) obtained by subtracting the principal periodic basis of the periodicity transform shown in Figure 7.3 from the original time series shown in Figure 7.1. The red line shows the linear fit to the residual variation. 165
- Figure 7.5. Power spectra of the temporal variation in the occurrence frequency of ice events detected at the HA01 station over the 6-year period from late 2001 to early 2008, estimated by periodogram (blue line) and eigenvector (red line) methods. 166
- Figure 7.6. Fragment of the cross-correlation between the occurrence frequency of ice events and the annual cycle, taken around its maximum. The cross-correlation plot shows that the occurrence frequency correlates with the annual cycle with a 20-week time lag. 168
- Figure 7.7. Monthly climatology SST averaged over the Eastern Antarctic coastal zone from 63°S to 65°S and 60°E to 160°E. 169
- Figure 7.8. Fragment of the cross-correlation function between the occurrence frequency of ice events and the Eastern Antarctica SST, taken around its maximum at 13.5 weeks. 170
- Figure 7.9. Weekly average air temperature measured at Casey station over the six-year period from 2002 to 2007. 171
- Figure 7.10. Cross-correlation between the occurrence frequency of ice events 172

and the weekly average air temperature at Casey in 2002 - 2007.
The correlation has its maximum at about 17-week time delay.

- Figure 7.11. Weekly averaged absolute values of the wind speed measured at Casey station over the six-year period from 2002 to 2007. 173
- Figure 7.12. Principal periodic basis of the time series shown in Figure 7.11 derived from the periodicity transform and corrected for the mean value. The period of this basis function is 53 weeks. 174
- Figure 7.13. The cross-correlation function between the occurrence frequency of ice events and the principal periodic basis of the weekly average wind speed at Casey from 2002 to 2007 as shown in Figure 7.12, taken around its maximum. The wind speed variation correlates with the occurrence frequency with a time lag of 9 weeks. 175
- Figure 7.14. Daily Antarctic sea ice extent observed over a 5-year period from 2001 to 2004. 176
- Figure 7.15. The cross-correlation between the occurrence frequency of ice events and the Antarctic sea ice extent, taken around its maximum at a time lag of -14 weeks. 177
- Figure 7.16. Temporal variations of the weekly averaged signal level from the ice events observed at HA01 over the period from 2002 to 2007 (blue line with dots) and the principal periodic basis derived from the periodicity transform and corrected for the mean value of the time series (red line). The period of the basis function is 53 weeks. 178
- Figure 7.17. The cross-correlation between the occurrence frequency and signal level of ice events observed at HA01 in 2002 – 2007, taken around 179

its maximum. The time lag between the seasonal variations in the signal level and occurrence frequency is about 11.5 weeks.

- Figure 7.18. Time lags (weeks) from the annual reference cycle estimated for the 180 seasonal variations of the acoustic and metocean parameters which are: solar radiation (**SR**); air temperature in Eastern Antarctic coastal zone (**AT**); sea surface temperature off Eastern Antarctica (**SST**); signal level of ice events received at HA01 (**SL**); occurrence frequency of ice events detected at HA01 (**OF**); wind speed at Casey in the Eastern Antarctica (**WS**); and Antarctic sea ice extent (**IE**).
- Figure A.1. Waveform (left panel) and spectrogram of a signal received at 204 HA01 from an ice event in summer. The arrival of mode 1 marked out by the oval can be easily recognized.
- Figure A.2. Waveform (left panel) and spectrogram of an ice event detected in 205 summer. Mode 1 contributes most to the energy of this signal.
- Figure A.3. Waveform (left panel) and spectrogram of an ice event detected in 206 summer. The arrivals of higher modes highly scattered in the frequency-time domain contributes much to the total energy of this signal. The frequency components around 15 Hz almost disappeared in the spectrum of mode 1 arrival.
- Figure A.4. Waveform (left panel) and spectrogram of a signal received at 207 HA01 from an ice event in winter. The signal bandwidth is noticeably narrower than that of the typical ice events observed in summer, which is a result of higher attenuation at higher frequencies due to stronger scattering by the sea surface roughness in the winter polar conditions.

Figure A.5. Rectangular spectrogram matrix used to determine the energy ratio 209
of mode 1 arrival and background noise in the analysis window.
The dashed lines show the frequency dispersion curves numerically
modelled for the winter environmental conditions along the longest
path to the Antarctic coast (upper line) and the summer conditions
along the shortest path to Antarctica.

Figure A.6. Same as Figure A.5, but for the signal shown in Figure A.3. The red 210
triangle indicates the upper off-diagonals in which the spectral
energy components are summed to estimate the background noise
level.

LIST OF TABLES

Table 2.1.	The principal characteristics of the HA01 hydroacoustic station.	13
Table 3.1.	Properties of the seafloor acoustic model chosen for modelling the acoustic propagation along the path from Antarctica to the Indian Ocean.	53
Table 4.1.	Mean values and standard deviation (SD) of back-azimuth estimates for six selected Antarctic ice tremor events and four seismic events. TR - tremor event; SE - seismic event; MS and AS stand for the main shock and aftershock of the Great Sumatra-Andaman Earthquake respectively.	90
Table 4.2.	The mean values and standard deviation (SD) of back-azimuth estimates for 13 selected series of airgun signals from different off-shore seismic surveys. SSE means seismic survey events.	92
Table 4.3.	The sources of underwater acoustic explosions and their shot times, coordinates, shot depths, true and measured back-azimuth from HA01, inverted group velocities, bearing errors due to horizontal refraction, and the azimuth residual values. The azimuth residual is the difference between the true and measured azimuth, minus the bearing error due to the effect of horizontal refraction (HR denotes horizontal refraction).	114
Table 4.4.	The sources of underwater acoustic explosions and their shot times, coordinates, shot depths, true and measured azimuths from H08S, inverted group velocities and the azimuth residual values. The azimuth residual is the difference between the true and measured	118

azimuth, minus the bearing error due to the effect of horizontal refraction (HR denotes horizontal refraction)

- Table 5.1. Arrival times of selected signals and coordinates of their origin 133
located from the back-azimuth measurements by triangulation and
verified via numerical modelling of travel time differences
- Table 6.1. Back-azimuth sectors of the clusters of more numerous ice events, 154
the longitudes of the Antarctic coastline corresponding to the edges
of these sectors, and the Antarctic ice-related features observe within
these sectors.

CHAPTER 1

INTRODUCTION

1.1 Overview

This chapter gives an introduction to this PhD research project and an overview of the thesis structure. A review of the research background, which leads to the motivation and provides rationale of the study, is presented in Section 1.2. The objectives of this study are given in Section 1.3, followed by the outline of the thesis.

1.2 Rationale of the study

1.2.1 Ice disintegration as one of indicators of climate change

Climate is a statistical description of the mean and variability of relevant meteorological and oceanographic quantities over a period of time ranging from months to years. These quantities are most often variables over the Earth surface such as temperature, wind, precipitation, and some other meteorological characteristics (Houghton et al., 2001). The climate of a region is affected by a number of factors, such as its latitude, terrain, altitude, persistent ice or snow cover, as well as nearby oceans and their currents. In the sense of long-term changes, the state of the global climatic system is always varying due to extraterrestrial factors (e.g. gradual change in Solar output and Solar system geometry), internal large-scale processes in the coupled ocean, atmosphere and land systems, and influences of human activities (Solomon et al., 2007). Global warming, i.e. the increase in the average temperature of the Earth's near-surface air and oceans since the early 20th century and its projected continuation, which is believed by many to be induced by a substantial increase of the emission of greenhouse gases (Lashof and Ahuja, 1990), is now an overwhelming scientific consensus and has become an increasing concern for environmental scientists and the general public (Solomon et al., 2007).

Among the diverse regions of the Earth, the Polar regions are particularly sensitive to global climate change. Most of the recent global climate and circulation models predict that the warming caused by an increase in atmospheric CO₂ will affect the poles first and most strongly (e.g. Manabe et al., 1992, Manabe et al., 1994). Rising temperature causes melting of ice sheets and disintegration and melting of ice shelves. In the past two decades, the ice calving intensity on the Antarctic shelf, one of the major indicators of global climate change (Mercer, 1978, Doake and Vaughan, 1991, Scambos et al., 2000), has been extraordinary, not only in the frequency, but also in the volume of ice mass calved. For example, several massive tabular icebergs broke off from the Ross and Larsen ice shelves in West Antarctica (Perkins, 2001, Rott et al., 1996, Rott et al., 2002, Shepherd et al., 2003). The West Antarctic Ice Sheet rests on a submerged volcanic archipelago, with great ice streams flowing relatively rapidly and forming two major ice shelves (Ross and Ronne-Filchner) toward the sea. If the grounded part of the West Antarctic Ice Sheet was to float or melt, sea level would rise about 6 meters around the world, with devastating effects, particularly on the continental coasts and low-lying islands (Huybrechts and Oerlemans, 1990).

Because of the crucial role played by Antarctica in the global climate system, it is essential to continuously monitor and analyse changes in Antarctic ice rifting and breaking processes leading to disintegration of the ice shelves, and to further understand the effect of those changes on the rest of the planet.

1.2.2 Conventional ice shelf monitoring methods

Two different approaches to monitor ice in the Polar regions are generally used: remote sensing and local seismic-acoustic observations. The remote sensing approach can be either active or passive remote sensing of ice activities from above the surface using various forms of electromagnetic radiation (e.g. Simon et al., 1994). The observation is usually performed using sensors mounted in or on a suitable platform, which can be an in-shore station, a helicopter/airplane, or a satellite. Figure 1.1 shows three satellite images which clearly demonstrate the evolutionary process of a large iceberg calving from the Pine Island

Glacier in the Amundsen Sea during the period from late 2000 to late 2001 [http://visibleearth.nasa.gov/view_rec.php?id=2319]. A number of research centers worldwide have strength in remote sensing of Polar snow and ice, in particular the Center for Remote Sensing of Ice Sheet (CReSIS) in the University of Kansas, US (<https://www.cresis.ku.edu/>), National Snow and Ice Data Center (NSIDC), US (<http://nsidc.org/>), Center for Polar Observation and Modelling (CPOM), UK (<http://www.cpom.org/>), Antarctic Sea Ice Processes & Climate (ASPeCt) (<http://www.aspect.aq/>), and Australian Antarctic Division (<http://www.aad.gov.au/>). Particularly, year-round high-resolution satellite images of the Antarctic ice shelves provided by NSIDC (http://nsidc.org/data/iceshelves_images/) can be used to monitor major ice streams and outlet glaciers along the Antarctic coast. Although remote sensing of the ice cover is far-reaching and comprehensive in its coverage, and can well observe post factum massive calving events, it lacks for the capability to monitor numerous ice shelf rifts and breaks of smaller scale, which precede major calving events and contribute substantially to the ice disintegration processes around the entire continent (Perkins, 2001).

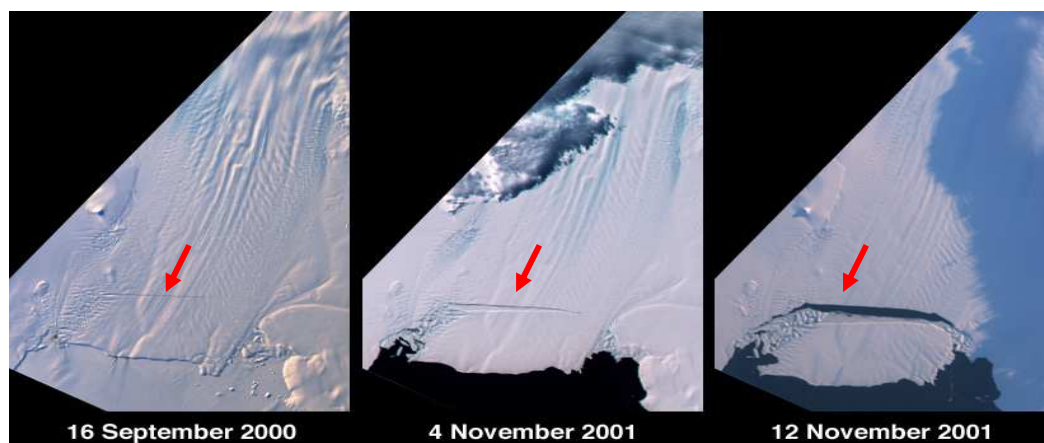


Figure 1.1. Satellite images of the rifting and calving process of a large iceberg from the Pine Island Glacier in the Amundsen Sea during the period from late 2000 to late 2001 [http://visibleearth.nasa.gov/view_rec.php?id=2319]. The red arrows point at the ice rift position.

Local observations with a network of seismo-acoustic stations deployed on ice shelves or on icebergs can provide detailed data for detection of invisible rifting ice events and for investigation of their mechanism and process (MacAyeal et al., 2008). Other in-situ methods of observation are also used to monitor ice rifting processes. For example, in the joint Australian-US experiment on the Amery Ice Shelf, seismo-acoustic recordings were accompanied with geodetic observations of ice shelf fractures by measuring the horizontal and vertical motion of ice across the fracture zone with the use of GPS units (Bassis et al., 2005). The deployment scheme of a seismo-acoustic network near the tip of a large active rift on the Amery Ice Shelf is shown in Figure 1.2. This observation method requires great effort and expense for logistic support of the Polar expeditions and at present is not capable of providing long-term, large-scale monitoring of the entire Antarctic ice shelf.

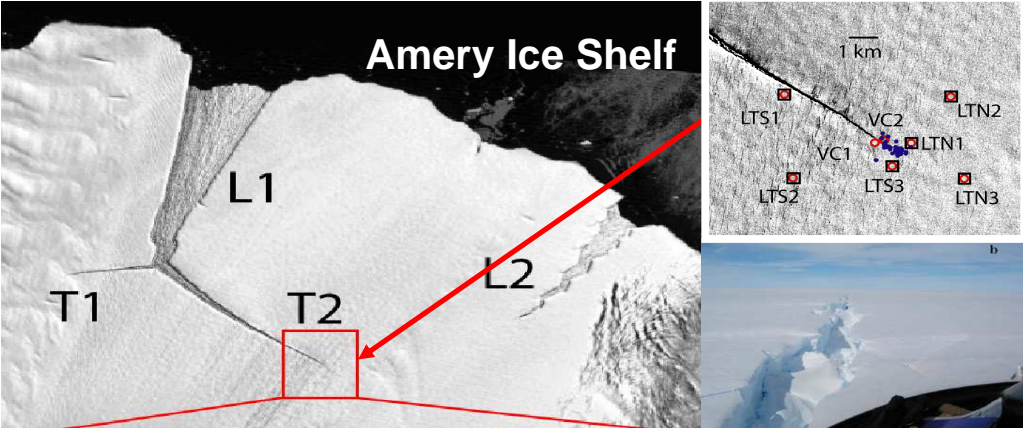


Figure 1.2. A network of seismo-acoustic stations across the fracture zone in the Amery ice shelf deployed in the joint Australian-US experiment (Bassis et al., 2005). L and T in the left panel represent longitudinal-to-flow rift and transverse-to-flow rift respectively. The right panel shows the photo of the tip of the rift T2 (bottom) and the location of the instruments around the tip (top). VC refers to seismic station and LTS and LTN refer to the GPS baselines.

1.2.3 Remote Hydroacoustic Monitoring as an innovative approach to ice monitoring

Combined with the existing methods for detecting and assessing ice break up in Antarctica, remote acoustic observation using hydroacoustic listening stations in the ocean can provide additional and potentially very efficient means to monitor ice shelf breaks over large sectors of the Antarctic coast. This new approach is believed to allow us to track out the occurrence frequency and location of numerous ice break-up events in the Antarctic shelf.

Cracking and calving of ice shelves produce intense, low frequency noise in the form of elastic (both compressional and shear) waves propagating in the ice bulk and converting into acoustic waves in the surrounding water (Bassis et al., 2005). These low frequency acoustic signals can propagate over thousands of kilometers in the ocean depending on the specific environmental conditions along the propagation paths (Heaney et al., 1991, Munk and Baggeroer, 1994, Dushaw et al., 2001).

The capability of acoustic monitoring to remotely observe large-scale changes (including climatic ones) in the ocean has been examined and proven in several international experiments and projects, such as the Heard Island Feasibility Test experiment (Munk and Baggeroer, 1994) and the Acoustic Thermometry of Ocean Climate (ATOC) project (Dushaw et al., 2001). The Transarctic Acoustic Propagation experiment in 1994 detected basin-scale warming of the Intermediate layer of Atlantic water in the Arctic Ocean for the first time (Mikhalevsky et al., 1995, Gavrilov et al., 1995, Mikhalevsky et al., 1999). The Arctic Climate Observations using Underwater Sound (ACOUS) program with 14-month long experimental observations revealed several peculiarities of current warming in the Arctic Ocean (Mikhalevsky and Gavrilov, 2001, Gavrilov and Mikhalevsky, 2002, Brekhovskikh et al., 2002). Moreover, the ACOUS experiment proved the capability of acoustics to remotely monitor the mean thickness of sea ice in the Arctic Ocean (Gavrilov and Mikhalevsky, 2006).

In the past decade, many efforts have been made on the development of hydroacoustic systems and the application of hydroacoustic observation to remotely monitor sub-sea seismic and volcanic activities and movements of large icebergs (Fox et al., 1995, Fox and Dziak, 1998, Hagerty et al., 2000, Smith et al., 2003, Graeber and Piserchia, 2004, Dziak et al., 2007, Talandier et al., 2002, Talandier et al., 2006). The installation of a global network of hydroacoustic stations (Lawrence, 1999) and creation of the International Data Center (Bratt, 1996, Hanson et al., 2001) as part of the International Monitoring System (IMS) of the Comprehensive Nuclear-Test-Ban Treaty (CTBT) program provide a unique opportunity to investigate sources of underwater noise in the ocean on a broader scale than it was possible before. As shown in Figure 1.3, there are six hydrophone stations of the IMS hydroacoustic network deployed in the Indian Ocean (HA01 off Cape Leeuwin, Western Australia; HA04 off Crozet Island, France; and HA08 off the Chagos Archipelago, Diego Garcia US Navy support facilities), in the Pacific Ocean (HA11 off Wake Island, USA and HA03 off Juan Fernandez Island, Chile) and in the Atlantic Ocean (HA10 off Ascension Island, USA). More details about the hydrophone stations will be given in Chapter 2.

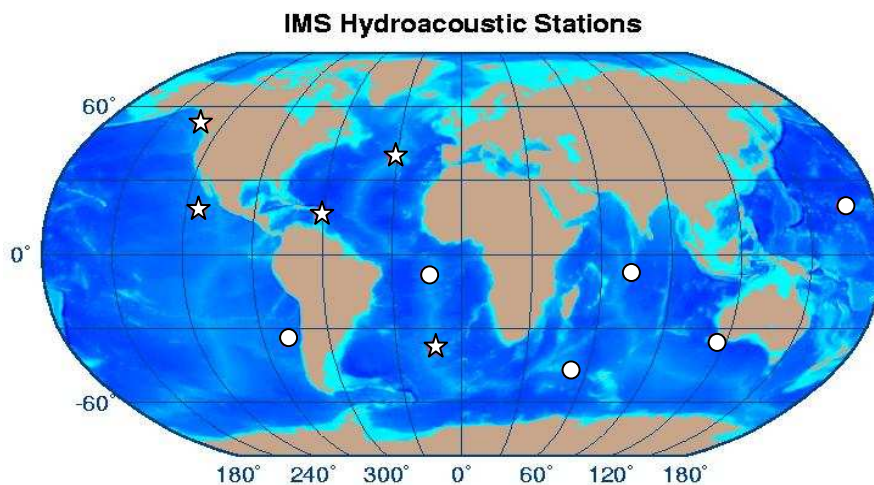


Figure 1.3. The global network of CTBT IMS hydroacoustic stations. Star signs indicate the locations of the 5 IMS T-phase stations deployed on small islands and circle signs show the 6 hydrophone stations in the ocean.

Sea noise recordings at the IMS hydroacoustic stations have been processed in different studies, which involved primarily scientific objectives rather than nuclear test monitoring. Significant results on Antarctic ice-related events have been obtained using the IMS hydroacoustic data (e.g. Chapp et al., 2005, Hanson and Bowman, 2006, Talandier et al., 2006). Chapp et al. (2005) reported two distinct types of low-frequency harmonic tremor signals observed at the hydroacoustic stations in the Indian Ocean. They are correlated with drifting icebergs and glacial features along the coast of Eastern Antarctica. The generation mechanism of both signal types was interpreted as acoustic resonant emission by an ice plate of whole icebergs or by fluid-filled cavities within ice masses. Using a network of hydrophones and seismic sensors deployed on an iceberg, MacAyeal et al. (2008) recently revealed that certain signals referred to as iceberg harmonic tremors received from tabular icebergs were produced by a stick-slip process during collisions between large iceberg and ice shelf masses, which is consistent with the conclusion made by Talandier et al. (2006). Hanson and Bowman (2006) referred to transient signals from the Eastern Antarctic coast located by the hydroacoustic stations in the Indian Ocean as ice events, and carried out an analysis of spatial and temporal variations of such events observed during 286 days in 2003. Although the dataset analysed was relatively short, Hanson and Bowman revealed seasonal change in the frequency of occurrence of ice events.

Despite the significant results achieved in the above studies, there have been no specific investigations made 1) to characterize numerous transient signals arriving regularly from Antarctica and examine their origin, 2) to analyse long-term changes in their occurrence and spatial distribution and 3) to study correlation of the underwater noise generated in Antarctica with changes in the environmental parameters, including seasonal variations, interannual changes and potential trends associated with climate change. It is believed that most of the transient acoustic signals propagated in the ocean from Antarctica are emitted by ice rifting and breaking processes on the Antarctic ice shelves and icebergs. This supposition can be corroborated through other kinds of observation conducted in some selected regions of the Antarctic shelf in parallel with the remote acoustic observation. In particular, underwater acoustic measurements made in Antarctica close to the shore and an analysis of the satellite imagery of ice shelves and icebergs can be used for this purpose. An

analysis of temporal and spectral characteristics of the transient signals received from Antarctica is another way to distinguish ice rifting and breaking events detected at the remote hydroacoustic stations from other sources of transient noises in the ocean.

The class of transient signals arriving at the IMS hydroacoustic stations from ice rifting and breaking events on the Antarctic shelf will be hereinafter referred to as ice events in most instances, which does not include harmonic tremors and other long lasting noises emitted by icebergs.

1.3 Aims of the study

Driven by the motivation described above, this study aims to investigate the feasibility of remote monitoring of Antarctic ice rifting and breaking activities on ice shelves and icebergs using the two IMS hydroacoustic stations in the Indian Oceans, the Cape Leeuwin station (HA01) and the Diego Garcia South station (H08S), and to explore the correlation of Antarctic ice breaking noise with various climate related factors. To achieve this goal, this study considers a number of relevant scientific and technical aspects with the following specific objectives:

1. Collect and process acoustic data recorded at the two IMS hydroacoustic stations in the Indian Ocean; identify the most likely sources of remote low-frequency noise recorded at these stations and classify signals received from these sources; select the signals arrived presumably from Antarctic ice breaking events;
2. Provide a physical interpretation of the principle characteristics of the signals received from Antarctic ice events by modelling long-range propagation from Antarctica to the IMS stations; examine the origin of the signals interpreted as ice events by comparing the ice events remotely observed at the IMS stations with underwater acoustic recordings made in Antarctica, with satellite imagery of some ice events and with results of numerical modelling;
3. Analyse bearing accuracy of the hydroacoustic stations. Such an analysis is essential for accurate localization of ice events and for an analysis of their spatial distribution;

4. Locate Antarctic ice events utilizing one or two hydroacoustic stations;
5. Analyse the spatial variation of the occurrence frequency of the ice events and its correlation with the Antarctic glacial features.
6. Explore long-term changes in the occurrence frequency and intensity of the ice events and analyse their association with variations of climate related metocean characteristics.

1.4 Structure of the thesis

The project involves a number of somewhat distinct problems and therefore, rather than a separate literature review chapter being provided, the background knowledge and literature relevant to the specific problem will be introduced and reviewed in the corresponding chapter where necessary.

Chapter 2 presents the methods of collection and processing of hydroacoustic data recorded at the two IMS hydroacoustic stations in the Indian Ocean. Classification of sources of coherent signals received at the Cape Leeuwin hydroacoustic station is described, and the temporal and spatial distributions of all coherent signals received at both HA01 and H08S hydroacoustic stations are displayed. The statistical analysis of the principle characteristics of Antarctic ice events is also demonstrated in this chapter.

The origin of signals characterized as ice events is investigated and verified in Chapter 3 using other kinds of experimental observations as well as numerical modelling. A normal mode model is used for numerical modelling of sound propagation from Antarctica to the IMS hydroacoustic stations in the Indian Ocean. This includes an investigation of the transmission loss, which is due in particular to seafloor interaction and sea surface scattering along the propagation path, the effects of mode coupling and frequency dispersion, as well as modelling of the time-frequency structure of the received signals. The chapter ends with examples of experimental observations confirming the correlation between the received signals classified as ice events and the Antarctic ice shelf breaking processes.

An analysis of the bearing accuracy from the two IMS hydroacoustic stations is carried out in Chapter 4. The errors of back-azimuth estimation for hydroacoustic events from the IMS hydroacoustic stations caused by various factors are analysed. These factors include: possible errors in the arrival time difference measurements of signals received on different hydrophones, and random and systematic deviations of hydrophones' positions from the touch-down locations of the hydrophones' moorings determined during installation. The effect of horizontal refraction on bearing error estimation is also explored in this chapter.

Chapter 5 explores different approaches to localization of Antarctic ice events, using either one or two hydroacoustic stations. Particularly, the feasibility of locating sources of transient sound signals from Antarctica using only the Cape Leeuwin station is examined, based either on a comparison of the modelled and measured time-frequency structures of the received signals or on the measured cut-off frequencies of the signal spectra.

Chapter 6 examines the spatial variation of the Antarctic ice events and its association with the Antarctic glacial features. The azimuth dependence of the propagation loss due to the range from the IMS stations to Antarctica varying with the direction of observation, which may potentially affect the apparent spatial distribution, is also investigated.

Chapter 7 explores the long-term temporal variation of the ice events' occurrence and intensity. This includes an analysis of variations in the occurrence frequency of ice events in both time and frequency domains. Moreover, an examination of the correlation between the occurrence frequency of ice events and climate-related metocean characteristics is also made. The metocean characteristics considered are in particular the sea surface temperature off Eastern Antarctica, the air temperature and wind speed over the Eastern Antarctica coastal zone, and Antarctic sea ice extent.

A summary of the findings in this study and recommendations for the future work are given in Chapter 8.

CHAPTER 2

CTBT HYDROACOUSTIC DATA PROCESSING AND HYDROACOUSTIC EVENT CLASSIFICATION

2.1 Overview

This chapter describes the method of collection of hydroacoustic data at two of the three IMS hydroacoustic stations in the Indian Ocean, preliminary processing of the collected data and classification of sources of the received signals.

Section 2.2 provides a brief introduction on the IMS hydroacoustic network and technical details of two of the three hydroacoustic stations in the Indian Ocean, namely the Cape Leeuwin station (HA01) and the Diego Garcia South station (H08S). Section 2.3 is focused on hydroacoustic data collection activities for the study, which involved the efforts from the Centre for Marine Science and Technology (CMST), Curtin University and Technology, and its collaborators: Geoscience Australia and the Comprehensive Nuclear-Test-Ban Treaty Organization. Details of the preliminary data processing will be given in Section 2.4. This section describes the algorithm for detection and selection of coherent signals from remote sources of underwater noise in the continuous sea noise recordings through data processing. In section 2.5, the most common sources of spatially coherent signals received at the IMS stations are classified based on the waveform and spectrogram features of the signals. Section 2.6 presents the temporal and spatial distribution of all sources of coherent signals received at both HA01 and H08S stations. A statistical analysis of principle characteristics of the signals received from ice events, such as their signal level, the frequencies of peak power spectral density, and the signal-to-noise-ratio, is considered in Section 2.7. A brief summary of this chapter is given in section 2.8.

2.2 Background

2.2.1 IMS hydroacoustic network

The Comprehensive Nuclear-Test-Ban Treaty (CTBT) is a convention that outlaws nuclear test explosions, and upon its entry into force, an international organization, the Comprehensive Nuclear-Test-Ban Treaty Organization (CTBTO) was established with the headquarters in Vienna, Austria (www.ctbto.org) for the purpose of monitoring the countries' compliance with the treaty. The verification regime of the CTBT is designed to detect any nuclear explosion conducted on Earth – underground, underwater or in the atmosphere. As one of the critical elements of the CTBT verification regime, the International Monitoring System consists of 321 monitoring stations and 16 laboratories built worldwide for monitoring any sign of nuclear explosions using four complementary verification methods: seismic, hydroacoustic, infrasound and radionuclide monitoring methods. The network of the IMS hydroacoustic stations uses underwater sounds to monitor the oceans for underwater explosions. The network has 11 stations - six underwater hydrophone stations and five T-phase stations on islands - in eight countries around the world at the locations shown in Figure 1.3.

An IMS hydrophone station has either one or two so-called triplets, i.e. triangular horizontal arrays of three hydrophones separated 1-2 km from each other. Figure 2.1 shows this type of layout for the HA01 station. The hydrophones are submerged near the Sound Fixing and Ranging (SOFAR) channel axis at a depth of about 1100 meters, so that they are capable of long-range acoustic reception. The stations are cabled to the shore, which allows data transmission in real time via satellite to the International Data Center (IDC) in Vienna. The principal characteristics of the HA01 hydroacoustic station are listed in Table 2.1 (Lawrence, 2003).

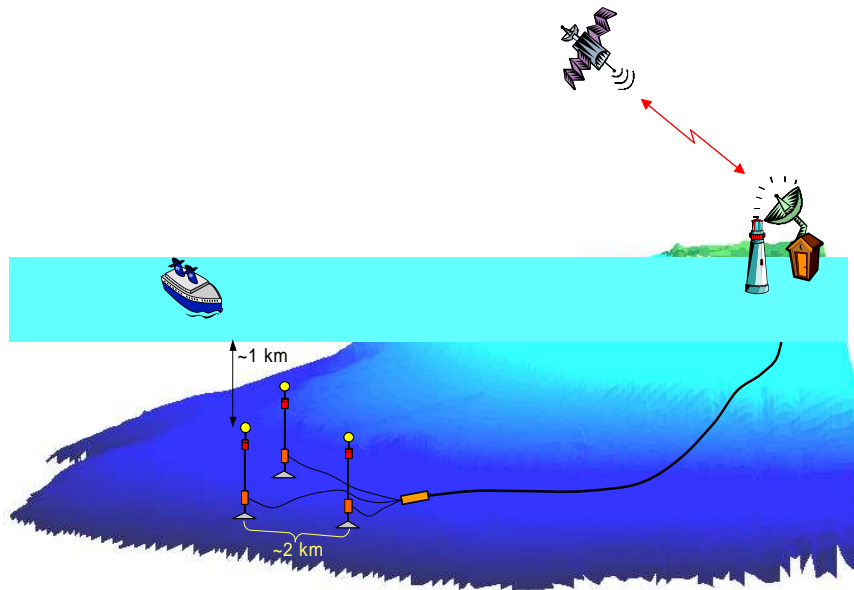


Figure 2.1. General layout of the HA01 hydroacoustic station. Three hydrophones are deployed in a triangular shape with a separation of about 2 km. They are submerged in the SOFAR channel at a depth of around 1100 meters. The hydrophones are cabled to the data collection and communication facility on shore for real-time data transmission via satellite to the International Data Center in Vienna.

Table 2.1. The principal characteristics of the HA01 hydroacoustic station.

Principal Characteristics	
Maximum Peak Sound Pressure Level	215 dB re 1 μ Pa
Maximum Overload Recovery Time	25 seconds
Calibrated pressure levels	Yes
Dynamic Range	120 dB
Frequency Band	1 - 100 Hz @ - 3 dB
Sampling Rate	250 samples/second
Max. Cable Length	225 km
Timing Accuracy	\pm 1 ms of GPS Time
Min. System Operational Life	20 years

2.2.2 *Two hydroacoustic stations in the Indian Ocean and their Antarctic observation coverage*

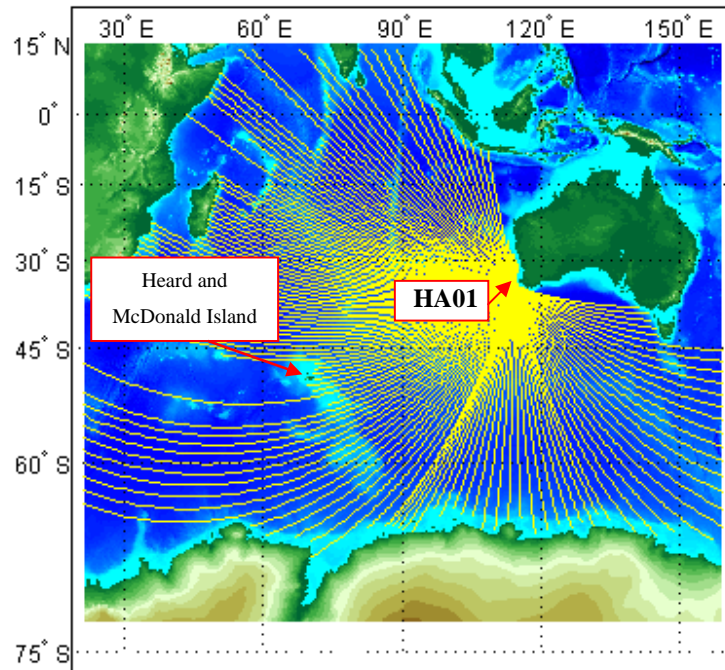


Figure 2.2. Unblocked geodetic ray paths (yellow lines) launched from the HA01 station to the Indian Ocean and part of Southern Ocean plotted over the bathymetry map. The ray paths were assumed to be blocked if they cross an area with a sea depth of less than 300 meters.

The study is based on the hydroacoustic data recorded at the HA01 station and the H08S station. A wide sector of the Eastern Antarctica coastline with the longitudes from approximately 10° E to 150° E can be acoustically observed from these two stations. Figure 2.2 shows the unblocked geodetic ray paths from the HA01 station to the Indian and part of Southern Ocean. The sector of the Antarctic coast observed acoustically from the HA01 station spans approximately from 50°E to 150°E, which corresponds to back-azimuth from the HA01 station varying from 158° to 210°. The range from the HA01

station to the Antarctica coastline varies from 3400 km to 5000 km. The coverage of the Antarctic coast by the H08S station is approximately from 10°E to 130°E, with blockages by Heard and McDonald Islands, as can be noticed in Figure 2.3. The back-azimuth from the H08S station to the observable Antarctic coastline spans angles from 158° to 190°. The distance from the H08S station to the Antarctic shelf varies from 6,000 km to 7,400 km.

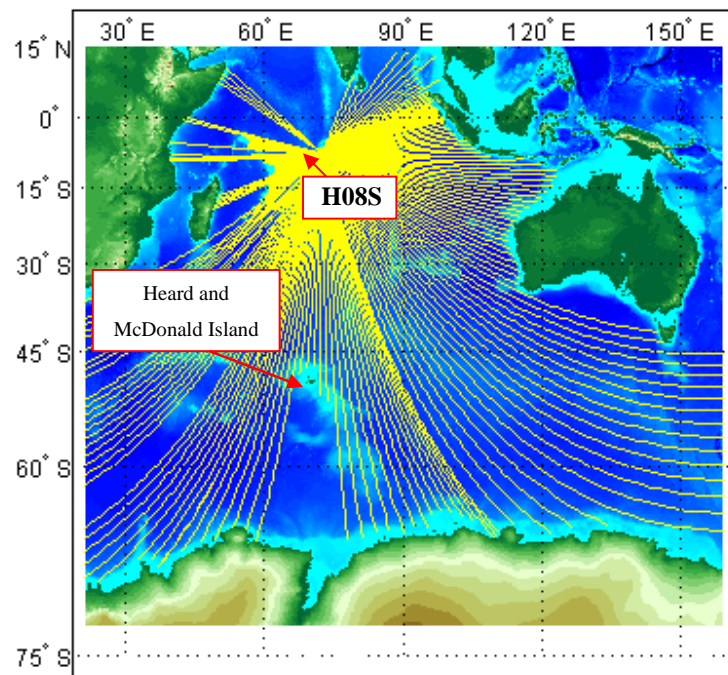


Figure 2.3. Unblocked geodetic ray paths (yellow lines) launched from the H08S station to the Indian Ocean and part of Southern Ocean plotted over the bathymetry map. The ray paths were assumed to be blocked if they cross an area with a sea depth of less than 300 meters.

2.3 CTBT hydroacoustic data collection from the HA01 and H08S station

The CTBT hydroacoustic data have been collected from three different sources. As the collaborative partner of this research project with the CMST, Geoscience Australia provided the data from the HA01 station covering the period from 2003 to early 2008. The CTBTO provided full two-year datasets from the H08S station collected in 2004 and 2005. Finally, the U. S. Army Space and Missile Defence Command (SMDC) Monitoring Research Program allowed downloading CTBT hydroacoustic data from their website (<http://www.rdss.info/>) for scientific research purposes. The data obtained from the SMDC are the HA01 data from late 2001 to the end of 2002 and the H08S data from 2002 to 2003. Overall, more than six years of the CTBT hydroacoustic data from the HA01 station and nearly four years of the data from the H08S station have been collected.

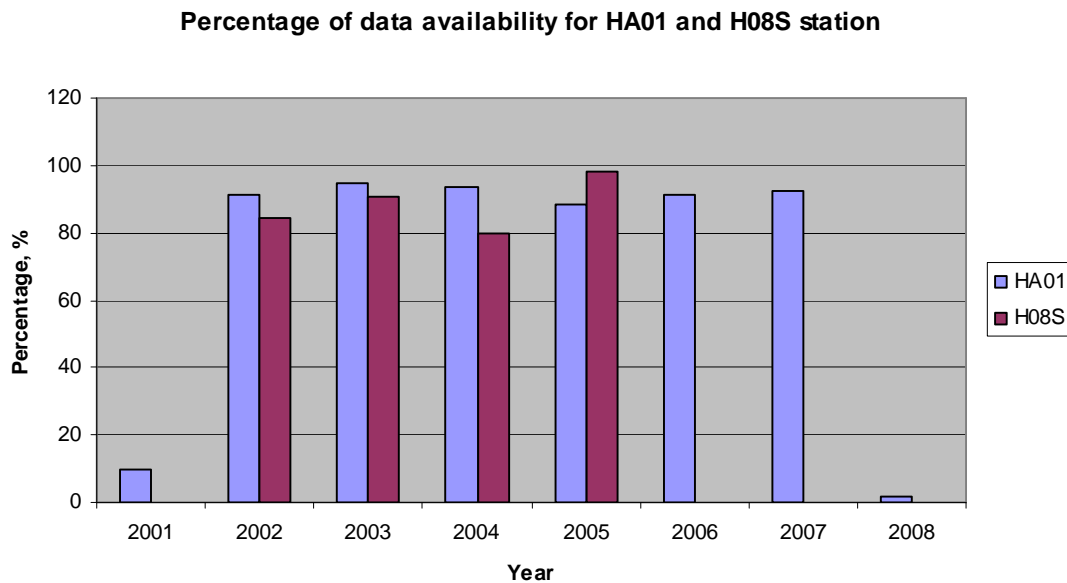


Figure 2.4. Percentage of annual hydroacoustic data availability for the HA01 and H08S stations from 2001 to 2008.

The percentage of annual data availability for both stations from 2001 to 2008 is shown in Figure 2.4. The availability of hydroacoustic data from HA01 station in 2002 - 2007 is nearly 90%. For 2001 and 2008, the percentage of data availability appears to be very low,

but the available data are from late 2001 to early 2008, without breaking the continuity of the whole dataset, as can be seen from the monthly data availability shown in Figure 2.5. Also from Figure 2.5, we can see that the data availability for HA01 is high and nearly constant over the years, with monthly data availability mostly over 80%.

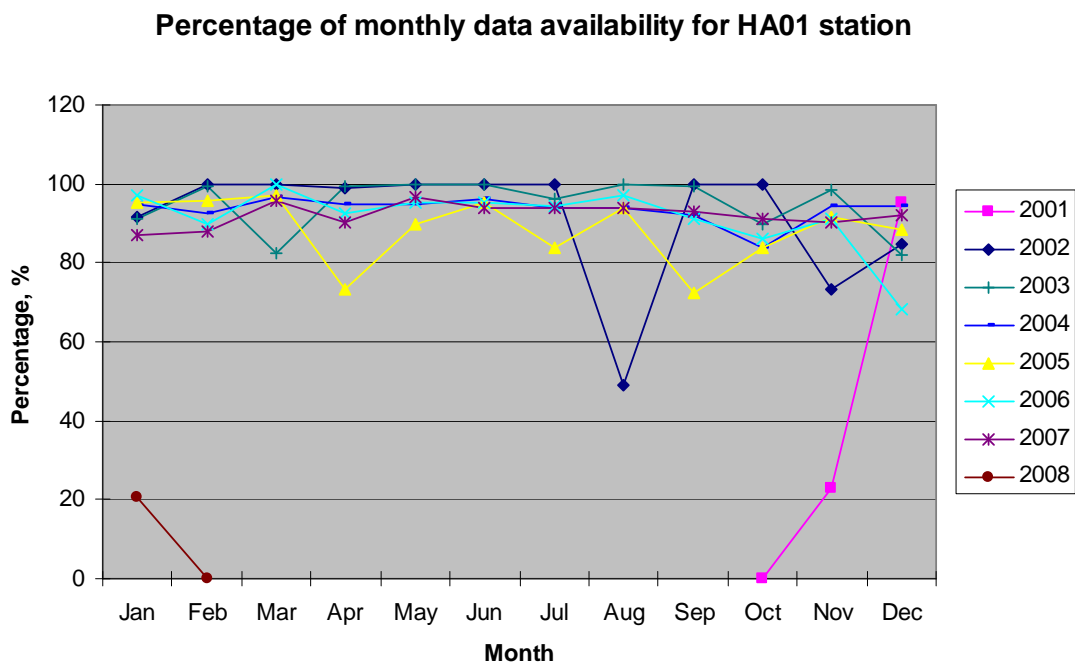


Figure 2.5. Percentage of monthly hydroacoustic data availability for the HA01 station from 2001 to 2008.

The 4-year hydroacoustic dataset from H08S has an annual availability over 80%, with half of it above 90%. There are a few notable disruptions in the data continuity over the four years, which can be seen from the monthly data availability shown in Figure 2.6. They took place in July - August of 2002, November - December of 2003, and July - September of 2004, when data collection was interrupted due to a system fault or when channel synchronization was corrupted. For the other months over the four years, the percentage of monthly data availability is mostly above 90%.

The collected hydroacoustic data with a high percentage of data availability covering a substantial period of time for both stations, especially HA01, are vital for the statistical analysis of ice events presented in Chapter 6 and Chapter 7 of the thesis.

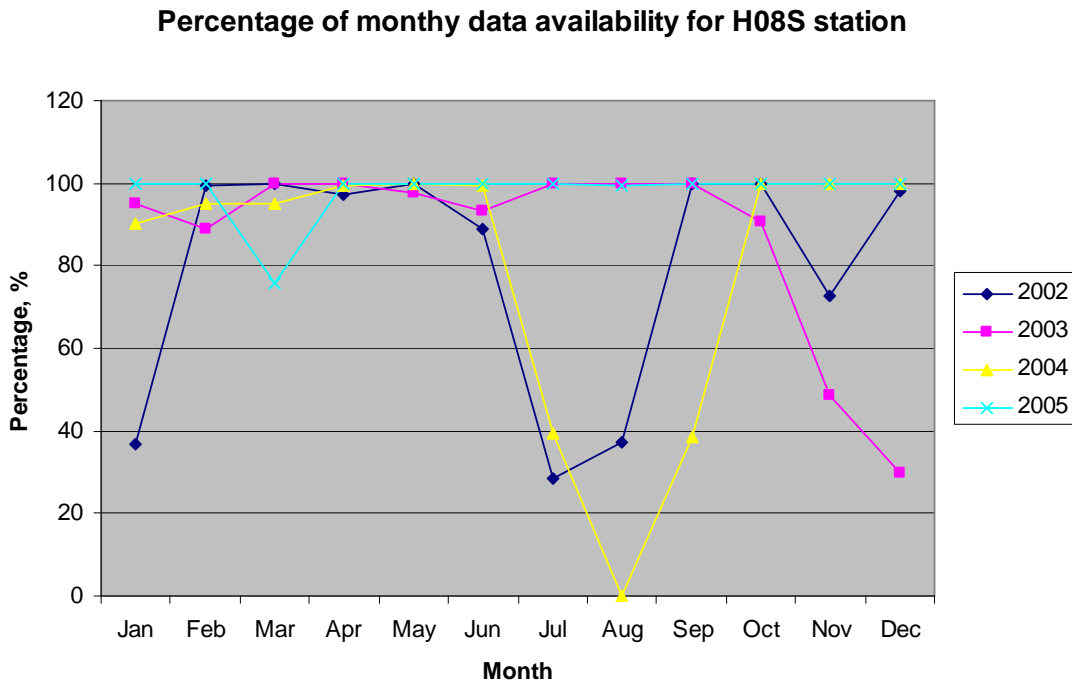


Figure 2.6. Percentage of monthly data availability for the H08S station from 2002 to 2005.

2.4 Preliminary hydroacoustic data processing

The algorithm for the preliminary processing of the sea noise data recorded at the IMS stations involves the steps shown by the flow chart in Figure 2.7. These steps were implemented using a set of MATLAB routines and each step will be described in detail in the following sections. The aim of this processing algorithm is to detect all fragments of continuous sea noise recordings with coherent signal arrivals and select signals for which the back-azimuth of arrival can be accurately estimated for further signal classification and source location.

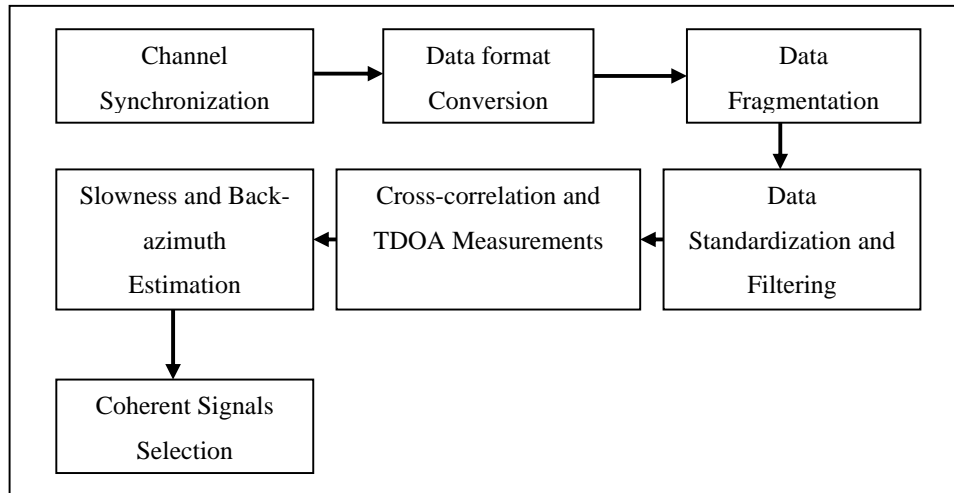


Figure 2.7. Basic flow chart of the preliminary processing of the hydroacoustic data from the IMS stations. TDOA stands for Time Difference of Arrivals.

2.4.1 Hydrophone channel synchronization

Data recordings in the three channels of each CTBT hydroacoustic station must be synchronized for further data analysis, which involves cross-correlation of signals received on different hydrophones, calculation of the time difference of arrivals (TDOA) as well as estimation of the back-azimuth and the slowness, to be discussed in Sections 2.4.3 and 2.4.4. All the collected CTBT hydroacoustic datasets consist of two components: files with digital data recordings and recording log files. For each station, the data recorded in three different channels were archived separately on the same daily or hourly basis. In most cases, the signals in the three channels were recorded without gaps and therefore have exact synchronization with one another. In cases of discontinuity in data recording due to failures in the data acquisition and communication system, a single data recording file was broken into a number of signal fragments, with missing data samples between the fragments. Normally, such an interruption occurred simultaneously in all three channels and causes no problem with synchronization. However, sometimes recording breaks occurred at different times in different channels and, consequently, lead to synchronization problems. In this case, the recording log files were used to perform synchronization. The

data logged in these files include the date of recording, the start time of each recording section in milliseconds counted from 00:00:00 January 1st 1970, station and channel number, number of samples in the recording section, the sampling rate and the data format. The process of channel synchronization involved selection of the time intervals when the signal samples were taken at the same times in all three channels.

2.4.2 Raw data conditioning

The CTBT hydroacoustic raw data were archived in three different binary formats referred to as 't4', 's4' and 's3', of either 32 or 24 bit integer. Based on the archived data format and the number of samples obtained from the recording log file, the raw recordings of the three channels were imported into the MATLAB environment for further processing.

In order to automatically search for arrivals of signals which are coherent in all three channels of the IMS hydroacoustic stations, a MATLAB routine for processing hydroacoustic data divided the continuous noise recordings in each channel into fragments of 20 seconds. Fragments with coherent signals are referred to as hydroacoustic events. This fragment length was selected because the majority of the transient signals received from Antarctica are shorter than 20 seconds as demonstrated later in Section 2.5. The start time of each set of 20-s fragments with coherent signals in the three channels is regarded as the arrival time of a hydroacoustic event. Fragmentation significantly increases the efficiency of the searching algorithm, as it allows the cross-correlation to be calculated by applying a FFT simultaneously to a large number of groups of 3 signal fragments being the same 20-s time sections in three channels.

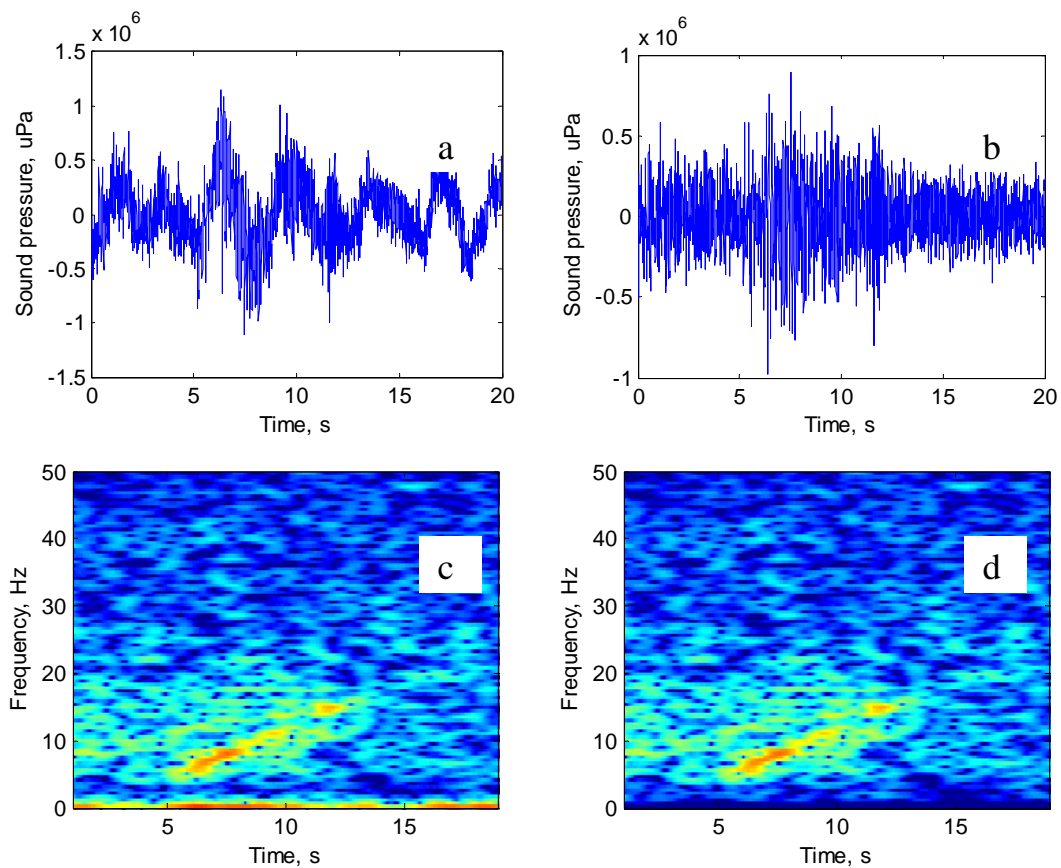


Figure 2.8. Waveforms (top) and spectrograms (bottom) of the detected event before (left) and after (right) low-frequency filtering. The transient seen in the spectrogram is a weak ice event.

The 20-second fragments were converted into acoustic pressure by removing a DC offset present in the raw data and multiplying the waveform samples in ADC counts by the known conversion coefficient. The unfiltered waveform contains very strong low frequency components below 2 Hz, as shown in Figure 2.8(c), which result most likely from the motion of the hydrophone's moorings under currents. A 6th-order high-pass infinite impulse response (IIR) Butterworth filter with a cut-off frequency of 2.5 Hz was used to remove this low-frequency noise. This filter has a nearly constant magnitude and phase response over the pass-band. A comparison of the waveform and spectrogram of one signal fragment before and after filtering is shown in the Figure 2.8.

2.4.3 Cross correlation and the time difference of arrivals (TDOA)

TDOA estimates were made by locating the maximum of the cross-correlation between signals in each pair of the three hydrophones. The cross-correlation function was calculated using FFT as described in Page 443 of (Bendat and Piersol, 2000) and TDOA were calculated in four different frequency bands: 2.5-15 Hz, 15-30 Hz, 30-60 Hz, and 60-100 Hz. These frequency bands were selected based on the typical frequency bands expected for different sources of noise in the ocean, such as ice events, seismic signals, whale calls and some others, which will be discussed in Section 2.5. If the cross-correlation maximum in at least one frequency band exceeded a preset threshold of 0.5 in at least one pair of hydrophones and 0.3 in all three pairs, then fragments were regarded as detected hydroacoustic events. The waveforms of these fragments were stored in the event database along with the maximum cross-correlation and the TDOA estimates made in the frequency bands of high correlation.

2.4.4 Slowness and back-azimuth estimation of hydroacoustic events

The distance from Antarctica to the IMS hydroacoustic stations is of an order of 10^3 km, which is much larger than the triplet dimension of the receive array. Therefore a Plane Wave Fitting (PWF) method (Pezzo and Giudicepietro, 2002) can be applied to estimate the back-azimuth of the event at the receive stations. The TDOA estimate $t_{i,j}$ for each pair of hydrophones in the triplet was obtained using cross-correlation as described in Section 2.4.3. The TDOA estimates $t_{i,j}$ made for each pair of hydrophones in the triplet were used as input parameters for the PWF method. The relation between TDOA represented in vector form by \mathbf{t} and the horizontal slowness \mathbf{p} (inverse of the group velocity) of a plane wave received on a horizontal receive array can be written as the dot product

$$\mathbf{t} = \Delta\mathbf{x} \cdot \mathbf{p} \quad (2.1)$$

where $\Delta\mathbf{x}$ denotes the relative position of the hydrophones $\{x_i, y_i\}$ and \mathbf{p} is a two-element vector with the horizontal components $\{p_x, p_y\}$. Because the number of linear equations in

system (2.1) is larger than the number of unknown variables p_x and p_y , equation (2.1) can be solved with respect to \mathbf{p} using the least square method (Press et al., 2007):

$$\mathbf{p} = (\Delta\mathbf{x}^T \Delta\mathbf{x})^{-1} \Delta\mathbf{x}^T \mathbf{t} \quad (2.2)$$

where T denotes the matrix transpose operation. The back-azimuth α and the group velocity v (i.e. the velocity of acoustic energy propagation) can then be calculated as $\alpha = \tan^{-1}(p_x / p_y)$ and $v = 1/|\mathbf{p}|$.

The final selection of hydroacoustic events detected at the IMS station was made based on the group velocity estimates via PWF, which should be within reasonable range of variation for remote sources of noise. This range was set to be from 1.40 km/s to 1.52 km/s based on possible variations of the modal group velocities within the frequency band of analysis. Events with group velocity estimates outside these limits are signals most likely from remote sources with low Signal-to-Noise Ratio (SNR), from close sources (e.g. whales and shipping noise) or electric noise in the data acquisition system.

2.5 Coherent signal classification based on waveforms and spectrograms

The source of each detected signal was manually classified into one of six event categories that are defined based on certain characteristics of its waveform, spectrogram and back-azimuth of arrival. During the classification process, if it is found that a transient event was split between two adjacent coherent fragments, a new 20-s fragment was determined by shifting its 20s window over the two adjacent fragments to fully cover the transient event. Five event categories for which the signal origin was identified will be discussed with some examples in the next five sections. The sixth category includes coherent signals from remote sources of underwater noise of unknown origin and they will be referred to as unknown events for simplicity. For the signals received at the H08S station from remote sources of underwater noise, only some of these associated with certain events of interest, e.g. some ice events, underwater explosions and some others were classified.

2.5.1 Whale calls

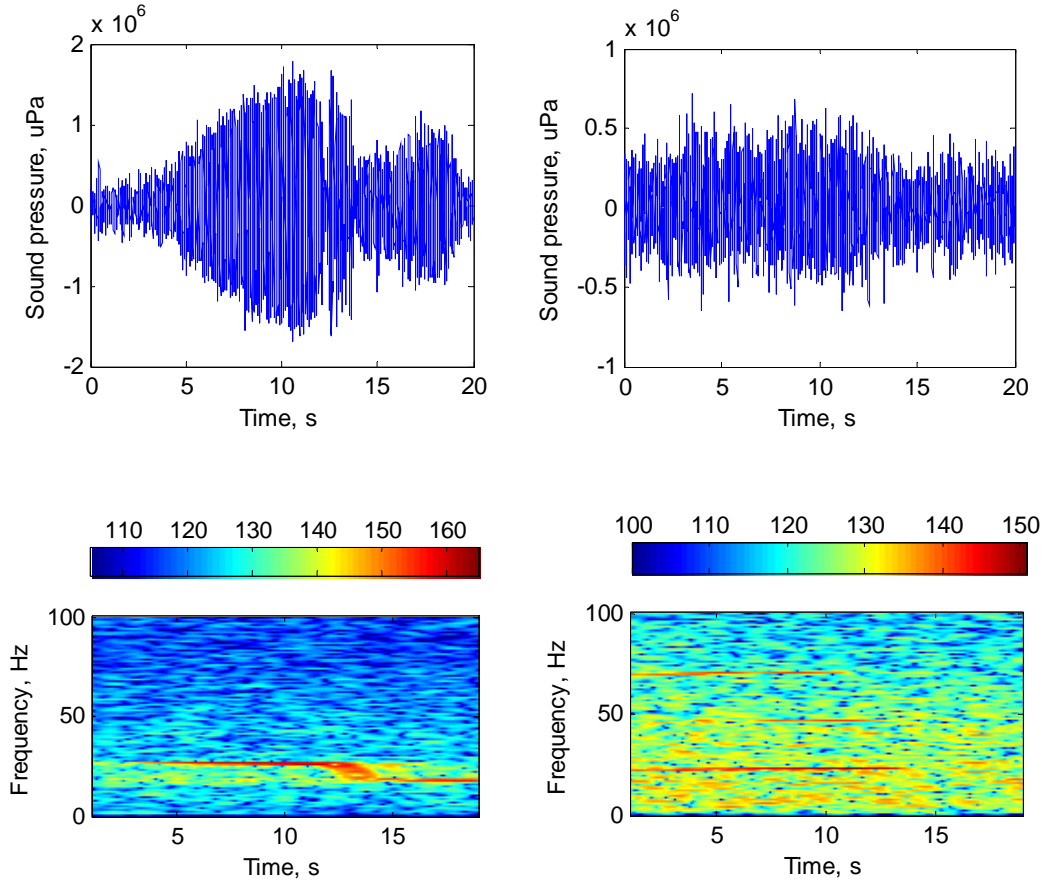


Figure 2.9. The waveform (top panels) and spectrogram (bottom panels) of Antarctic blue (left panels) and Pygmy (right panels) whale calls, received at one of the HA01 hydrophones in 2007.

Among all possible noises of biological origin, only whale calls were recognized in the detected signal because of the limited frequency band of the IMS receive system of 125 Hz. Two species of blue whales, Antarctic blue whale and Pygmy whale are mainly observed in the acoustic recordings at the HA01 station. The spectrum of the Antarctic blue whale call normally has a nearly constant tone centered at around 25 - 27 Hz followed often by a lower frequency tone at about 20 Hz, which forms a so-called Z-shaped spectrogram typical for calls by this species (Cummings and Thompson, 1971, McCauley et al., 2000,

McCauley and Salgado, 2005). Calls by Pygmy whales usually have a few harmonics spanning frequencies from about 20 to 80 Hz. The waveform and spectrogram of calls by the two whale species located near the receive array are shown in Figure 2.9. The waveform of remote calls is significantly distorted by multipath propagation effects.

2.5.2 Man-made signals

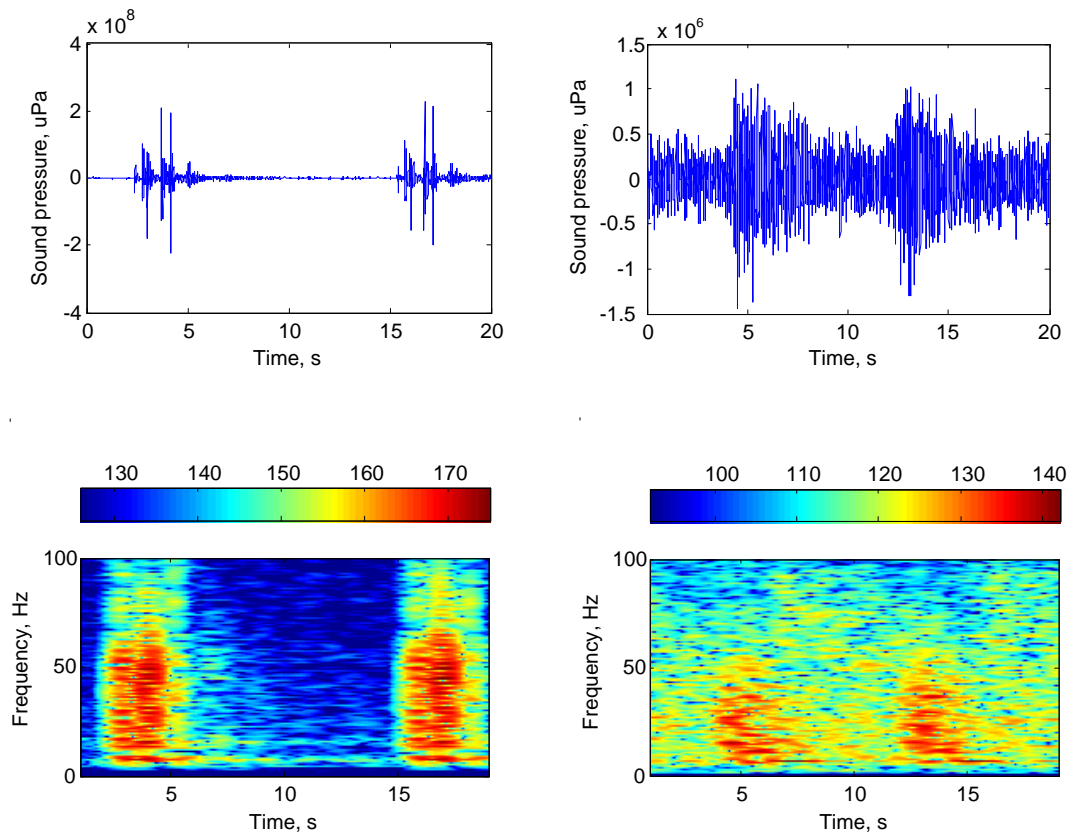


Figure 2.10. Left panels: the waveform (top) and spectrogram (bottom) of an air-gun signal from an offshore seismic survey near Cape Leeuwin received at HA01 on day 305 in year 2004; right panels: the waveform (top) and spectrogram (bottom) of an air-gun signal from an offshore seismic survey on the north west shelf of Australia, received at H08S hydroacoustic station with the arrival date of day 55 in 2005.

The majority of man-made signals received at the two IMS stations are air-gun signals from offshore seismic exploration surveys. The waveform of air-gun signals consists of repetitive impulses. The width of the frequency band of these impulsive signals depends on the source spectrum of airgun arrays, range between the survey location and the acoustic receiver, as well as the ocean environment along the propagation path. As demonstrated in Figure 2.10, for the seismic survey located close to the receive station, the energy of air-gun signals is high within a relatively wide band from very low frequencies to more than 70 Hz, and separate multi-path arrivals can also be identified in the waveform. For air-gun signals from remote surveys received at H08S (right panel of Figure 2.10), the energy of signals at frequencies higher than 50 Hz is absent in the signal spectra due to higher transmission loss over larger propagation ranges

Noise from ship operation can also be occasionally detected as a coherent signal at the HA01 station. Its main feature is the mid-frequency energy distribution as shown in Figure 2.11.

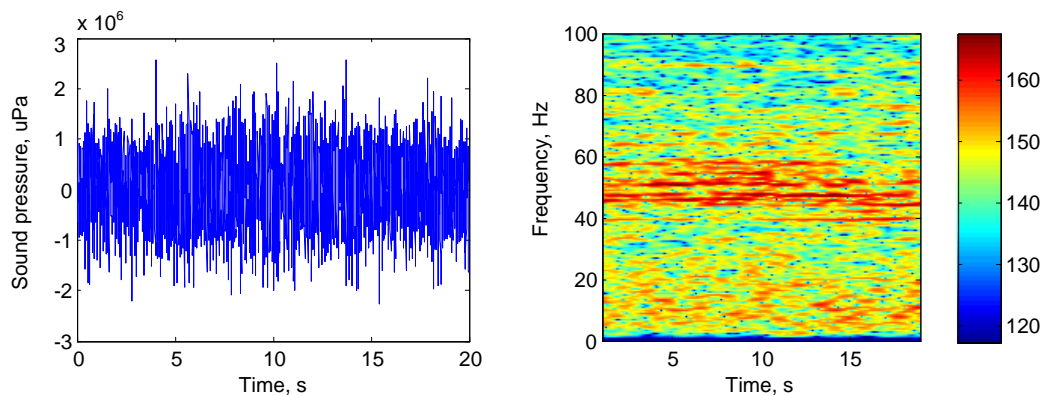


Figure 2.11. The waveform (left panel) and spectrogram (right panel) of ship noise observed at HA01.

2.5.3 Seismic signals

Signals from sub-sea seismic events, commonly referred to as T-phase signals, are typically from several tens of seconds to tens of minutes long and are characterized by high energy at very low frequencies (Hanson and Bowman, 2006), as can be seen in the waveform and spectrogram of a seismic signal received at HA01 shown in Figure 2.12. Sources of the underwater seismic activity are mainly located along the Central, Southeast and Southwest Indian mid-ocean ridges, in the Sumatra fault zone and around the seismically active Macquarie Ridge, as in the reference (Hanson and Bowman, 2005).

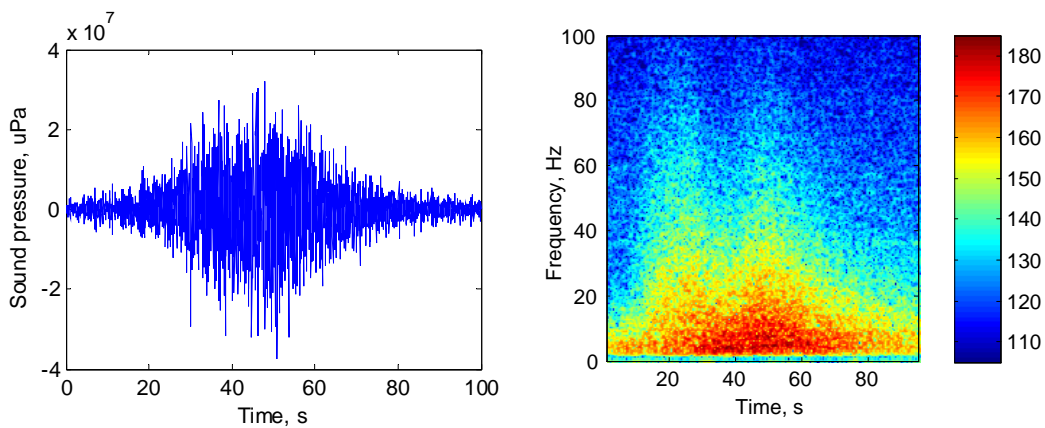


Figure 2.12. The waveform (left panel) and spectrogram (right panel) of a seismic event detected at HA01 on day 306 in 2003.

2.5.4 Harmonic tremor signals from Antarctica

One distinct type of the coherent signals arriving always from the direction of Antarctica exhibits a fundamental frequency component of around or below 10 Hz, often accompanied with a number of harmonics up to frequencies of several tens of Hz, as shown in Figure 2.13. This type of signal is sometimes referred to as a harmonic tremor in the literature (Chapp et al., 2005). It was suggested that such signals could be emitted by resonant vibrations in an ice plate shaping most of the tabular icebergs or in fluid-filled cavities within the ice mass of an iceberg (Chapp et al., 2005). It has been recently demonstrated by

in-situ observations in Antarctica that such vibrations can be forced by a stick-slip process during collisions between large icebergs or between a large iceberg and an ice shelf (Talandier et al., 2006, MacAyeal et al., 2008).

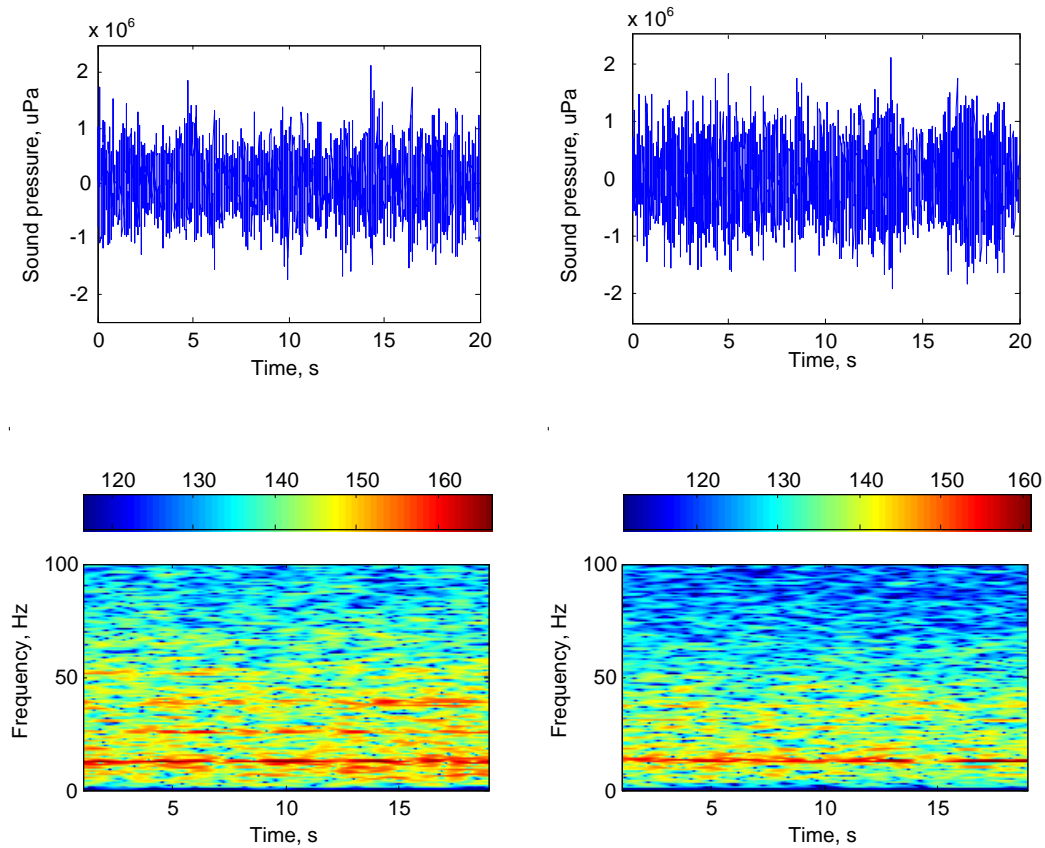


Figure 2.13. The waveform (top) and spectrogram (bottom) of noise fragments from two harmonic tremor events with (left) and without (right) higher frequency harmonics observed at the HA01 station on Day 4 in 2007. Back-azimuth to these events was 192.14° and 194.97° respectively.

2.5.5 Antarctic ice cracking or breaking signals (ice events)

Numerous short transient signals of a specific type are regularly detected at the IMS stations, originating from the direction of Antarctica. The magnitude, duration and

frequency band of these signals can be different, but they are always featured with a strong frequency dispersion characteristic, as shown in the spectrogram in Figure 2.14. The low frequency components of these signals arrive noticeably earlier than the higher frequencies. This type of frequency dispersion is referred as negative, because the propagation speed of acoustic waves decreases with increasing frequency. For most of these pulse-like signals, the frequency range of their energy spectrum is below 35 Hz with the low cut-off frequency around 3-5 Hz. The signal arrival structure in the time-frequency domain normally reveals one distinct signal arrival, which can be clearly seen in the spectrogram shown in Figure 2.14. A noise-like precursor without any definite arrival pattern often precedes the distinct final arrival, which is demonstrated in the left panel of Figure 2.15. In some signals, another distinct signal arrival preceding the ultimate one can also be recognized in the spectrogram, as shown in the right panel of Figure 2.15. It is noticed that the dispersion characteristic of this preceding arrival is steeper than that of the final one. A physical explanation of such an arrival structure for the transients received from Antarctica will be given in the next chapter. An algorithm for automatic discrimination of ice event signals from other coherent signals has been developed in CMST as part of an Australian Research Council (ARC) Discovery Project and it is described in Appendix A.

Hanson and Bowman (2006) observed this type of signal in the IMS hydroacoustic data collected in 2003 and related them to either thermal fracturing of ice or sea ice ridging in Antarctica. We separate this specific type of signal from other signals arriving from the Southern Ocean and Antarctica (e.g. harmonic tremors and seismic events), based on their distinctive features. Signals as this type, referred to as ice events, and are hypothesized to originate from Antarctic ice breaking or cracking events. This hypothesis will be comprehensively investigated in Chapter 3 by numerical modelling and using data from other kinds of observation.

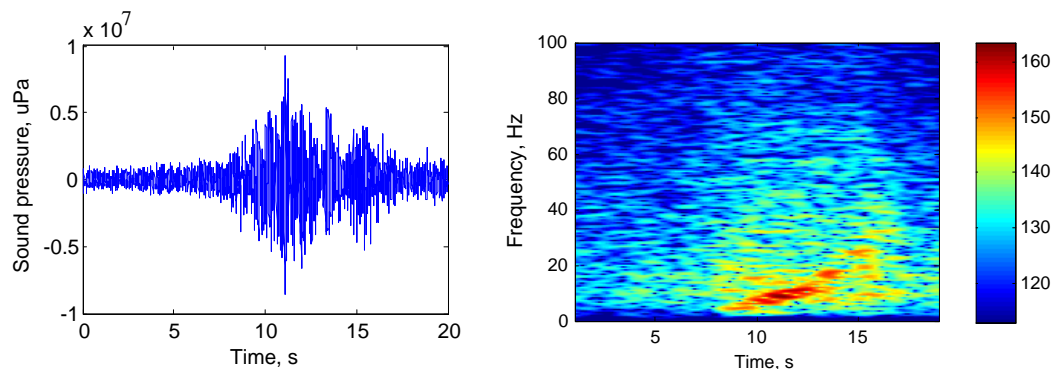


Figure 2.14. The waveform and spectrogram of a sea noise fragment which contains an ice event detected at HA01 on Day 9 in 2007. Back-azimuth to this event is 165.95° .

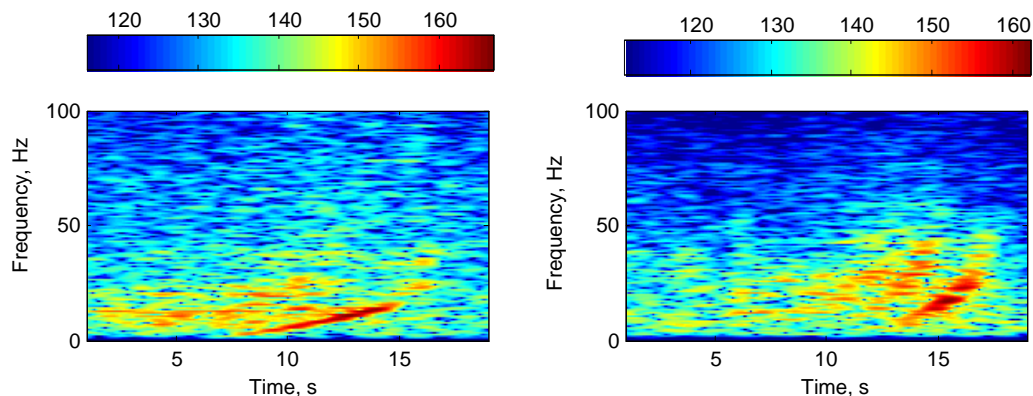


Figure 2.15. Typical spectrograms of Antarctic ice events having one dominant arrival with a noise-like precursor (left panel) and two distinctive arrivals with a noisy precursor (right panel).

2.6 Temporal and spatial distributions of all coherent signals

Using the data processing steps of described in Section 2.4, a total of 706,517 hydroacoustic events (coherent signals in 20-s recording fragments) were detected at the HA01 station over a 6-year period of observation in 2001-2008, and 603,444 events at H08S over a 4-year period from 2002 to 2005. The signal arrival time, RMS amplitude around the maximum, back-azimuth and group velocity were measured for each detected event. In order to reveal the temporal change in the occurrence of events and their spatial

distribution, the detection time in terms of the day of observation starting from 01/01/2002 and back-azimuth of all events were binned into 7-day by 2-degree bins. Figures 2.16 and 2.17 show the distribution of the percentage of time τ_{ij} , when coherent noise events were observed at HA01 and H08S respectively, where $\tau_{ij} = \frac{n_{ij} \times 20s}{7days} \times 100\%$ and n_{ij} being the number of 20-s coherent noise fragments found in the i th 7-day and j th 2-degree bin.

It is evident from the event distribution shown in Figure 2.16 that the Antarctic coast and the surrounding ocean over the continental shelf, observed from HA01 at back-azimuth angles from approximately 158° to 210° , are the major source of low-frequency noise at this station. The other sources of frequent and intense noise signals are seismic events along the Sumatra fault zone and a number of seismically active parts of the mid-ocean ridges in the Indian Ocean. It is also notable that the Sumatra fault zone had been relatively noiseless in 2003 and 2004 until the Great Sumatra Earthquake, after which this zone was almost uninterruptedly generating seismic signals in 2005 and beyond, including the Sumatra aftershock in March 2005. Manmade signals, mainly air-gun signals from seismic offshore surveys, also make a noticeable contribution to the noise received at HA01. These signals arrive mostly from the Western Australia continental shelf.

Figure 2.17 shows the distribution of hydroacoustic events detected at the H08S station. Airgun signals from seismic offshore surveys in Western Australia waters contribute much to the noise observed at H08S. The most frequent air-gun signals were observed from the surveys conducted on the north-west shelf of Western Australia since 2003, which were not detectable at the HA01 station due to the continent blockage. Even though the H08S station is much farther from Antarctica than HA01, the Antarctic coast and the surrounding ocean are still one of the main sources of low-frequency noise for this station, which covers the back-azimuth range from 150° to 195° . There is a sector between bearing of 176° and 188° in the Antarctic direction within which remote hydroacoustic events were very rarely detected. This is most likely due to the propagation blockage of ice-related sounds by Heard Island and McDonald Island (see Figure 2.3). The main shock of Great Sumatra

Earthquake and its aftershock, as well as the continuous seismic noise from the Sumatra fault zone since the main shock, are also captured in this distribution.

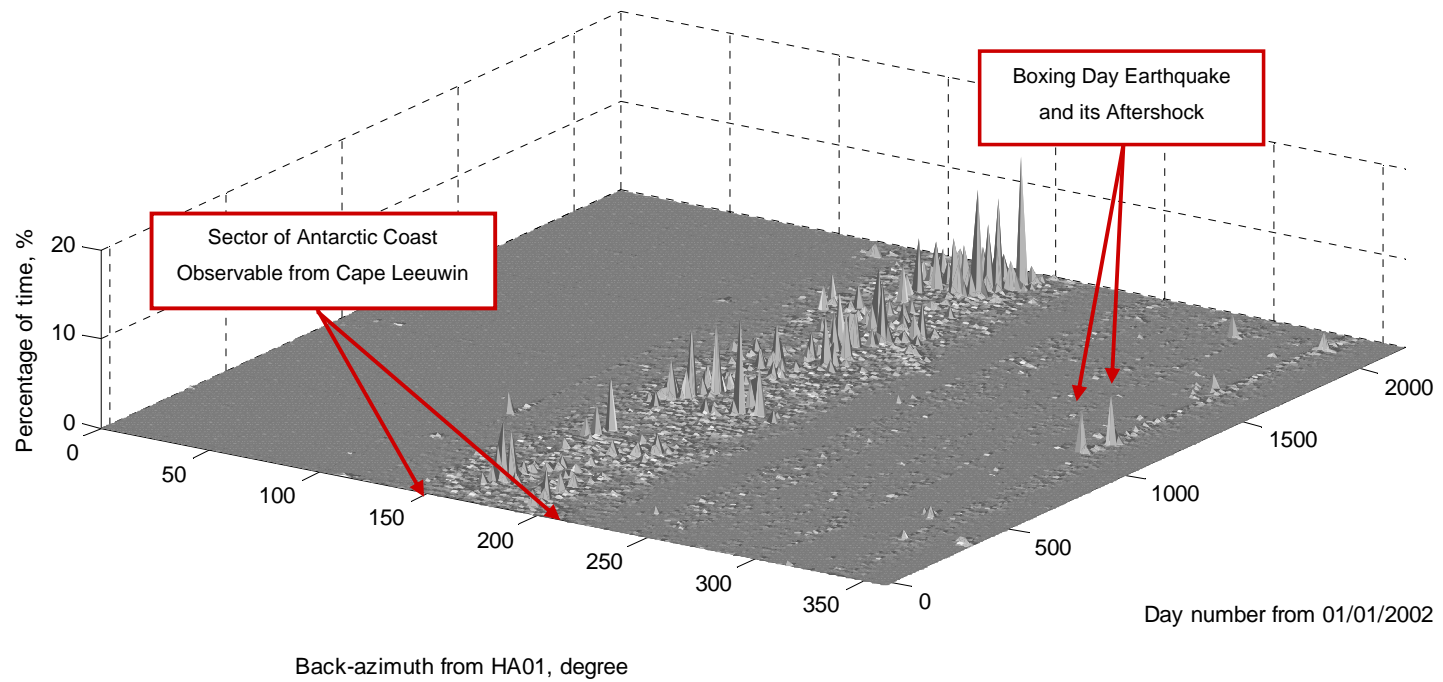


Figure 2.16. Percentage of time when coherent low-frequency noise signals were observed at HA01, versus the day of observation and the back-azimuth to signals sources.

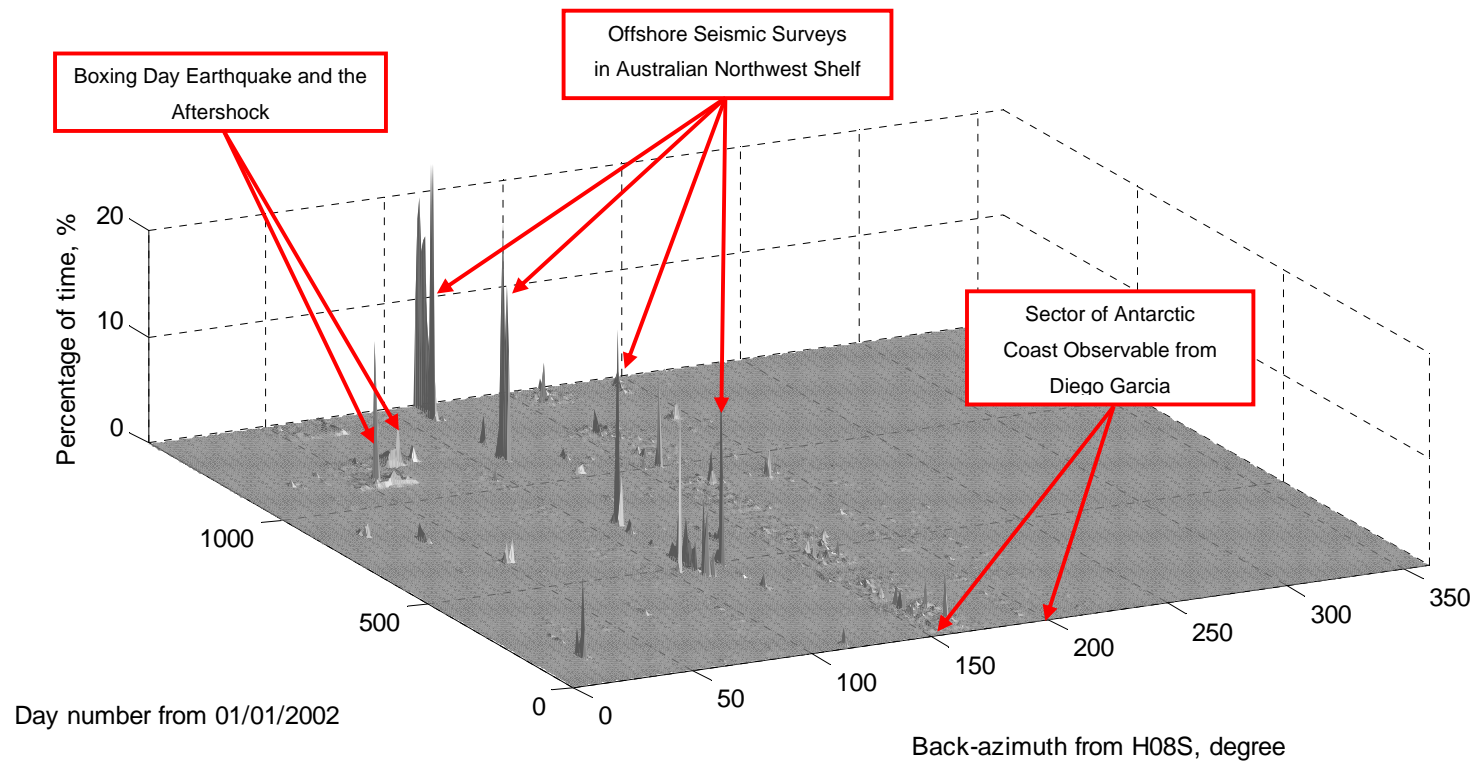


Figure 2.17. Percentage of time when coherent low-frequency noise signals were observed at H08S, versus the day of observation and the back-azimuth to signals.

2.7 Statistical analysis of the principal characteristics of ice events detected at the HA01 station

This section presents a statistical analysis of the sound pressure level, frequency of the peak power spectral density and the signal-to-noise ratio (SNR) of the signals received at HA01 and classified as ice events. This provides useful information for further investigation of the sound pressure level of ice events at the origin and the optimum frequency of sound propagation from Antarctica to HA01 discussed in Chapter 3. Estimates of the SNR will be needed in Chapter 4 for assessing the accuracy of event location from the IMS stations.

For each 20-s fragment containing the signal from an ice event, the signal-plus-noise RMS amplitude ψ_{sn} is taken as the RMS value of a 2-s waveform section centred at the maximum signal amplitude. The noise amplitude ψ_n is defined as the minimum RMS value of all 10 2-s sections in the 20-s fragment. The sound pressure level in decibels (dB) is determined as

$$SPL = 20\log(\psi_{sn}^2 - \psi_n^2) \quad , \quad (2.3)$$

and the SNR in dB as:

$$SNR = 10\log((\psi_{sn}^2 - \psi_n^2) / \psi_n^2) \quad (2.4)$$

The histogram of the sound pressure level for all ice events detected at HA01 is demonstrated in Figure 2.18. The pressure level varies from 100 dB to 130 dB, with a peak at about 110 dB.

The distribution of the SNR of ice signals is shown in Figure 2.19. As can be seen, the majority of ice signals have a SNR over 2 dB with the peak of the SNR histogram at around 5 dB. The distribution of frequencies at the peak power spectral density of ice signals is presented in Figure 2.20. The power spectral density was calculated using a 2-s window with 50% overlap. The frequencies of peak power spectral density range from 5 Hz to 30 Hz, with the maximum at between 7 - 10 Hz.

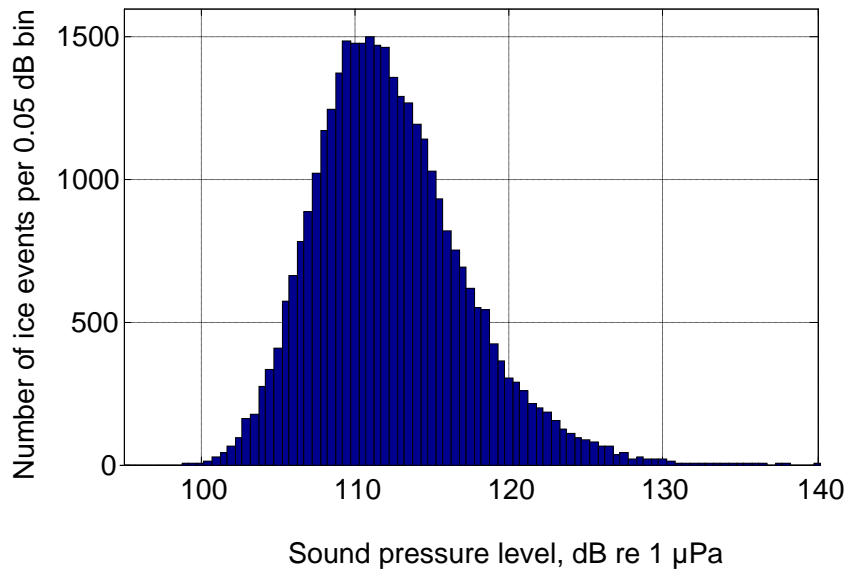


Figure 2.18. Histogram of the sound pressure level of ice events detected at HA01 over the six year period from 2002 to 2007. The sound pressure level resolution is 0.05 dB.

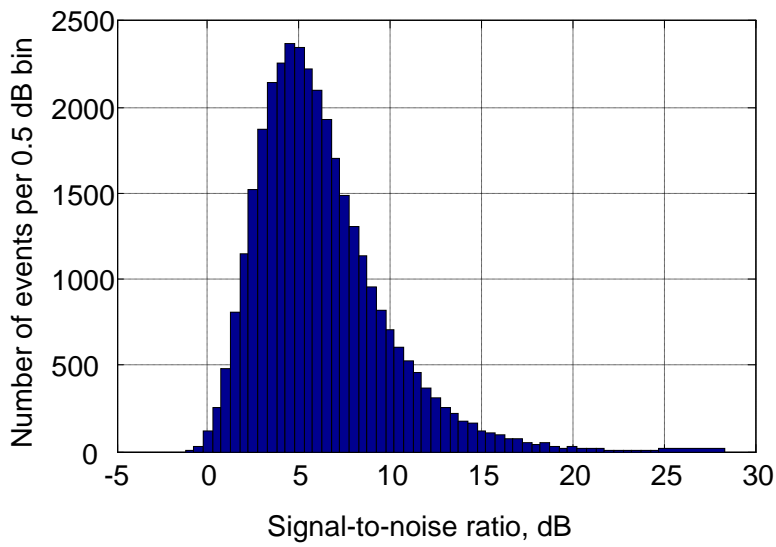


Figure 2.19. Histogram of the signal-to-noise ratios of ice events received at HA01. The SNR resolution is 0.5 dB.

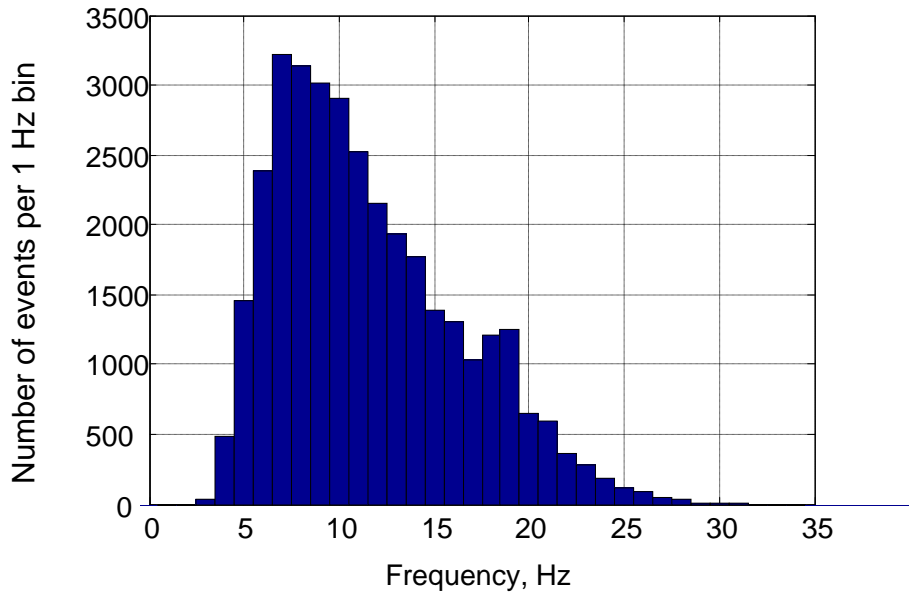


Figure 2.20. Histogram of the frequencies of peak power spectral density calculated for the ice events received at HA01. The frequency resolution is 1 Hz.

2.8 Concluding remarks

The methods and results of preliminary processing and analysis of the six-year acoustic data collected from the HA01 station and the four-year dataset from the H08S station were presented in this chapter. The main findings from the analysis presented are as follows:

Processes generating underwater noise in Antarctica are one of the major sources of low-frequency underwater noise signals in the Indian Oceans, particularly in its southern part. The Sumatra fault zone persistently produces intense underwater noise which has been received as spatially coherent low-frequency hydroacoustic signals at both HA01 and H08S stations since the Great Sumatra Earthquake in December 2004. Offshore seismic exploration surveys are another major source of low-frequency underwater noise, especially for the H08S station, which frequently receives air-gun signals from seismic surveys conducted on the northwest shelf of Western Australia.

Short transient signals with specific temporal and spectral characteristics are frequently detected at the two IMS hydroacoustic stations in the Indian Ocean. These signals arrive from the direction of Antarctica and are believed to be produced by ice cracking and breaking events and are therefore referred to as ice events. A statistical analysis of the principle characteristics of these signals at HA01 was also made in this chapter. The assumption on the origin of this type of signals will be investigated through numerical modelling and analysis of other experimental data in Chapter 3. Moreover, combined with the numerical investigation of the ice event signal arrival structure in the next chapter, an algorithm for automatic detection of the ice event signals is suggested and examined in Appendix A.

CHAPTER 3

NUMERICAL MODELLING OF ACOUSTIC PROPAGATION FROM ANTARCTICA AND EXPERIMENTAL INVESTIGATION OF THE ORIGIN OF ICE EVENTS

3.1 Overview

This chapter investigates numerically and experimentally the principal characteristic of a specific type of signals classified as Antarctic ice event and briefly introduced in Section 2.5.5. The aim of this analysis is to identify the origin of such events. These signals always arrive from Antarctica at both HA01 and H08S IMS hydroacoustic stations, and feature a pulse-like waveform with a single dominant arrival exhibiting strong negative frequency dispersion terminating the signal. The chapter presents results of numerical modelling of the acoustic propagation from Antarctica to these two hydroacoustic stations in the Indian Ocean, an investigation of the time-frequency arrival structure expected for the received signals generated by Antarctic ice breaking events, and a comparison between the observed and modelled arrival structures of the signals from ice events.

The scenario for numerical modelling considered in this chapter includes long-range low-frequency broadband acoustic propagation in a multi-megameter range dependent ocean acoustic waveguide. The effect of horizontal refraction of acoustic propagation due to spatial variations of the waveguide will be considered in Chapter 4. A normal-mode model is applied to model the acoustic propagation in this thesis, because this type of model offers the potential for efficient numerical simulation and a clear physical interpretation of the long-range low-frequency propagation in the ocean.

Section 3.2 provides a theoretical background for acoustic propagation modelling. The wave equation for sound propagation in the ocean is introduced along with the normal mode approach to solving this problem numerically for a range dependent ocean acoustic

waveguide. Acoustic scattering from ocean surface roughness and the numerical modelling of broadband signal propagation are also considered. The sound propagation from Antarctica to the IMS hydroacoustic stations in the Indian Ocean is investigated using the normal-mode model in Section 3.3. Propagation paths from Vincennes Bay, Antarctica (66.5°S, 109.5°E) to the HA01 and H08S stations are selected for the modelling demonstration. The modelling objectives are to analyse the principal characteristics of sound propagation along the paths, such as transmission loss, mode coupling, and inter-modal and intra-modal dispersion effects. A comparison between experimental observation and numerical modelling of the arrival structure of transient signals propagated from Antarctica to the IMS station is also presented in this section. Other kinds of observation of ice breaking events in Antarctica conducted in parallel with the remote acoustic observation from the IMS stations, such as underwater acoustic recordings made in Antarctica and analysis of satellite imagery of the Eastern Antarctica ice shelves, are discussed in Section 3.4, in order to confirm the origin of the signals detected at the IMS stations and identified as ice events. Section 3.5 briefly summarizes the main findings made in this chapter.

3.2 Background theory

3.2.1 Acoustic wave equation and its normal mode solution

The Helmholtz equation for acoustic wave propagation, as well as the boundary conditions at the sea surface and seafloor, form a theoretical basis for the numerical models most frequently used in underwater acoustics for modelling acoustic fields in the ocean, such as the ray approximation, parabolic equation approximation, wavenumber integration and normal mode methods. Omitting the temporal variation term $\exp(j\omega t)$, for a point harmonic acoustic source of unit amplitude in an azimuth-independent ocean medium, the Helmholtz equation can be represented in cylindrical coordinates in the following form (Jensen et al., 2000):

$$\frac{\rho(r, z)}{r} \frac{\partial}{\partial r} \left(\frac{r}{\rho(r, z)} \frac{\partial p}{\partial r} \right) + \rho(r, z) \frac{\partial}{\partial z} \left(\frac{1}{\rho(r, z)} \frac{\partial p}{\partial z} \right) + \frac{\omega^2}{c^2(r, z)} = -\frac{\delta(r)\delta(z - z_s)}{2\pi r} \quad (3.1)$$

where $p(r, z, \omega)$ is the acoustic pressure as function of range r , depth z and circular frequency ω , $c(r, z)$ is the sound speed, $\rho(r, z)$ is the medium density, z_s is the source depth, and δ is the Dirac delta function. In a layered, range independent ocean medium, the acoustic pressure can be expressed through an inverse Hankel transform as:

$$p(r, z) = \int_0^\infty p(k_r, z) J_0(k_r r) k_r dk_r \quad (3.2)$$

where J_0 is the Bessel function of the first kind of zero order. It can be represented as a sum of the Hankel functions of first and second kind:

$$J_0(k_r r) = \frac{1}{2} [H_0^{(1)}(k_r r) + H_0^{(2)}(k_r r)] \quad (3.3)$$

By substituting Equation (3.2) into Equation (3.1), one can separate the variables r and z in the wave equation and obtain a second order differential equation for the pressure $p(z, k_r)$ as a function of z :

$$\left[\frac{d^2}{dz^2} + (k^2 - k_r^2) \right] p(k_r, z) = \frac{\delta(z - z_s)}{2\pi} \quad (3.4)$$

where k_r is the horizontal component of the wavenumber $k = \omega/c(z)$. To satisfy the radiation condition at $r \rightarrow \infty$, only the Hankel function of first kind is kept for the outgoing waves at infinity. The acoustic field can be determined by solving Equation (3.4) for a continuous wavenumber spectrum of the pressure $p(k_r, z)$ subject to the appropriate boundary conditions and then carrying out the inverse Hankel transform Equation (3.2). The direct numerical integration in Equation (3.2) can be performed very efficiently via the Fast Field Program (FFP) algorithm, one of the wavenumber integration approaches (Jensen et al., 2000), based on Fast Fourier Transform (FFT) technique (Oppenheim and Schaffer, 1989b).

In contrast to the wavenumber integration approach, the normal mode method uses complex contour integration in Equation (3.2) rather than direct numerical integration. The solution of Equation (3.2) is found on the complex wavenumber plane k_r as the sum of residues at the poles, plus a branch line integral. Each pole corresponds to a normal mode in the waveguide. The normal mode solution of Equation (3.2) can be represented as

$$p(r, z) = \frac{i}{4\rho(z_s)} \sum_{m=1}^M \psi_m(z_s) \psi_m(z) H_0^{(1)}(k_{rm} r) - \int_{C_{BR}} \quad (3.5)$$

where $\int_{C_{BR}}$ is the branch line integral, and M is the number of discrete modes. The eigenvectors $\psi_m(z)$ and eigenvalues k_{rm} of the Sturm-Liouville differential operator in the left part of Equation (3.4) subject to the boundary conditions are shapes and wavenumbers of normal modes respectively. They can be found using several numerical techniques. We used the computer program KRAKEN (Porter and Reiss, 1984), a finite-difference approach, to solve this eigenvalue problem.

The normal modes are subject to the orthonormality condition:

$$\int \frac{\psi_m(z) \psi_n(z)}{\rho(z)} dz = \begin{cases} 1, & \text{for } m = n \\ 0, & \text{for } m \neq n \end{cases} \quad (3.6)$$

The branch line integral in Equation (3.5), which represents the contribution of a continuous spectrum of the so-called leaky modes, can usually be neglected at large distances r compared to the sea depth. Moreover, the Hankel function $H_0^{(1)}(k_{rm} r)$ can be approximated by an exponential function at large distances. In this case, the pressure field can be found in an approximate form as

$$p(r, z) \cong \frac{P_0}{\rho(z_s)} \left(\frac{2\pi}{r} \right)^{1/2} \sum_{m=1}^M k_{rm}^{-1/2} \psi_m(z_s) \psi_m(r, z) \exp\{-i(k_{rm} r - \pi/4)\} \quad (3.7)$$

where P_0 is the acoustic pressure at a unit distance (1 m) from the source. The phase and group velocities of mode m are $v_m(\omega) = \omega/k_{rm}$ and $u_m(\omega) = d\omega/dk_{rm}$ respectively. The dependence of u_m on frequency is sometimes referred to as intra-modal dispersion, and similarly, the dependence of u_m on mode number m as inter-modal dispersion. For each mode m , there is a frequency f_m below which the imaginary component of the wavenumber k_{rm} increases significantly and, consequently, the mode attenuates rapidly with range. This frequency is called a mode cut-off frequency.

3.2.2 Normal modes in range-dependent environment

A coupled-mode model has been developed to numerically solve the problem of acoustic propagation in a range dependent ocean environment using the normal mode approximation. The fundamental assumption in this approximation is that that sound field at each particular distance from the source can be represented by a sum of the normal modes with the shapes and wavenumbers corresponding to local environmental conditions constituting a so-called reference waveguide. Dividing the propagation path into a number of short segments, within which the waveguide is assumed to be range independent, the final acoustic field can be approximately calculated by coupling the sound field solutions for each range segment to satisfy the boundary conditions at the vertical interfaces between the segments. Such coupling leads to scattering modes into waves propagated in both forward and backward directions. Evans (1983) included both forward and backward scattered components in his two-way coupled-mode algorithm for sound field numerical modelling. Porter, Jensen and Ferla (1991) neglected the backscattered waves, as it is insignificant in relatively slowly varying media, and formulated a one-way coupled-mode model, which significantly increased the computational efficiency.

Another coupled-mode based approach is to partly analytically solve Equation (3.1), assuming that the spatial variation of the propagation conditions is slow such that the pressure can be represented as a sum of the local modes with complex coefficients varying only with range (Brekhovskikh and Godin, 1999):

$$p(r, z) = \sum_{m=1}^M \phi_m(r) \psi_m(r, z) \quad (3.8)$$

It is also assumed that the total number of propagating modes M does not change with range. Substituting Equation (3.8) into (3.1), and taking into account the orthonormality condition for the local modes (Equation (3.6)), one can obtain the following system of M ordinary differential equations:

$$\frac{1}{r} \frac{d}{dr} \left(r \frac{d\phi_n}{dr} \right) + \sum_{m=1}^M A_{mn} \phi_m + \sum_{m=1}^M 2B_{mn} \frac{d\phi_m}{dr} + k_m^2 \phi_n = -\frac{\delta(r) P_0 \psi_n(z_s)}{2\pi r} \quad (3.9)$$

where

$$A_{mn} = \int \frac{1}{r} \frac{\partial}{\partial r} \left(r \frac{\partial \psi_m}{\partial r} \right) \frac{\psi_n}{\rho} dz \quad (3.10)$$

$$B_{mn} = \int \frac{\partial \psi_m}{\partial r} \frac{\psi_n}{\rho} dz \quad (3.11)$$

are the mode coupling coefficients that govern the interaction between different modes in the waveguide.

In a slowly varying waveguide, the modal amplitudes $\phi_m(r)$ can be represented by a product of the exponential term rapidly varying with phase and a complex coefficient slowly varying with range due to mode coupling (Chiu et al., 1996):

$$\begin{aligned} \phi_m(r, \omega) &= U_m(r, \omega) \exp \left\{ -i \int_0^r k_{rm}(r', \omega) dr' \right\} r^{-1/2} \psi_m(z_s) \\ &= A_m(r, \omega) r^{-1/2} \psi_m(z_s) \end{aligned} \quad (3.12)$$

where $A_m(r, \omega) = U_m(r, \omega) \exp \left\{ -i \int_0^r k_{rm}(r', \omega) dr' \right\}$ will be referred to as the coupled mode amplitude. Such decomposition of the complex modal amplitudes allows us to numerically solve the system in Equation (3.9) – (3.11) in a more efficient computational way (Gavrilov and Mikhalevsky, 2001) and is therefore used for numerical modelling of mode coupling in this study. Further simplification can be made by neglecting the coupling terms in Equation (3.9), i.e. assuming that the modes propagate adiabatically in the waveguide without coupling with each other. The acoustic field under the adiabatic-mode approximation can be calculated using the following equation (Jensen et al., 2000):

$$p(r, z, \omega) \cong P_0 \frac{\exp(-i\pi/4)}{\rho(z_s)} \left(\frac{2\pi}{r} \right)^{1/2} \sum_{m=1}^M \psi_m(0, z_s, \omega) \psi_m(r, z, \omega) \frac{\exp(-i \int_0^r k_{rm}(r', \omega) dr')}{\sqrt{k_{rm}(r, \omega)}} \quad (3.13)$$

3.2.3 Acoustic propagation loss due to scattering from rough boundaries

Sound attenuation in the ocean due to scattering from sea surface and seafloor roughness must be considered if the propagated acoustic waves interact strongly with any of the rough boundaries of the ocean acoustic waveguide. There have been numerous studies on wave scattering from randomly rough surfaces in different research areas, which is

comprehensively reviewed in Ogilvy's book (1991). The vertical scale of surface roughness in the wave scattering theory is commonly measured by the Rayleigh parameter $\mu \equiv 2k\sigma \cos \theta_0$, where k is the wavenumber, θ_0 is the angle of incidence and σ is the root-mean-square (RMS) height of the surface roughness. Rayleigh parameter values $\mu \ll 1$ indicate small roughness, while $\mu \gg 1$ corresponds to large roughness. Small-perturbation and Kirchhoff approximations are two methods commonly used for modelling acoustic wave scattering from rough surfaces. The small-perturbation approximation is valid only if the sound waves reflected from the surface are slightly altered by its small roughness. The necessary condition for this is $\mu \ll 1$. The Kirchhoff approximation, also known as a tangent plane method, requires the roughness of the surface to be sufficiently smooth, i.e. $2ka \cos(\theta) \gg 1$ where a is the local radius of curvature of the scattering surface (Brekhovskikh and Lysanov, 1991).

The effect of surface scattering on the acoustic propagation loss can be taken into account by modelling the coherent (i.e. ensemble-average) reflection coefficient and reflection loss from a rough boundary of the ocean waveguide and incorporating the angular dependence of this coefficient into numerical models of sound propagation in the ocean.

Using small perturbation of the boundaries in the normal mode model and a small-slope approximation for surface scattering, Kuperman et al. (1975, 1977) derived the mode attenuation coefficients associated with the coherent reflection loss from the surface roughness. In this approximate model, the mode attenuation coefficient due to sea surface scattering is:

$$\gamma^{(scat)} = \frac{\rho\sigma^2 k_{zm}}{2k_{rm}} \left(\left. \frac{d\psi_m(z)}{dz} \right|_{z=0} \right)^2 \quad (3.14)$$

Here σ is the RMS height of the surface roughness and $k_{zm} = \sqrt{\frac{\omega^2}{c^2(0)} - k_{rm}^2}$ is the vertical wavenumber.

3.2.4 Broadband modelling

Modelling of broadband signal propagation is implemented through Fourier synthesis of the solutions found in the frequency domain. The signal spectrum at the receiver is

$$p(\mathbf{r}, \omega) = S(\omega)g(\mathbf{r}, \omega) \quad (3.15)$$

where $S(\omega)$ is the source spectrum and $g(\mathbf{r}, \omega)$ is the acoustic channel transfer function calculated for an acoustic source of unit amplitude at different frequencies using one of the appropriate numerical models of sound propagation, e.g. the normal mode model in this study (Equation (3.13)). To obtain the waveform of the received signal, the inverse Fourier transform is applied to $p(\mathbf{r}, \omega)$, which can be evaluated most efficiently using the Fast Fourier Transform (FFT) algorithm. The frequency sampling interval $\Delta\omega$ of the modelled transfer function must be chosen such that time interval $T = 1/\Delta\omega$ is larger than the maximum temporal spread of the channel impulse response expected for the modelled propagation conditions and propagation range. The spread of the impulse response depends on the waveguide dispersion characteristics (multipath propagation) and range.

3.3 Numerical modelling of sound propagation from Antarctica to the IMS hydroacoustic stations

The adiabatic normal mode model is used in this section to investigate the sound propagation from Antarctica to the IMS hydroacoustic stations in the Indian Ocean, to examine the mode and frequency dispersion effects along the propagation paths and to simulate numerically the waveform and spectrogram of the signals received at the IMS stations from sources of impulsive noise in Antarctica, such as ice cracking and breaking events.

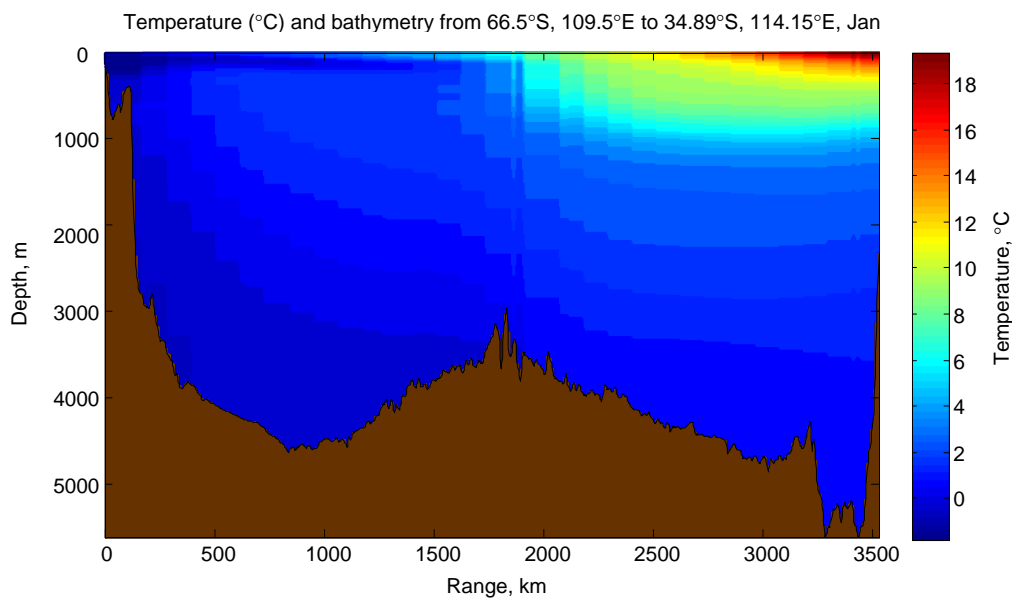
3.3.1 Sound speed profiles from Antarctica to the IMS stations in the Indian Ocean

Temperature and salinity data are required to derive the sound speed profile along the modelled propagation path. Climatological seasonal and monthly temperature and salinity data with one-degree resolution in both latitude and longitude for the whole world ocean

were obtained from the World Ocean Atlas 2005 (WOA05) (Antonov et al., 2006, Locarnini et al., 2006). The seasonal climatology data in WOA05 are presented at 33 standard depths from the sea surface to 5500 m, while those for the monthly climatology data are given only at 24 standard depths from 0 m to 1500 m. Because temporal variations of climatology data in deep water layers are relatively small, the monthly data can be reasonably accurately extrapolated into deeper water below 1500 m by filling with the corresponding seasonal data taken at the same location. The hydrostatic pressure needed for calculation of the sound speed was obtained from the depth and latitude of each sample using Saunders and Fofonoff's formula (Saunders and Fofonoff, 1976). The bathymetry data were taken from the ETOPO2 Global 2-Minute Gridded Elevation Data (<http://www.ngdc.noaa.gov/mgg/fliers/01mgg04.html>). The temperature, salinity and bathymetry data were interpolated into an equally spaced horizontal grid along the propagation path, and the sound speed profile at each grid point was calculated using Chen-Millero-Li' formula (Millero and Li, 1994) and then interpolated onto a vertical grid with 10-m resolution.

The January temperature, salinity and sound speed vertical profiles along the paths from Vincennes Bay in Antarctica (66.5°S, 109.5°E) to the HA01 and H08S hydroacoustic stations are shown in Figure 3.1 and 3.2 respectively. The sea depth at the source location is around 200 m. In the deep water layers at depths below 2000 meters, where the temperature and salinity keep relatively constant, the sound speed increases monotonically with depth due to the increasing hydrostatic pressure. For the water column above 2000 m depth, the major feature of the sound speed field along the acoustic paths is the frontal zone at the Antarctic Convergence which divides the acoustic path into two sections with very distinct conditions of acoustic propagation. Along the southern section, the water temperature and salinity have minimum values near or at the sea surface and, therefore, the sound speed also has a minimum near the surface and forms a near-surface acoustic channel. The acoustic propagation in this region experiences strong interaction with the rough sea surface, which is either the ridged sea ice canopy appearing in the southern parts of the acoustic path in winter or an ice-free sea surface perturbed by wind waves, which are frequently high in the Southern Ocean. Scattering from the sea surface roughness along the southern section of

the acoustic path results in high attenuation of the acoustic energy. The acoustic propagation loss increases rapidly with frequency due to the surface scattering and, hence, only low frequency signals can propagate over large distances in such conditions. To the north of the Antarctic Convergence Zone (ACZ), the cold and less saline, northward-flowing Antarctic waters predominantly sink beneath warmer sub-Antarctic waters, which makes the sound speed minimum dive abruptly to a depth of about 1000 m. Sound refracts towards the sound speed minimum, so this depth forms the axis of a low-loss acoustic channel called the SOFAR channel. The shallow-angle rays or normal modes of low order can propagate in the SOFAR channel without interaction with the sea surface and the seafloor. Associated with the temperature and salinity variation, the SOFAR channel for the path to HA01 is nearly range-independent along the section north of the ACZ, while the depth of the SOFAR channel along the path to H08S decreases gradually with the range closer to the receive station (Figure 3.2).



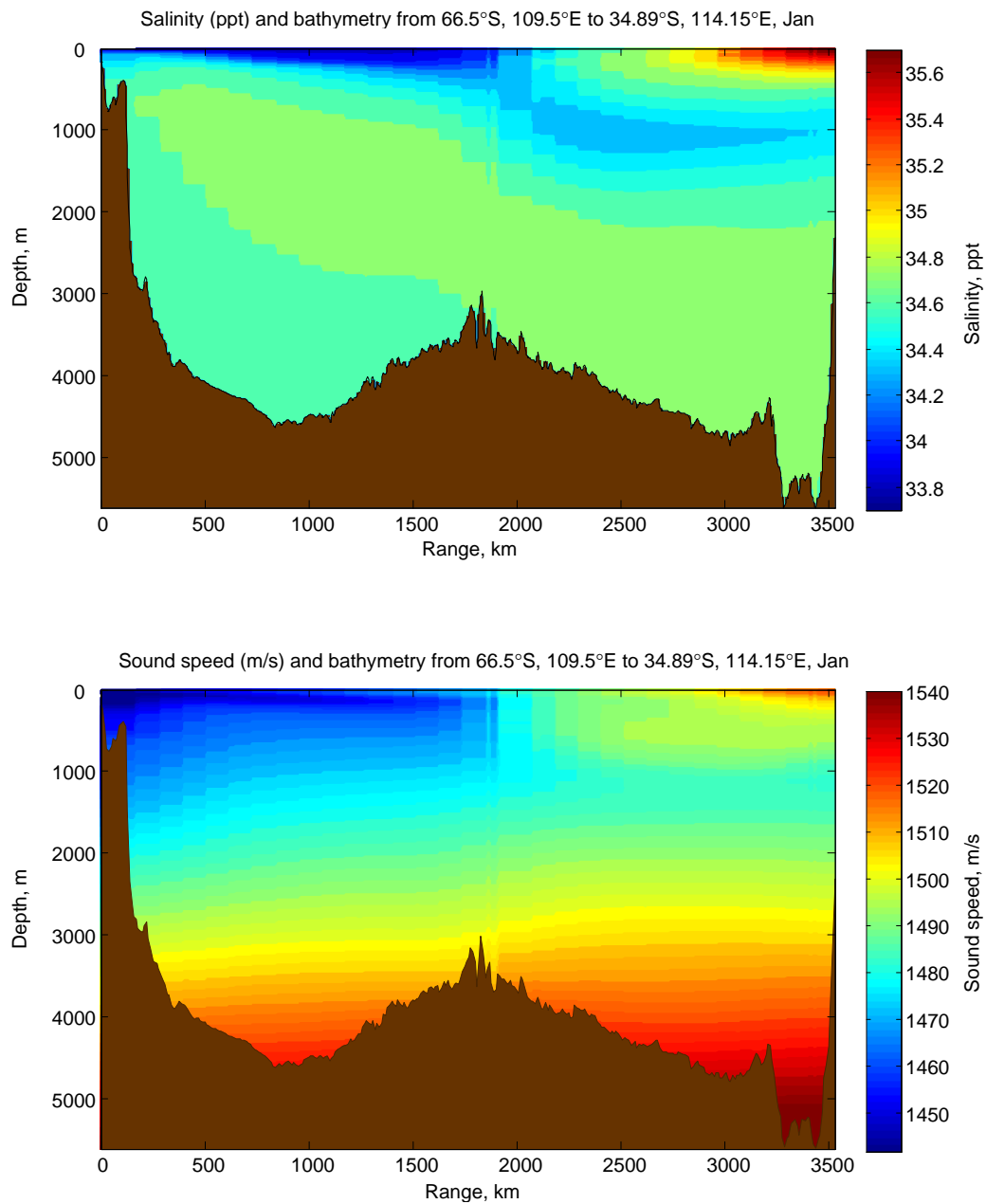
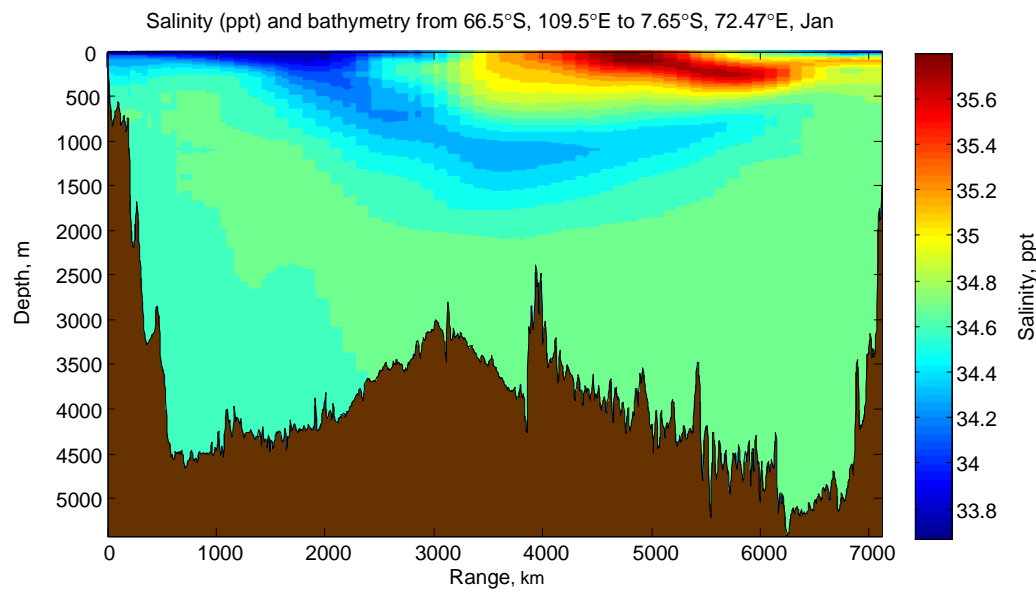
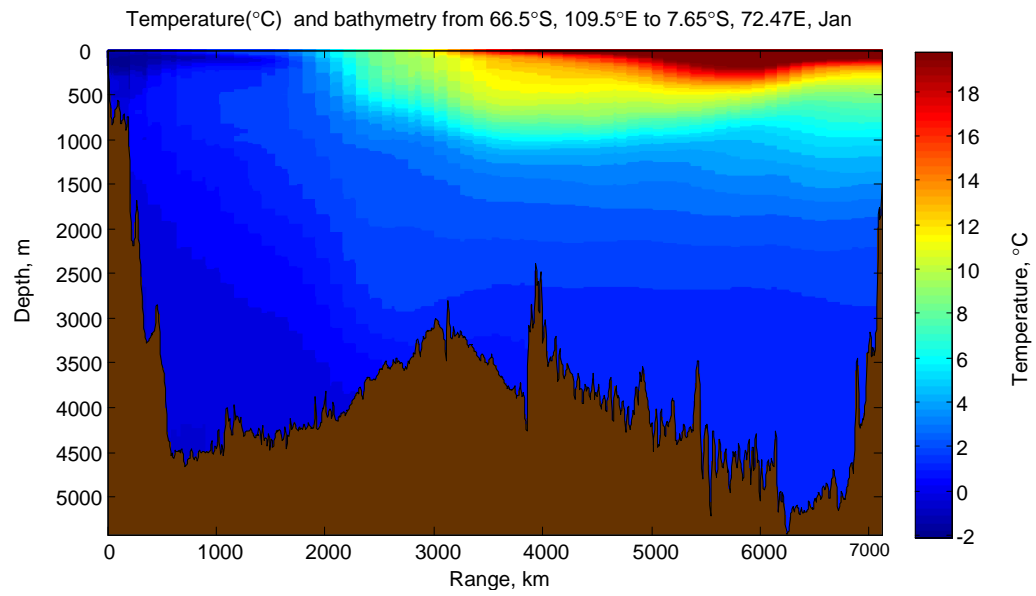


Figure 3.1. The temperature (top panel), salinity (middle panel) and sound speed (bottom panel) profiles along the path from Vincennes Bay, Antarctica (66.5°S, 109.5°E) to the HA01 hydroacoustic station (34.89°S, 114.15°E), with monthly climatology data for January.



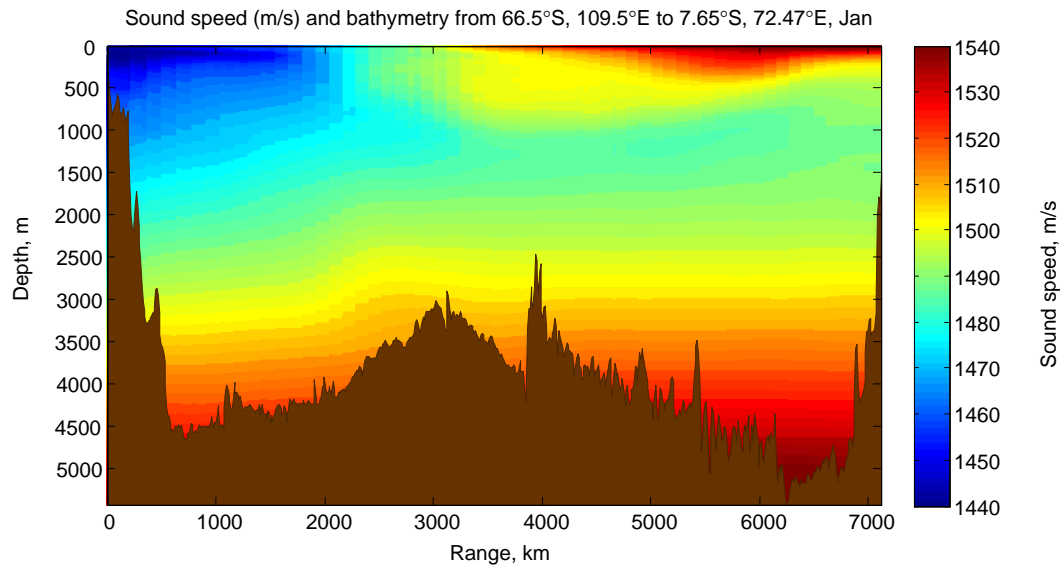


Figure 3.2. The temperature (top panel), salinity (middle panel) and sound speed (bottom panel) profiles along the path from Vincennes Bay, Antarctica (66.5°S, 109.5°E) to the H08S station (7.65°S, 72.47°E), with monthly climatology data for January.

3.3.2 *Transfer function of the ocean acoustic channel*

The adiabatic-mode model (Equation (3.13)) introduced in Sections 3.2.2 was used to numerically investigate the acoustic propagation from Antarctica to the IMS stations in the Indian Ocean. The normal mode shapes and wavenumbers in Equation (3.13) were calculated using the KRAKEN algorithm implemented in Matlab. The frequency band of modelling was from 3 Hz to 50 Hz, which covers the frequency range of the signals from ice event observed at the two selected IMS stations in the Indian Ocean. There are two major factors that influence the transmission loss of low frequency signals from Antarctica to the Indian Ocean. These factors are the interaction with the seafloor over shallow water regions and the sea surface scattering in the polar environment. To model these two phenomena, it is essential to define appropriate boundary conditions, such as the structure and acoustic properties of the sediments and the spectral characteristics of the sea ice roughness. In our model, the mode attenuation due to surface scattering was calculated using Equation (3.14) for small-slope surface roughness (Kuperman, 1975, Kuperman and Ingenito, 1977). In the absence of more detailed data, the RMS height of surface roughness was assumed to be range independent and equal to 3 m, which corresponds to the wave height most frequent in the southern parts of the Southern Ocean, according to remote sensing observations [<http://www.bom.gov.au/weather/ant/>].

Acoustic properties of the seafloor in the Southern Ocean are also poorly known and not mapped. Therefore, we chose a simple model consisting of two layers of acoustically fluid sediment overlaying a rigid basement. Acoustic properties of the upper layer were defined assuming that it consists mainly of sand. The details of the seafloor model are given in Table 3.1. At low frequencies of tens of Hz, sound attenuation due to acoustic absorption in sea water is very small, compared to the surface and bottom reflection losses, and therefore was neglected in the model.

Table 3.1. Properties of the seafloor acoustic model chosen for modelling the acoustic propagation along the path from Antarctica to the Indian Ocean.

	Thickness (m)	Compressive sound speed (m/s)	Sound speed gradient (1/s)	Density (g/cm ³)	Attenuation (dB/km*Hz)
Layer 1	100	1800	1.5	1.8	0.1
Layer 2	100	2000	1.0	2.1	0.3
Basement		3000	0	2.4	1.0

To analyse the effect of different factors on attenuation of individual modes along the propagation path, we define the transfer function of an individual mode m as

$$\zeta_m = \exp(i \int_0^r k_{rm}(r', \omega) dr') / \sqrt{k_{rm}'(r, \omega)} \quad (3.16)$$

where the mode wavenumber $k_{rm}(r, \omega) = k_{rm}'(r, \omega) + ik_{rm}''(r, \omega) + i\gamma^{(scat)}(r, \omega)$ includes the real part $k_{rm}'(r, \omega)$ and an imaginary part, which governs mode attenuation with range. The imaginary part consists of two components: $k_{rm}''(r, \omega)$ is the attenuation coefficient due to interaction with the seafloor and $\gamma^{(scat)}(r, \omega)$ the attenuation coefficient due to surface scattering loss. Such a definition of the mode transfer function disregards the spreading loss common for all modes and the influences of the modal shapes at the source and the receiver which affect the modal excitation coefficients and the signal amplitude at the receiver. Therefore, this function reflects only the effects of losses from bottom attenuation and sea surface scattering.

Figure 3.3 demonstrates the transfer functions of modes 1 - 4 at the receivers of HA01 and H08S in the frequency band of 3-50 Hz for an acoustic source located in Vincennes Bay. The corresponding sound speed profiles along the two paths are shown in Figures 3.1 and 3.2. It is clearly seen in this figure that the amplitude of modes is very small below a certain frequency which increases with mode number. This frequency corresponds to the cut-off frequency of individual modes propagated along the shallow-water section of the acoustic path over the Antarctic continental shelf. Figure 3.4 shows the attenuation (dB/km)

of modes 1 - 4 over this section. It is clearly seen from this Figure that the attenuation of individual modes due to interaction with the seafloor over the continental shelf increases with mode number and decreases with frequency, as discussed in Section 3.2.1. Therefore, mode 1 dominates the other modes in the propagated acoustic signals below 20 Hz. On the other hand, mode attenuation due to acoustic scattering by the rough sea surface increases rapidly with frequency along the path section south of the Antarctic Convergence. At a given frequency, the propagation loss due to surface scattering decreases with mode number. The modes of lower order, trapped in a thinner water layer near the sea surface, experience more interaction with the rough boundary and hence attenuate faster. As a result, the attenuation of each mode is minimum at a certain frequency which increases with mode number, as can be clearly seen in Figure 3.3.

Figure 3.5 shows the transfer functions of the first four modes at 30 Hz as a function of range to the receiver for the two propagation paths. At this relatively high frequency, the attenuation due to bottom interaction is still the main factor for the propagation loss of higher modes. In contrast to the higher modes, sea surface scattering is the major factor affecting attenuation of mode 1 along the southern section of the paths in the Southern Ocean. It is also noted that mode 1 experiences more propagation loss in the Southern Ocean along the path to the H08S station than that to HA01. This occurs because the path to H08S has a longer section with the near-surface channel south of the ACZ than that to HA01. For the path sections north of the ACZ, low-order modes propagate in the SOFAR channel with no interaction with the sea surface and the seafloor at relatively low frequency, and therefore the mode transfer functions remain nearly constant.

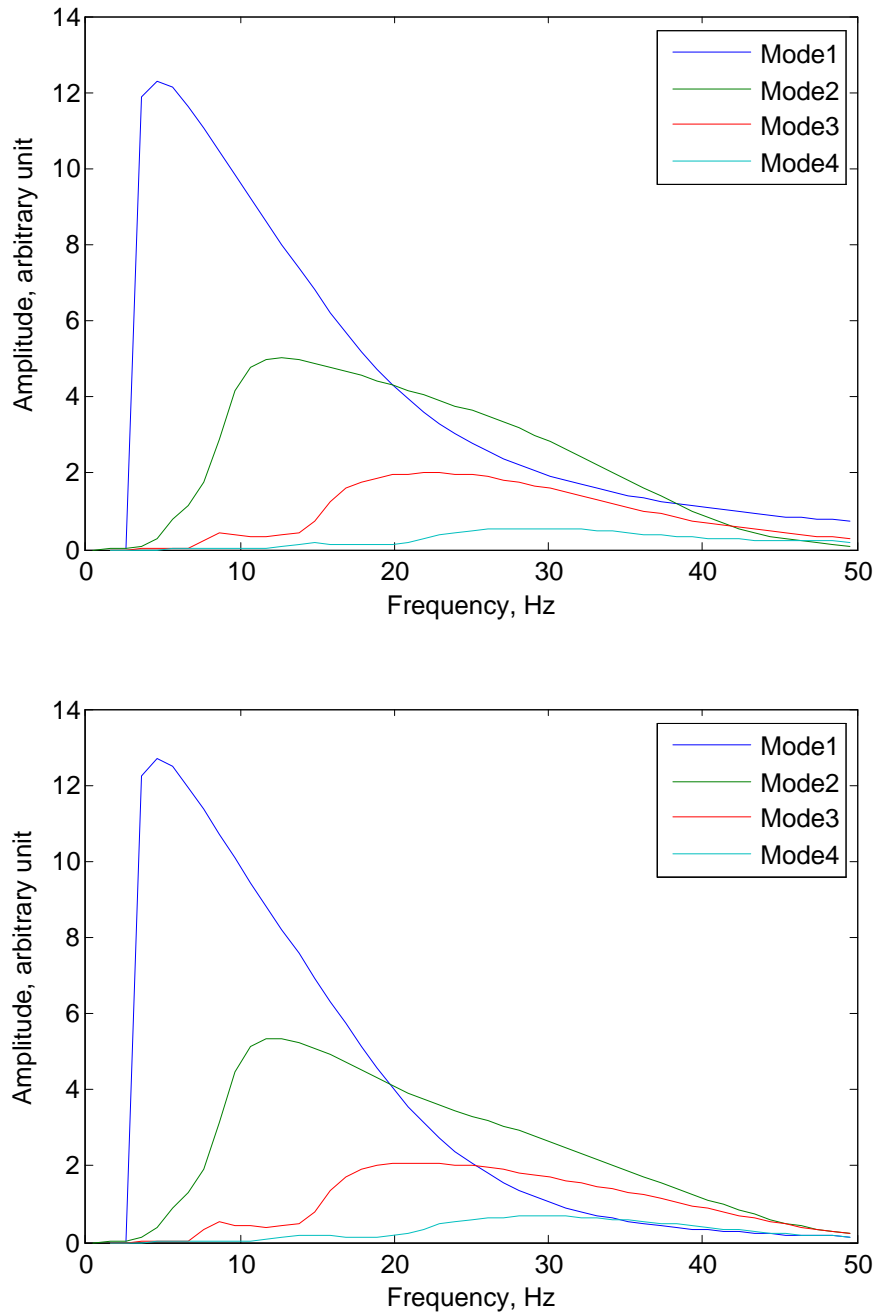


Figure 3.3. Amplitude (arbitrary unit) of the transfer function of modes 1 to 4 as a function of frequency numerically modelled using the adiabatic mode model for the propagation path from Vincennes Bay in Antarctica to HA01 (top panel) and to H08S (bottom panel), shown disregarding cylindrical spreading.

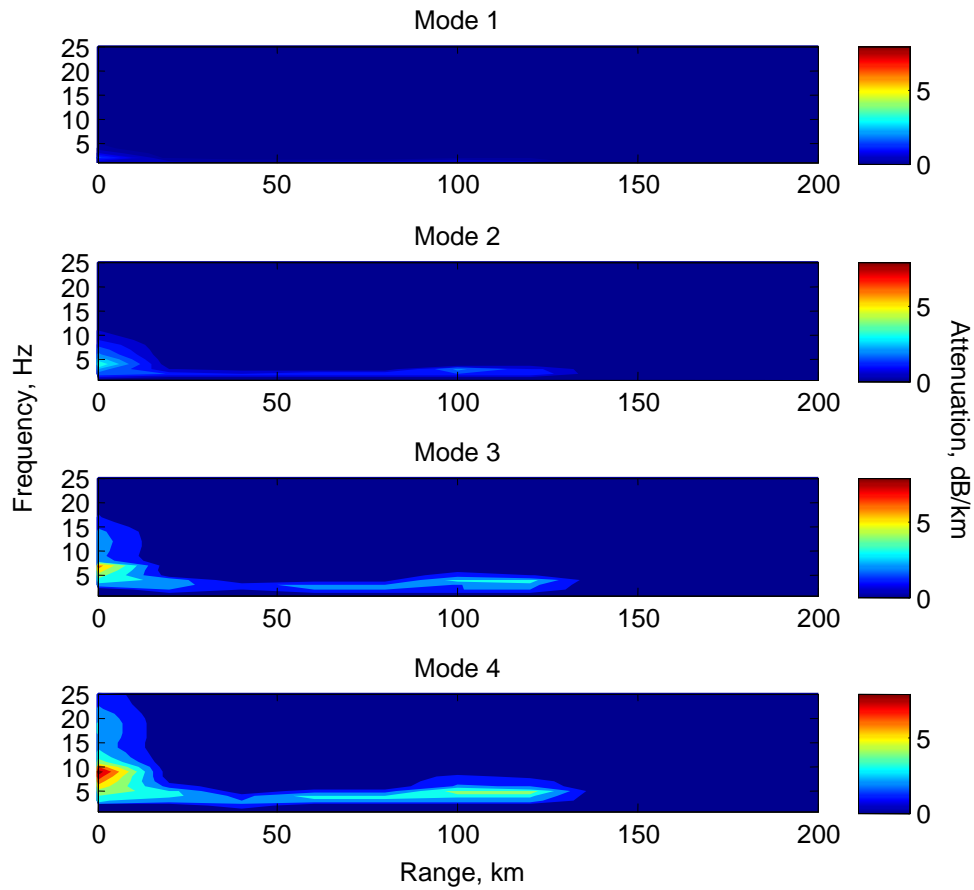


Figure 3.4. Variations of the attenuation coefficient (dB/km) of modes 1-4 along the initial 200-km section (over the Antarctic continental shelf) of the propagation path from Vincennes Bay in Antarctica to HA01 (shown in Figure 3.1)

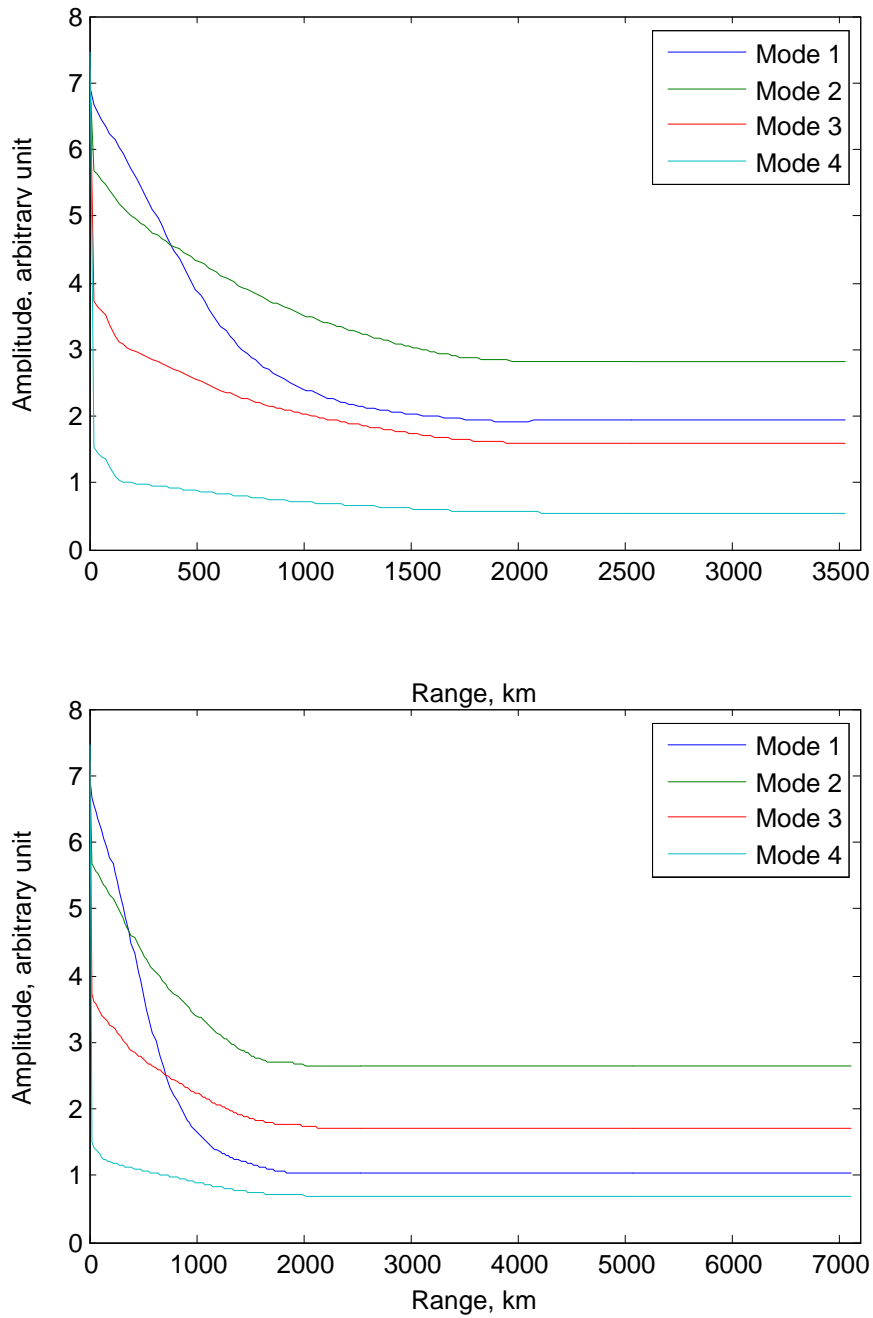


Figure 3.5. Variations of the amplitude (arbitrary unit) of the transfer function of modes 1 to 4 at 30 Hz with along the propagation paths from Vincennes Bay to HA01 (top panel) and to H08S (bottom panel) numerically modelled using the adiabatic mode model, shown disregarding cylindrical spreading.

3.3.3 The dependence of propagation loss on sea depth, source depth and frequency

As seen from Equation (3.13), the amplitudes of individual modes at the receiver depend on the mode transfer function and the product $\psi_{ms}(z_s) \times \psi_{mr}(z_r)$, where $\psi_{ms}(z_s)$ and $\psi_{mr}(z_r)$ are the amplitudes of mode m at the source and receiver depths respectively. The depths of the IMS hydrophones are fixed and the sea depths at hydrophones' positions are also determined, therefore, the mode amplitude at the receiver $\psi_{mr}(z_r)$ is dependent only on mode number and frequency.

For the modes at the source position ψ_{ms} , because the majority of Antarctic ice events are from Antarctic coastal regions with sea depth of tens to hundreds of meters, as will be discussed in Chapter 5, the sea depth has impact on the propagation of those modes at low frequencies. Figure 3.6 shows the attenuation coefficient (i.e. imaginary part of horizontal wavenumber) of the first two modes as a function of sea depth and frequency in the typical Antarctic coastal region. The sound speed profile is taken from the region of Vincennes Bay, Antarctica for winter season, and the sea depth parameters are from Table 3.1. It can be seen that mode one can propagate in most cases except at very low frequency in very shallow water. While for mode two, the propagation is much more limited and the curve of its cut-off frequency, which decreases with the sea depth, can be clearly noted in the right panel of Figure 3.6. For instance, at frequencies lower than 20 Hz, mode two can not propagate when the sea depth is below 80 m. The sea depth has to be above around 250 m for mode two to propagate at 5 Hz.

Antarctic ice events are expected to occur mainly near the sea surface. However, some ice shelves and large icebergs have underwater parts more than a hundred meters deep, so the source depth may be somewhat different for different ice events and, therefore, the mode amplitude at the source $\psi_{ms}(z_s)$ is also source depth dependent. Due to the strong acoustic surface channel in the Polar environment, mode one dominates against higher modes through the shallow water column with tens to hundreds of meters sea. As an example, Figure 3.7 shows the product $\psi_{ms}(z_s) \times \psi_{mr}(z_r)$ as a function of source depth and

frequency for the first two modes. In this instance, the source is located in Vincennes Bay with sea depth of around 200 m and the receiver is one of the HA01 hydrophones. The January sound speed profile along the acoustic path is taken for modelling. For mode 1, the peak value of the product occurs at a source depth of 100 m and slightly increases with frequency. The product for mode 2 has a pattern with negative and positive peak values appearing alternatively across the depth. Over the frequency range of 3-30 Hz, the product $\psi_{ms}(z_s) \times \psi_{mr}(z_r)$ for mode 1 is higher than that for mode 2 for any source depth within the range analysed. Taking this into account along with the transfer function of individual modes presented in the previous section, one can conclude that mode 1 is expected to dominate at frequencies below 20 Hz in the signals received at HA01 and H08S from Antarctic ice event which occur in relatively shallow water of tens to hundreds of meters over the Antarctic continental shelf. According to the numerical modelling results, the optimum frequency of sound propagation with the minimum transmission loss is between 5 and 10 Hz, which is consistent with the most typical frequencies of the peak power spectral density of the signals from ice events detected at HA01 shown in the histogram in Figure 2.20.

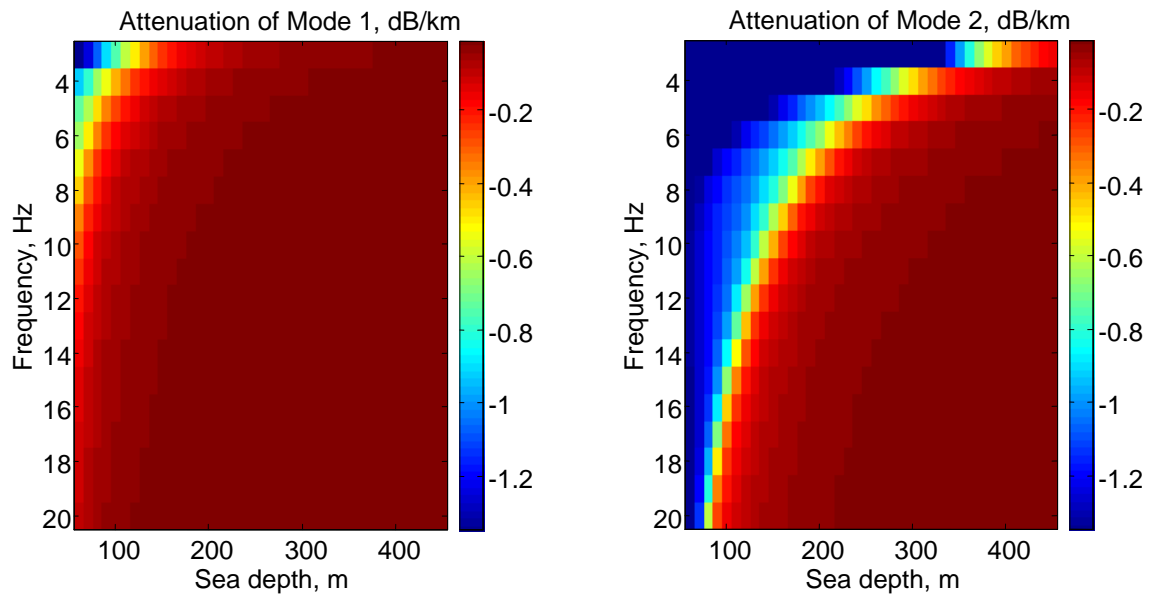


Figure 3.6. The attenuation (dB/km) as a function of sea depth and frequency for mode one (left panel) and mode two (right panel). The sound speed profile is taken from the region of Vincennes Bay, Antarctica for winter season, and the sea depth parameters are from Table 3.1.

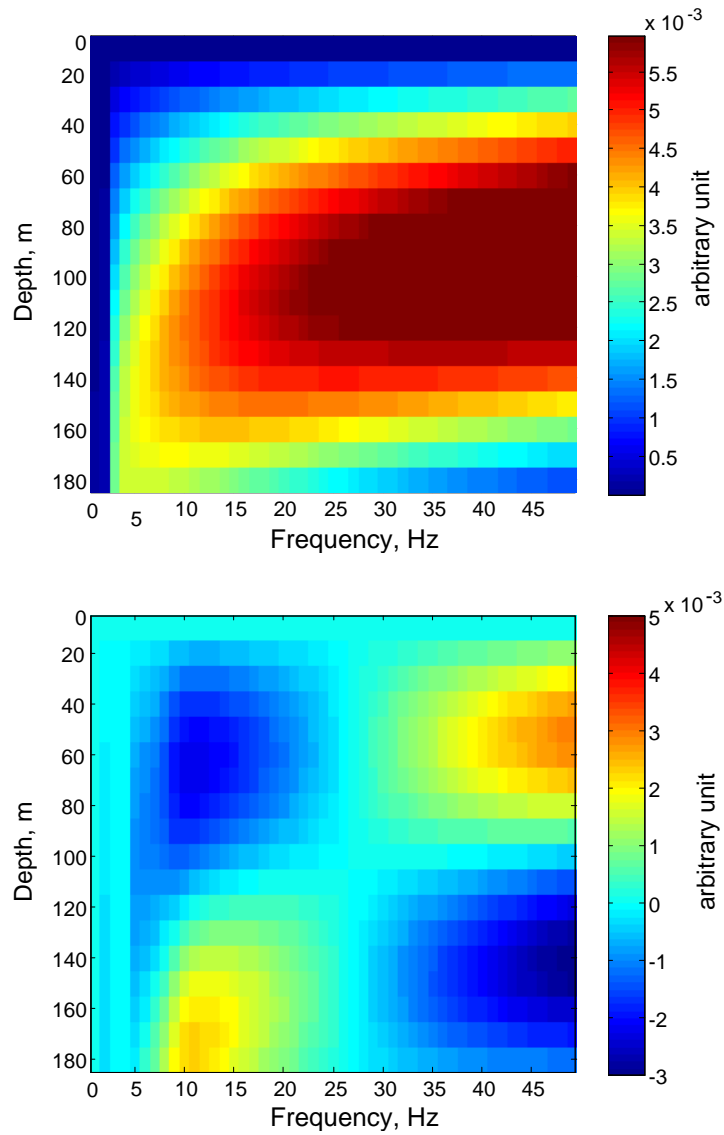


Figure 3.7. Product $\psi_{ms}(z_s) \times \psi_{mr}(z_r)$ as a function of source depth and frequency for mode 1 (top panel) and mode 2 (bottom panel). $\psi_{ms}(z_s)$ is the mode amplitude at the source position and $\psi_{mr}(z_r)$ is the mode amplitude at the HA01 hydrophone.

3.3.4 *Transmission loss*

The adiabatic mode transmission loss at 10 Hz along the acoustic paths from Vincennes Bay in Antarctica to the HA01 and H08S station is shown in Figure 3.8 in the top and bottom panels respectively. This figure clearly illustrates the difference between the acoustic propagation south and north of the Antarctic Convergence. In the polar region of the Southern Ocean, the acoustic energy is channelled near the sea surface and affected by the surface roughness. At the Antarctic Convergence, the acoustic energy dives rapidly into the deep SOFAR acoustic channel and interacts very little with the sea surface and the seafloor. Based on our numerical calculation for acoustic sources located in different parts of the observable Eastern Antarctic coastal zone with the sea depth varying from about 100 m to 500 m, the transmission loss to HA01 can be up to 120 dB. Taking into account the amplitude range of the ice signals received at HA01 being from 100 to 130 dB re 1 μ Pa, as shown in Figure 2.18, one can expect that the source level can be as high as 250 dB re 1 μ P @ 1m.

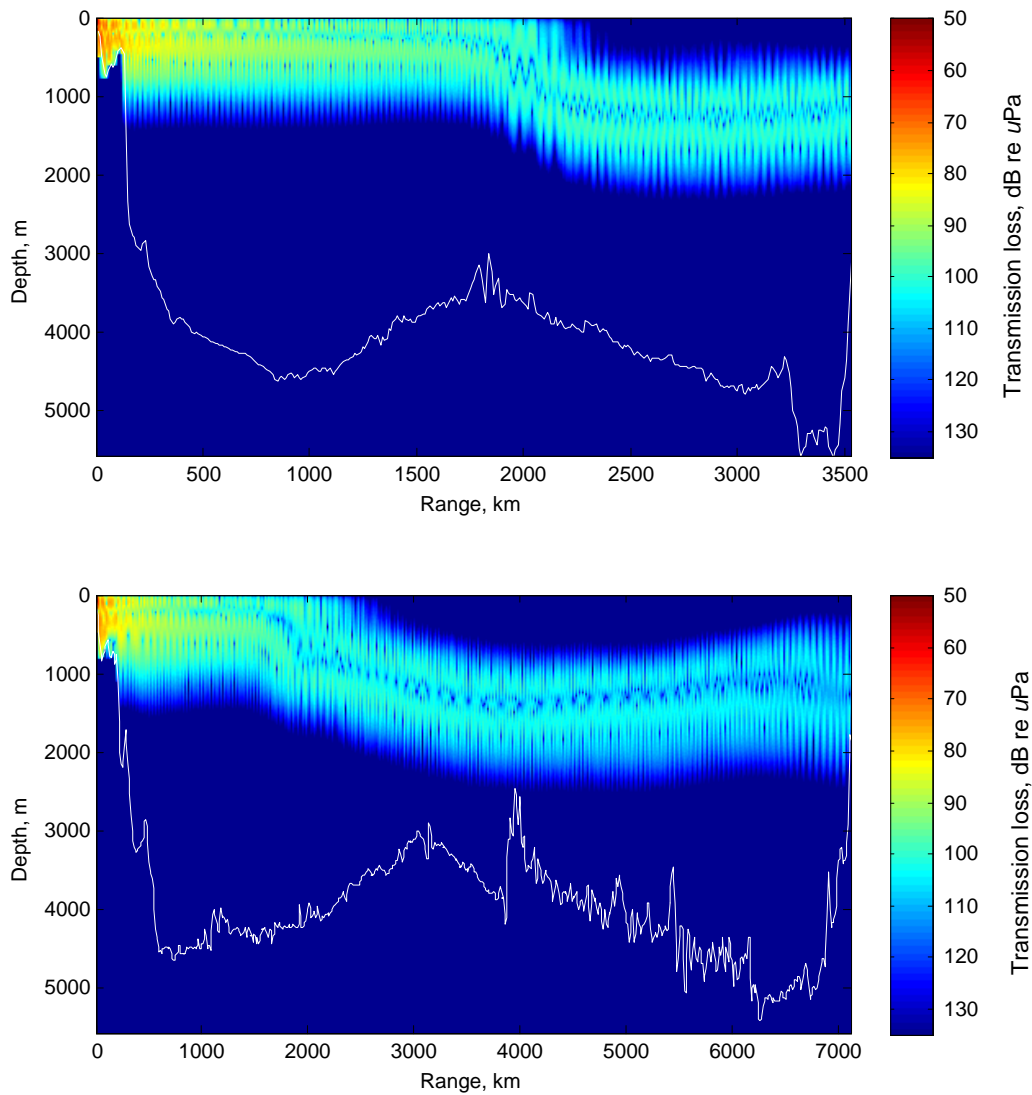


Figure 3.8. Adiabatic mode transmission loss (dB) at 10 Hz modelled along the path from Vincennes Bay to HA01 (top panel) and to H08S (bottom panel) for the source depth of 200 m.

3.3.5 Mode coupling effect

Variable bathymetry and horizontal gradients in the sound speed field along the acoustic path cause coupling of acoustic modes. The mode coupling effect may also lead to noticeable variations of the modal travel times and amplitudes (Gavrilov and Mikhalevsky,

2001, Gavrilov and Mikhalevsky, 2006). Any acoustic path from Antarctica to the hydroacoustic stations in the Indian Ocean is essentially range dependent, because it crosses the Antarctic continental slope, the Antarctic Convergence Zone, and the continental slope near the receive station. Therefore, it is important to investigate possible effects of mode coupling on the modal travel time and amplitudes that may affect the prediction of the arrival structure of the signals received at the IMS stations, which is discussed later in this chapter, and the localization of Antarctic ice events discussed in Chapter 5. Assuming that the spatial variation of the acoustic propagation conditions along the paths from Antarctica is relatively gradual, an approximate solution for the complex amplitudes of coupled modes propagated from Antarctica to the IMS stations can be derived using the system of equations in Equation (3.9), the approximation given by Equation (3.12), and the computational algorithm described in detail in the reference (Gavrilov and Mikhalevsky, 2001). In the analysis of the mode coupling effect, we disregard the influence of the amplitudes of mode shapes at the source and receiver.

The absolute values of the complex amplitude $A_m(r, \omega)$ (see Equation (3.12)) of modes 1 to 4 at 20 Hz along the propagation paths from Vincennes Bay, Antarctica to the two IMS stations are shown in Figure 3.9. The continental slopes at the beginning and end of the path are quite steep for both paths. The mid-ocean ridge is not high enough to influence propagation of low-order modes in the SOFAR channel. The sharp frontal zone at the Antarctic Convergence is in the middle of the acoustic path. The mode coupling effects are revealed as rapid fluctuations of the modal amplitudes with distance. For the propagation path to HA01, mode coupling affects the amplitudes of low-order modes only over the Antarctic continental slope and across the Antarctic Convergence, while the coupling effect along the path to H08S is noticeable also over the continental slope near the receiver. Mode 1 is least sensitive to sea depth variations on the Antarctic shelf, because its energy is trapped in a thinner near-surface layer of water (see the panel (a2) in Figure 3.11). Moreover, this mode is also least sensitive to the sound speed changes with range across the ACZ and in the SOFAR channel. Sea depth at the HA01 station is large enough not to significantly affect the low-order modes that carry most of the signal energy. The mode coupling effect near the H08S station is also relatively weak.

The transfer functions of modes 1 – 4 perturbed by variations of $\phi_m(r, \omega)$ (see Equation (3.12)) with frequency are shown in Figure 3.10 for both propagation paths. The mode coupling induces fluctuations in the mode transfer functions superimposed the gradual variation predicted by the adiabatic-mode model. These fluctuations are relatively small, especially for mode 1, so that the general trend of amplitude variation with frequencies remains similar to that predicted by the adiabatic-mode model. Therefore, the adiabatic-mode approximation can be used to numerically predict with reasonable accuracy characteristics of modes in the signals received at the IMS stations from sources of noise in Antarctica. This approximation is most accurate for mode 1, which dominates the higher modes at low frequencies in the signals received at both HA01 and H08S stations.

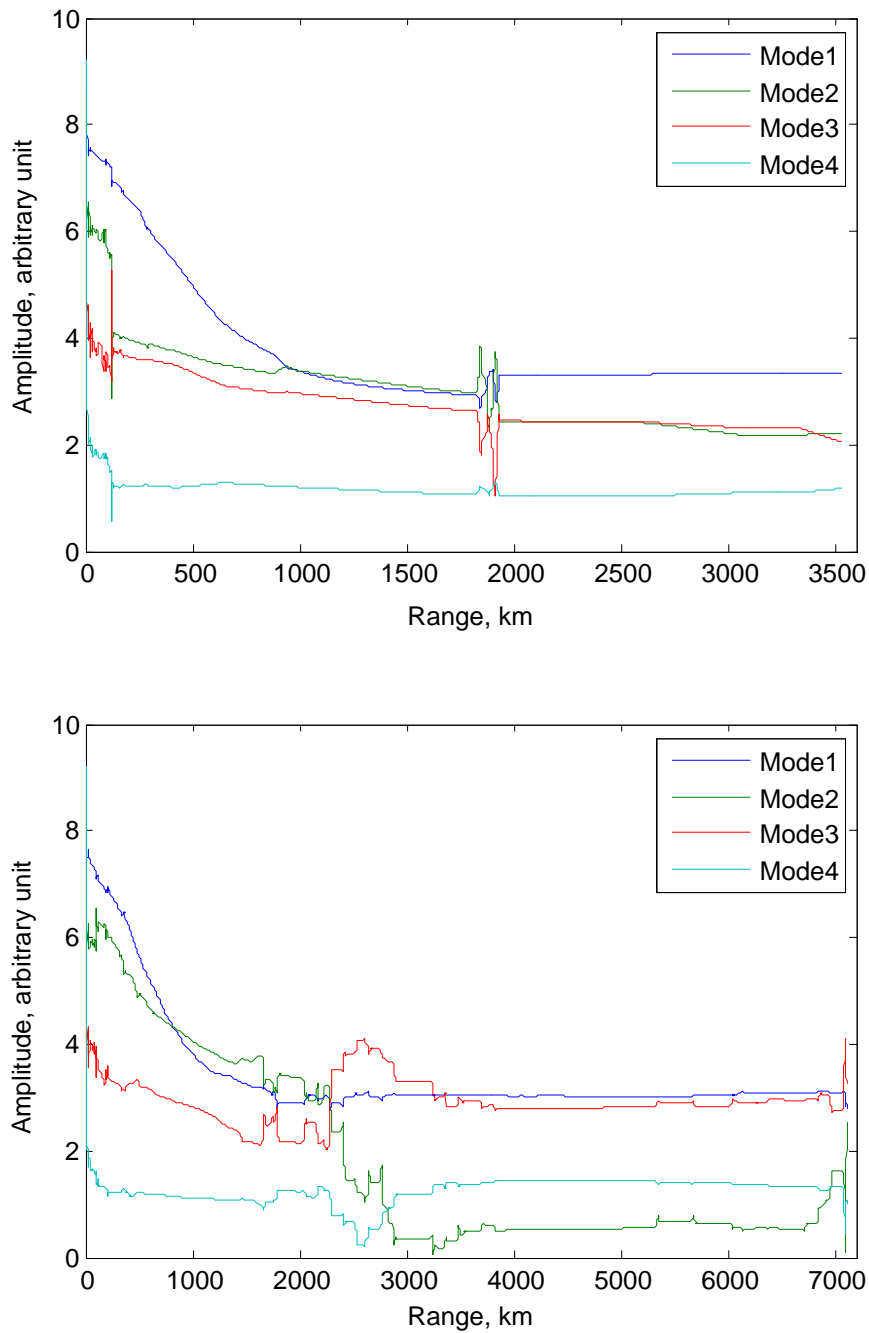


Figure 3.9. Absolute value of the amplitude $A_m(r, \omega)$ (arbitrary unit) (see Equation (3.12)) of modes 1 to 4 at 20 Hz as a function of range numerically modelled using the coupled-mode model for the propagation path from Vincennes Bay to HA01 (top panel) and H08S (bottom panel).

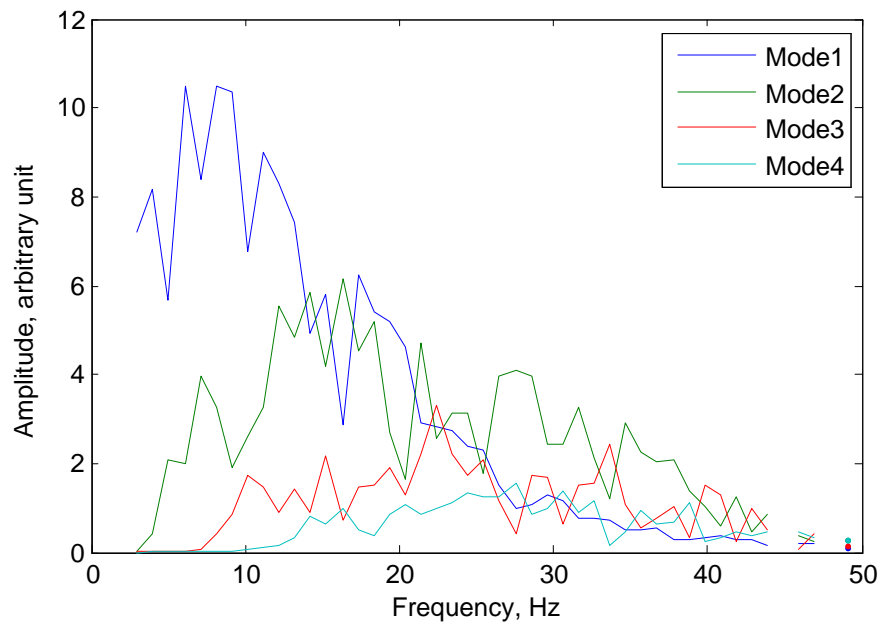
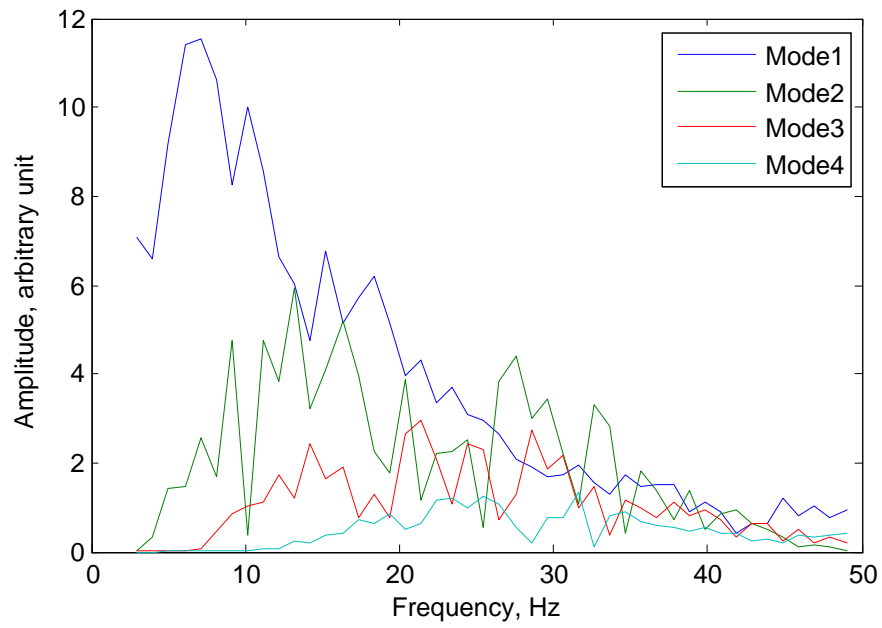


Figure 3.10. Absolute value of the amplitude (arbitrary unit) of modes 1 to 4 at the receivers of HA01 (top panel) and H08S (bottom panel) numerically modelled using the coupled-mode model.

3.3.6 Mode and frequency dispersion

As shown in Section 2.5.5, the transient signals received at the IMS stations from Antarctic ice events reveal strong frequency dispersion. In this section, the dispersion effect of the sound propagation from Antarctica to the Indian Ocean is numerically investigated.

Figure 3.11 shows the sound speed profiles typical for the acoustic path sections in the southern part of the Southern Ocean and in the Indian Ocean (panels (a1) and (b1)), the shapes of the first three modes (panels (a2), (a3), (b2) and (b3)), and the variations of their group velocities with frequency (panels (a4) and (b4)) in these two regions. For the region south of the ACZ, mode 1 has strong negative frequency dispersion at frequencies higher than the critical frequency, i.e. the group velocity decreases with frequency, as shown in panel (a4). This can be explained by noting that the thickness of the water layer within which the acoustic modes are trapped by the near-surface channel decreases with frequency as shown in panel (a2). This results in the acoustic energy of lower frequency penetrating to deeper water, where the sound speed is higher, and therefore propagating with a higher group velocity. It should also be noted that there exists an intermodal dispersion phenomenon in the acoustic channel, i.e. the group velocity of modes is different and increases with mode number in the polar environment. This is also due to deeper penetration of the energy of higher modes in the near-surface acoustic channel, as seen in panel (a3). The group velocity of mode 1 becomes weakly dependent on frequency above approximately 35 Hz, when the energy of mode 1 becomes concentrated within the near-surface channel and does not penetrate much into deeper water layers. Modes 2 and 3 exhibit a weaker dispersion effect in comparison with mode 1. For sound propagation in the SOFAR channel north of the ACZ, the first three modes undergo only weak intermodal and intramodal dispersion at frequencies above about 3 Hz, as demonstrated in panel (b4). The frequency range below 3 Hz is not considered in further analysis, because of the high attenuation due to bottom interaction along the shallow water section of the propagation path over the Antarctic continental shelf.

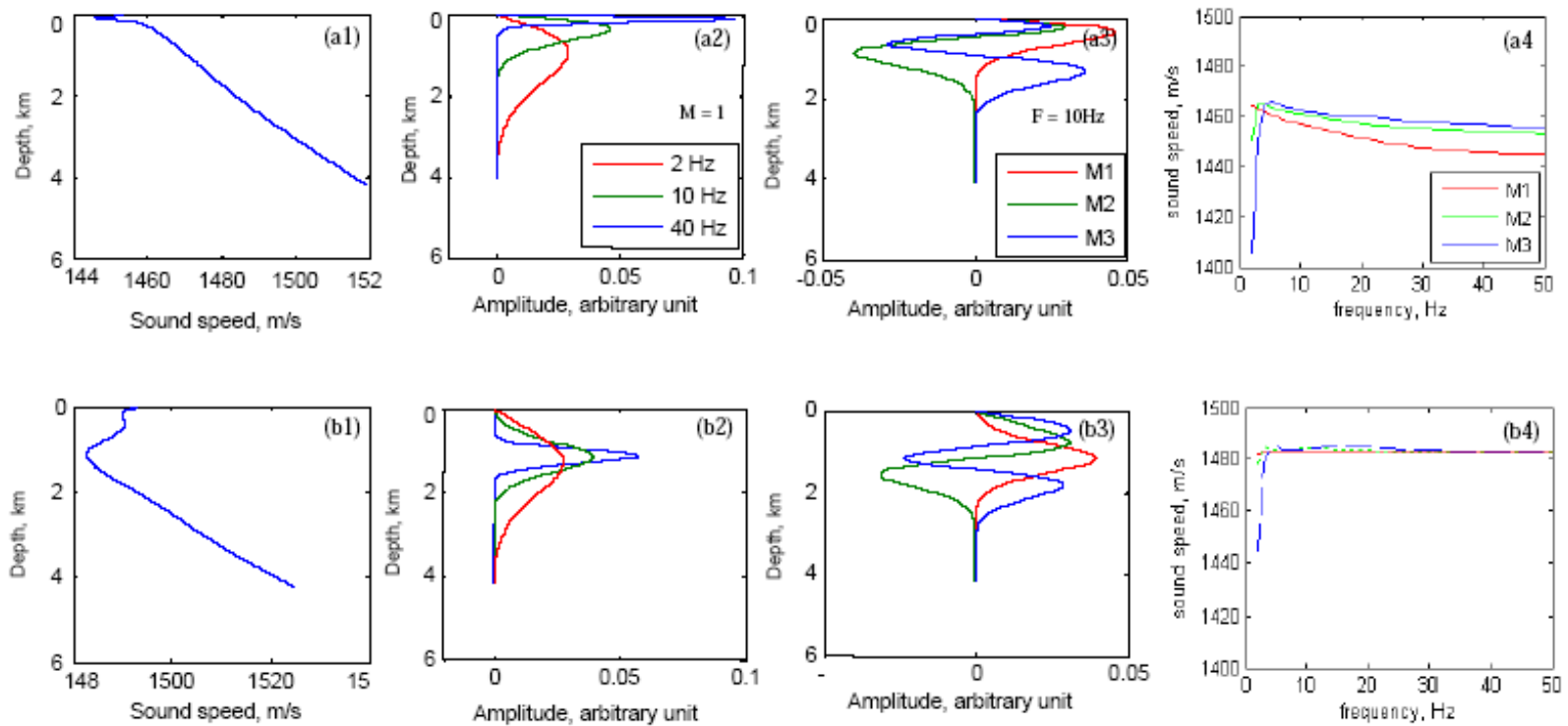


Figure 3.11. The sound speed profiles typical for the acoustic path sections in Southern Ocean south of ACZ (panel (a1)) and in the Indian Ocean (panel (b1)); the corresponding shapes of mode 1 at 2, 10 and 40 Hz (panels (a2) and (b2)), shapes of the first three modes at 10 Hz (panels (a3) and (b3)), and the group velocities of the first three modes (panels (a4) and (b4)) versus frequency.

The variations of the group velocity of modes 1 and 2 along the propagation path from Vincennes Bay to HA01 modelled using the January climatology data are shown in Figure 3.12. This figure clearly demonstrates that the frequency dispersion for modes 1 and 2 is very strong over the path in the Southern Ocean region south of the ACZ, and becomes almost negligibly small along the path north of the ACZ. In relatively shallow regions over the Antarctic continental shelf, the dispersion of both modes within the frequency band of interest above 3 Hz is also relatively weak.

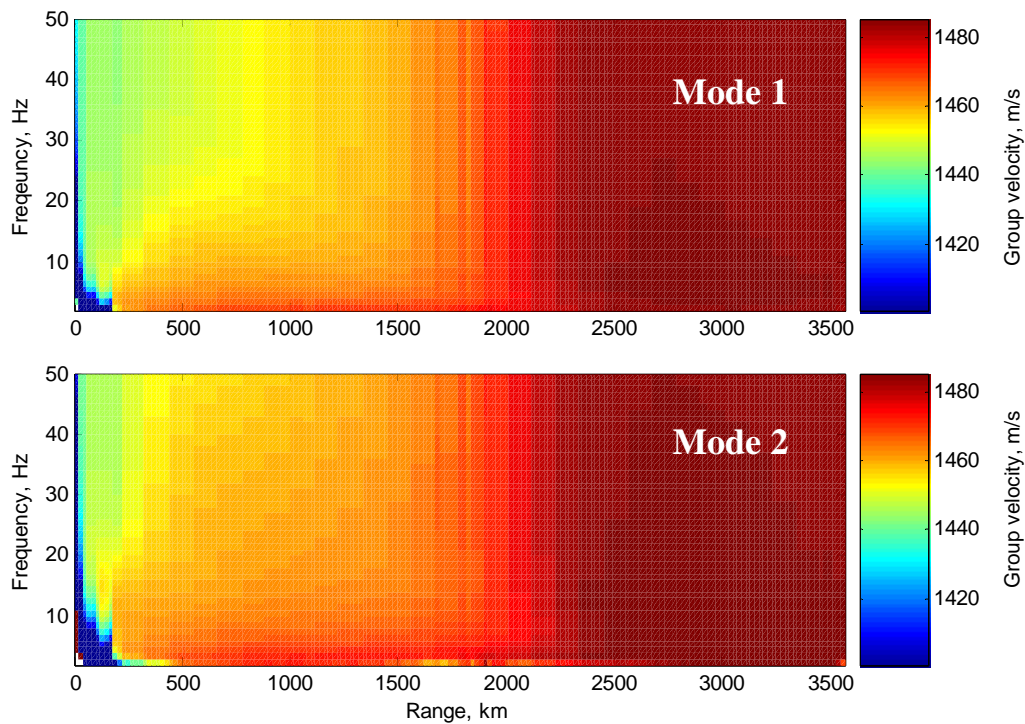


Figure 3.12. Variations of the group velocity (m/s) of modes 1 (top panel) and 2 (bottom panel) versus frequency and range along the modelled acoustic path from Vincennes Bay in Antarctica to the HA01 station.

3.3.7 Modelled arrival structure of the signal from ice events

Numerical modelling of the waveform of a transient signal propagated from a source of impulsive noise in Antarctica to the HA01 station is presented in this section. Underwater acoustic signals from diverse ice cracking and breaking events in Antarctica have not been measured near their origin and comprehensively analysed so far. Based on a general physical notion and observations presented in the following section, we assumed that most of the ice cracking and breaking events emit short impulsive signals and, therefore, modelled the waveform by a Gaussian pulse:

$$s(t) = A \exp(-t^2 / \sigma^2) \quad (3.17)$$

with the pulse width $\sigma = 20$ ms and amplitude A at 1 m from the source. The waveform of such an impulsive signal, filtered in the frequency band of 3-50 Hz, is demonstrated in Figure 3.13. The mode transfer function in Equation (3.13) was calculated with 1-Hz resolution and then interpolated to 1/16-Hz resolution to model the maximum spread of the acoustic channel impulse response of 16 s. The modelled waveform and spectrogram of this impulsive signal emitted in Vincennes Bay and received on the HA01 hydrophone are shown in Figure 3.14 and Figure 3.15 respectively. The source depth in this particular scenario was assumed to be 100 m and the sound speed along the path was derived from the January climatology data.

The modelled signal received at HA01 is considerably longer than the emitted one. The arrivals of modes 1 and 2 are distinct in the spectrogram. A trace of mode 3 can also be recognized. Mode 1 arrives last and has the broadest frequency band and the highest amplitude. Mode 2 does not have frequency components below 5 Hz and its dispersion characteristic is less profound. The spectrogram of the modelled signal is similar to that of some signals from ice events observed at HA01 (e.g. the spectrogram shown in the right panel of Figure 2.16). In contrast to the modelled signal, most of the ice event signals observed at HA01 do not have a distinct arrival of mode 2, which is most likely caused by stronger attenuation along the shallow water part of the path, as well as stronger coupling of mode 2 with the higher modes across the ACZ and hence stronger scattering of its energy into other modes. The relation between characteristics of modes 1 and 2 in the

received signal depends on a number of factors, such as the sea depth at the source location, source depth, length of the propagation path in the polar environment and acoustic properties of the seafloor along the shallow water section, as demonstrated in the previous sections. It follows from the comparison of experimental and modelling results that the trailing signal arrival which is distinct in the spectrogram is the mode 1 arrival and the emitted impulsive signals could be as short as tens of milliseconds at their origin. The majority of such impulsive signals are most likely emitted by ice breaking and cracking events. This assumption will be further examined in the next section by comparing the results of remote acoustic observation from the IMS stations in the Indian Ocean with results of other observations in Antarctica.

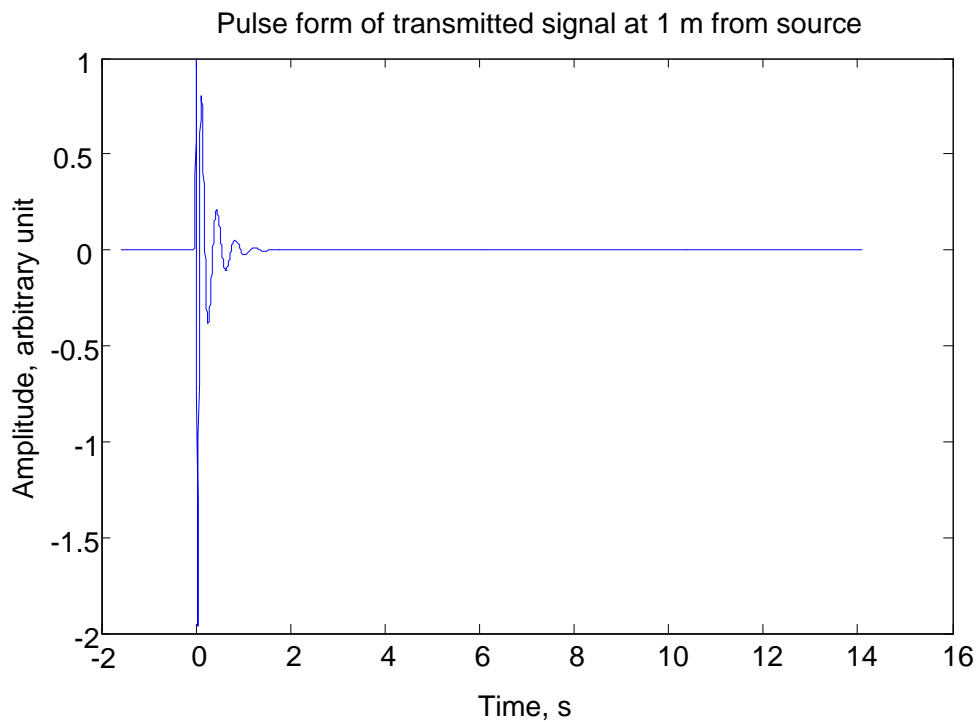


Figure 3.13. The waveform of a Gaussian pulse with a width of 20 ms and unity amplitude filtered in the frequency band of 3-50 Hz.

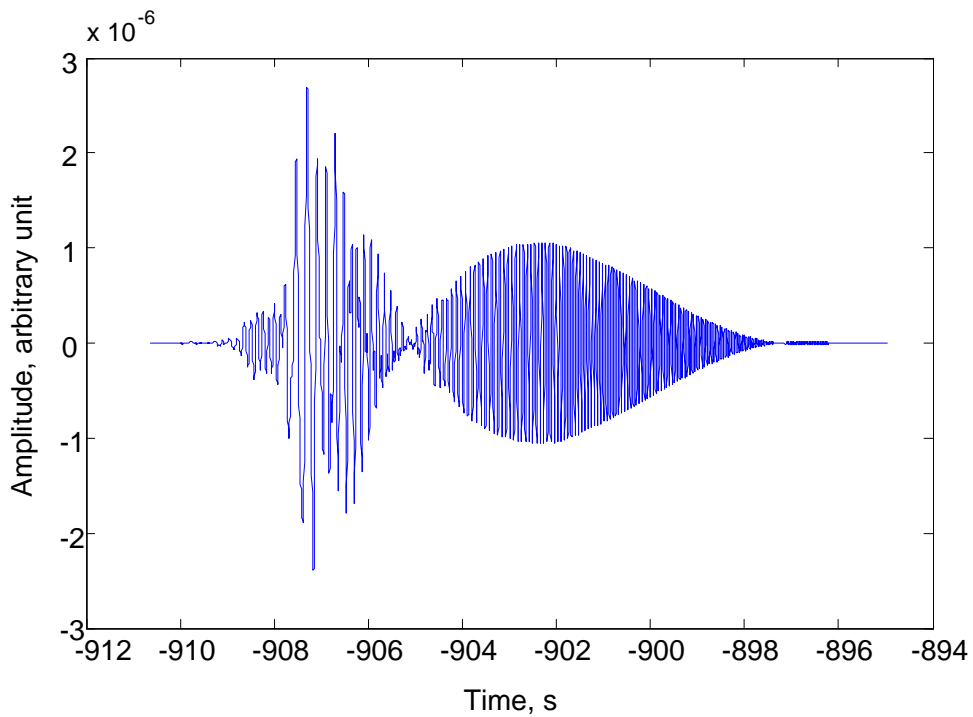


Figure 3.14. Modelled waveform of the signal received on the HA01 hydrophone from an ice event in Vincennes Bay. The waveform of the emitted signal is shown in Figure 3.12.

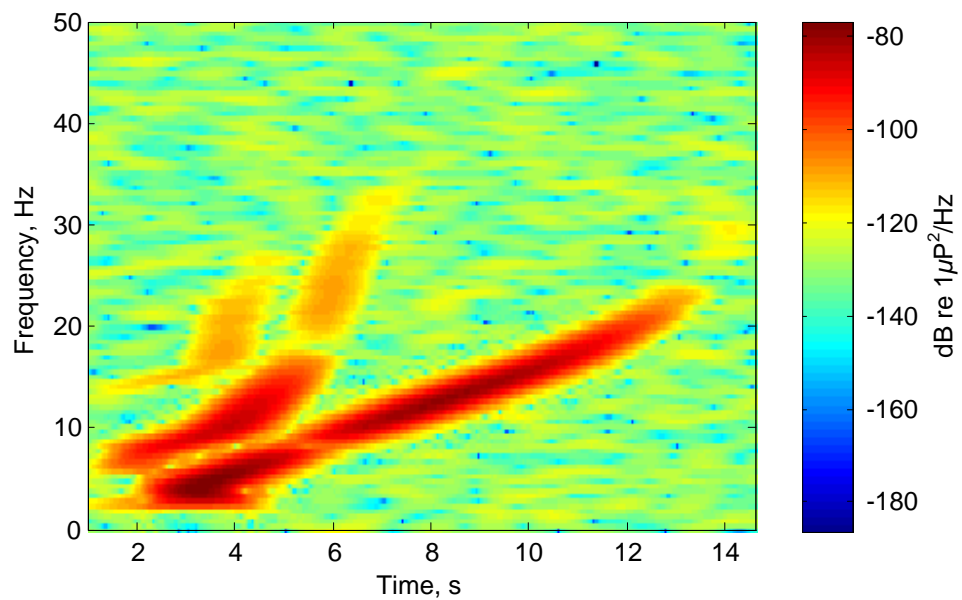


Figure 3.15. Spectrogram of the modelled signal shown in Figure 3.13.

3.4 Simultaneous observation of ice breaking events from the IMS stations in the Indian Ocean and by other observational means in Antarctica

Two different ways of observing ice rifting and breaking events in Antarctica will be considered in this section in order to demonstrate that the short transients arriving at the IMS stations from Antarctica are originated from Antarctic ice rifts and break-ups.

3.4.1 Underwater acoustic signals from ice events observed in Antarctica

In 2004 an autonomous sea noise logger was installed by the Australian Antarctic Division (AAD) on the Eastern Antarctica continental slope about 200 km north of Cape Poinsett, not far from Casey Polar station, as part of the Australian Marine Mammal Research program [<http://www.marinemammals.gov.au/research-and-activities/acoustics>]. This noise logger (Casey logger) was deployed at (63.82°S, 111.75°E) on the seafloor in a sea depth of about 3000 m. It recorded sea noise intermittently over nine months. During this period, a number of underwater noise events occurred in this part of the Antarctic continental shelf and were observed at both the sea noise logger in Antarctica and the HA01 station in Australia. A series of intense impulsive signals detected at both the Casey logger and HA01 on Day 117 in 2004 is shown in the left panels of Figure 3.16. The back-azimuth to the source of these signals from HA01 is 178.8°. The right panels of the figure show the waveforms and spectrograms of the first event in the series recorded on the Casey logger (top) and one of the HA01 hydrophones (bottom). The signals received in Antarctica consist of multiple arrivals of short pulses resulting from multiple reflections from the top and bottom boundaries. A comparison of the signal arrival structure, i.e. the travel time difference and amplitudes of different arrivals, with signals numerically predicted for an impulsive source at different depths and different ranges in the local environmental conditions, showed that this event took place near the sea surface at a distance of about 180 km from the logger. This localization process will be detailed in Chapter 5. When played back, this signal series sounds as a series of rifts and breaks, which occurred most likely from a large iceberg drifting west of the logger at that time. The corresponding signal at

HA01 reveals strong frequency dispersion in a series of few discrete arrivals of mode 1 recognized in the spectrogram.

Figure 3.17 shows another example of an ice event detected at both Casey logger and HA01 on Day 102 in 2004. The back-azimuth to this event from HA01 is about 180° . Based on the signal arrival structure and local environmental conditions (sea depth and sound speed profile), the distance to this event from the noise logger was estimated to be about 100 km (Gavrilov and Li, 2007). This is consistent with the back-azimuth estimate for this event from HA01, because the bearing angle from HA01 to the Casey noise logger is 180.1° .

It is necessary to note that the depth of the Casey logger deployed on the seafloor in relatively deep water was not optimum for receiving signals from remote sources located near the sea surface in the upward refracting polar acoustic environment. Under such conditions, the logger could receive only high-order modes (steep rays) of signals from relatively close sources of noise and could not hear well remote events located in shallower water over the continental shelf closer to the shore.

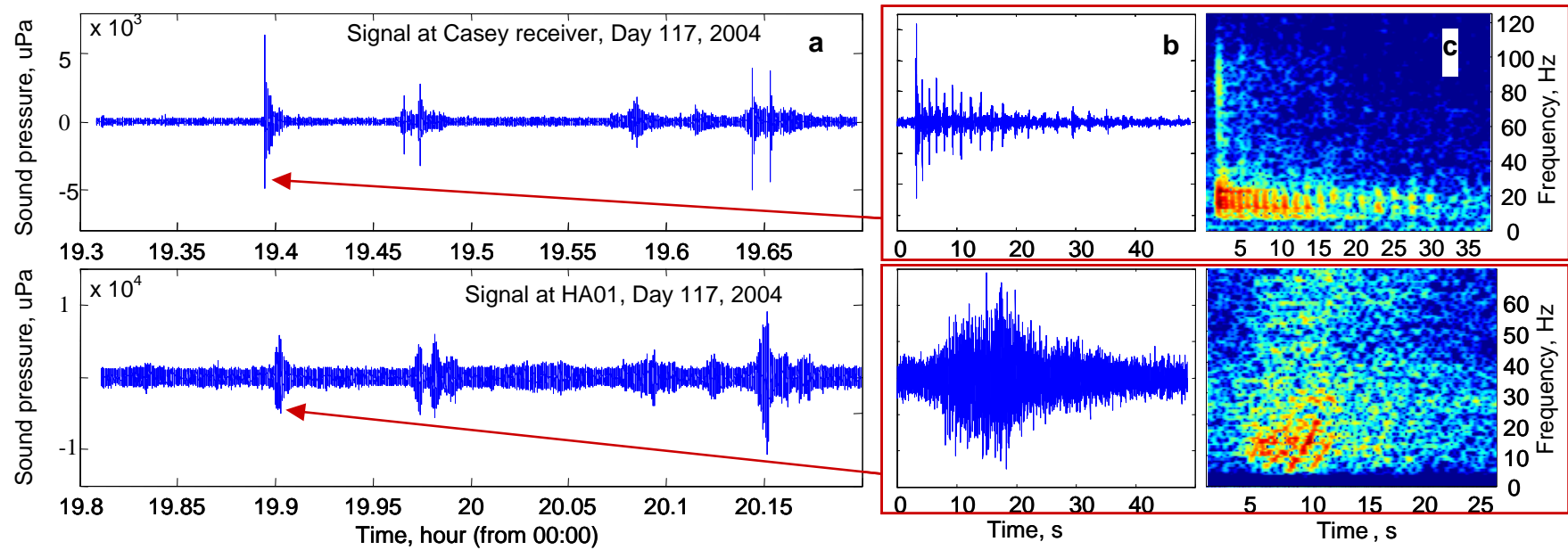


Figure 3.16. (a) Signals from the same series of transient noise events occurred on Day 117 in 2004 and recorded on the Casey sea noise logger in Antarctica (top) and at the HA01 station (bottom), and the waveform (b) and spectrogram (c) of the first event in the series at the noise logger (top) and HA01 (bottom).

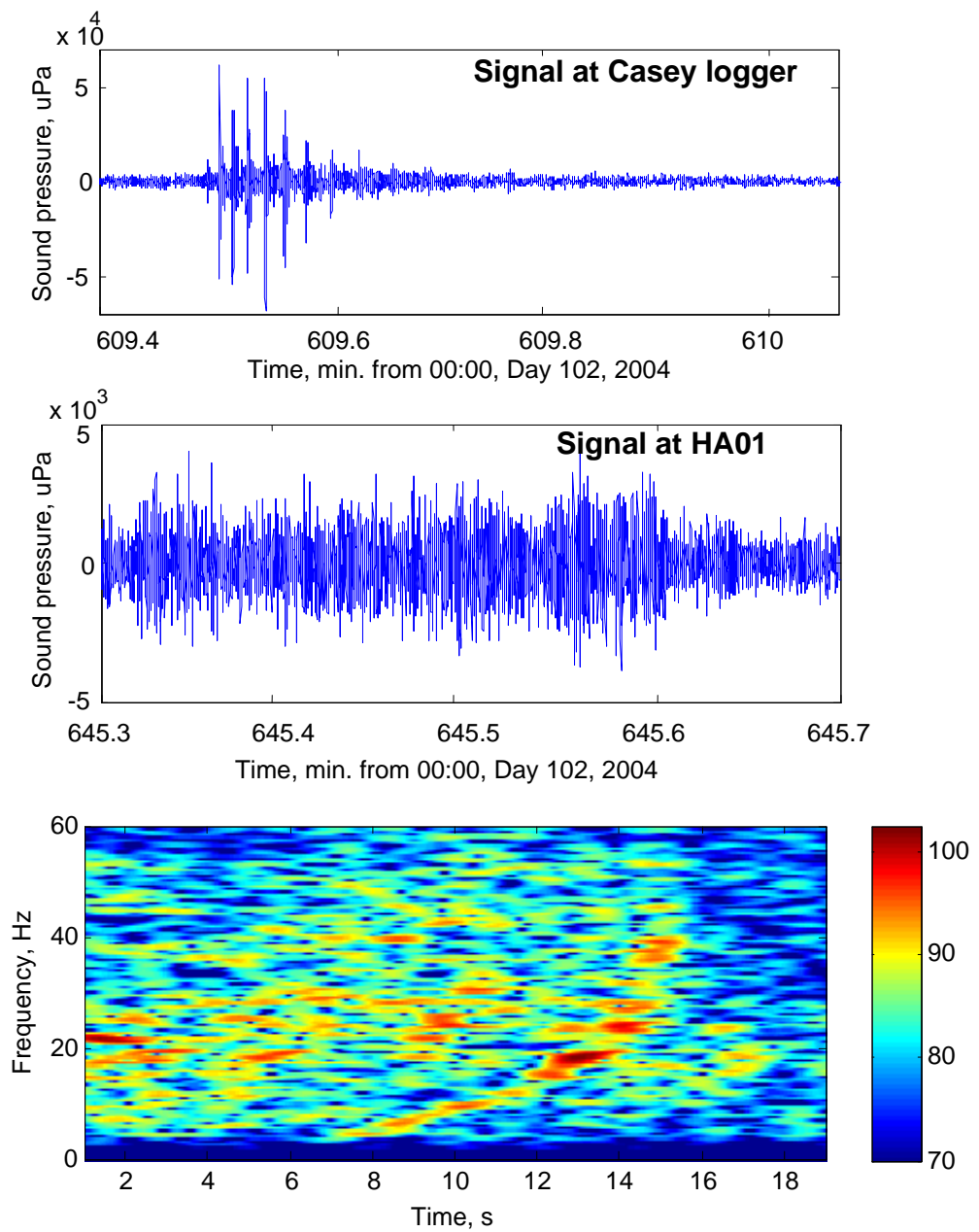
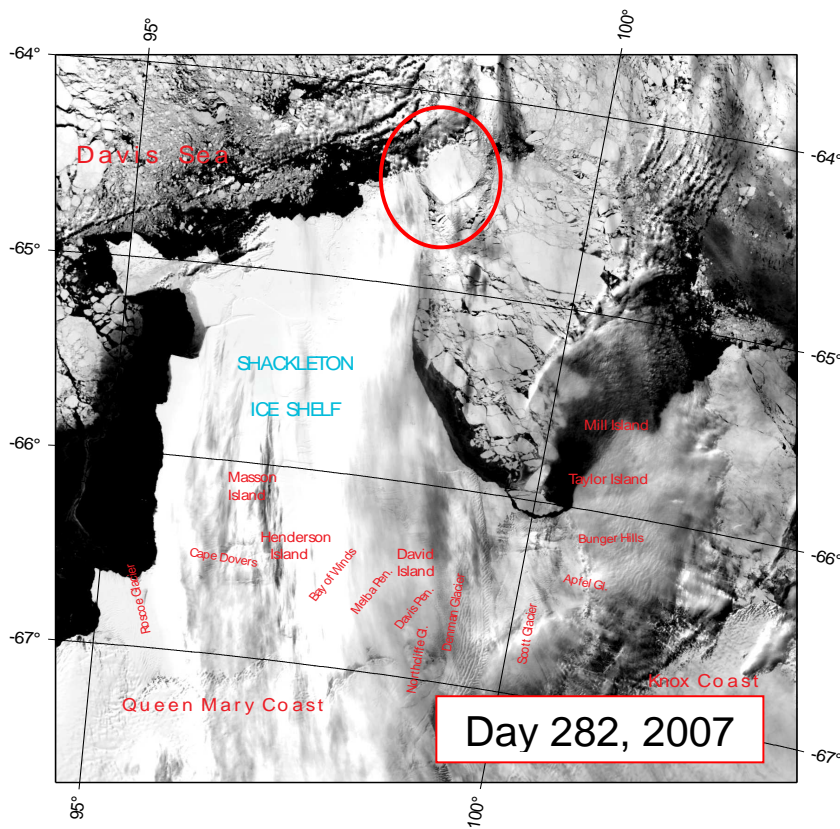
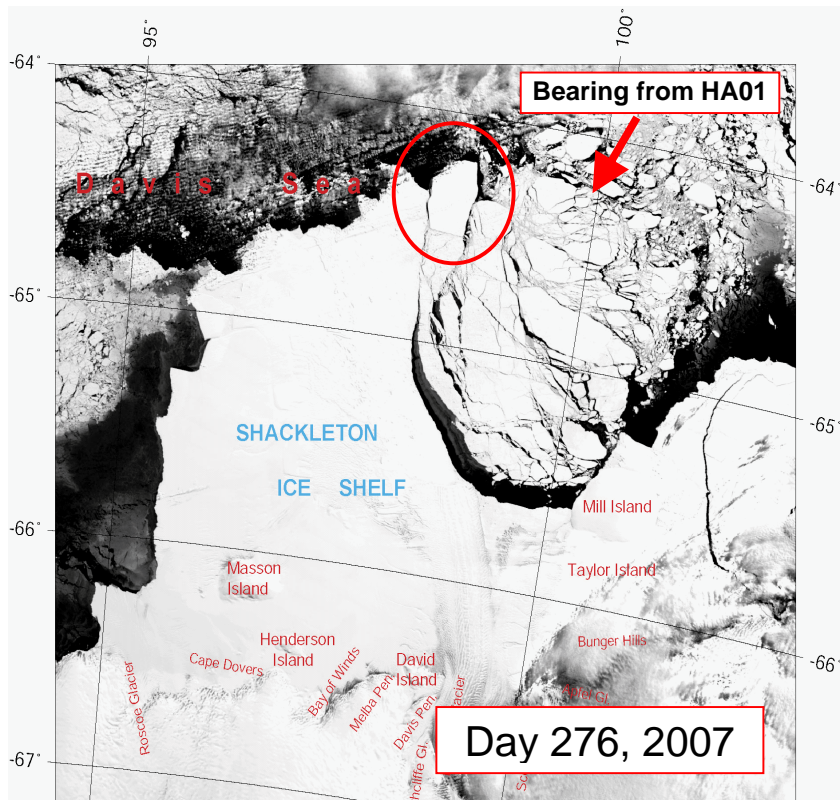


Figure 3.17. The waveform of signal from an ice event recorded on Day 102 in 2004 on the Casey sea noise logger (top panel) and at HA01 (middle panel), and the spectrogram of the signal at HA01 (bottom panel).

3.4.2 Signals from ice break off the Shackleton Ice Shelf

A remarkable iceberg calving process off the Shackleton Ice Shelf in 2007 was observed through examination of the MODIS satellite images of the Antarctic ice shelves available from Antarctic Ice Shelf Image Archive in National Snow and Ice Data Center (NSIDC) (http://nsidc.org/data/iceshelves_images/). Some of these images are shown in Figure 3.18. The image in the top panel of the figure, covering the Shackleton Ice Shelf and surrounding ocean, was taken at 2:50am on Day 276. A large rift is clearly seen in the northern tip of the ice shelf separating a huge piece of ice indicated by the red arrow. The image shown in the middle panel was taken on Day 282. It shows this iceberg about 30 km long, calved off the shelf and moved towards the ocean. Nearly one week later, the new iceberg was completely detached and drifting into the Davis Sea, as demonstrated in the bottom panel. A long series of signals from the early stage of this rifting and calving process were received at the HA01 station. The waveform and spectrogram of these signals and measured back-azimuth angles from HA01 are shown in Figure 3.19. In this one-hour long recording, we can clearly see short signals from a couple of major rift and break events followed by the final calving of the iceberg which began making continuous broadband noise while moving and scratching the ice shelf.



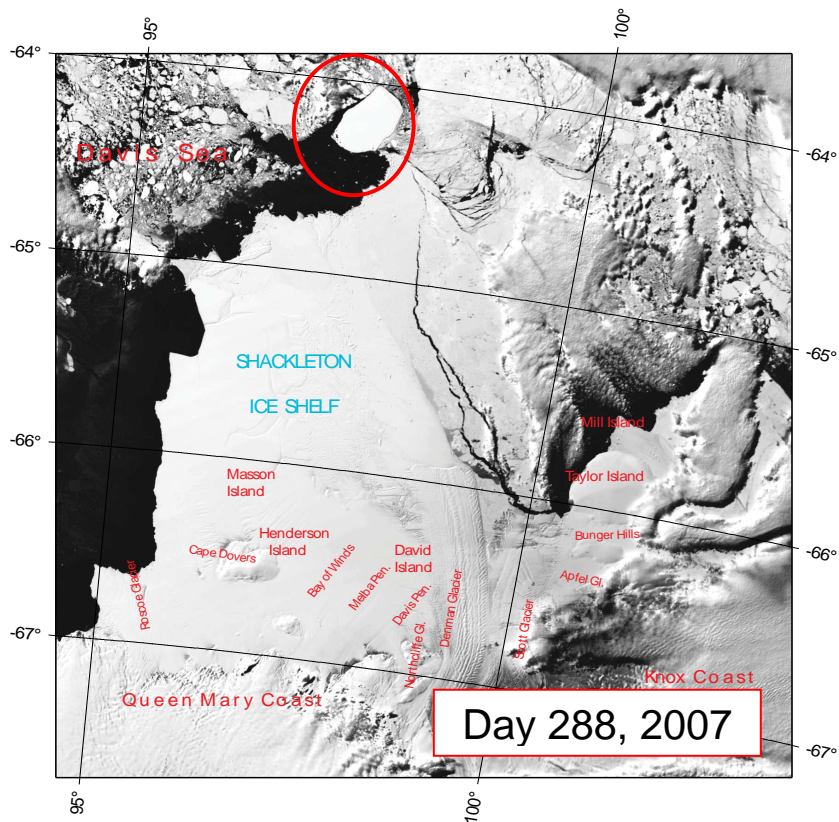


Figure 3.18. Three MODIS satellite images of the Shackleton Ice Shelf and the surrounding ocean taken on Days 276 (top panel), 282 (middle panel) and 288 (bottom panel) in 2007. The red circles indicate the new iceberg calved on Day 276. The red arrow shows the bearing direction from HA01 to the source of underwater noise.

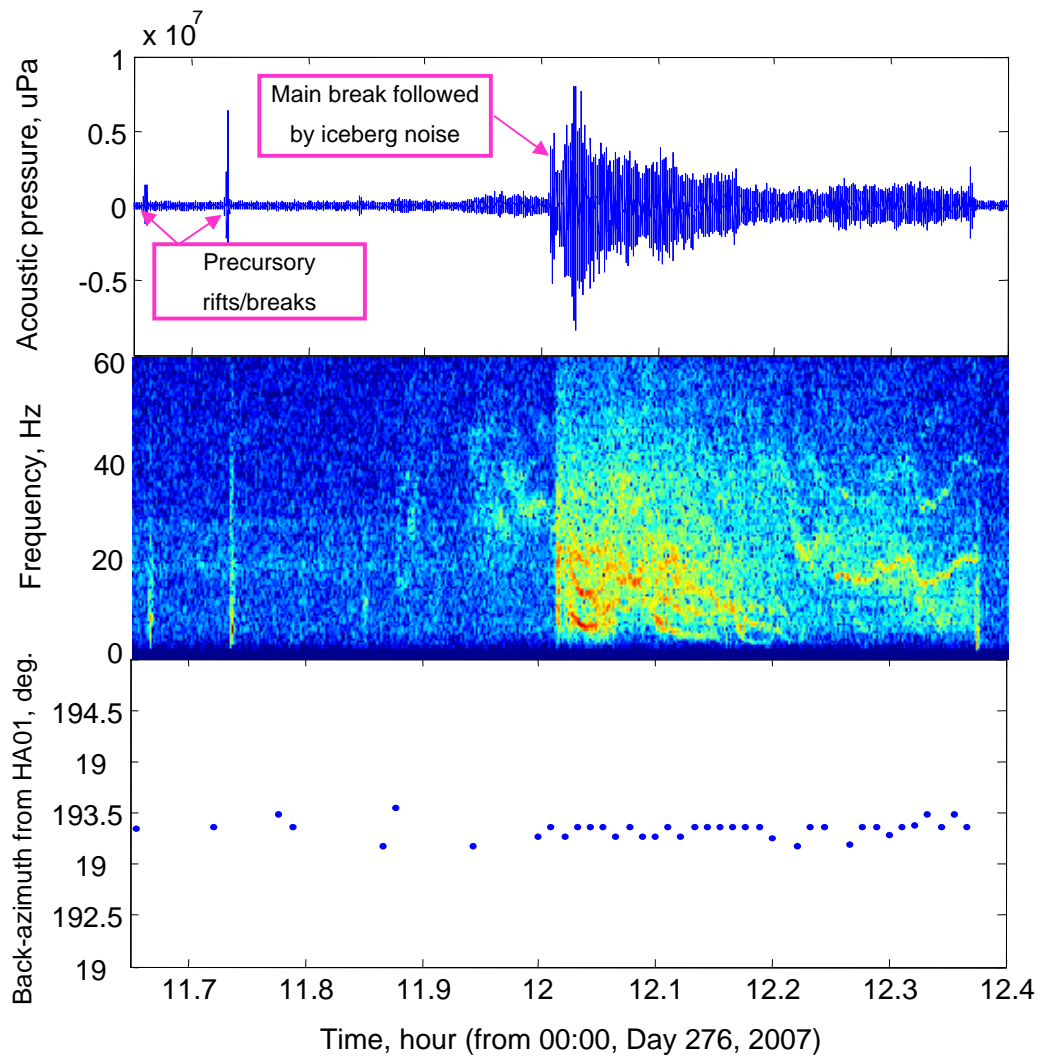


Figure 3.19. The waveform (top panel), spectrogram (middle panel) and measured back-azimuth of the signal from an ice calving event off Shackleton ice shelf observed at the HA01 station on Day 276 in 2007.

3.5 Concluding remarks

Combining results of numerical modelling and observations by different means, the characteristics of sound propagation from Antarctica to the IMS hydroacoustic stations in the Indian Ocean were investigated and the origin of the short transient signals received at these stations from Antarctica was examined.

It is found that the near-surface acoustic channel in the Southern Ocean south of the ACZ acts as a mode and frequency filter such that mode 1 undergoes the least transmission loss at frequencies below 20 Hz along the path to the IMS receivers. The propagation in the near-surface channel in the Polar ocean environment also induces strong intermodal and intramodel dispersion effects. The mode coupling effect due to the variation of the sound speed and sea depth with range along the propagation path is negligible except for the relatively short initial section over the Antarctic continental shelf and the path section across the Antarctic Convergence. In the frequency band of analysis, mode 1 is least sensitive to the interaction with the seafloor and the mode coupling effect.

A comparison between the signal arrival structure from ice events observed at the HA01 station and the results of numerical modelling demonstrates a good agreement and supports the hypothesis that Antarctic ice cracking or breaking events are the origin of the transient signals with strong frequency dispersion which arrive at the IMS station from Antarctica.

Simultaneous remote observation of a large ice rifting and calving event on the Shackleton Ice Shelf by visual means from satellites and by acoustic means from the HA01 station in Australia demonstrates that remote acoustic observations in the ocean are capable of detecting and locating ice rifting events which precede ice break up and iceberg calving in Antarctica.

CHAPTER 4

BEARING ERROR ANALYSIS FOR HA01 AND H08S HYDROACOUSTIC STATIONS

4.1 Overview

This chapter examines the bearing capability of the IMS hydroacoustic stations through an investigation of various factors that potentially cause bearing estimation errors. Bearing calibration is then conducted in order to improve the bearing accuracy of the HA01 and H08S stations.

As shown in Section 2.4.4, for long-range hydroacoustic monitoring, the back-azimuth to hydroacoustic events observed at the IMS stations can be estimated by application of Plane Wave Fitting (PWF) method (Pezzo and Giudicepietro, 2002) using TDOA estimates for different pairs of hydrophones of the triangular receive array. The covariance matrix of estimates for the slowness \mathbf{p} can be derived from Equation (2.1) as follows (Menke, 1984):

$$\text{cov}(\mathbf{p}) = [(\Delta\mathbf{x}^T \Delta\mathbf{x})^{-1} \Delta\mathbf{x}] \text{cov}(\mathbf{t}) [(\Delta\mathbf{x}^T \Delta\mathbf{x})^{-1} \Delta\mathbf{x}]^T \quad (4.1)$$

From Equation (4.1), we can see that the back-azimuth estimate via PWF is constrained by the errors of both TDOA estimates \mathbf{t} and the relative position of hydrophones $\Delta\mathbf{x}$. As described in Section 2.4.4, the back-azimuth to coherent events detected at the IMS stations has been initially estimated under assumptions that the TDOA are accurately measured and the three hydrophones of each station are in their nominal positions, which correspond to the touch-down coordinates of hydrophones' moorings. In reality, however, the above assumptions do not hold. The TDOA estimation accuracy is subject to errors of peak location in the signal cross-correlation function. Moreover, the hydrophones are considered to have both constant and variable horizontal deviations from their nominal locations, which result in systematic and variable components of bearing errors. In addition, horizontal refraction along the acoustic propagation paths also potentially causes bearing estimation errors relative to the true bearing from the receive station to hydroacoustic events.

Effects of the above mentioned factors on bearing accuracy of the IMS stations are thoroughly examined in this chapter. Section 4.2 gives an analysis of bearing errors from the TDOA estimates. Random bearing errors due to temporal horizontal motion of the hydrophones are investigated in Section 4.3. In this section, a model is proposed for estimation of the RMS bearing error as a function of the back-azimuth to the acoustic source and the standard deviation of the receivers' horizontal position. Estimates of the random errors of bearing from HA01 and H08S are made based on the variation of back-azimuth measurements for long-lasting low-frequency hydroacoustic events observed from these stations. Section 4.4 numerically examines the bearing azimuth error due to horizontal refraction along transoceanic acoustic propagation paths. The dependence of bearing errors on mode number and frequency is also numerically modelled and verified using the underwater acoustic signal from the Great Sumatra Earthquake. Section 4.5 investigates the systematic bearing error due to inaccuracy of the touch-down positions of hydrophones' moorings which were determined during system deployment. A number of underwater explosions with exactly known coordinates are selected for assessing the systematic errors. The bearing calibration for the systematic error is conducted by minor alteration of moorings' relative positions, which is done by inverting the TDOA measurements for the sources of known location using a least square approach. A simultaneous observation of an ice collision event made both acoustically from HA01 and visually from a MODIS equipped satellite (<http://modis.gsfc.nasa.gov/about/>) is demonstrated in this section as further evidence of the systematic bearing error at the HA01 station. Section 4.6 gives the concluding remarks.

4.2 Bearing errors from the differential travel times

The error of the TDOA measurements $t_{i,j}$ made through cross-correlation of the signals at two receivers i and j depends on the sampling interval, the Signal-to-Noise Ratio (SNR), the signal bandwidth and duration. As Equation (2.2) shows, the x and y components of the slowness \mathbf{p} are linear sums of the TDOA measurements \mathbf{t} . If the components of \mathbf{t} are

normally distributed, then the x and y components of the slowness will also be normally distributed. The diagonal elements of $\text{cov}(\mathbf{t})$ are the variance of the TDOA estimates t_{ij} . This variance can be estimated as (Bendat and Piersol, 2000) in Page 298:

$$\sigma^2(t_{ij}) \approx \frac{0.865}{(\pi B)^2} \varepsilon[\widehat{R}_{ij}(t_{ij})], \quad (4.2)$$

where

$$\varepsilon[\widehat{R}_{ij}(t_{ij})] \approx \frac{1}{2BT} [2 + SNR_i^{-1} + SNR_j^{-1} + (SNR_i \times SNR_j)^{-1}] \quad (4.3)$$

is the mean square error of the correlation coefficient estimate for two signals $S_i(t)$ and $S_j(t)$, B is the frequency bandwidth, T is the signal length, and SNR_i and SNR_j are the signal-to-noise ratio (SNR) of signals $S_i(t)$ and $S_j(t)$ respectively. The SNR of most signals from ice events selected for this analysis exceeds 2 dB as shown in Figure 2.19, the bandwidth varies from about 10 Hz to 30 Hz and the signal duration is of order of 10 seconds. Hence, the standard deviation of the TDOA estimates should not exceed 4 milliseconds for the minimum signal bandwidth of 10 Hz, which is comparable to the 4-millisecond sampling interval of the IMS hydroacoustic recordings. The errors of the correlation maximum location due to quantization are uniformly distributed within the sampling interval $\Delta t = 4$ ms with the variance $\sigma^2(t) = \Delta t^2 / 12$ and the standard deviation of about 1 ms. The TDOA errors resulting from the limited signal bandwidth, duration and SNR and signal quantization can be assumed to be statistically independent for different pairs of receivers and, hence, the non-diagonal elements of the covariance matrix $\text{cov}(\mathbf{t})$ in Equation (4.1) are negligible compared to the main diagonal elements. Once the covariance matrix of the slowness \mathbf{p} is determined using Equation (4.1) and the estimates for $\text{cov}(\mathbf{t})$, the standard deviation of the back-azimuth estimate can be determined using an approximation for small variations. The back-azimuth variance can be expressed as:

$$\text{var}(\varphi) = \left\langle \left[\tan^{-1} \left(\frac{\widehat{p}_x + \delta p_x}{\widehat{p}_y + \delta p_y} \right) - \tan^{-1} \left(\frac{\widehat{p}_x}{\widehat{p}_y} \right) \right]^2 \right\rangle \quad (4.4)$$

where \hat{p}_x and \hat{p}_y are the mean values of the slowness components derived from Equation (2.2) and δp_x and δp_y are statistical errors of the estimate. Applying the formula for arctangent difference, expanding $\text{var}(\varphi)$ into a power series about \hat{p}_x and \hat{p}_y , and ignoring all terms of the order higher than $O(\delta p_{x,y})$, one can obtain:

$$\text{var}(\varphi) \approx \frac{\sigma^2(\delta p_x) \hat{p}_y^2 - \text{cov}(\delta p_x \delta p_y) \hat{p}_x \hat{p}_y + \sigma^2(\delta p_y) \hat{p}_x^2}{\hat{p}_x^4 + 2\hat{p}_x^2 \hat{p}_y^2 + \hat{p}_y^4} \quad (4.5)$$

where $\sigma^2(\delta p_{x,y})$ and $\text{cov}(\delta p_x \delta p_y)$ are the main diagonal and off-diagonal elements of the matrix $\text{cov}(\mathbf{p})$ respectively. If the off-diagonal elements of $\text{cov}(\mathbf{t})$ are all zeros and the variance $\sigma^2(t)$ does not exceed $(4\text{ms})^2$, according to the previous estimates, then the bearing error derived from Equations (4.1) and (4.5) will be smaller than approximately 0.15° for any back-azimuth to the source location.

4.3 Random bearing errors due to temporal horizontal motion of the hydrophones

Apart from the contribution from the TDOA errors, the bearing error may also be caused by the horizontal deviation of the hydrophones from their nominal position due to variable tilt of the moorings affected by ocean currents. This error component can be much larger than that caused by the errors of the TDOA estimates. We will ignore the common component of horizontal deviation of all hydrophones in the array, as it has negligible effect on bearing estimates, and refer to the bearing error caused by the residual deviation component as a random bearing error. This error will be estimated for both HA01 and H08S stations using a number of long-lasting low-frequency hydroacoustic events, such as the ice harmonic tremors, subsea seismic events and signals from offshore seismic surveys.

4.3.1 Numerical analysis of random bearing errors

In the absence of measurement data on the motion of individual receivers of the IMS hydroacoustic stations, we made the following assumptions to estimate possible bearing errors due to the variable deviation of the receivers' horizontal position. The horizontal deviation of the receivers in the IMS triangular receive arrays is likely to have a common component resulted from the general large-scale current field, which can be variable in time, but nearly uniform within the array span of about 2 km. For the mooring length of several hundreds of meters, this common deviation component can be as large as several tens of meters, but it does not introduce significant errors of bearing to remote sources located at thousands of kilometers from the receive array. Smaller scale deviation components which are different for different moorings are likely to be superimposed on the common component because of small differences in the local current profiles, slightly different length of the mooring cables and likely auto-oscillations of the mooring systems under the ocean current field. We assume that these differential components of receivers' horizontal deviation are random, normally distributed, and statistically independent, i.e. incoherent. Based on such assumptions, the slowness covariance matrix can be estimated using Equation (4.1), in which the receivers' relative position $\Delta \mathbf{x}$ is taken to be the expected values, i.e. the bottom touchdown location of the moorings, and the horizontal deviation of the receivers is accounted for in the variance of the differential travel times. If the incoherent deviation of individual receivers is horizontally isotropic and has the standard deviation δx , then the elements of the covariance matrix $\text{cov}(\mathbf{t})$ in Equation (4.1) are:

$$t_{ij} = \begin{cases} 2\delta x^2 / c^2 & i = j \\ \delta x^2 / c^2 & |i - j| = 1 \\ -\delta x^2 / c^2 & |i - j| = 2 \end{cases} \quad (4.6)$$

where c is the group velocity of a broadband signal, which is approximately equal to the local sound speed.

Figures 4.1 and 4.2 show the root-mean-square (RMS) bearing error estimated for the HA01 and H08S stations using Equation (4.1), (4.5), and (4.6) for different back-azimuths

within the full sector of 0 - 360° and different standard deviations δx of the receivers' position.

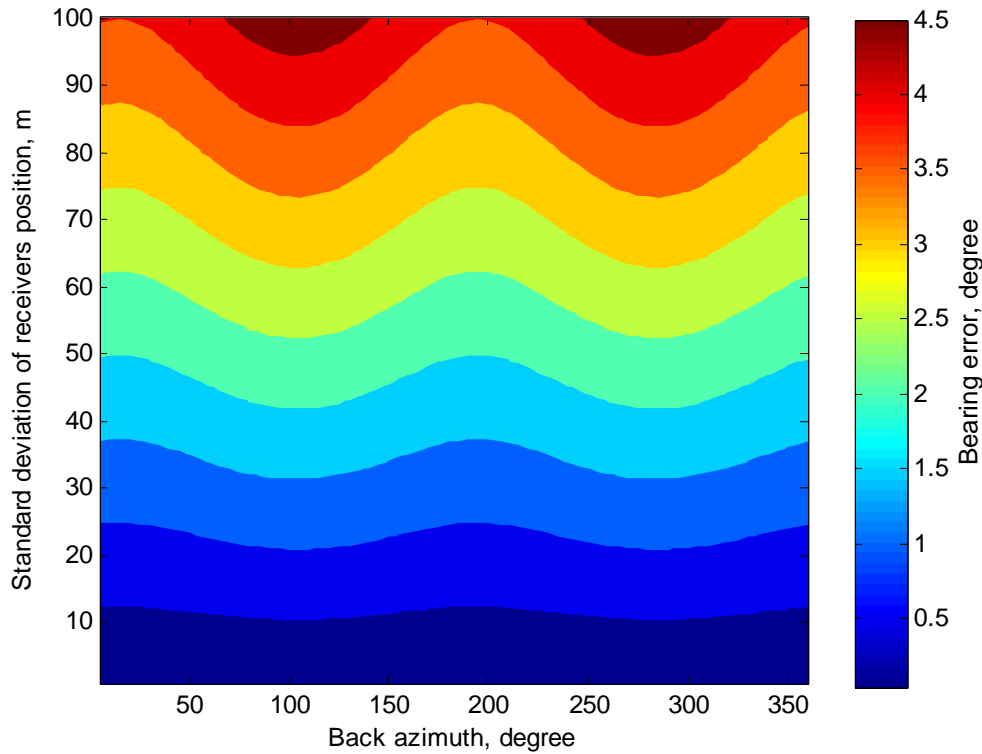


Figure 4.1. RMS bearing errors for HA01 as a function of the back-azimuth to located sources and the standard deviation of the receivers' horizontal position.

As seen from Figure 4.1 and Figure 4.2, the uncertainty of the receivers' position is much more critical for bearing estimation than the errors of TDOA estimates. For example, only 10-m standard deviation of the receivers' horizontal position leads to a nearly half degree RMS error of bearing estimates for both stations. It is also noted that the bearing errors have azimuth dependence, which is weak at small δx and becomes more significant at larger δx . The bearing errors are somewhat less sensitive to the motion of hydrophones at the H08S station than that at HA01. This is because of the slightly larger size of the H08S hydrophone triplet compared to that of HA01 (sides of the H08S triplet are about 2.086km, 2.240km and 2.255km, while those of HA01 are about 1.914km, 1.968km and 1.699km).

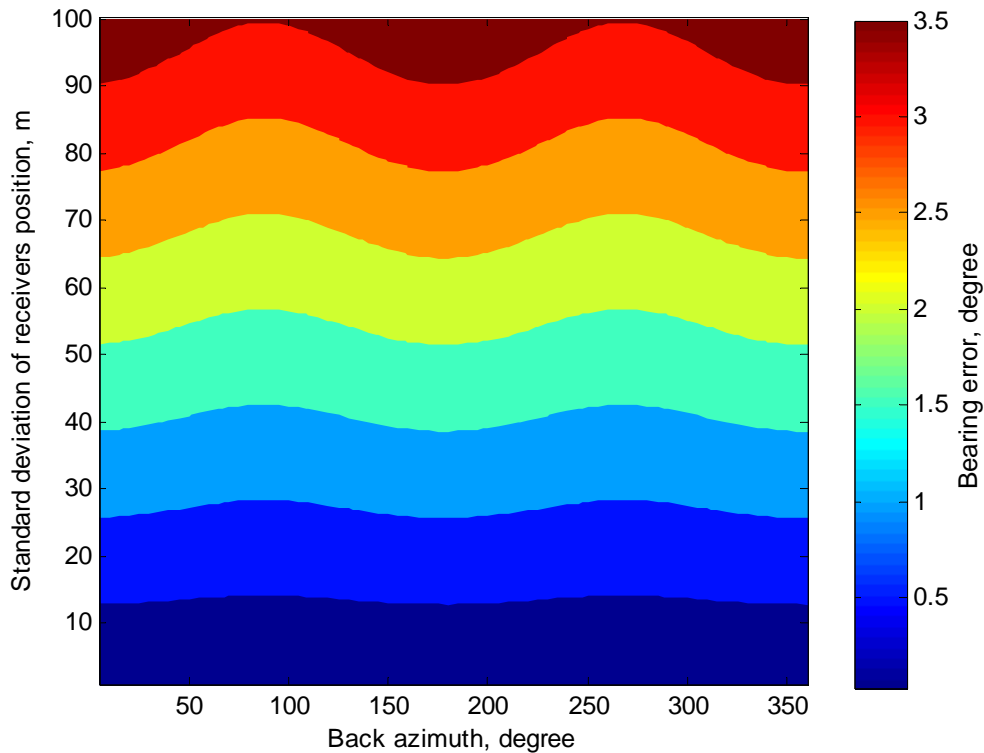


Figure 4.2. RMS bearing errors for H08S station as a function of the back-azimuth to located sources and the standard deviation of the receivers' horizontal position.

4.3.2 Experimental estimation of random bearing error

4.3.2.1 The HA01 station

Among the hydroacoustic events with their signals observed and classified at HA01, harmonic tremor signals from Antarctic icebergs and seismic events have relatively long duration. The tremor events have various durations from tens of minutes to several hours. Sometimes icebergs make noise for several days with shorter or longer interruptions. Some subsea seismic events consist of a series of shocks of different, usually decreasing magnitudes, which can last from several days to months. Both types of events have their maximum energy in the low frequency range of several Hz as demonstrated in Sections 2.5.3 and 2.5.4. A number of tremor and seismic events of long duration and high SNR

were selected to estimate the random error of bearing from HA01. These events and the estimates of random bearing errors are presented in Table 4.1. In the selection process, only stationary sections of measurements for those events are considered, i.e. over the sections no significant trends were observed in the mean and standard deviation of measured back-azimuth values.

Table 4.1. Mean values and standard deviation (SD) of back-azimuth estimates for six selected Antarctic ice tremor events and four seismic events. TR - tremor event; SE - seismic event; MS and AS stand for the main-shock and aftershock of the Great Sumatra-Andaman Earthquake respectively.

Events	Duration [year/day]	Mean [°]	SD [°]
TR 1	02/151.54 ~ 02/152.36	163.93	0.09
TR 2	03/217.38 ~ 03/217.46	162.74	0.16
TR 3	04/170.14 ~ 04/170.88	195.57	0.18
TR 4	05/061.83 ~ 05/075.11	180.24	0.19
TR 5	06/003.87 ~ 06/004.65	181.95	0.09
TR 6	07/214.75 ~ 07/224.07	191.77	0.11
SE 1	03/233.54 ~ 03/367.50	121.25	0.40
SE 2	07/273.25 ~ 08/009.30	128.09	0.31
SE 3 (MS)	04/361 ~ 05/010	331.56	0.65
SE 4 (AS)	05/087 ~ 05/101	333.27	0.24

For the six selected tremor signals with azimuth ranging from about 160° to 200°, the standard deviation of back-azimuth estimates is below 0.2°. If compared with the modelling result shown in Figure 4.1, such small standard deviation of back-azimuth estimates corresponds to only a few meters of deviation of the HA01 hydrophones from their nominal position. The standard deviation values of back-azimuth estimates for the four earthquake events, including two events in the Southern Ocean and another two from the main-shock and aftershock of the Great Sumatra-Andaman Earthquake, are larger than those values

from the tremor events. This can be expected considering that a seismic event consisting of a series of subsea shocks is not a point acoustic source, even if observed from a large distance. The epicenters of individual shocks can be spread over relatively large areas or along larger ruptures, as happened with the Sumatra Earthquake. Moreover, seismic waves emitted by a deep subsea earthquake are converted into acoustic waves in the water column over a large area of the seafloor, primarily over the continental slope, so that the actual horizontal dimension of the underwater noise source originating from an earthquake can be as large as hundreds of kilometers. In contrast to the seismic sources, the horizontal dimension of large Antarctic icebergs varies typically from several hundreds of meters to several tens of kilometers, which introduces uncertainty of bearing of only a few tenths of a degree at distances of more than 3 Mm between the source of noise and the receive array. Therefore, the estimates made for the iceberg tremor events were considered to be more accurate than those for the selected seismic events. Based on these estimates, it can be concluded that the random bearing error from the HA01 station to hydroacoustic events in Antarctica is around 0.2° , i.e. far less than half a degree.

4.3.2.2 The H08S station

At the H08S station, we did not observe sufficient harmonic ice tremor events with signals of high enough SNR for accurate back-azimuth measurements. However, a number of long series of airgun signals from seismic surveys have been observed at H08S, mainly in the direction to the Australian northwest shelf. These series of events are clearly seen along with their back-azimuth from H08S in Figure 2.17. Airgun signals received at H08S from 13 seismic surveys over the period from 2002 to 2005 were selected to estimate the random bearing error of the station. The duration of the selected series of signals and the mean value and standard deviation of back-azimuth to these events are shown in Table 4.2. Similarly to the HA01 station, the standard deviation of the random error of bearing from H08S is around or less than 0.2° for most of the analysed events.

Table 4.2. The mean values and standard deviation (SD) of back-azimuth estimates for 13 selected series of airgun signals from different off-shore seismic surveys. SSE means seismic survey events.

Seismic surveys	Surveys lasting time [year/day]	Mean [°]	SD [°]
SSE 1	02/130.50 ~ 02/143.76	20.52	0.19
SSE 2	02/339.27 ~ 02/363.45	123.85	0.26
SSE 3	03/105.85 ~ 03/213.55	110.07	0.16
SSE 4	03/121.83 ~ 03/143.40	122.32	0.14
SSE 5	04/ 14.50 ~ 04/ 31.92	111.21	0.13
SSE 6	04/ 62.52 ~ 04/ 92.30	35.81	0.18
SSE 7	04/116.32 ~ 04/130.06	111.00	0.11
SSE 8	04/138.90 ~ 04/172.10	123.07	0.20
SSE 9	05/ 32.92 ~ 05/ 65.82	111.38	0.23
SSE 10	05/134.25 ~ 05/139.30	113.30	0.08
SSE 11	05/144.65 ~ 05/186.42	111.06	0.20
SSE 12	05/174.05 ~ 05/231.10	112.80	0.15
SSE 13	05/341.90 ~ 05/364.75	101.34	0.14

4.4 Effect of horizontal refraction on bearing estimation

To examine all possible errors of location of remote hydroacoustic events from the IMS hydroacoustic stations, it is necessary to investigate the effect of horizontal refraction of sound propagation in the ocean on bearing estimates. The horizontal refraction can be induced by both large-scale horizontal variations of the sound speed field in the ocean and changes in the sea depth (Doolittle et al., 1988, Jensen et al., 2000).

4.4.1 Numerical solution for horizontal rays

In this study, we followed the computational procedure proposed for the analysis of the Perth-Bermuda propagation experiment results (Heaney et al., 1991). It involves a combination of an adiabatic mode theory in the vertical dimension and a ray theory in the horizontal dimension and, therefore, takes into account horizontal refraction of individual modes due to both transverse sound speed gradients and bottom interaction over the continental slopes and sea mounts. The ray model is constructed on the surface of the Earth represented by an ellipsoid of rotation and expressed in terms of the parameters ϕ , λ , and α , where ϕ and λ are the latitude and longitude respectively, and α is the azimuth angle measured clockwise from the north. The ray equations on an ellipsoid are:

$$\dot{\phi} = \cos \alpha / \mu(\phi) \quad (4.7a)$$

$$\dot{\lambda} = \sin \alpha / v(\phi) \cos \phi \quad (4.7b)$$

$$\dot{\alpha} = \frac{\sin \alpha}{v(\phi)} \tan \phi - \left(\frac{\sin \alpha}{\mu(\phi)} \frac{\partial}{\partial \phi} - \frac{\cos \alpha}{v(\phi) \cos \phi} \frac{\partial}{\partial \lambda} \right) \log N_n \quad (4.7c)$$

where $N_n = k_n / k_{n0}$ is an equivalent refraction index with k_n the horizontal wavenumbers of modes and k_{n0} an arbitrary reference value. Overdot designates the derivative with respect to arc length s . The variables μ and v are:

$$\begin{aligned} \mu(\phi) &= r_{eq} (1 - \varepsilon^2) / (1 - \varepsilon^2 \sin^2 \phi)^{3/2} \\ v(\phi) &= r_{eq} (1 - \varepsilon^2 \sin^2 \phi)^{1/2} \end{aligned} \quad (4.8)$$

where r_{eq} and ε are the equatorial radius and eccentricity of the Earth ellipsoid model respectively.

The last term in Equation (4.7c) accounts for distortion of the ray paths due to the transverse gradients of the horizontal wavenumber k_n based on Snell's law. If this term is neglected, the solutions of Equation (4.7) are geodesics on the ellipsoid as in Page 649 of (Bomford, 1980).

The modal horizontal wavenumbers were calculated using the KRAKEN program (Porter and Reiss, 1984) on a horizontal grid with a grid size of 0.1° for both latitude and longitude. The sound speed profiles and bathymetry were derived from the WOA-2005 climatology data and the ETOPO2 data respectively, as discussed earlier in Section 3.3.1, and then interpolated to 0.1° resolution. The system of ordinary differential equations (4.7) was numerically solved using a 4-th or 5-th order Runge-Kutta method (Press et al., 2007). In the integration process, the modal wavenumbers were interpolated within the current grid cell in order to reduce errors of numerical integration due to the limited grid size.

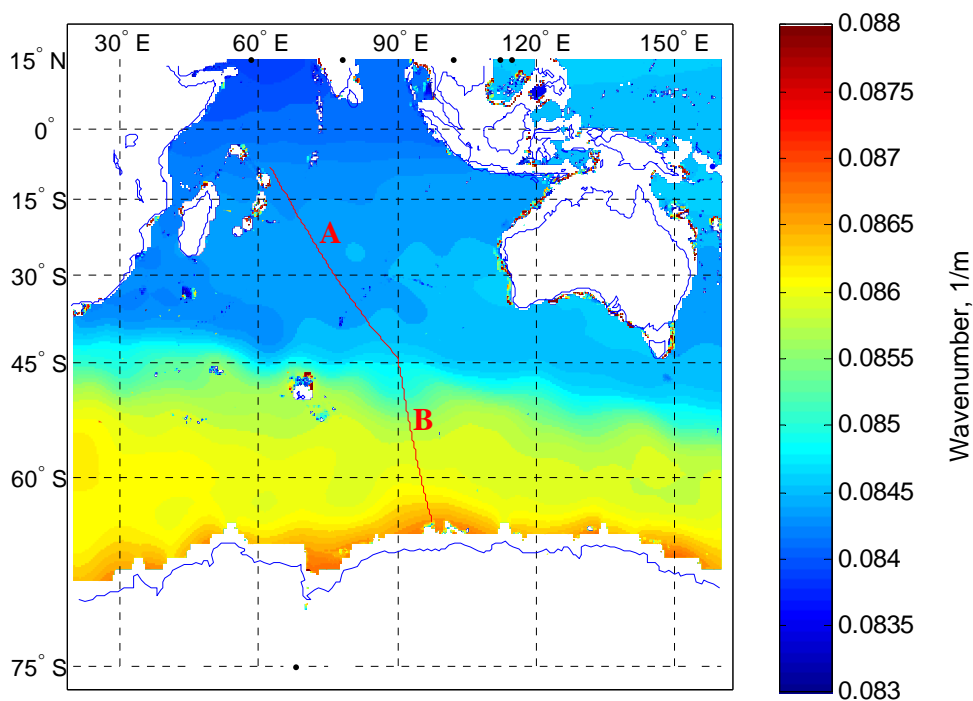


Figure 4.3. The spatial variation of the mode 1 wavenumber at 20 Hz in the Indian and Southern Oceans. The sound speed is derived from the winter climatology data. The horizontal resolution is 0.1° . Two transects (red lines) across the Indian Ocean from $[45^\circ\text{S } 90^\circ\text{E}]$ to $[9^\circ\text{N } 62.5^\circ\text{E}]$ (line **A**) and the Southern Ocean $[45^\circ\text{S } 90^\circ\text{E}]$ to $[64.8^\circ\text{S } 97.3^\circ\text{E}]$ (line **B**) are also shown in the map.

Figure 4.3 shows the spatial variation of the mode 1 wavenumber at 20 Hz in the Indian and Southern Oceans in the winter season. The spatial variation of the modal wavenumbers exhibits general features which are common for different modes at different frequencies. The Antarctic Convergence Zone is a transition area which divides the whole ocean region into the northern part with generally lower values of the modal wavenumbers and the southern part with higher values. In the Southern Ocean region south of the ACZ, the wavenumber increases with latitude. In the temperate ocean region north of the ACZ, the modal wavenumbers are relatively larger in the region south and southwest of Australia compared to the other regions. In the tropical ocean region, the modal wavenumbers slightly decrease towards the north.

4.4.2 Potential effect of horizontal refraction on bearing estimation

In the deep water regions, the normal modes propagating over large distances are trapped either in the SOFAR channel in the temperate ocean or in the near surface channel in the high-latitude areas of the Southern Ocean and, therefore, the modal wavenumbers are dependent primarily on the sound speed profile rather than the bathymetry. In this section, we select two geodesic transects revealing the strongest horizontal wavenumber gradients in two distinctive deep ocean environments: The deep water regions of Indian Ocean and Southern Ocean. The aim is to investigate possible ray distortion for the rays which cross the transects in the perpendicular direction, and to analyse the potential effect of horizontal refraction on bearing estimation in the two regions. The ray distortion is assessed with respect to the rate of azimuth deviation from the geodetic line represented by the last term of Equation (4.7c).

4.4.2.1 In the Indian Ocean

The transect selected in the deep water region crosses the Indian Ocean from [45°S 90°E] to [9°N 62.5°E], which is shown as red line A in Figure 4.3. Figure 4.4 shows the sound speed profile in the month of August and the bathymetry along the transect. In the region north of the Antarctic Convergence Zone (ACZ), the sound speed profile in the temperate

area has relatively sharp SOFAR channel with the axis of about 1000m depth. Towards the north along the transect, the minimum in sound speed profile becomes broader with the axis of the channel diving to nearly 2000m in the tropical area.

The rate of azimuth deviation from the geodetic line for ray trajectories of different modes at different frequencies along the transect is shown in Figure 4.5. If considering only the effect of changes in the sound speed, the strongest azimuth deviation rate takes place at the beginning of the transect, where the sharpness of the sound speed minimum around the SOFAR channel axis decreases rapidly along the transect. For the rest of the transect, the deviation rate is nearly zero except for the regions where the modes of low order and low frequency have interaction with the ocean ridges. It is also seen in Figure 4.5 that the ray deviation rate along this transect is almost independent of mode number and frequency for the modes trapped in the water column. This is consistent with the conclusion made in Section 3.3.6 that in the SOFAR channel region, the sound propagation has almost no intermodal and intramodal dispersion. For modes interacting with the seabed, e.g. mode 3 at 20 Hz and mode 1 at 5 Hz based on numerical results, the ray deviation rate varies significantly over the mid-ocean ridges where the interaction occurs.

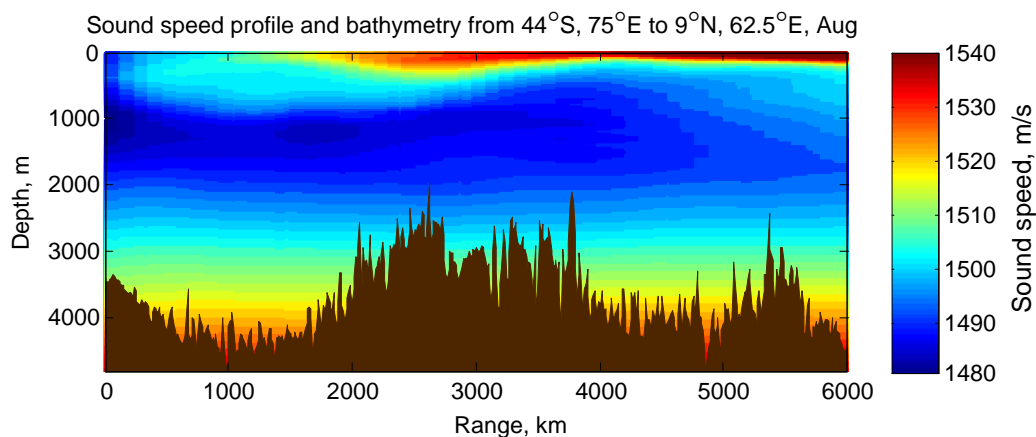


Figure 4.4. The sound speed profile in the month of August and the bathymetry along the transect across the Indian Ocean from [44°S 90°E] to [9°N 62.5°E].

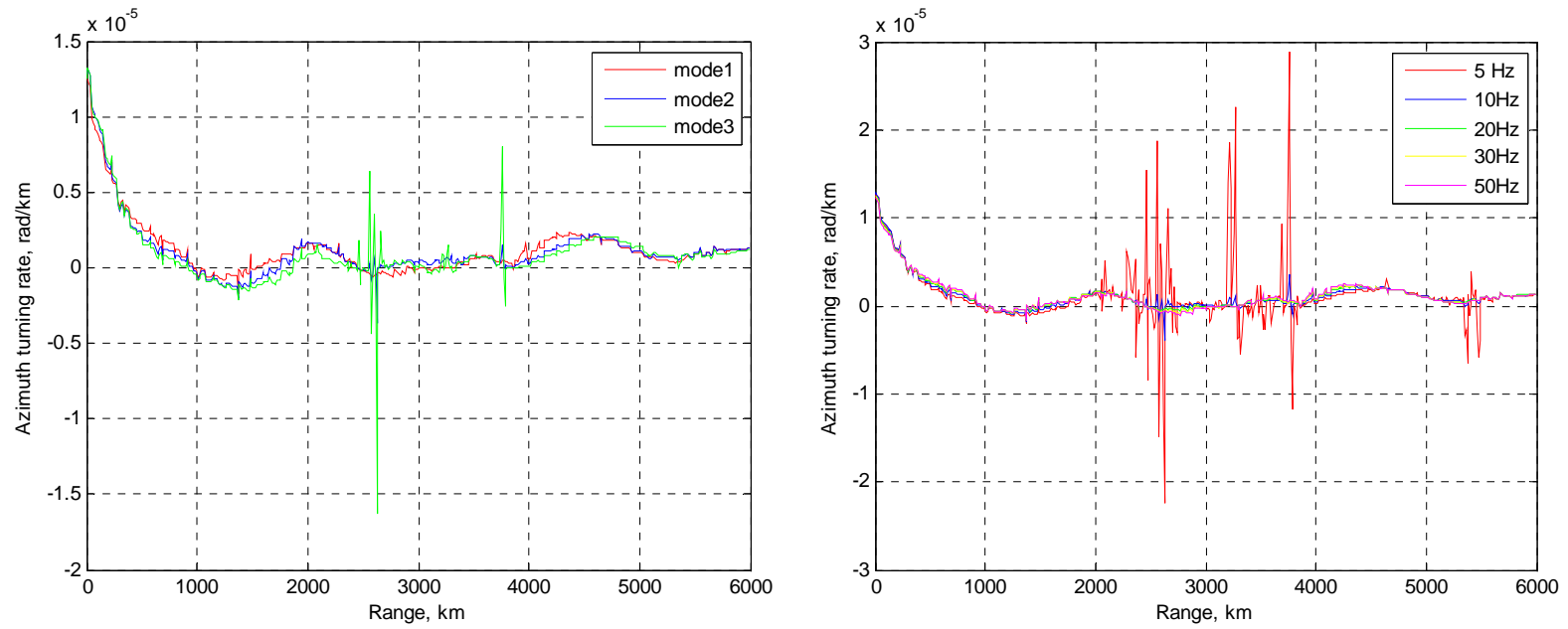


Figure 4.5. The azimuth deviation rate of rays from the geodetic line due to the wavenumber gradient along the transect in the Indian Ocean from [44°S 90°E] to [9°N 62.5°E]. Left panel shows the azimuth deviation rate for modes 1-3 at 20 Hz and the right panel shows the deviation rate for mode 1 at different frequencies.

4.4.2.2 In the Southern Ocean

The transect selected in the deep water region that crosses the ACZ and the Southern Ocean is from [45°S 90°E] to [64.8°S 97.3°E], which is shown as red line **B** in Figure 4.3. It can be seen from Figure 4.6 that the sound speed profile along the transect evolves from a deep SOFAR channel in the temperate ocean to the surface acoustic duct in the Southern Ocean, and then the stronger polar upward channel.

As demonstrated in Figure 4.7, the azimuth deviation rate along the transect in the Southern Ocean slightly decreases with mode number and increases with frequency. Such dependence takes place because higher order modes at lower frequencies penetrate deeper in the water column and hence are less sensitive to rapid changes in the sound speed in the upper water layer across the ACZ. It can be noted that the ray deviation rate across the ACZ and over the Southern part of the Southern Ocean region is much higher than that along the transect in the Indian ocean, with a factor of around four for mode 1 at 20 Hz.

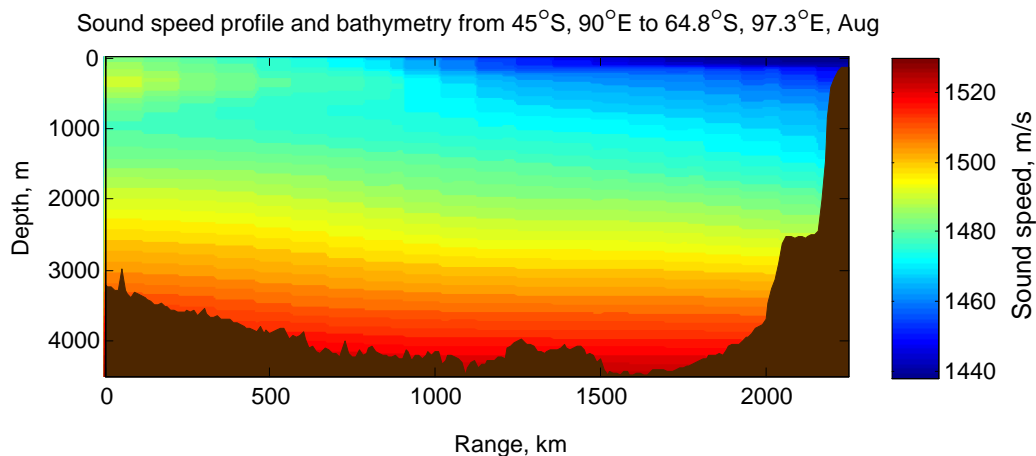


Figure 4.6. The sound speed profile in the month of August and the bathymetry along the transect crossing the ACZ and the Southern Ocean from [45°S 90°E] to [64.8°S 97.3°E].

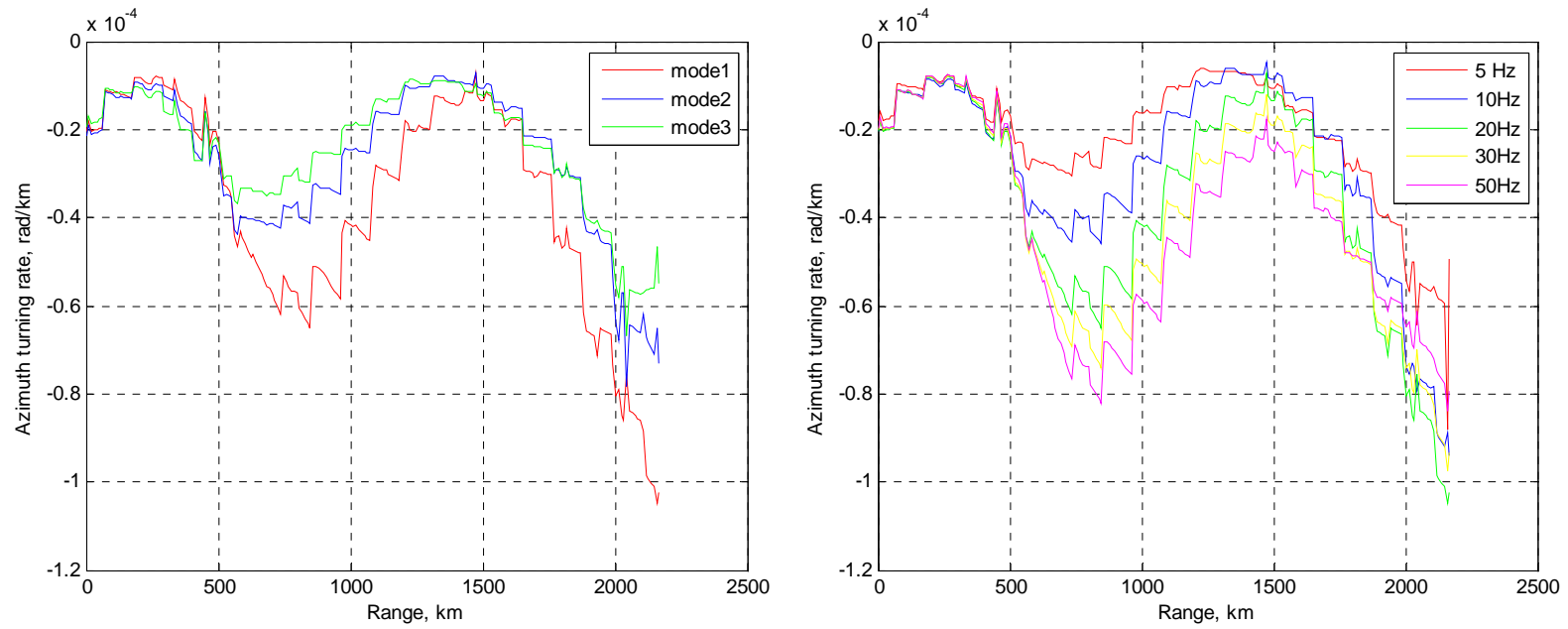


Figure 4.7. The azimuth deviation rate of rays from the geodetic line due to the horizontal wavenumber gradient along the transect in the southern Ocean from [45°S 90°E] to [64.8°S 97.3°E]. Left panel shows the deviation rate of the first three modes at 20 Hz and the right panel shows the same for mode 1 at different frequencies.

The horizontal refraction of sound propagation in shallow water region is also briefly investigated in this section. In shallow water regions, the acoustic propagation at low frequency has much stronger interaction with seafloor than in deep water regions, and therefore horizontal wavenumber has dependence on both sound speed profile and bathymetry. Consequently, the variation of the bathymetry in shallow water regions has a much stronger effect on the horizontal refraction of the propagation, especially for the Australian continental shelf near HA01 which has a downward refracting sound speed profile. The Antarctic continental shelf region has an upward refracting sound speed profile, and compared with Western Australian coastal region, the horizontal wavenumber has relatively less dependence on the bathymetry variation in this region.

4.4.3 Deviation of bearing from the IMS hydroacoustic stations to detected hydroacoustic events due to horizontal refraction

As follows from Equation (4.7c), the horizontal refraction of sound propagation depends on the transverse gradient of the modal wavenumber along the propagation path. This gradient differs significantly along different acoustic paths to the IMS stations, as can be noticed in Figure 4.3. Therefore, the deviation of back-azimuth estimates at the IMS stations from the true bearing to the source of underwater noise depends very much on the source location. The bearing deviations at the IMS stations for different source locations were calculated by changing the launch angle of the acoustic path from the receiver array. The bearing deviation was calculated as the residual $\Delta\theta = \theta_1 - \theta_2$, where θ_1 is the launch angle of the path and θ_2 is the true azimuth to each grid point along the acoustic path subject to horizontal refraction. The launch angle interval used for modelling was about 0.2° , and the range grid size was 10 km. Finally, the calculated residuals $\Delta\theta$ were interpolated onto a regular 1-degree grid of geographic coordinates which covered most parts of the Indian and Southern Oceans observed from the IMS stations.

4.4.3.1 The HA01 station

Figure 4.8 shows the bearing deviation at HA01 due to horizontal refraction of mode 1 at 20 Hz and 50 Hz for different source locations in the Indian and Southern Oceans. For this example, the sound speed profiles were calculated from the winter climatology data. For the entire region, the bearing error due to refraction reveals strong dependence on azimuth and range from the receive station. The bearing deviation for HA01 does not exceed 0.2° for most parts of Indian Ocean region north of the ACZ, except the shallow water regions over the continental slope and seamounts. When the source of noise is located beyond the ACZ in the Southern Ocean, relatively strong wavenumber gradients across the ACZ cause noticeable deviation of the back-azimuth observed at HA01 from the true bearing to the source location. The bearing errors due to refraction are less than 0.2° for the source location observed from HA01 at the azimuth of about 195° along which the propagation path is almost perpendicular to the ACZ frontal zone and therefore is negligibly affected by horizontal refraction. The absolute value of bearing errors generally increases with azimuth moving away from this direction on both sides and reaches the maximum value of nearly 1° in the westernmost and easternmost parts of the Southern Ocean observed from HA01. For mode 1, the bearing deviation doesn't differ much between 20 Hz and 50 Hz, as can be seen from Figure 4.8. The bearing deviation due to horizontal refraction has little dependence on the seasonal change in the sound speed, as was concluded from similar modelling results for the climatology data of different seasons.

4.4.3.2 The H08S station

Figure 4.9 shows the same as Figure 4.8, but for the H08S station. For this station, the propagation path from Antarctica, which is least distorted by horizontal refraction, arrives at the receivers at an azimuth of around 185° . The variation of bearing errors both sides from this azimuth is generally similar to that for HA01. The bearing errors for sources located in the northeast part of the Indian Ocean are considerable because the propagation path is nearly parallel to strong gradients of the modal wavenumbers in this area.

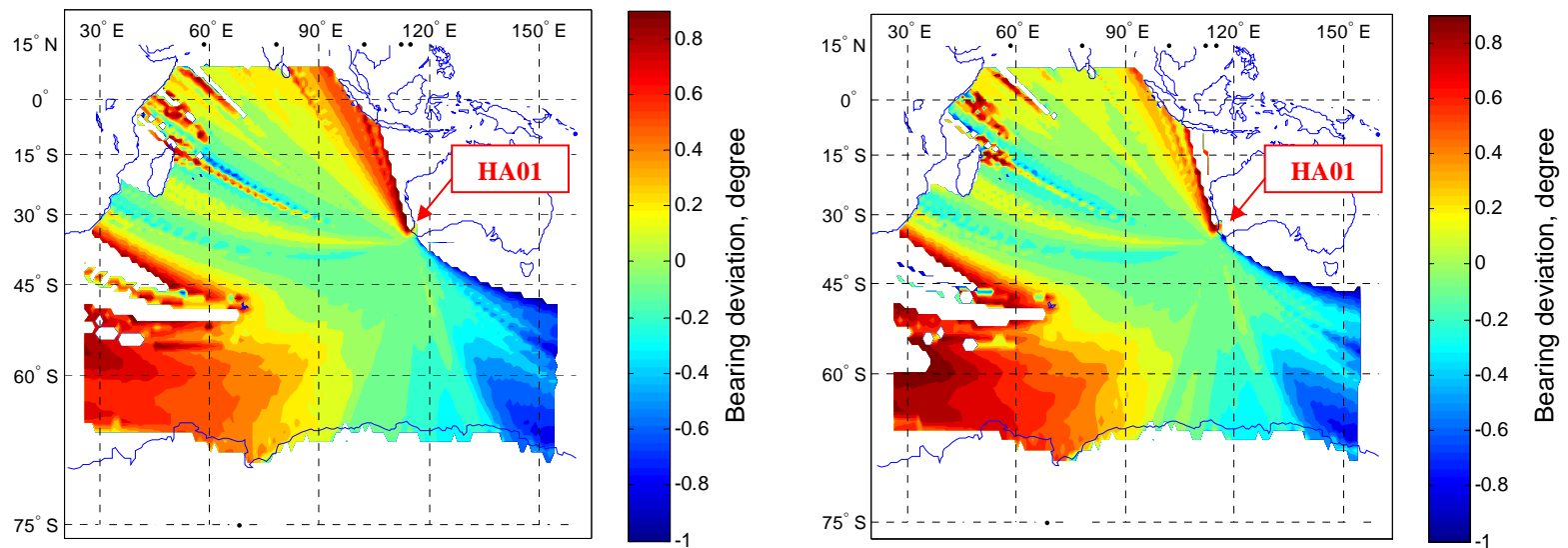


Figure 4.8. Bearing deviation from the true azimuth observed at HA01 for noise sources located in the Indian and Southern Oceans. The deviation errors are due to horizontal refraction calculated for mode 1 at 20 Hz (left panel) and 50 Hz (right panel) for winter climatology data.

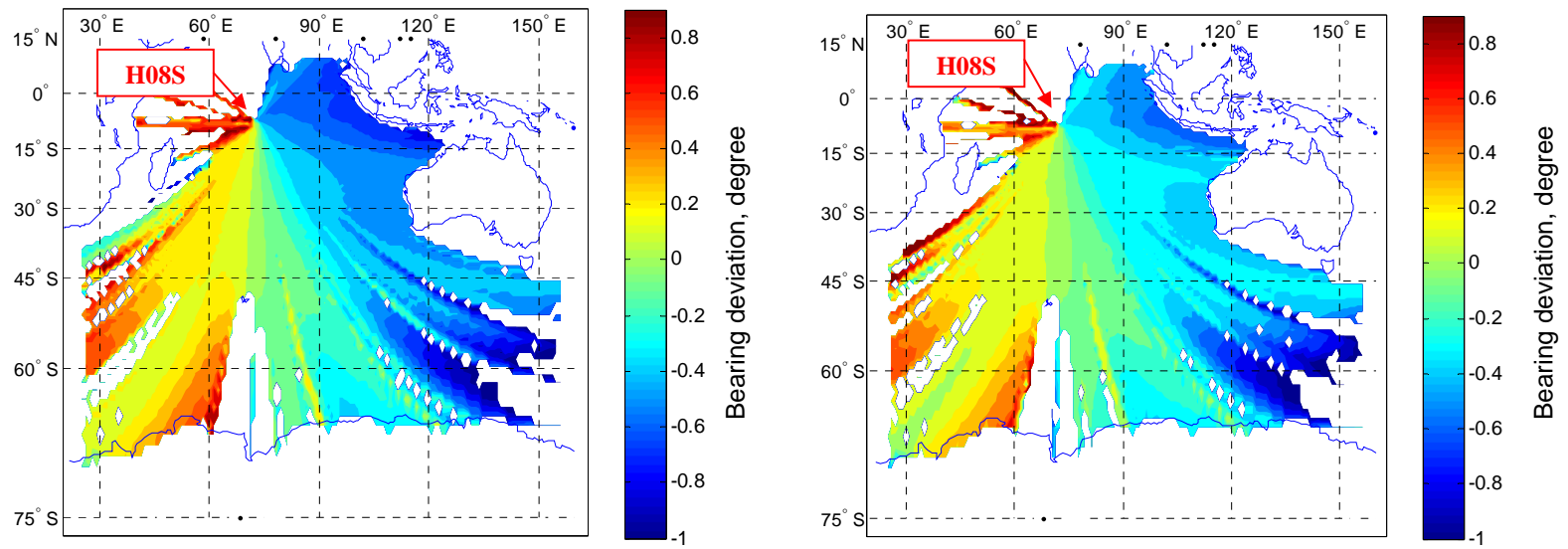


Figure 4.9. Same as Figure 4.8, but for H08S.

4.4.4 Experimental observation of the frequency dependence of horizontal refraction effect on bearing estimation of hydroacoustic events

In this section, a case study is presented for the investigation of the frequency dependence of the horizontal refraction effect on bearing estimation of hydroacoustic events using hydroacoustic stations. The bearing errors from the HA01 station to low-frequency seismic events in the Sumatra coastal zone due to horizontal refraction are predicted for different modes and frequencies. The numerical results are then compared with the back-azimuth estimation for the location of the Great Sumatra-Andaman Earthquake by analysing the received signals in different frequency bands.

Predicted bearing errors from the HA01 station to the Sumatra coastal zone due to horizontal refraction are calculated for mode one at three frequencies: 4.5 Hz, 7.5 Hz and 10.5 Hz, as presented in Figure 4.10. Overall the bearings over the whole Sumatra coastal area have clockwise deviations, and the deviations reveal strong frequency dependence. At 4.5 Hz, the bearings have nearly one degree deviation from the true azimuths, the strongest in the three frequencies. Bearings at 7.5 Hz also have nearly half degree deviation, followed by the smallest deviations at 10.5 Hz. It is also interesting to note that the difference between bearings at 4.5 Hz and 7.5 Hz is nearly half a degree, while that between 7.5 Hz and 10.5 Hz is noticeably smaller.

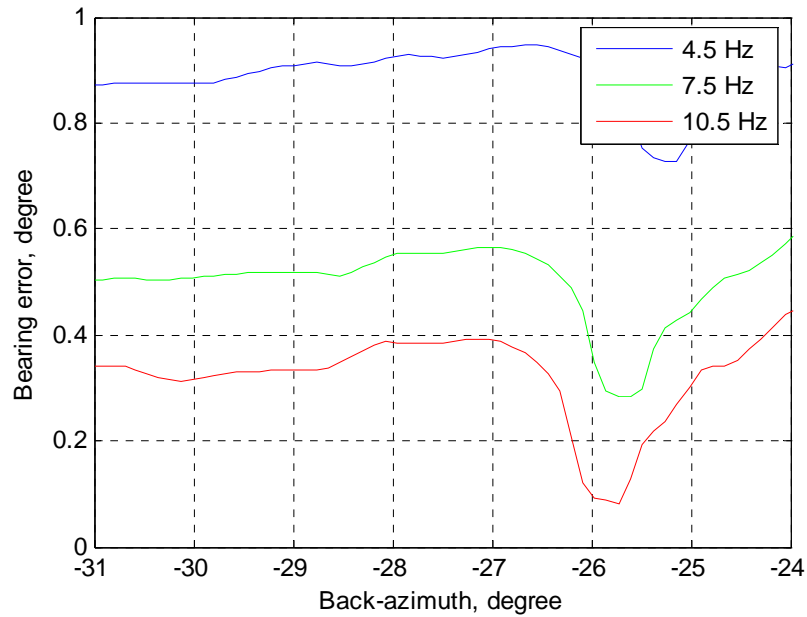


Figure 4.10. Bearing errors due to horizontal refraction numerically predicted for mode 1 at frequencies of 4.5Hz, 7.5Hz and 10.5Hz. Climatology data are taken for the winter season.

A signal section received at HA01 from the Great Sumatra-Andaman earthquake, which occurred on 26 December 2004 (Lay et al., 2005), is analysed for verification of the above modelling results. The signal of 10 minutes duration from the main-shock of the earthquake received at one channel of the HA01 station is shown in the top panel of Figure 4.11. The 10-minute signal in each channel was divided into 10-second sections and the back-azimuth estimate of each section was calculated in three different 1/3-octave frequency bands with central frequencies of 4.5Hz, 7.5 Hz and 10.5Hz. The back-azimuth estimates over all 10-second sections are presented in the bottom panel. For all three frequency bands, the variation of the back-azimuths in the first 8 minutes reveals anti-clockwise changes of nearly 3 degrees. This is because the earthquake rupture propagated to the North Northwest (NNW) along the Sumatra fault zone in this period (Ammon et al., 2005).

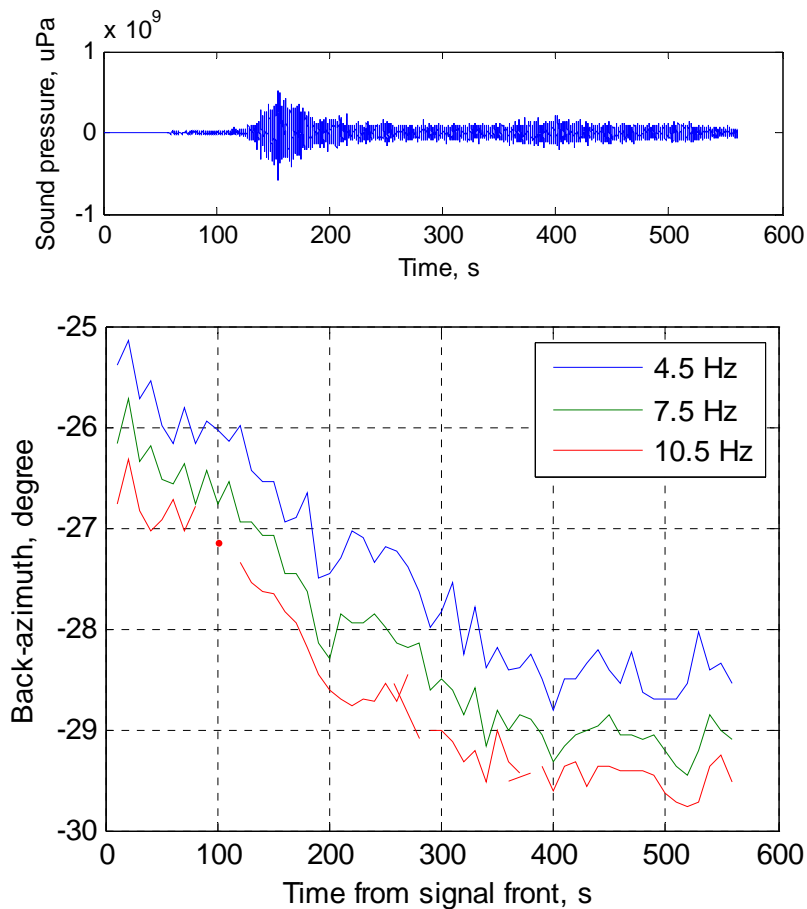


Figure 4.11. Top panel: The 10-minute signal of the main-shock of the Great Sumatra-Andaman Earthquake received at one channel of the HA01 station; Bottom panel: The back-azimuth estimates to the earthquake made from HA01 station in three different 1/3-octave frequency bands with the central frequencies of 4.5Hz, 7.5Hz and 10.5Hz.

It can also be noted that the measured back-azimuths decrease with frequency. The difference between measured back-azimuths at 4.5 Hz and 7.5 Hz is slightly over half a degree, while that between 7.5 Hz and 10.5 Hz is smaller. These observations agree with the modelled results shown in Figure 4.10. This comparison between observation and numerical modelling results suggest that horizontal refraction is the major factor leading to the frequency dependence of the bearing estimation of the Great Sumantr-Andaman Earthquake from HA01. This case study also demonstrates that for certain locations of underwater noise events in the ocean, the effect of horizontal refraction on bearing estimation from the IMS hydroacoustic stations can be significant in the presence of other

errors, e.g. the random bearing error presented in Section 4.3 and systematic error which will be discussed in Section 4.5.

4.5 Systematic bearing error estimation and calibration

Possible errors of moorings' positioning during deployment of the IMS hydroacoustic stations, which might lead to significantly inaccurate touch-down locations of the hydrophone's moorings to be used for hydroacoustic event location, can be a source of time-independent or systematic errors of bearing from the IMS stations. Efforts have been made by previous studies for calibration of either absolute or relative hydrophones' position within individual hydroacoustic stations. Harben and Rodgers (2000) calibrated the horizontal coordinates (latitude and longitude) and depth of three hydrophones of the hydroacoustic station deployed off the Pacific coast of California, using signals received from a towed airgun in the near field. They achieved the accuracy better than 100 meters in latitude, longitude and depth for each of the three hydrophones. Graeber et al. (2006) used a set of well constrained hydroacoustic events to refine the relative hydrophones' position of the HA01 station and consequently improved the accuracy of back-azimuth estimation from this station.

Although the systematic bearing error is superimposed on the random bearing errors, it can be statistically estimated given the exact bearings to a large number of sample events with known coordinates. Moreover, the systematic errors which are larger than the random errors are significant for assessing the location accuracy of the IMS station. Consequently, when estimating the systematic error, we can ignore the random bearing errors and use a smaller number of sample events for calibration of the triplet geometry. Using a number of underwater explosions with known positions, the systematic bearing errors of the two IMS stations are explored in this section by inversion of the measured travel time differences from the sample events to different hydrophones in the triangular array. Refraction was also taken into account in the course of calibration of the IMS stations for the systematic bearing errors.

4.5.1 A geometric model for bearing calibration of the IMS hydroacoustic station

A simple geometric model is proposed in this section for calibration of the systematic bearing error resulted from errors in the receivers' mooring position. This analysis is made in the Cartesian coordinate system by projecting geographical coordinates of individual receivers onto an X - Y plane. Under the condition that the acoustic source is far enough from the hydroacoustic station, the propagation paths can be represented in the horizontal coordinates x and y ignoring the depth difference of the source and receivers. Let the coordinates (x_1^0, y_1^0) of one of the three receivers' moorings, referred to as mooring 1, be a reference position with relative coordinates $(0, 0)$, which does not change when correcting the triple geometry through inversion of TDOA measurements. Let also the original (i.e. nominal uncorrected) relative coordinates of moorings 2 and 3 be (x_2^0, y_2^0) and (x_3^0, y_3^0) respectively, and the coordinates of the n -th located event be (x_r^n, y_r^n) . The corrected relative coordinates of moorings 2 and 3, (x_2, y_2) and (x_3, y_3) respectively, are assumed to have deviations $(\delta x_2, \delta y_2)$ and $(\delta x_3, \delta y_3)$ from the nominal positions. The TDOA measurement T_{ij}^n from the n -th event on a pair of hydrophones i and j , can be expressed as a function of the column vector of deviations $\tilde{\delta} = (\delta x_2, \delta y_2, \delta x_3, \delta y_3)^T$ as:

$$T_{ij}^n = f_{ij}^n(\tilde{\delta}) \quad i, j = 1, 2, 3 \text{ \& } i \neq j, \quad (4.9)$$

where the superscript T denotes the matrix transpose operation. If the deviations of moorings from their nominal positions are small compared to the dimension of the triplet, then T_{ij}^n can be expanded in a power series about the x and y components of deviation from the original coordinates and only the linear terms of the expansion can be kept:

$$T_{ij}^n = f_{ij}^n(\tilde{\delta}^0) + \left. \frac{\partial f_{ij}^n}{\partial(\delta x_2)} \right|_{\tilde{\delta}^0} \delta x_2 + \left. \frac{\partial f_{ij}^n}{\partial(\delta y_2)} \right|_{\tilde{\delta}^0} \delta y_2 + \left. \frac{\partial f_{ij}^n}{\partial(\delta x_3)} \right|_{\tilde{\delta}^0} \delta x_3 + \left. \frac{\partial f_{ij}^n}{\partial(\delta y_3)} \right|_{\tilde{\delta}^0} \delta y_3 \quad (4.10)$$

where the vector of the original deviations $\tilde{\delta}^0 \equiv (\delta x_2^0, \delta y_2^0, \delta x_3^0, \delta y_3^0)^T$ is a zero column vector.

The formula for the TDOA residuals, which are the differences between predicted and measured values, can be obtained from (4.10):

$$T_{ij}^n - f_{ij}^0(\tilde{\delta}^0) = \left. \frac{\partial f_{ij}^n}{\partial(\delta x_2)} \right|_{\tilde{\delta}^0} \delta x_2 + \left. \frac{\partial f_{ij}^n}{\partial(\delta y_2)} \right|_{\tilde{\delta}^0} \delta y_2 + \left. \frac{\partial f_{ij}^n}{\partial(\delta x_3)} \right|_{\tilde{\delta}^0} \delta x_3 + \left. \frac{\partial f_{ij}^n}{\partial(\delta y_3)} \right|_{\tilde{\delta}^0} \delta y_3 \quad (4.11)$$

In the matrix notation, one can express (4.10) as:

$$\mathbf{Y}^n = \mathbf{A}^n \tilde{\delta} \quad (4.12)$$

where the vector of the TDOA residuals is

$$\mathbf{Y}^n = [T_{21}^n - f_{21}^n|_{\tilde{\delta}^0}, T_{31}^n - f_{31}^n|_{\tilde{\delta}^0}, T_{23}^n - f_{23}^n|_{\tilde{\delta}^0}]^T \quad (4.13)$$

and \mathbf{A}^n is a 3×4 matrix of the TDOA derivatives.

Equation (4.12) can be expanded for N sample events located from the hydrophones' triplet, as follows:

$$\mathbf{Y} = \mathbf{A} \tilde{\delta} \quad (4.14)$$

where \mathbf{Y} is a column vector with $3N$ elements, and \mathbf{A} is a $3N \times 4$ matrix:

$$\mathbf{Y} = \begin{bmatrix} \mathbf{Y}^1 \\ \mathbf{Y}^2 \\ \vdots \\ \mathbf{Y}^n \end{bmatrix}; \quad \mathbf{A} = \begin{bmatrix} \mathbf{A}^1 \\ \mathbf{A}^2 \\ \vdots \\ \mathbf{A}^n \end{bmatrix} \quad (4.15)$$

The least square solution for $\tilde{\delta}$ can be obtained as follows:

$$\tilde{\delta} = [\mathbf{A}^T \mathbf{A}]^{-1} \mathbf{A}^T \mathbf{Y}. \quad (4.16)$$

Assuming the sound speed v is the same along the three propagation paths to the three receivers, the travel time differences between hydrophones from the n -th event can be calculated as:

$$T_{21}^n = f_{21}^n(\tilde{\delta}) = \frac{1}{v} (\sqrt{x_r^{n2} + y_r^{n2}} - \sqrt{(x_r^n - x_2 - \delta x_2)^2 + (y_r^n - y_2 - \delta y_2)^2}) \quad (4.17)$$

$$T_{31}^n = f_{31}^n(\tilde{\delta}) = \frac{1}{v} (\sqrt{x_r^{n2} + y_r^{n2}} - \sqrt{(x_r^n - x_3 - \delta x_3)^2 + (y_r^n - y_3 - \delta y_3)^2}) \quad (4.18)$$

$$T_{23}^n = f_{23}^n(\tilde{\delta}) = \frac{1}{v} \left(\sqrt{(x_r^n - x_2 - \delta x_2)^2 + (y_r^n - y_2 - \delta y_2)^2} - \sqrt{(x_r^n - x_3 - \delta x_3)^2 + (y_r^n - y_3 - \delta y_3)^2} \right) \quad (4.19)$$

4.5.2 Experimental estimation of the systematic bearing error and calibration of array geometry

Based on the simple geometric model described in Section 4.5.1, the difference between the nominal and actual positions the hydrophones' moorings in the triad can be found from Equation (4.16), providing a number of calibration events with known coordinates are available. Blackman proposed several experiments aimed at calibrating the IMS hydroacoustic stations in the Indian Ocean and some of them have been implemented in the past few years (Blackman et al., 2003, Blackman et al., 2004, Blackman and Groot-Hedlin, 2005, Blackman and Jenkinm, 2007). Because of the high transmission loss along some experimental acoustic paths and part of the data missing in the HA01 and H08S recording collections, only some SUS explosions made in 2003 during the cruise of R/V Melville were detected at both HA01 and H08S stations with a SNR sufficient for bearing calibration purposes. The vessel transit from Cape Town to Cocos Keeling Island passed almost along a great-circle track across the Indian Ocean, as shown in Figure 4.12 (Blackman et al., 2003). The distances from the locations of SUS explosions to HA01 were from about 2330 km to 9740 km and that to H08S was from 1360 km to 5150 km. The SUS charges were fired at depths of 610m and 915m. At these detonation depths, the peak energy spectrum density of the explosion at around 100 Hz corresponds to a source spectral density of about 270 dB re $1\mu\text{Pa}^2/\text{Hz}$ at 1 meter. The ship was stationary during each explosion, so the GPS coordinates of the drop point provided the source location with an accuracy of about 10m.

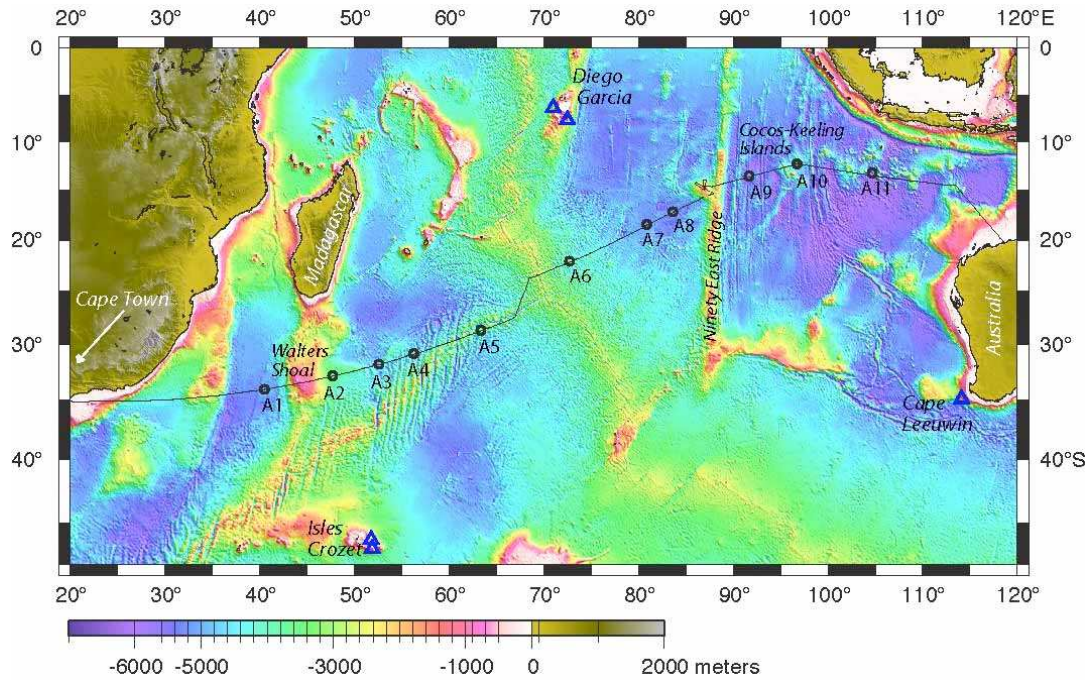


Figure 4.12. Track of the R/V Melville cruise in May/June 2003 overlain on shaded bathymetry of the Indian Ocean. The IMS hydroacoustic stations are shown by triangles and the locations of explosions are shown by circles (Blackman et al., 2003).

In addition to the signals from the SUS explosions made in the IMS calibration experiment, strong signals from two big explosions made in the Bay of Bengal on May 5 2004 at known coordinates (Bowman et al., 2005), were also recorded at both IMS stations and are included in this analysis as calibration events.

4.5.2.1 The HA01 station

The sources of the seven calibration events, and their shot times, coordinates, shot depths and back-azimuths from HA01 are shown in the first five columns of Table 4.3. All of these explosions were made in deep water and the signals from these explosions underwent multi-path propagation in the SOFAR acoustic channel. To account for multi-path propagation effects, a Progressive Multi-Channel Correlation (PMCC) method (Cansi, 1995) was used for measuring the TDOA at the HA01 hydrophones needed for estimating the

propagation slowness and back-azimuth by the plane wave fitting algorithm. In the PMCC method, the correlation of signals at three receivers i, j, k , is calculated within a sliding frequency window in a series of frequency bands to obtain the following closure relation:

$$r_{ijk} \equiv \Delta t_{ij} + \Delta t_{jk} + \Delta t_{ki} = 0 \quad (4.20)$$

where Δt_{ij} is the TDOA at receivers i and j . Due to the background noise and the finite sampling rate, the consistency condition in Equation (4.20) may have a small deviation from zero even for fully coherent signals. The waveform of the explosive signals used for this analysis has a relatively short and sharp peak and, therefore, a single time window of about one second long was selected for the correlation analysis, rather than a series of sliding windows. The passband of 20 Hz was selected for the sliding frequency window, and applied in the frequency range from 10 Hz to 70 Hz, where the coherence of background noise was low. The signal-to-noise ratio of all windowed calibration signals is well above 10 dB and, therefore, according to Equation (4.2), the error of TDOA estimates for each pair of receivers should be less than the signal sampling interval of 4 ms. The threshold for the consistency criterion r_{ijk} was 0.02 s. The TDOA estimates in different frequency bands were considered to be suitable for azimuth estimation, if the consistency criterion (4.20) did not exceed this threshold. As additional criteria for selecting TDOA measurements, the cross correlation coefficient was tested to be at least 0.5 and the group velocity estimates to be within 1.40 - 1.50 km/s.

The inverted group velocities, measured azimuth, bearing errors due to horizontal refraction, and azimuth residuals are shown in the last four columns of Table 4.3. The azimuth residual of each calibration event is the difference between the measured and true back-azimuth to the event from the HA01 station, minus the bearing error expected from horizontal refraction modelled along the propagation path. Note that the back-azimuth estimates at HA01 for all seven calibration events, corrected for the effect of horizontal refraction, have a small clock-wise deviation from their actual values.

Figure 4.13 shows the HA01 triplet patterns before and after correction of the relative positions of the three moorings in the Cartesian coordinate system. The size of the corrected triplet pattern is inversely proportional to the sound speed. To draw the corrected triplet pattern, which is shown in Figure 4.13, the sound speed was assumed to be the mean value of the inverted group velocities given in the 6th column of Table 4.3. After correction, the HA01 triplet appears to be slightly anti-clockwise rotated relative to the original pattern. Using the original and corrected HA01 triplet coordinates, the systematic bearing error is calculated as a function of azimuth, which is shown in Figure 4.14. The systematic error is slightly azimuth dependent and the average clockwise deviation is around 0.8° , which is noticeably larger than the measured random errors, which are less than 0.2° .

Table 4.3. The sources of underwater acoustic explosions and their shot times, coordinates, shot depths, true and measured back-azimuth from HA01, inverted group velocities, bearing errors due to horizontal refraction, and the azimuth residual values. The azimuth residual is the difference between the true and measured azimuth, minus the bearing error due to the effect of horizontal refraction (HR denotes horizontal refraction).

Sources of Explosion	Shot time [year/day/hour]	Coordinates [latitude longitude]	Shot Depth (m)	True Azimuth [°]	Group Velocity (km/s)	Measured Azimuth [°]	Bearing error due to HR [°]	Azimuth residual [°]
A6 SUS3	03/149/04.3394	[-22.0848 72.7422]	915	278.18	1.472	278.62	-0.36	0.78
A7 SUS3	03/151/11.8699	[-18.4374 80.9182]	915	290.38	1.466	291.69	0.13	1.18
A8 SUS2A	03/152/09.2333	[-17.1759 83.6751]	610	295.13	1.467	296.11	0.07	0.91
A10 SUS3	03/158/03.9227	[-12.2133 96.7966]	915	320.85	1.464	321.69	0.11	0.73
A11 SUS	03/160/00.6261	[-13.1980 104.6944]	915	336.05	1.466	337.52	0.35	1.12
Bengal Bay1	04/126/15.4678	[10.14 89.07]	-	327.33	1.466	327.94	0.29	0.42
Bengal Bay2	04/126/16.2794	[10.01 89.50]	-	327.75	1.467	328.41	0.29	0.48

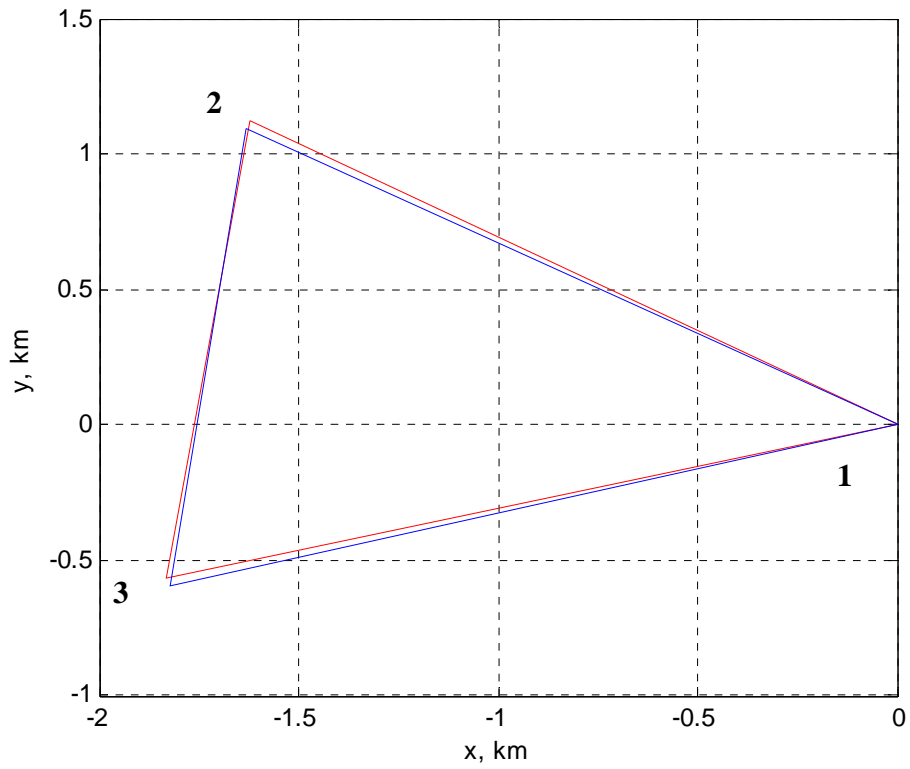


Figure 4.13. The patterns of the HA01 triplet in the Cartesian coordinate system before and after correction. The blue line represents the pattern based on the relative positions of the moorings determined during deployment; the red line is the result obtained after correction of the relative coordinate using Equation (4.16) and the seven explosive signals. The coordinates of hydrophone 1 are fixed as a reference position.

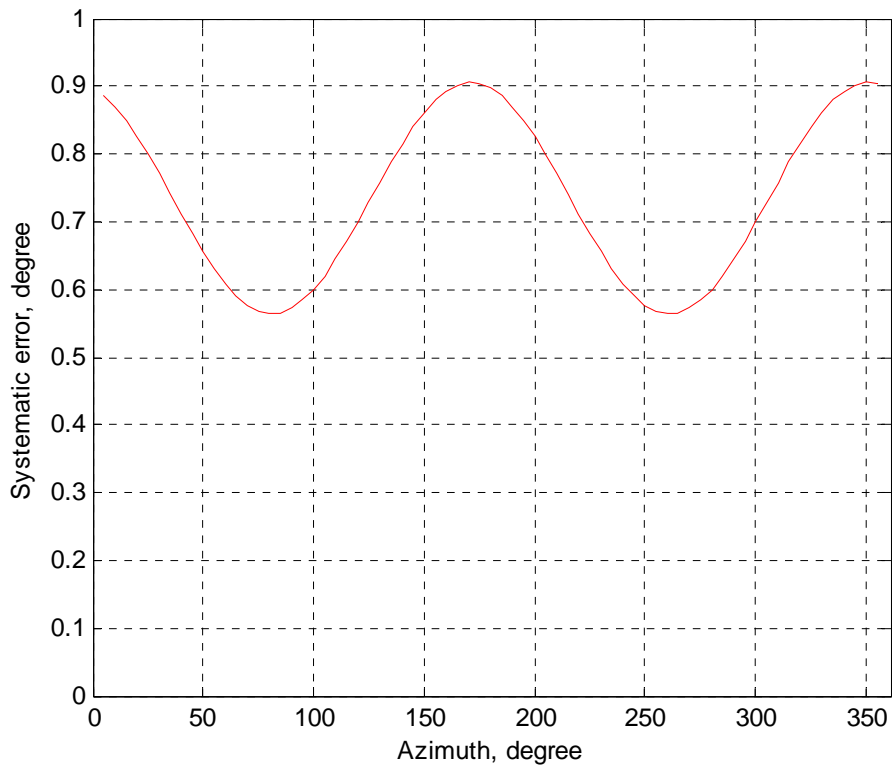


Figure 4.14. Systematic bearing error as a function of back-azimuth from HA01 calculated for the original and corrected coordinates of the HA01 moorings.

4.5.2.2 The H08S station

The same bearing calibration procedure was applied to the H08S station as that to HA01 discussed in Section 4.5.2.1. The sources of the ten explosive events used for calibration, and their shot times, coordinates, shot depths and back-azimuths from H08S are shown in the first five columns of Table 4.4. The inverted group velocities, measured back-azimuth, bearing errors due to horizontal refraction, and azimuth residues are shown in the last four columns of Table 4.4. Figure 4.15 shows the H08S triplet patterns before and after correction of the relative positions of the H08S moorings in the Cartesian coordinate system. Figure 4.16 shows the systematic bearing error of H08S due to inaccurate original positioning of the hydrophones' moorings, calculated as a function of back-azimuth from H08S to the located source. Compared with the HA01 station, H08S appears to have a

much smaller systematic bearing error, which is about 0.2° on average and comparable with the random errors.

Table 4.4. The sources of underwater acoustic explosions and their shot times, coordinates, shot depths, true and measured azimuths from H08S, inverted group velocities and the azimuth residual values. The azimuth residual is the difference between the true and measured azimuth, minus the bearing error due to the effect of horizontal refraction (HR denotes horizontal refraction)

Sources of Explosion	Shot time [year/day/hour]	Coordinates [latitude longitude]	Shot Depth (m)	Actual Azimuth [°]	Group Velocity (km/s)	Measured Azimuth [°]	Bearing error due to HR [°]	Azimuthal residual [°]
A6 SUS3	03/149/04.3394	[-22.0848 72.7422]	915	179	1.4811	179.52	0.12	0.41
A6 SUS2	03/149/04.4308	[-22.0848 72.7422]	610	179	1.4702	179.59	0.12	0.47
A7 SUS3	03/151/11.8699	[-18.4374 80.9182]	915	143.37	1.4727	143.62	0.34	-0.01
A7 SUS2	03/151/11.9711	[-18.4374 80.9182]	610	143.37	1.477	143.69	0.34	-0.01
A8 SUS2A	03/152/09.2333	[-17.1759 83.6751]	610	131.97	1.4743	132.07	-0.27	0.37
A8 SUS2B	03/152/09.3333	[-17.1759 83.6751]	610	131.97	1.4743	132.07	-0.27	0.37
A9 SUS3	03/156/10.8133	[-13.4945 91.4886]	915	108.72	1.4688	108.39	-0.39	0.05
A10 SUS3	03/158/03.9227	[-12.2133 96.7966]	915	102.69	1.4885	102.33	-0.54	0.17
Bengal Bay1	04/126/15.4678	[10.14 89.07]	-	43.33	1.475	43.37	-0.29	0.32
Bengal Bay2	04/126/16.2794	[10.01 89.50]	-	44.29	1.474	44.47	-0.29	0.47

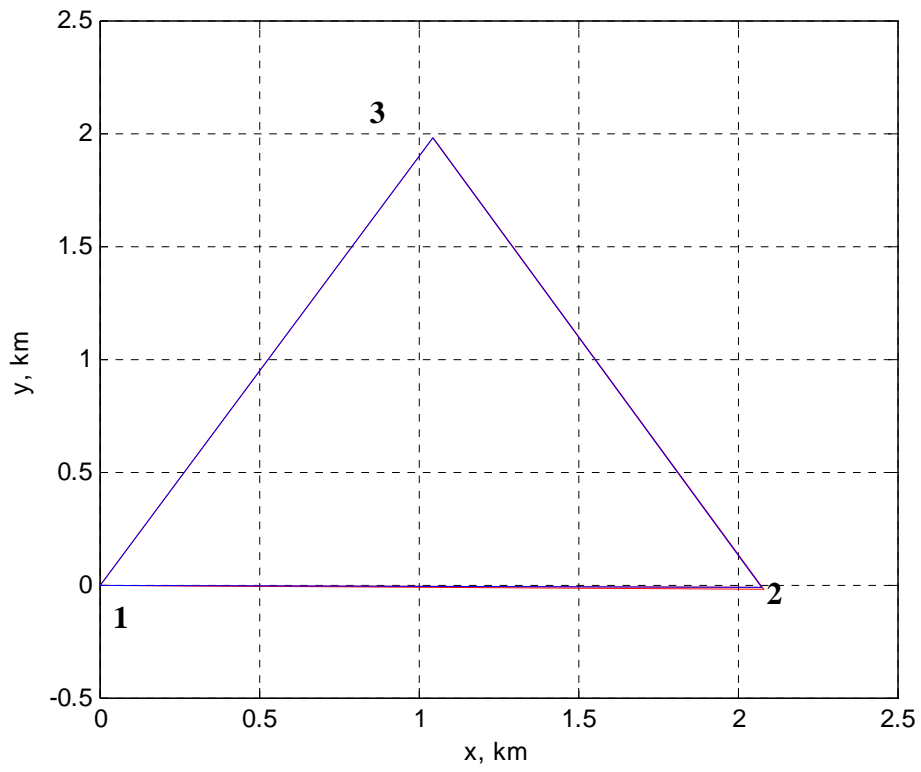


Figure 4.15. The patterns of the H08S triplet in the Cartesian coordinate system before (blue) and after (red) correction.

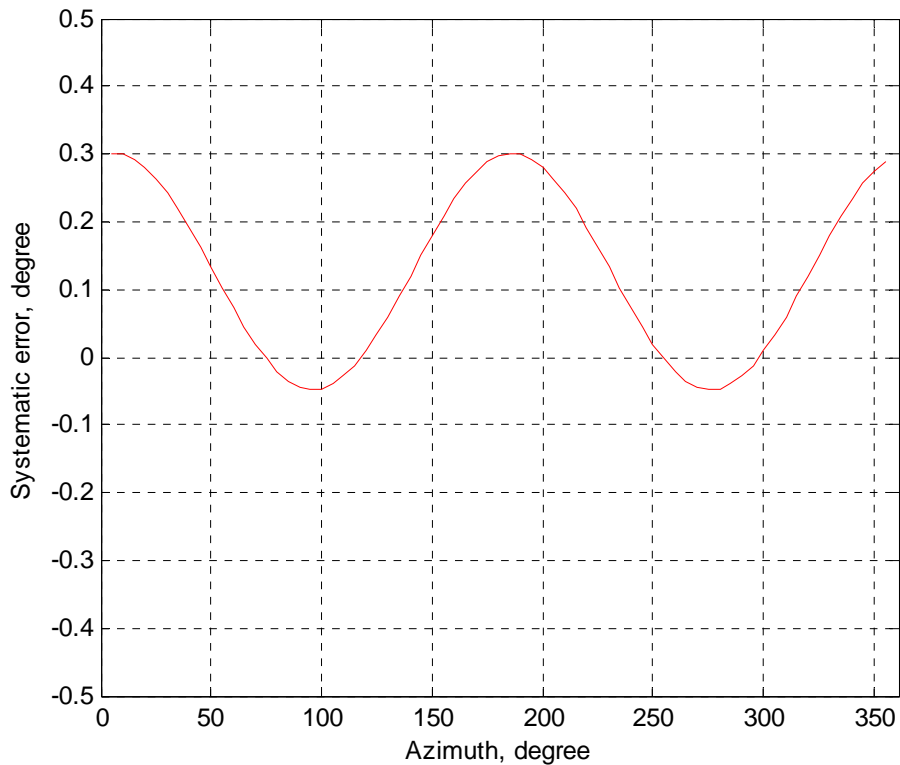


Figure 4.16. Systematic bearing error as a function of back-azimuth from H08S calculated for the original and corrected coordinates of the H08S moorings.

4.5.3 Examination of the systematic bearing error from HA01 using acoustic and satellite observations of Antarctic icebergs

A series of ice harmonic tremor signals lasting from late Julian day 260 until the middle of Julian day 262 in 2003 was observed at the HA01 station. The measured back-azimuths to these events before and after correction of the HA01 triplet position are shown in Figure 4.17. According to the calibration result shown in Figure 4.14, the systematic bearing error in this direction of about 164° is around 0.8° . The error due to horizontal refraction along the path to the Antarctic coast in this direction is expected to be as small as approximately 0.05° , as follows from Figure 4.18. Over the 1.5-day period of observation, the mean value

of the back-azimuths to these tremor events, corrected for the systematic error, varied gradually from 163.3° to 164.0° with a standard deviation of nearly 0.2° .

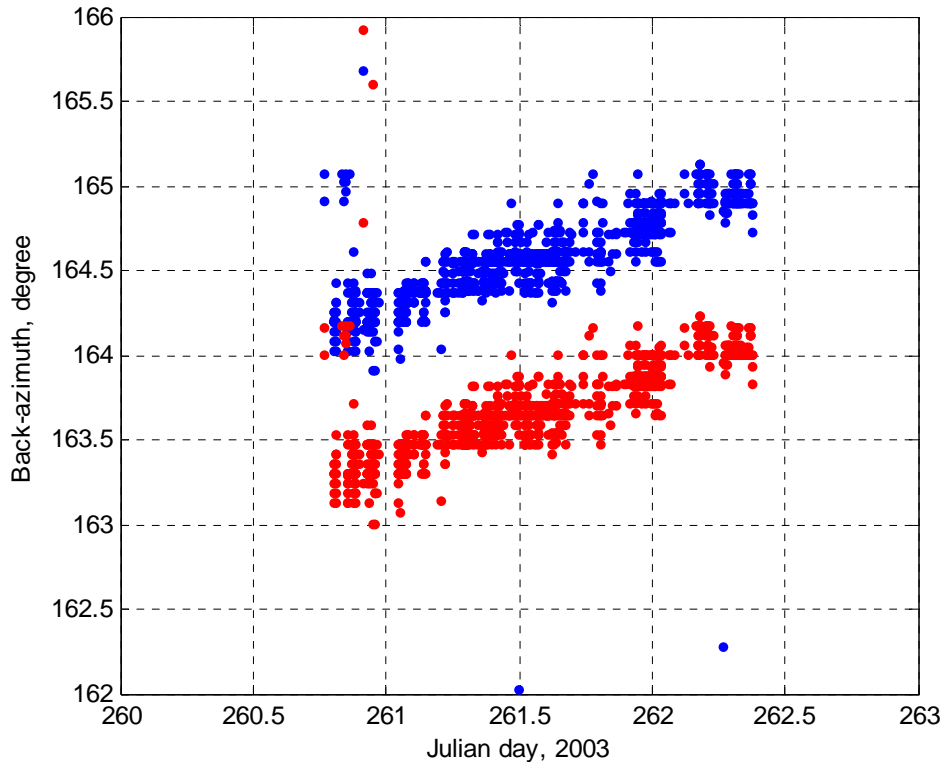


Figure 4.17. Back-azimuth to a series of harmonic tremor signals received at HA01 as a function of signal arrival times. Blue and red dots show the measurements made respectively before and after correction for the systematic bearing error of about 0.8° .

An investigation of Antarctic iceberg activity for this time period and part of the continental shelf, which corresponds to the measured back-azimuth, was conducted using the Antarctic Iceberg Tracking Database (AITD) (<http://www.scp.byu.edu/data/iceberg/database1.html>). According to this database, during the period of acoustic observation of these tremor signals, a large iceberg identified as C008 was located in the same direction from HA01 as the back-azimuth to the tremor signals. These tremor signals are believed to be generated by collisions of iceberg C008 with the ice shelf of Dibble Glacier.

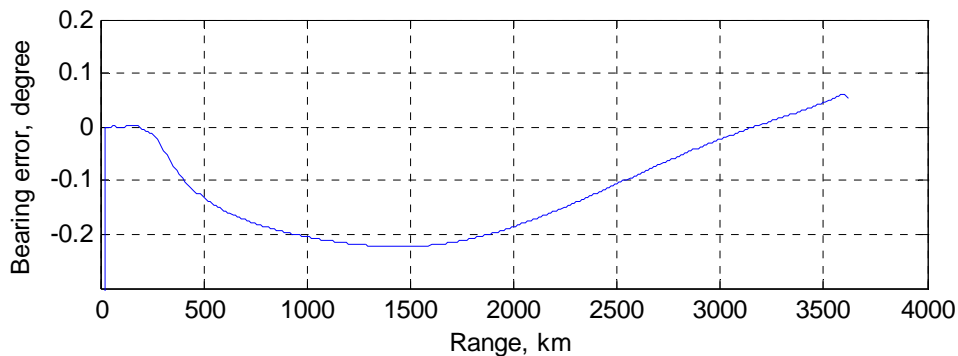


Figure 4.18. Bearing error along the path from HA01 to Dibble Glacier in Antarctica due to horizontal refraction of mode 1 at 10 Hz in summer. The launch angle at HA01 is 163.5° . The error is calculated as a residual of the true back-azimuth to an acoustic source located along the path at different distances from HA01 and the launch angle of the path from HA01. For the source location in the Antarctica ($R > 3500$ km), the error is expected to be about 0.05° .

Two MODIS photographs of the Eastern Antarctica ice shelf, taken from satellites on Julian day 256 and 268 are shown in Figure 4.19. The locations of iceberg C008 on these two days is clearly seen in the images. The iceberg position on day 261 is shown in the right panel of Figure 4.19 by a blue colour iceberg contour, placed according to the AITD data. Bearing from HA01 to the tremor event at its beginning time is shown by two bars, of which the width indicates the standard deviation of measurements. The blue bar shows the bearing direction obtained for the nominal position of the HA01 triplet, while the red one indicates the direction after correction of the triplet geometry to remove the systematic bearing error. The back-azimuth to this event measured after correction of the array geometry corresponds exactly with the part of the ice shelf edge that iceberg C008 drifted by and most likely collided with on day 261. According to the overall variation of the azimuth and the duration of this series of tremor signals, the total distance that iceberg C008 had drifted, scratching the ice shelf, was about 35 km with an average drifting speed of 0.93 km per hour.

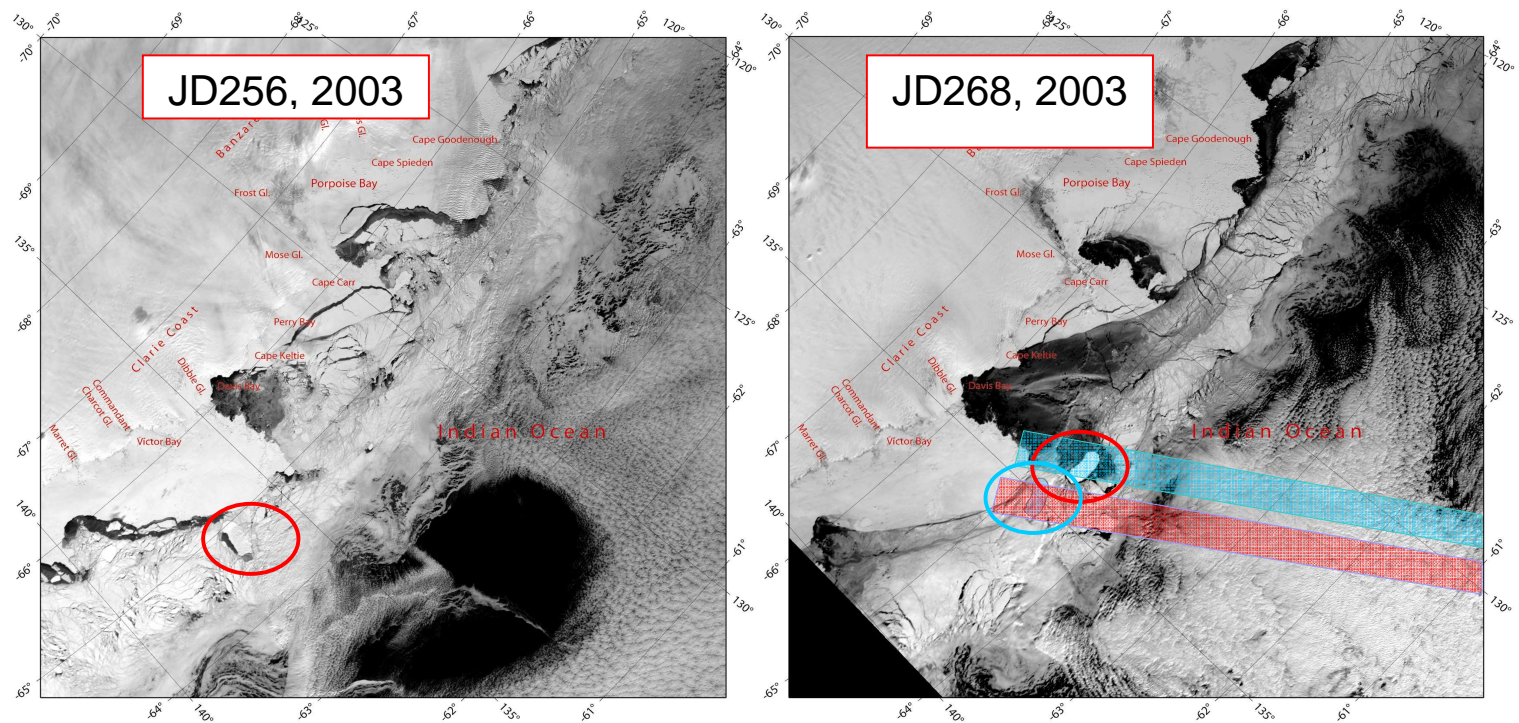


Figure 4.19. Two MODIS satellite images taken on Julian days 256 (left panel) and 268 (right panel) in 2003 showing the locations of iceberg C008 drifting along the ice shelf off Victor Bay (highlighted by red circles). The iceberg position on day 261 is shown in the right panel by a blue colour iceberg contour (highlighted by a blue circle), placed according to the AITD data. The blue and red bars in the right panel show the directions from HA01 to the detected tremor events measured before (blue) and after (red) correction of the HA01 array geometry. The bar width indicates the standard deviation of measurements.

4.6 Conclusions

In this chapter, an analysis of bearing errors due to various factors was carried out for both HA01 and H08S stations. The factors include the errors of TDOA measurements, the effect of horizontal refraction along the propagation paths, horizontal motion of the hydrophones moored on long cables, and errors in the original positioning of the hydrophones' moorings. The following conclusions have been drawn based on the analysis:

1. The bearing error due to the error of TDOA measurements depends on the signal sampling interval, SNR, signal bandwidth and duration. For most of the ice events observed at the IMS stations, the SNR was over 2 dB, the frequency bandwidth was larger than 10 Hz and the signal duration was longer than 5 seconds. For such signal parameters, the effect of TDOA measurement errors on the bearing accuracy is less than 0.15° and can be neglected compared to other sources of error.

2. The random component of the bearing error, caused by variable horizontal deviations of hydrophones deployed on long mooring cables and moving under ocean currents, was estimated to be around 0.2° for both stations, which corresponds to the differential horizontal deviation of different hydrophones in the array by a few meters.

3. The dependence of refraction on mode number and frequency is different for different ocean regions. In the deep water region of the Indian Ocean, the refraction effect is small and has little dependence on mode number and frequency, whereas it is noticeably stronger in the Southern Ocean, especially across the ACZ, where the refraction slightly decreases with mode number at a given frequency and increases with frequency for individual modes. The strongest refraction effect takes place at low frequency over the areas of the continental shelf with rapidly varying bathymetry. The refraction effect strongly depends on the angle at which the acoustic path crosses the ACZ and the continental slope. The absolute value of bearing deviation at the HA01 and H08S stations, induced by horizontal refraction, can be considerable, up to 1° for sources located in the easternmost and westernmost parts of the eastern Antarctica coastal zone observed from the IMS stations.

4. An analysis of back-azimuth measurements from the IMS stations to sources of underwater noise of known location resulted in the conclusion that there is a systematic bearing error most likely due to inaccurate positioning of the hydrophone moorings in the receive triplets. The mooring positions in the triplets were corrected based on inversion of the TDOA measured for different locations of explosive sources. For the HA01 station, the systematic error varies around 0.8° clockwise, depending on azimuth to the source, which is significant compared to the random errors which are less than 0.2° . This result was supported by a simultaneous observation of an ice collision event in Antarctica made both acoustically from HA01 and visually from satellite images. Also, the estimate of the systematic bearing error for HA01 made in this study is consistent with the result obtained by Graeber et al. (Graeber et al., 2006). For the H08S station, the estimate of the systematic error is around 0.2° clockwise, which is comparable with the random errors and, hence, can be ignored.

CHAPTER 5

LOCALIZATION OF ANTARCTIC ICE EVENTS

5.1 Overview

Measurements of the back-azimuth to various hydroacoustic events from both HA01 and H08S stations were discussed in Chapter 2. An investigation of the bearing accuracy of both stations was carried out in Chapter 4. These measurements and this error analysis provide sufficient information to analyse azimuthal variations of the signal arrival from Antarctic ice events. However, in order to conduct a more accurate analysis of the spatial distribution of such events, it is necessary to develop methods for localization of such events in Antarctica, using the azimuth of signal arrival and other signal characteristics measured at either one or two hydroacoustic stations.

Providing the back-azimuths to a hydroacoustic event observed from the two hydroacoustic stations are known, the location of the event can simply be estimated by triangulation as the intersection point of the two great circles passing through the receive stations at the measured azimuth angles (Chapp et al., 2005). Moreover, an additional comparison between modelled and measured differences of the travel times from the located source to the two receive stations can also be made to evaluate the accuracy of the event azimuthal location by the intersection of bearings from these stations. The Prototype International Data Center of the CTBTO has developed a system to automatically form event hypotheses based on the hydroacoustic observation of the back-azimuths and arrival times of the detected signals, combined with their seismic and infrasonic detections (Hanson et al., 2001, Hanson and Bowman, 2006).

In this chapter, various schemes for localizing Antarctic ice events, using either the HA01 station alone or both HA01 and H08S stations are considered and examined. The localization uncertainty of these schemes will also be discussed. Section 5.2 introduces the most straightforward approach based on locating events by triangulation from the two IMS stations using the back-azimuth measurements. The errors of localization by this method

are also considered in this section. Example results of localization of some ice events detected at both IMS stations are given and verified by comparing the measured and modelled differences of the signal travel times. Section 5.3 presents the feasibility study of ice event localization using a single hydroacoustic station. The HA01 station was used in this study to examine the localization method. In the approach proposed and examined in this section, ice events are located using the back-azimuth measurements of signal arrivals at HA01, as well as range estimates based on a comparison of the measured and modelled frequency dispersion characteristics of the signals. The dependence of the localization accuracy on seasonal variations of the sound speed is investigated. A comparison of the event localization results by the two different methods, i.e. using one or two hydroacoustic stations, is also made. Section 5.4 presents an alternative approach to locate ice events by a single hydroacoustic station based on the observed cut-off frequency of mode 1 in the time-frequency arrival structure of the received signals. Section 5.5 gives the concluding remarks.

5.2 Antarctic ice event localization by triangulation

In order to locate Antarctic ice events by triangulation, we have to detect signal arrivals from the same event at both HA01 and H08S stations and to accurately estimate the back-azimuths of the signal arrivals. As discussed in Chapter 2, Antarctic ice events have been identified in the hydroacoustic data collected from the HA01 station. For the data collected from the H08S station, all hydroacoustic events with coherent signal arrivals have been detected and stored, but not all of them have been classified with respect to the most likely source of noise. The signals received at H08S from the same event as those detected at HA01 were picked out, based on the back-azimuth and arrival time measurements at HA01 using the following procedure:

- 1) The location of an ice event on the Antarctic shelf is roughly estimated by projection of the back-azimuth bearing from HA01 onto the Antarctic coastline;

2) The signal travel time difference from the guess location to the HA01 and H08S stations is estimated through numerical modelling of acoustic propagation, as is the expected back-azimuth of the signal arrival at H08S. Consequently, the time interval within which the signal arrival at the H08S station is expected can then be determined.

3) A search is then carried out for a signal with a similar waveform and spectral characteristics, and with a back-azimuth close to the expected one, which arrived at the H08S station within a time window around the predicted arrival time. The length of the search window is selected to allow for possible errors in the numerical prediction of the travel time difference.

Once the signal from the same Antarctic ice event is identified in the H08S recordings, the event can be located by triangulation using the back-azimuth estimates from both stations.

The ice events detected at the HA01 station cannot always be observed at the H08S station, and vice versa, because of different propagation conditions, including propagation blockage by islands and shoals, along the two different paths. For further analysis, the nine most intense signals from the ice events detected at HA01 in 2003 which were also observed at H08S were selected. The locations of the events on the Antarctic shelf were derived by triangulation from the back-azimuth estimates as shown in Figure 5.1. The detection time and the coordinates of the azimuthal locations of these nine events are given in columns 1-5 of Table 5.1.

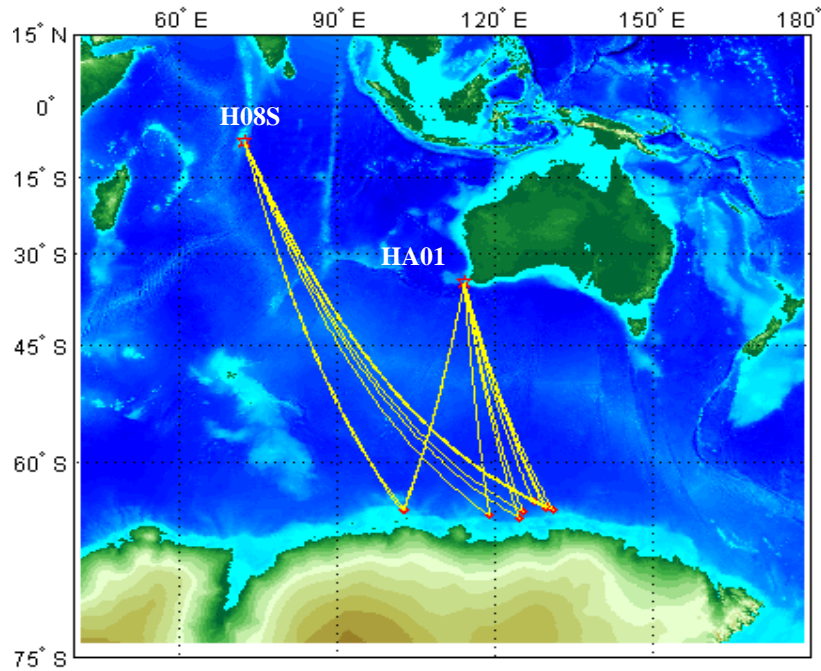


Figure 5.1. Localization of nine intense Antarctic ice events, observed at both HA01 and H08S stations in 2003. Red dots indicate the locations of the events by triangulation from the two stations.

Figure 5.2 shows the waveform and spectrogram of one of the signals from the same ice event observed at both HA01 and H08S stations. For this particular case, the waveforms of the two signals look similar, but the signal amplitude at the H08S station is considerably lower than that at the HA01 station. The frequency band of the signal received at HA01 ranges from several Hz to nearly 35 Hz. The signal consists of prominent arrival pulse of mode 1 dispersed over frequency. A much smaller part of the signal energy arrives earlier than mode 1, but it does not form a distinct pulse because of random-like dispersion over time and frequency. At the H08S station, the frequency band of the ice signal is narrower and limited to approximately 20 Hz. The spectrogram of the ice signal at H08S has a less definite modal appearance, although the arrival of mode 1 can be recognized in the spectrogram at the end of the signal. Frequency dispersion of mode 1 at the HA08 station is noticeably stronger and the energy contribution from the noise-like precursor is relatively higher than that at HA01. According to the results of numerical modelling presented in

Chapter 3, higher attenuation at higher frequencies and stronger frequency dispersion along the paths to the HA08 station result from longer propagation of the signal in the polar environment south of the Antarctic Convergence Zone.

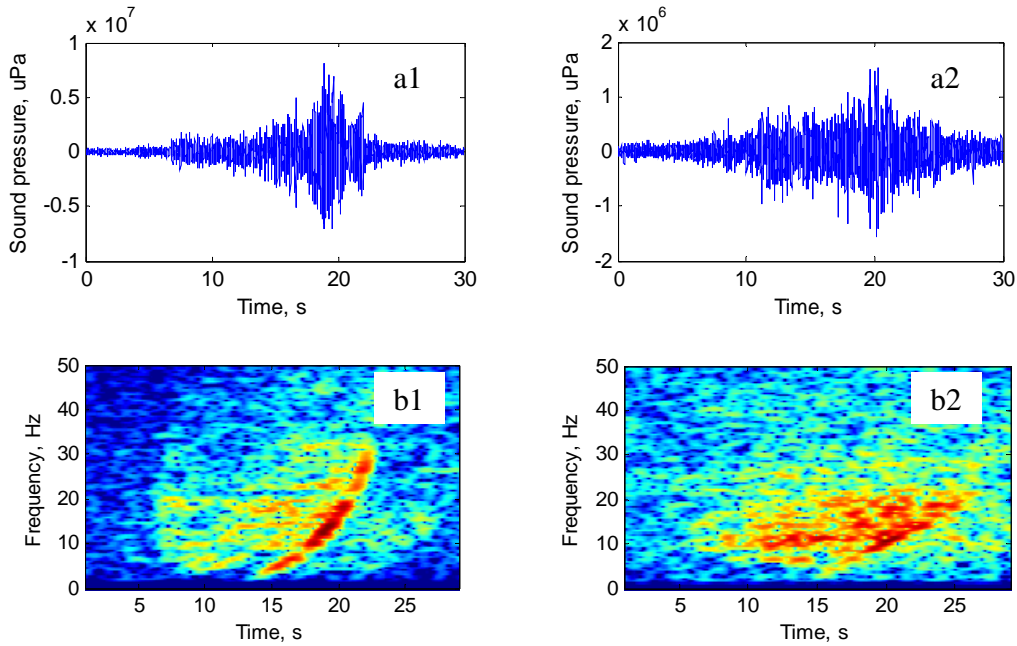


Figure 5.2. Waveforms (top panels) and spectrograms (bottom panels) of one of the signals from the same Antarctic ice event recorded at HA01 (left panels) and H08S station (right panels).

Because the back-azimuths from the IMS stations to the located events are measured with certain random errors, the event location determined by triangulation also has a random error. This random error can be assessed in terms of the confidence region within which the measurement sample subject to random errors is located with certain probability (or confidence level). In 2-D target location, the confidence region is usually limited by an ellipse, referred to as an error ellipse of chosen confidence level. The error ellipse can be calculated using the covariance matrix \mathbf{C} of the estimates for the source coordinates latitude ϕ , longitude λ and an assumption regarding the random errors of back-azimuth measurements. The random errors of back-azimuth measurements are assumed to be normally distributed with the standard deviation $\delta\alpha_1$ and $\delta\alpha_2$ at HA01 and H08S

respectively. The covariance matrix of the source location, determined by triangulation using the measured azimuths α_1 and α_2 , can be calculated from the following equations:

$$\mathbf{C} = (\mathbf{A}^T \mathbf{A})^{-1} \quad (5.1)$$

where $\mathbf{A} = \mathbf{E}\mathbf{J}$, \mathbf{E} is a 2 by 2 diagonal matrix with the main diagonal elements $1/\delta\alpha_1$ and $1/\delta\alpha_2$, and

$$\mathbf{J} = \begin{Bmatrix} \frac{\partial\alpha_1}{\partial\phi} & \frac{\partial\alpha_1}{\partial\lambda} \\ \frac{\partial\alpha_2}{\partial\phi} & \frac{\partial\alpha_2}{\partial\lambda} \end{Bmatrix} \quad (5.2)$$

is the Jacobian matrix for back-azimuth estimates for given coordinates of the source. The Jacobian can be analytically derived for a spherical model of the Earth. If the measurement errors are normally distributed, then the distance from the mean estimate for the location point to each location sample is χ^2 distributed and the size of the error ellipse can be calculated from the quantile of the χ^2 distribution, which corresponds to the chosen confidence level. The locations of four selected ice events determined by triangulation from the two IMS stations and the error ellipses calculated for the same RMS error of back-azimuth measurements of 0.5° at both HA01 and H08S and confidence level of 95% are shown in Figure 5.3.

The travel times of the signals from ice events to the IMS stations can be numerically predicted for a known source location. However, the source location cannot be derived via inversion based only on the signal arrival times at two remote receivers. In a horizontally stratified ocean with no range dependence of the sound speed, there are multiple source locations lying along a hyperbolic line that satisfy the travel time difference. In the real ocean environment, the solution of the inverse problem lies along more complicated lines of which the points can be found only approximately through numerical modelling of acoustic propagation in a range dependent ocean environment and bathymetry (Chapp et al., 2005). Nevertheless, a comparison of the observed and predicted arrival time differences at two hydroacoustic stations provides effective verification of the source location derived from back-azimuth by triangulation.

Because the ice signals are significantly dispersed, we estimate the signal arrival time by the arrival peak of mode 1 within a relatively narrow frequency band of 5–15 Hz where the mode 1 has maximum energy. The accuracy of arrival time measurements in this narrow frequency band is about 0.5 s. The area for searching for the points that satisfy the arrival time differences measured at two stations is limited to a 5×5 degree grid around the location derived from triangulation (column 5 in Table 5.1). Then the travel times from the grid nodes to the receive stations are numerically predicted for the corresponding seasonal environmental conditions and the curve of inverse solution is evaluated through spatial interpolation. For all of the selected events, the inverse solution curve crosses the 95% confidence ellipse of the event location (Figure 5.3), and the shortest distance from the back-azimuth location to the curve is less than 50 km (see the last column in Table 5.1). This means that the results of numerical prediction are quite consistent with the experimental observation and the location of events derived from triangulation is in agreement with the signal arrival time measurements.

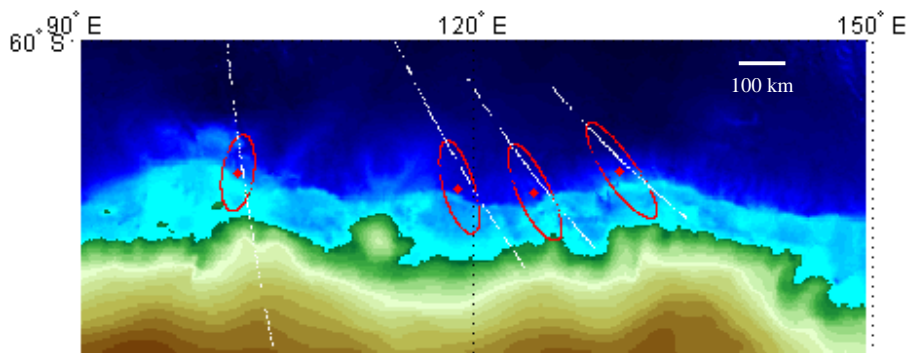


Figure 5.3. Locations of four selected ice events detected at HA01 and HA08 and error ellipses of 95% confidence (red lines). The white lines show the source locations that satisfy the travel time difference of signals measured at both stations. The error ellipses were calculated assuming that the random errors of back-azimuth estimates are Gaussian distributed with a standard deviation of 0.5° .

Table 5.1. Arrival times of selected signals and coordinates of their origin located from the back-azimuth measurements by triangulation and verified via numerical modelling of travel time differences

Arrival date	Arrival at HA01 (h)	Arrival at H08S (h)	ΔT^a (h)	Location by triangulation ^b	Modelled location ^c	ΔT Residual ^d (s)	ΔL^e (km)
2003, 017	02.0306	02.7386	0.7080	[65.069°S, 118.936°E]	[64.829° S, 119.696°E]	23.3	44.79
2003, 055	04.8629	05.6627	0.7998	[64.289°S, 129.810°E]	[64.003°S, 130.415°E]	19.1	43.32
2003, 071	00.0091	00.8101	0.8010	[63.775°S, 127.307°E]	[63.585°S, 127.832°E]	-15.3	33.52
2003, 082	13.9080	14.5391	0.6311	[64.612°S, 102.388°E]	[64.672°S, 102.808°E]	-11.8	21.16
2003, 083	17.1758	17.9500	0.7742	[65.299°S, 124.554°E]	[65.029°S, 125.279°E]	-21.7	45.41
2003, 087	02.6669	03.4706	0.8037	[64.410°S, 129.491°E]	[64.220°S, 129.616°E]	-8.5	22.03
2003, 102	08.2570	08.8750	0.6180	[64.527°S, 102.694°E]	[64.467°S, 102.084°E]	17.6	30.07
2003, 133	22.1207	22.9292	0.8085	[64.551°S, 131.036°E]	[64.311°S, 131.546°E]	-15.8	36.33
2003, 158	01.7799	02.5542	0.7743	[64.764°S, 125.291°E]	[64.864°S, 124.976°E]	8.9	18.66

^a Difference between signal arrival times at HA01 and H08S (hours)

^b Location of events derived by triangulation from the back-azimuths from two receive stations

^c Location of events that are consistent with the arrival time difference at two stations and closest to the location estimates from triangulation

^d Difference between the observed arrival time difference at two stations and the travel time difference modelled for the location derived from back-azimuth triangulation (seconds)

^e Distance between the location by triangulation and the modelled curve satisfying the travel time difference at the two stations

5.3 Localization of Antarctic ice events based on modal frequency dispersion

It is important to locate as many ice events detected at the hydroacoustic stations as possible in order to analyse the spatial distribution of such events. The localization of ice events can be implemented by triangulation with two bearing measurements from both HA01 and H08S stations, as described in Section 5.2. However, such a localization approach using the two IMS stations has some limitations. Firstly, the observable sectors of the Antarctic coastline from these two stations are different. The overlapping part of the two sectors spans the Antarctic coast from approximately 50°E to 130°E , which is noticeably smaller than the whole observable sector of $10^{\circ}\text{E} - 150^{\circ}\text{E}$. Secondly, ice events occurring on the Antarctic continental shelf at longitudes of around $65^{\circ}\text{E} - 70^{\circ}\text{E}$ will not be detected at the H08S station due to the blockage of the propagation path by Kerguelen, Heard and McDonald Islands. Moreover, the variations of transmission loss and arrival structure distortion along different propagation paths make it difficult to detect and identify the arrivals from the same event at different hydroacoustic stations. These problems would be overcome to some extent if ice events could be located by a single hydroacoustic station, i.e. HA01. This approach requires estimation of the range between the events and the receive station in addition to the back-azimuth estimates for signal arrivals at the station.

Range estimation to a remote broadband source can be achieved using a single hydrophone through an analysis of the time-frequency structure of received signals, which relates to the modal group velocity as a function of frequency and mode number, i.e. to the intramodal or intermodal dispersion resulting from the ducted acoustic propagation in the ocean. For the ocean environment of the ATOC experiment in 1998 with a deep sound channel, Kuperman et al. (2001) tried to locate the source near the channel axis based on the energy focusing of different modal groups in the time-frequency domain. Ewing and Worzel (1948) suggested estimating the range by comparing the total dispersion of a pulse to the total span of possible group speed in the propagation environment. T. C. Yang (1984b, 1984a) proposed a method for the high-resolution measurement of frequency dispersion of broadband impulsive signals that propagated over a long range in the Arctic acoustic environment with

a near-surface sound channel. Based on this method, he suggested and examined a range estimation technique using frequency dispersion of low order modes.

As demonstrated from experimental observations in Chapter 2 and from numerical modelling in Chapter 3, there exists a significant intermodal dispersion effect for the acoustic propagation in the Southern Ocean south of the ACZ. Moreover, in this ocean region, mode 1 experiences strong frequency dispersion in the frequency range of 5 Hz – 35 Hz. In contrast to the polar ocean environment, none of the low-order modes undergo significant intramodal dispersion at frequencies above 5 Hz in the SOFAR channel of the temperate ocean. All the Antarctic ice events observed at the IMS hydroacoustic stations reveal a dominant arrival pulse of mode 1 characterized by strong frequency dispersion. In this section, this effect is used to carry out range estimation to ice events using only the HA01 station. The approach suggested here is based on the measured and modelled frequency dispersion characteristics of the mode 1 arrival at the HA01 station. Combined with the back-azimuth estimate, this method allows us to implement localization of ice events in Antarctica.

5.3.1 The time-frequency structure of signals from ice events

The high-resolution measurement of the time-frequency structure of the highly dispersive signal received from an ice event is critical for range estimation. Under the time-frequency uncertainty principle, the frequency uncertainty can not be less than the reciprocal of the signal duration, if the received waveform is the only information about the signal arrival structure (Oppenheim and Schaffer, 1989). Therefore, for the conventional time-frequency structure measurement, i.e. by sonogram /spectrogram analysis, one has either to sacrifice frequency resolution in order to achieve the required time resolution, or to improve the frequency resolution at the cost of the time resolution by elongating the time window, within which the measured frequency may not necessarily correspond to the instantaneous frequency at the centre of the selected signal section.

Based on the prior theoretical knowledge of the mode spectrum expected for different arrival times, T. C. Yang (1984b) proposed a method for high-resolution determination of the mode frequencies as a function of arrival time.

For the condition of the range-independent Arctic Ocean environment, the low frequency impulsive signals propagated over long ranges consist of discrete dispersive normal modes. According to T. C. Yang, the shape of the power spectrum of modal arrival pulses within short time intervals $2\Delta t$ can be approximated by

$$|\sin[2\pi(f - f_n)\Delta t]/[2\pi(f - f_n)]|^2 \quad (5.3)$$

where f_n is the instantaneous frequency of mode n . The stationary phase approximation was used in the derivation of the theoretical power spectrum in a range-independent environment. The derivation procedure suggested by T. C. Yang (1984b) can be adapted to range-dependent acoustic propagation with intermodal and intramodal dispersion if the acoustic mode propagation is nearly adiabatic. This is expected for the propagation across the polar environment from Antarctica to the HA01 station, and consequently the mode spectrum shapes under the adiabatic mode propagation condition can also be approximated by Equation (5.3). The source spectra of ice events in Antarctica and the propagation from Antarctica to HA01 over the polar environment section are expected to be slowly varying over the low frequency band, therefore the length $2\Delta t$ of the spectrum analysis window is subject to the bound condition associated with the stationary phase approximation (Yang, 1984b):

$$\Delta t < 0.365 \left(\pi \frac{dt}{df} \right)^{1/2} \quad (5.4)$$

The algorithm for measuring the time-frequency structure of the transient signals from Antarctic ice events is divided into the following steps:

1) Divide the signal waveform into a series of segments with length satisfying the bound condition as given in the inequality (5.4). The length of each signal segment was taken to be around 0.5s in this study, which is applicable for most Antarctic ice event signals received at HA01;

2) Compute the power spectrum for each waveform segment extended by zero padding in order to achieve the required frequency resolution, which was chosen to be 0.5 Hz in this analysis;

3) Find the best fit of the measured and modelled spectra by shifting the assumed mode frequency f_n of the theoretical spectrum (Equation (5.3)). The mode frequency is determined when the difference between the integrals of the theoretical and measured spectra is less than a certain tolerance value, which was chosen to be 10% in this study, as suggested by T.C. Yang (1984b). The integral is calculated within the frequency band

$$2\pi|f - f_m| = \pi / 2\Delta t ;$$

4) Plot the mode frequencies against the time at the centre of each segment as the measured time-frequency structure of the mode arrival.

Figure 5.4 shows the spectrogram of a typical signal from ice events received at HA01 and the fine time-frequency structure of the mode 1 arrival derived using the above algorithm. Figure 5.5 demonstrates a comparison of the measured and predicted power spectra of the signal segment in which the mode frequency is about 11.2 Hz.

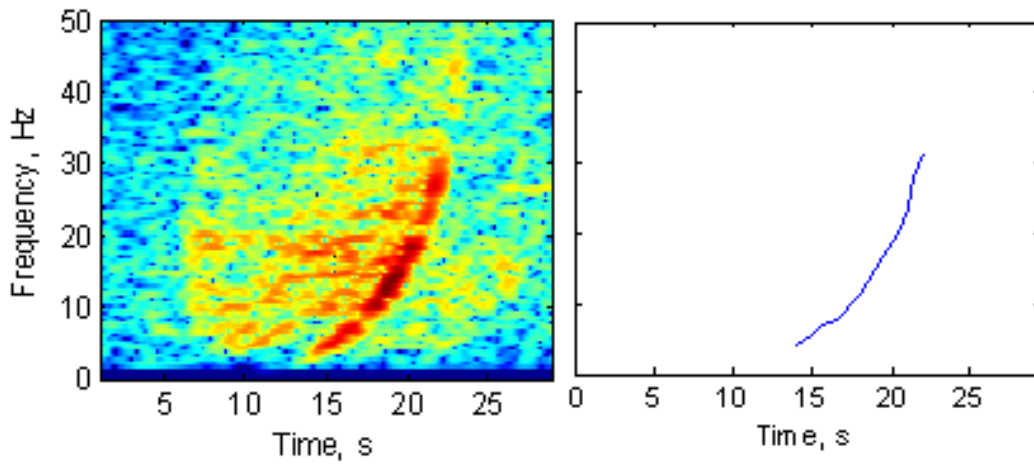


Figure 5.4. The spectrogram of an ice event signal received at the HA01 station (left panel) and its fine time-frequency structure measured with a resolution of 0.5 Hz (right panel).

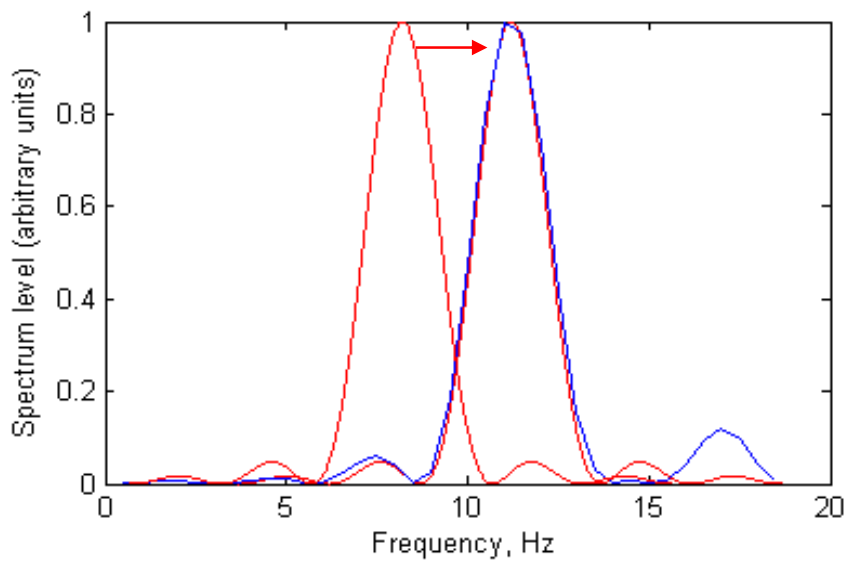


Figure 5.5. Fitting the theoretical (red lines) power spectrum of a signal segment to the measured one (blue line) by shifting the theoretical spectrum around the measured spectrum with the mode 1 frequency of 11.2 Hz.

5.3.2 The range estimation procedure

Range estimation for Antarctic ice events can be conducted by finding the best fit of the measured and modelled time-frequency structures of the mode 1 arrival. The frequency dispersion of mode one was modelled using a range-dependent adiabatic normal mode model, based on sound speed profiles derived from the monthly climatology data from the WAO-2005 and the ETOPO2 bathymetry data, as described in Chapter 3. The mode frequency dispersion was calculated on a 10-km grid along the geodesic line to the Antarctic coast which passes through the receive array location at the measured azimuth angle.

Because the actual travel time of the signal is not known, the measured and modelled arrival times of mode one are aligned at the lowest frequency present in the measured signal. The range R from an ice event to HA01 was determined by finding the following least square fit:

$$\min\left[\sum_{i=1}^N (t_i^{me}(f_i) - t_i^{mo}(f_i))^2\right] \quad (5.5)$$

where t_i^{me} is the centre of the i -th time window within which the instantaneous frequency f_i of mode one is measured and t_i^{mo} is the arrival time of mode one predicted by numerical modelling at the frequency f_i . The standard deviation of range estimation due to the error of the mode frequency measurement can be estimated as:

$$\sigma_R = \sqrt{(\mathbf{A}^T \mathbf{A})^{-1}} \quad (5.6)$$

where $\mathbf{A} = \mathbf{E}\mathbf{J}$, \mathbf{E} is a N by N diagonal matrix with the i -th main diagonal element $1/\sigma_{t_i}$, σ_{t_i} is the standard deviation of the travel time measurement at frequency f_i , and \mathbf{J} is the Jacobian, which is a column vector of partial derivatives of the modelled travel times t_i^{mo} with respect to range $(\partial t_i^{mo} / \partial r)|_R$. The modelled travel times t_i^{mo} of individual modes can be derived by integration of the slowness $S(r, f_i)$ along the propagation path from the source to the receiver:

$$t_i^{mo} = \int_0^R S(r, f_i) dr,$$

which gives the i -th component of \mathbf{J} :

$$\left. (\partial t_i^{mo} / \partial r) \right|_R = S(R, f_i). \quad (5.7)$$

The error of travel time measurements σ_{t_i} can be derived from the frequency measurement error as

$$\sigma_{t_i} = \frac{\partial t}{\partial f} \sigma_{f_i} = \frac{\partial S(R, f_i)}{\partial f} \sigma_{f_i} \quad (5.8)$$

Finally, the error of range measurement through inversion of the frequency dispersion can be estimated using Equations (5.6 - 5.8) and the error of frequency measurements σ_{f_i} . The slowness $S(R, f_i)$ in (5.7) and (5.8) is obtained from the numerical model of acoustic propagation.

In addition to the frequency measurement error σ_{f_i} , the range estimation error also depends on the frequency band of measurements and the number of frequencies used for the least square estimate. For $\sigma_{f_i} = 0.5$ Hz RMS and nine frequency estimates within a frequency band from about 4 Hz to about 20 Hz, the RMS error of range estimates is approximately 50 km.

5.3.3 Case studies

Two case studies are considered in this section to verify the feasibility of the proposed range estimation algorithm for Antarctic ice events based on frequency dispersion in the time-frequency structure of the signals received at the HA01 station. One of the signals from ice events was received at both HA01 and H08S stations on the 17th of January 2003. Its spectrogram observed at HA01 and the measured time-frequency structures are shown in Figure 5.4. A comparison between the location errors estimated for the source location by triangulation from the two stations and that using the time-frequency structure of the signal received only at HA01 is shown in Figure 5.6. In the right panel, the red dot shows the intersection of two back-azimuths from the two stations. The error ellipse of 95%

confidence level of the event location is indicated by the red line. This confidence ellipse is calculated assuming the RMS bearing errors of 0.5° for both stations. The region enclosed by the yellow ellipse is the 95% confidence region of the event location, estimated based on a normally distributed bearing error from the HA01 station with a standard deviation of 0.5° and an error of mode frequency measurement of 0.5 Hz RMS at nine frequencies from about 4 Hz to 20 Hz. The sound speed profile used in the model was derived from the January climatology data. It can be clearly seen from this comparison that the location estimate using only the HA01 station has an error comparable to that of the location using two stations.

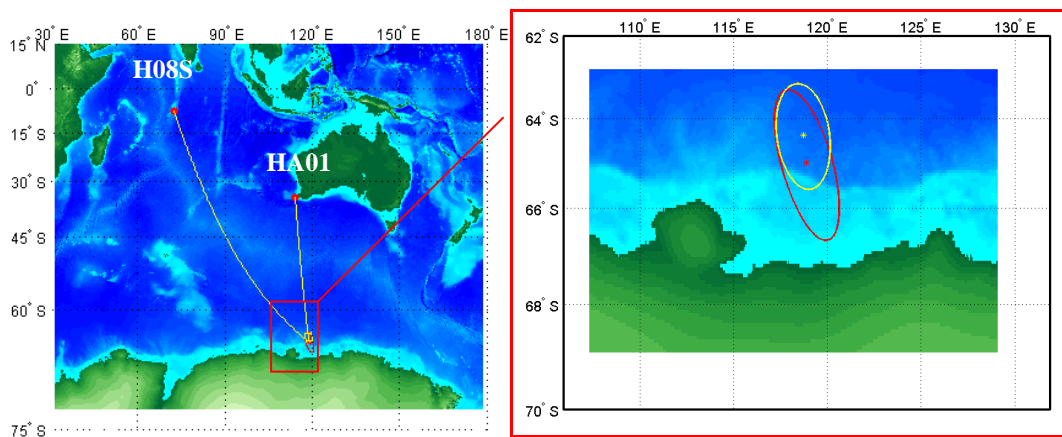


Figure 5.6. Ice event location (left panel) and a comparison of its errors (right panel) estimated for the location by triangulation from the HA01 and H08S stations (red) and for the location using the mode 1 frequency dispersion of the signal received only at HA01.

The error of the range estimation can also result from inaccuracy of numerical modelling, especially from the uncertainty of the sound speed profiles used for modelling. The monthly sound speed profiles derived from the objectively analysed and averaged oceanographic data are the mean values for each month averaged over the years and only reflect the large-scale spatial and long-term temporal variations of the acoustic propagation environment. Regarding the context of the long-range propagation in this study, we ignore the effects of smaller scale variations and only investigate the errors of range estimates due

to inadequate modelling of the sound speed profiles in terms of their large-scale variations. The left panel of Figure 5.7 shows the typical monthly sound speed profiles in the Southern Ocean beyond the ACZ, which clearly reveals that the near-surface acoustic propagation channel changes considerably with seasons. The deviation of range estimates from the original location shown in Figure 5.6 with the monthly change of the sound speed profiles used for modelling is shown in the right panel of Figure 5.7. The deviation of range estimates due to a wrongly chosen sound speed model along the acoustic path is significant. In this particular case, the maximum error is about 400 km, if the sound speed profiles typical for winter are used to estimate the range to this ice event which actually happened in summer. This takes place because the effect of near-surface ducting of acoustic propagation on frequency dispersion is considerably stronger in winter than in summer. Therefore it is essential to use the corresponding monthly sound speed profile when performing the range estimation for Antarctic ice events.

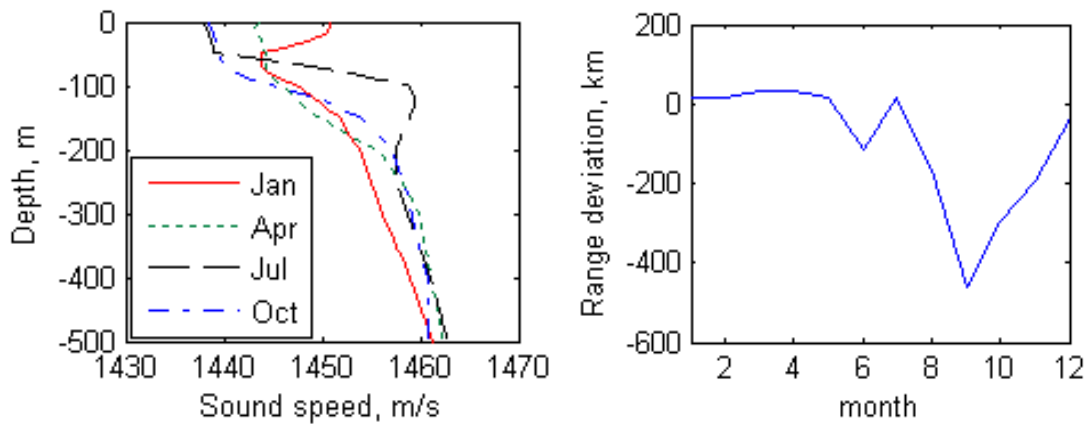


Figure 5.7. Left panel: the typical monthly sound speed profile in the top 500-m water layer in four different seasons in the Southern Ocean; Right panel: the error variation of the range estimates to the ice event obtained through frequency dispersion inversion of the mode 1 arrival at HA01 resulting from using different monthly climatology data. The error is calculated relative to the range to the location found by the intersection of two back-azimuths from HA01 and H08S.

The second case we will consider is the location of an Antarctic ice event observed at both HA01 station and Casey noise logger (see Chapter 3 for details of the Casey noise logger). The waveforms and spectrograms of the signals from this event recorded at HA01 and the noise logger are shown in the right panel of Figure 3.14. The time-frequency structure of the latest arrival of mode 1 within the frequency band from 5 Hz to 12 Hz and the time interval of about 3 seconds were used for range estimation from the HA01 station to this event. The location of the noise source was determined using the range estimate through inversion of frequency dispersion and the back-azimuth measurement from the HA01 station, which was 182.2° . The location obtained for the event, which occurred roughly at 180 km from the noise logger, was then verified by estimating the distance between the sound source and the noise logger, based on a comparison between the modelled and measured arrival structures of the signal received by the logger. The depth of a source of impulsive sound in the ocean can be determined from the travel time difference of the pairs of pulse arrivals with and without reflection from the sea surface near the source. For this particular event, the source depth was estimated to be about 350 m. The distance to the impulsive source can be estimated from the travel time differences between different multi-paths, if the sound speed profile and sea depth are known. Figure 5.8 shows a comparison of the measured and modelled relative arrival times of individual arrivals (left panel) and the arrival time differences of adjacent arrival peaks (right panel) for the distance from the source of 180 km. The modelled and measured values agree with each other quite well. Even after more than ten reflections from the sea surface and seafloor, the difference between the modelled and measured propagation times relative to the first arrival still remains less than one second for the distance between the logger and the estimated event location. The multipath arrival time differences between the adjacent arrival peaks in the modelled and measured signals are also in good agreement, although small deviations appeared on the curves. This case study provides further evidence that the location of an ice event, estimated through inversion of the frequency dispersion and back-azimuth measurements at a single receive station, is reasonably accurate.

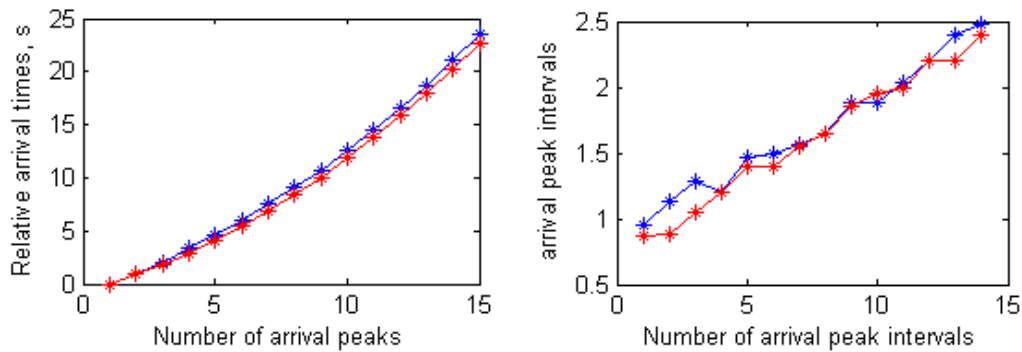


Figure 5.8. Comparison between the modelled (blue colour) and observed (red colour) relative arrival times of multipath arrivals (left panel) and the arrival time difference of adjacent arrival peaks (right panel). In the model, the distance from the sound source is assumed to be 180 km.

5.3.4 The limitation of ice event localization based on modal frequency dispersion

Not all signals from Antarctic ice events observed at the HA01 station reveal a distinct arrival of mode 1 with a broad frequency band as Figure 5.4 shows. Due to stronger coupling of the higher-order modes along the propagation path, some of the signals have a strong noise-like precursor preceding the final arrival of mode 1 and, therefore, the time-frequency arrival structure of mode 1 cannot be accurately determined using the method described in Section 5.3.1. Moreover, the frequency dispersion of mode 1 is weak over the shallow parts of the Antarctic continental shelf, as shown in Figure 3.10. Consequently, the location method proposed in this section has rather poor range resolution for the events located in the coastal shelf zone far from the continental slope.

5.4 Localization based on observed cut-off frequencies

As demonstrated experimentally in Chapter 2 and numerically in Chapter 3, the arrival pulse of mode 1 in the signals received at HA01 from Antarctic ice events has a low cut-off frequency. The majority of ice calving and breaking events are expected to produce broadband impulsive signals with spectra containing very low frequencies of a few Hz, so that the low frequency limit of the propagated signals is governed primarily by a limited

sea depth along the relatively shallow water section of the acoustic path over the Antarctic continental shelf. If the minimum sea depth along this section is estimated based on the cut-off frequency of mode 1, then the location of an ice event can be roughly determined by tracing the bathymetry profile along the acoustic path launched from HA01 at the measured back-azimuth angle. The cut-off frequency of the ice signals is estimated by identifying the lowest frequency component in the spectrum of the mode 1 arrival pulse. The spectrum is calculated for the initial 2.5-s long low-frequency section of the mode 1 arrival pulse identified in the spectrogram. The low cut-off frequency is determined at -3dB relative to the maximum spectral level.

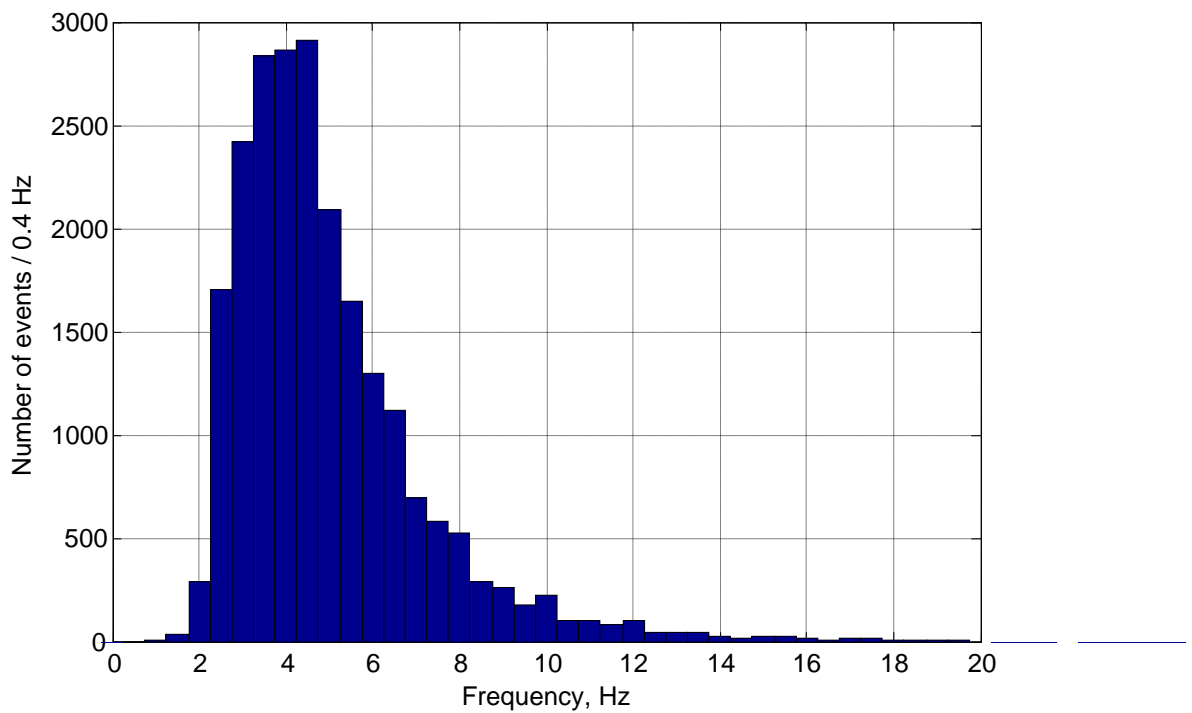


Figure 5.9. Histogram of the mode 1 cut-off frequency of the Antarctic ice events observed at HA01 over the period from late 2001 to 2005. The frequency bin size is 0.4 Hz.

The histogram of the cut-off frequencies of the Antarctic ice events observed at the HA01 station over the period from late 2001 to 2005 is shown in Figure 5.9. The majority of the cut-off frequencies are within the range from 2.5 Hz to 6 Hz. The cut-off frequency variation of the ice events received over the four years reveals little azimuth dependence, as demonstrated in Figure 5.10.

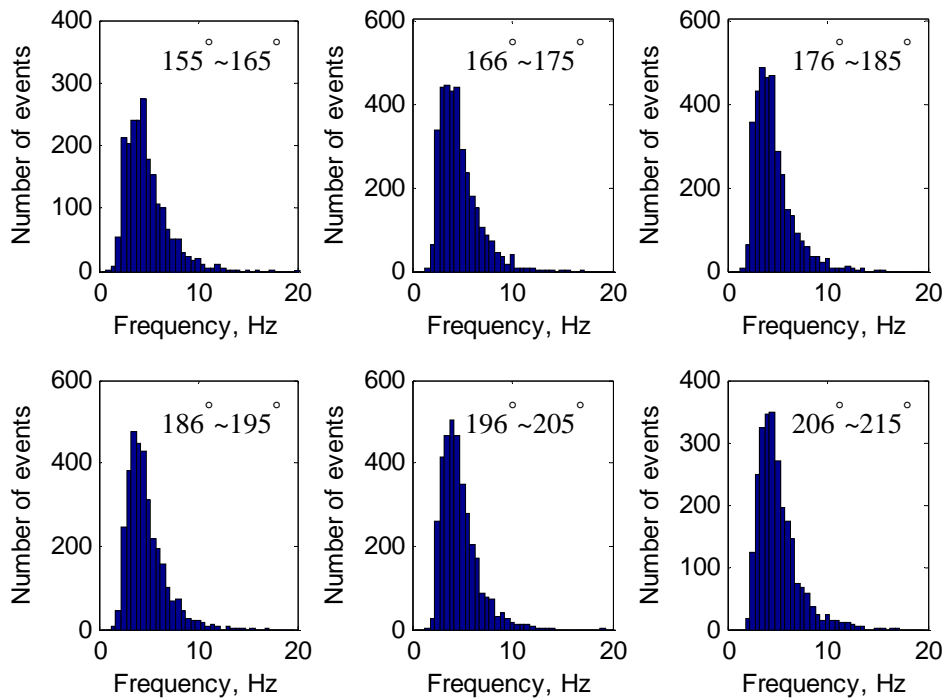


Figure 5.10. Histograms of the mode 1 cut-off frequencies of the ice events observed at HA01 within different back-azimuth sectors (shown in each panel) over the period from late 2001 to 2005. The frequency bin size is 0.4 Hz, the same as the frequency resolution of estimated values.

A Pekeris model of the ocean acoustic waveguide with a pressure-released sea surface and fluid bottom is used to estimate the sea depth that corresponds to the measured cut-off frequency. This simplified approach for sea depth estimation using measured cut-off frequency was verified based on numerical modelling regarding the Antarctic coastal shallow water region with surface acoustic propagation channel. The cut-off frequency of mode m f_{0m} in the Pekeris waveguide model is given by Jensen et al. (2000):

$$f_{0m} = \frac{\omega_{om}}{2\pi} = \frac{(m-0.5)c_1c_2}{2D\sqrt{c_2^2 - c_1^2}} \quad (5.9)$$

where D is the sea depth, c_1 is the sound speed in water and c_2 is the speed of compressional waves in the seafloor modelled as a half-space basement. The sea depth D can be obtained, if c_2 is known. In this analysis, the sound speed in the water column c_1 was set to be 1450 m/s. Three different values of the sound speed c_2 in the bottom were examined, which were: 1) 1650 m/s – soft sediment model; 2) 1800 m/s – sound speed at the top interface of the upper sediment layer in the acoustic model of the seafloor chosen for numerical modelling of acoustic propagation from Antarctica and 3) 3000 m/s – hard bottom, i.e. rock.

The majority of sea depth estimates from the mode 1 cut-off frequency of the ice signals observed at HA01 are less than 300 m for the soft model of the seafloor, as shown in the top panel of Figure 5.11. For the basic acoustic model of the seafloor of intermediate hardness used for numerical modelling of acoustic propagation in Chapter 3, the sea depth estimates from the cut-off frequency are about 50 m smaller than those for the soft bottom model. If the bottom is hard with the sound speed of 3000 m, then the most frequent estimates of the sea depth based on the mode 1 cut-off frequency lie below 150 m. This result implies that most of the ice events detected at the HA01 station occur in the relatively narrow Antarctic coastal zone with sea depths of 150-300 m. Consequently, the spatial analysis of the occurrence of Antarctic ice events can be carried out using only the back-azimuth data for the ice events observed at the HA01 station.

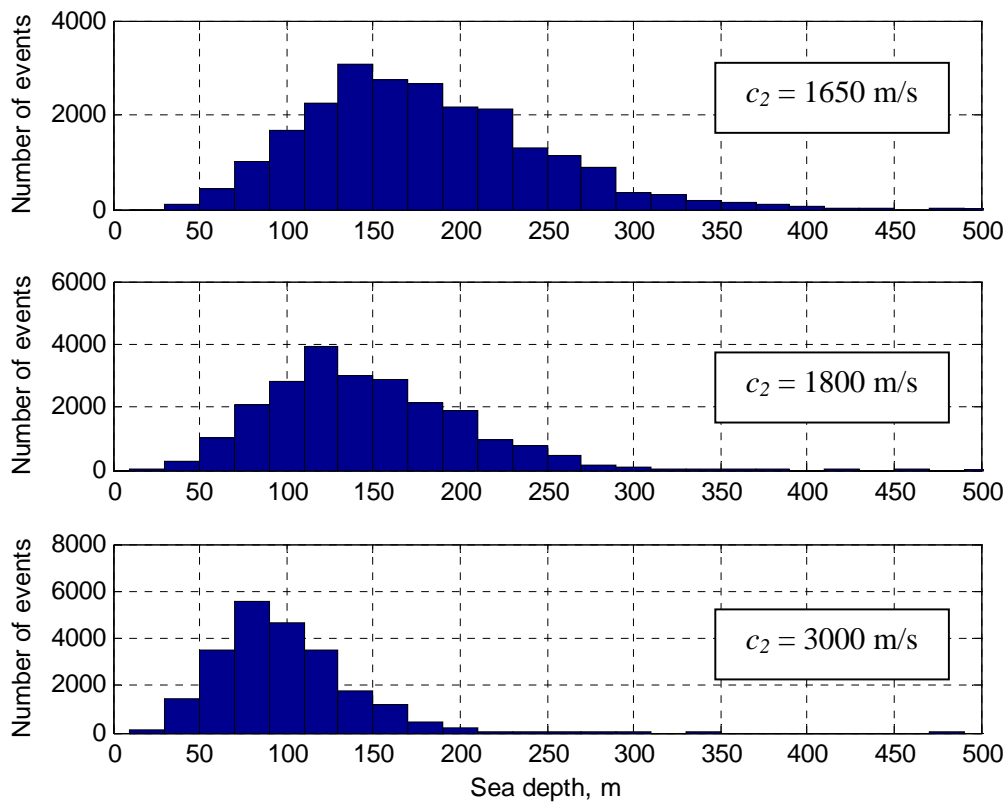


Figure 5.11. Histograms of the minimum sea depth along acoustic paths from ice events to HA01 derived from the mode 1 cut-off frequency of the ice signals received at HA01 over the period from late 2001 to 2005. Sea depth estimates are made for the soft (top panel), intermediate (middle panel) and hard bottom acoustic models. The depth bin size is 20 m.

5.5 Concluding remarks

Three different approaches to localize Antarctic ice events using either the two IMS stations in the Indian Ocean or only HA01 were considered in this Chapter. The localization of individual Antarctic ice events detected at both HA01 and H08S stations can be directly achieved by the intersection of the two geodesics launching from the two receive stations at the measured back-azimuth angles. The accuracy of such localization can be verified by comparing modelled and measured arrival time differences of the signals from the same ice event observed at the two stations.

Antarctic ice events can also be located using the back-azimuth measurement of a signal arrival at one receive station, i.e. HA01, and an estimate of the range to the sound source based on the LMS fitting of the measured and modelled frequency dispersion characteristics of the mode 1 arrival at this station. The uncertainty of localization based on the dispersive time-frequency arrival structure is comparable to errors of location by triangulation from the two stations. This approach is applicable only to the signals in which the mode 1 arrival pulse and its frequency dispersion characteristic are not significantly distorted by mode coupling along the path from Antarctica to the HA01 station.

By measuring the cut-off frequency of mode 1 in the signals from the ice events observed at the HA01 station, it was found that the majority of these events occurred in relatively shallow water over the Antarctic continental shelf at sea depths less than 300 m. Therefore the location of Antarctic ice events can be roughly determined by projecting the back-azimuth of signal arrivals measured at HA01 onto the Antarctic coastline.

CHAPTER 6

SPATIAL DISTRIBUTION ANALYSIS OF ANTARCTIC ICE EVENTS

6.1 Overview

The aim of this chapter is to analyse the spatial distribution of Antarctic ice events detected at the HA01 station and its association with Antarctic geographic or ice-related features. Also investigated are the effects of the propagation loss from Antarctica to HA01 on the spatial distribution of the detected events.

As shown in Chapter 5, the majority of Antarctic ice events observed at HA01 occur in relatively shallow water in the Antarctic coastal zone with sea depths of 150 – 300 m. Therefore, the location of those events can be roughly estimated by projecting the back-azimuth from the HA01 station onto the Antarctic coastline. Accordingly, the spatial distribution of Antarctic ice events is analysed in section 6.2 using the back-azimuths to these events measured at the HA01 station. The detection frequency of ice events is noticeably larger within a number of separate back-azimuth sectors. These sectors are attempted to be associated with some Antarctic geographic and ice-related features, such as glaciers, ice shelves and iceberg tongues. The consistency of the spatial distribution of ice events is examined by a comparison of the distributions observed in each year during the 6-year observation period from 2002 to 2007.

The propagation loss from different parts of the observed Antarctic coastal zone to HA01 can be noticeably different. This would potentially affect the sound level of the signals from ice events received at HA01 at different back-azimuth angles and, consequently, the number of events with the SNR high enough to be detected. As a result, the spatial distribution of ice events observed at HA01 can also be affected by the variation of the propagation loss with back-azimuth angle. This issue is considered in Section 6.3. Conclusions to this chapter are made in Section 6.4.

6.2 Spatial distribution of the ice events observed at HA01

All of the ice events detected at HA01 over a 6-year period from late 2001 to early 2008 were used to analyse their spatial distribution. The back-azimuth angles to these events were measured using the corrected relative positions of the three hydrophones of HA01 as discussed in Chapter 4.

The angular distribution of all detected ice events is shown in Figure 6.1 by a histogram of the back-azimuth angles measured at the HA01 station. The distribution reveals strong clustering of events. The number of events observed within several relatively narrow angular sectors is considerably larger than that within adjacent angular sectors. These angular sectors will be referred to as event clusters. Because there is no significant blockage of the acoustic paths by ocean ridges or islands within the sector of Eastern Antarctica observed from HA01, as illustrated in Figure 2.2, these clusters are most likely related to the Antarctic coastal areas where ice break up processes are more active.

Figure 6.2 shows the spatial variation in the number of ice events along the Eastern Antarctic coastal zone derived by projecting the measured back-azimuth bearing from the HA01 station onto the Antarctic coastline. The geographic and ice-related features, which correspond to the event clusters in the back-azimuth distribution are listed in Table 6.1. It was noticed that some of the clusters in the spatial distribution could be immediately associated with the Antarctic glacial features, such as ice shelves and iceberg tongues. For example, the Dibble Iceberg Tongue, which is known as origin of many newly calved icebergs, is observed from HA01 within the back-azimuth sector of Cluster 3. The direction to the Dalton Iceberg Tongue corresponds to Cluster 4. The Shackleton Ice Shelf is the main dynamic glacial feature within Clusters 6 and 7, as is the West Ice Shelf in Cluster 8. The most frequent ice events are located in the direction to Law Dome, which is a massive inland glacier east of Casey, Australian Antarctic station (66.26°S, 110.53°E). Clusters 2 and 9 correspond to relatively broader coastal regions at the two outermost parts of the observed Eastern Antarctic coast. The ice-related features, which could be associated with

the ice events observed within the corresponding sectors, are not identified. The back-azimuth sectors of Clusters 1 and 10 do not include the Antarctic coastline. The ice events observed within these sectors are most likely ice break up processes on icebergs drifting in the surrounding ocean north of the Ross Ice Shelf to the eastern edge of the observed sector and north of Enderby Land to the west.

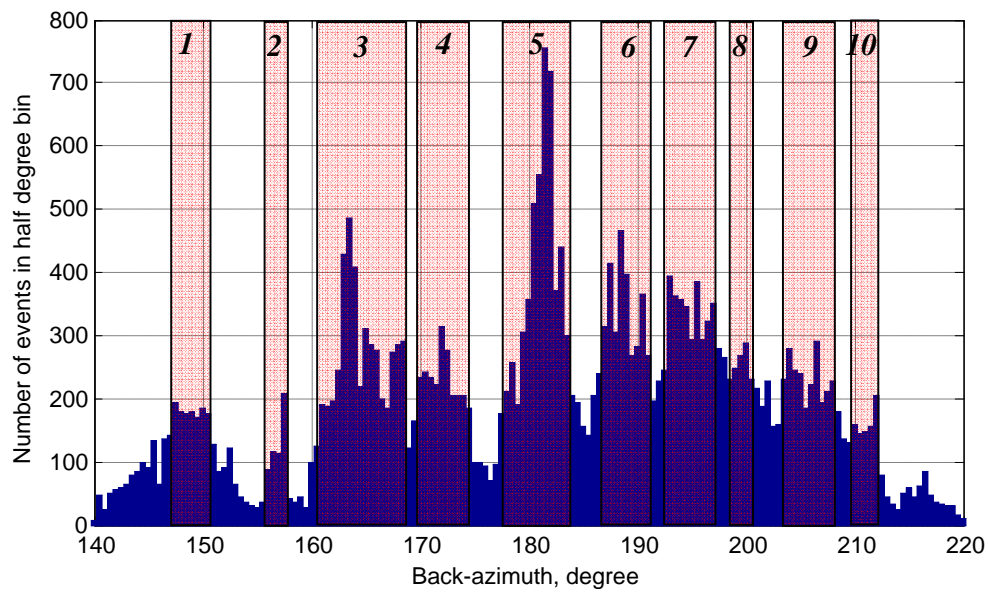


Figure 6.1 Histogram of the back-azimuth to the ice events observed at the HA01 station over the whole period from late 2001 to early 2008. The histogram bin width is half a degree. The vertical bars with numbers superimposed on the histograms indicate the clusters of most numerous ice events.

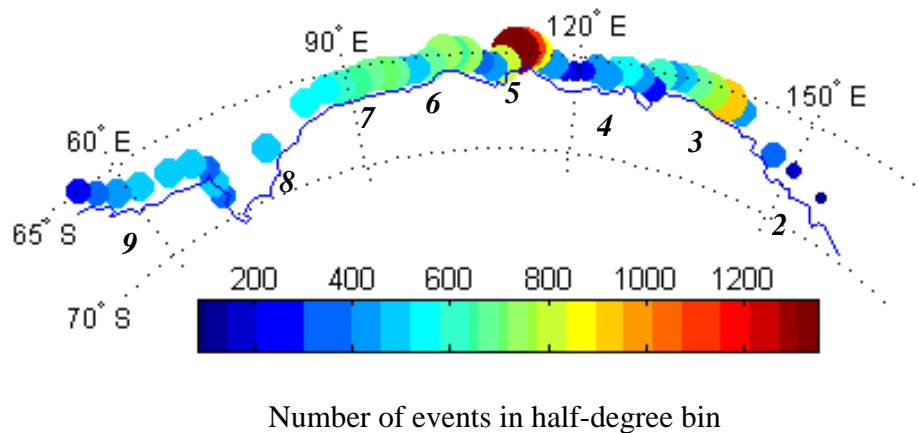


Figure 6.2. The spatial distribution of ice events along the Eastern Antarctic coastline represented by projecting the events back-azimuths shown in Figure 6.1 onto the Antarctic coastline. The number of events observed in one azimuth bins is indicated by size and colour-coded dots.

The consistency of the spatial distribution of ice events is examined by a comparison of the histograms of back-azimuth to the ice events detected in each year from 2002 to 2007, as presented in Figure 6.3. The number of ice events that occurred in each year in any particular half-degree back-azimuth sector varies considerably over the six years. However, the back-azimuth distributions for these six years reveal some similarity in the clusters of more frequent events indicated by the same vertical bars as those in Figure 6.1. Clusters 1 to 5 can be recognized in each of the annual histograms. This indicates that the Antarctic glacial features and icebergs in the five corresponding Antarctic coastal areas were consistently more active with respect to ice breaking or rifting events than the other areas in this six-year period. Clusters 6 and 7, which correspond to the directions to the western and eastern parts of the Shackleton Ice Shelf, consistently demonstrate a high occurrence of events and merge with each other in the annual histograms for some years. Cluster 8 is not distinguishable in most of the annual histograms, except for a spike of high event occurrence clearly seen in the corresponding back-azimuth sector in the histogram for 2006. This spike most likely resulted from a series of multiple ice break-ups that occurred on the ice shelf or iceberg north of the Amery Ice Shelf. Clusters 9 and 10 cannot be

distinguished in the annual histograms in contrast to that for the whole 6-year period of observation.

Table 6.1 Back-azimuth sectors of the clusters of more numerous ice events, the longitudes of the Antarctic coastline corresponding to the edges of these sectors, and the Antarctic ice-related features observe within these sectors.

Cluster number	Back-azimuth ($^{\circ}$)	Longitude ($^{\circ}$)	The Antarctic geographic or ice-related features
1	~147-151	N/A	Icebergs drifting north of the Ross Ice Shelf
2	156-158	~150-165	Little, Rennick and Matusевич Glaciers; Cook Ice Shelf.
3	~161-169	~130-143	Glacier de la Zelee, Glacier de l' Astrolabe, Glacier du Francais, Pourquoi Pas Glacier; Dibble and Blodgett Iceberg Tongues.
4	~170-174	~122-127	Dalton Iceberg Tongue and Voyeykov Ice Shelf;
5	~177-183	~110-118	Law Dome; Adams, Bond, Peterson, Vanderford and Totten Glaciers;
6	~187-191	~101-106	Eastern part of the Shackleton Ice Shelf;
7	~193-197	~90 - 97	Western part of the Shackleton Ice Shelf; Helen, Northcliffe and Denman Glaciers.
8	~199-201	~70 - 85	Amery Ice Shelf and Polar Record Glacier.
9	~204-208	~55-71	Wilma and Robert Glaciers.
10	~210-212	N/A	Icebergs drifting north of Enderby Land

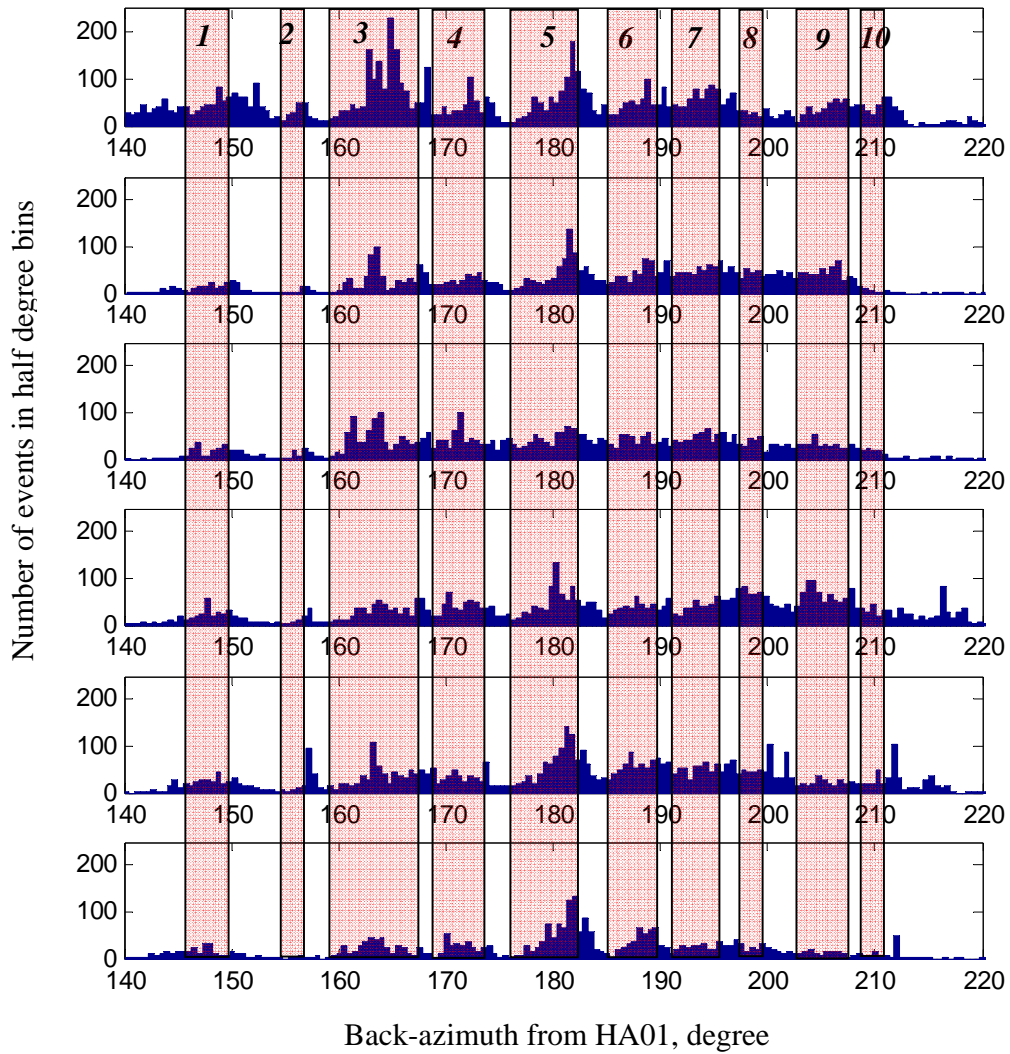


Figure 6.3. Histograms of the back-azimuths to the Antarctic ice events observed at the HA01 station in each year from 2002 (top panel) to 2007 (bottom panel). The azimuth bin width of the annual histograms is half a degree. The vertical bars of the event clusters are the same as those in Figure 6.1.

6.3 Azimuth dependence of the propagation loss from Antarctica to HA01

The environmental conditions along the acoustic propagation paths from different regions of the Antarctic coastal zone to the HA01 station vary, so that they depend on back-azimuth to each region observed from the station. This variation potentially causes an azimuth dependence of the transmission loss of the acoustic signals from ice events observed at HA01 and, consequently, may affect the detection rate of ice events. Therefore, the spatial distribution of the Antarctic ice events shown in Figure 6.1 may also be distorted by the effect of transmission loss variation.

Based on the results of numerical modelling discussed in Chapter 3, the transmission loss of low-frequency signals along the acoustic path from Antarctica to HA01 consists of three major components, which are 1) the transmission loss due to cylindrical spreading along the whole propagation path, 2) the loss induced by sea surface scattering in the near-surface acoustic channel in the Polar environment south of the ACZ and 3) the loss due to acoustic attenuation in the seafloor along the initial section of the acoustic paths in relatively shallow water over the Antarctic continental shelf. For mode 1 dominating in the signals from ice events observed at HA01, the total transmission loss along the propagation path to HA01 can be roughly approximated as:

$$TL \approx 10\log(R) + \bar{\alpha}_{sc}r_{po} + \bar{\alpha}_br_{sh} \quad (6.1)$$

where R is the distance from the source to the receiver, $\bar{\alpha}_{sc}$ is the average attenuation coefficient of mode 1 along the polar section of the propagation path of length r_{po} , and $\bar{\alpha}_b$ is the average attenuation coefficient of mode 1 along the shallow water section of length r_{sh} over the Antarctic continental shelf. The distance from the Eastern Antarctica coastline to the HA01 station varies from 3,400 km to 5,000 km, which results in a maximum difference in the transmission loss due to cylindrical spreading of less than 2 dB for the entire sector of observation. According to numerical modelling results, the attenuation coefficient of mode 1 at frequencies below 10 Hz due to sea surface scattering in the Polar environment does not exceed 10^{-4} dB/km if the sea surface is free of ice and the RMS height of surface waves is below 5 m. The section of the propagation paths from the

observable Eastern Antarctic coastline to HA01, which lies in the polar environment south of the ACZ, varies from 1,700 km to 3,500 km for the central and outermost parts of the observed sector respectively. Therefore, the maximum difference between the transmission losses of mode 1 at 10 Hz due to scattering by surface waves along the longest and shortest paths from Antarctica to HA01 should not exceed 1 dB. This means that the total effect of cylindrical spreading and sea surface scattering on the difference in the transmission losses along different paths from Antarctica is expected to be less than 3 dB.

The length of the shallow water section of the propagation paths from the Antarctic coast over the continental shelf varies considerably according to local bathymetry. However, there is no general trend in the variation of this length with back-azimuth from HA01. Taking into account that the most common low cut-off frequency of mode 1 and, consequently, the sea depth at the event locations do not vary noticeably with back-azimuth, as shown in Figure 5.11, one can expect that spatial changes in the transmission loss due to acoustic attenuation in the seafloor over the Antarctic continental shelf should not cause noticeable trends in the variation of the total transmission loss with back-azimuth to the ice events observed at HA01.

This assumption of weak dependence of the transmission loss of the ice signals on their back-azimuth from HA01 can be examined by analysing changes in the level of signals received in different directions. Figure 6.4 shows the mean value and the standard deviation of the signal level of ice events as a function of back-azimuth observed at HA01 in the polar summer and winter seasons over the six-year period from 2002 to 2007. All signals were binned into five-degree bins according to the measured back-azimuth. The winter season includes August and September when the sea ice extent approaches its maximum. The summer season includes February and March with the minimum ice extent.

The signal-plus-noise RMS amplitude A_{SN} was measured in a 0.5-s window around the maximum signal amplitude in a frequency band of 3-30 Hz. The noise RMS amplitude A_N was measured in the same frequency band. The signal level was calculated as:

$$SL = 10 \log_{10} (A_{SN}^2 - A_N^2) \quad (6.2)$$

It is clearly seen in Figure 6.4 that the azimuth dependence of the signal level is much less significant than the seasonal variation. There is a gentle negative trend in the winter signal level toward the western part of the observed sector. In summer, the plot does not reveal any significant trend in the mean signal level with back-azimuth. On the other hand, the seasonal change in the signal level is as large as nearly 6 dB. If we assume that the source level of ice events does not change on average with seasons, which is not quite evident, then the seasonal variation of the signal level could be explained only by the effect of changes in the transmission loss due to scattering from the ridged sea ice cover which has the maximum extent in winter. The effect of ice scattering was not included in the numerical model of acoustic propagation from Antarctica, mainly because the roughness characteristics of Antarctic sea ice were poorly known. However, it is known from several acoustic propagation experiments in the Arctic Ocean, that scattering from ridged sea ice is the major factor affecting the transmission loss in the polar environment (LePage and Schmidt, 1994). The correlation between the signal level and sea ice extent in Antarctica will be considered in the next chapter.

Based on the transmission loss estimates and signal level measurements, the variation of the transmission loss along the acoustic propagation paths from different parts of the observed sector of Eastern Antarctica to HA01 is small such that it should not significantly affect the detection rate of ice events located in different directions from HA01.

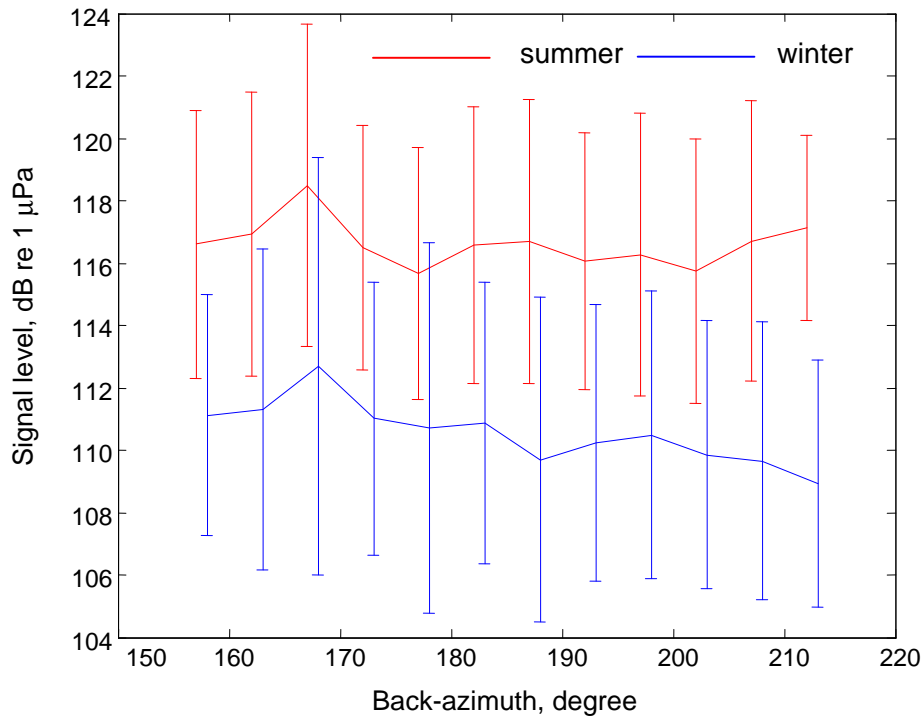


Figure 6.4. Mean value and standard deviation of the signal level versus the back-azimuth of the Antarctic ice events observed at HA01 in summer (red) and winter (blue) over the six-year period from 2002 to 2007. The frequency band of measurements is 3-30 Hz.

6.4 Concluding remarks

In this chapter, the spatial distribution of Antarctic ice events was analysed based on the back-azimuths to the events measured at the HA01 station. Potential effects of different transmission losses along different acoustic paths from Antarctica on the detection rate of ice events in different directions to the sector of Eastern Antarctica observed at HA01 were also considered.

It was found that the majority of ice events were observed within a number of back-azimuth sectors which corresponded to the directions to several glacial features on the Eastern Antarctica coast, such as Dibble and Dalton Iceberg Tongues, Shackleton Ice Shelf and glaciers around Law Dome. The Antarctic continental shelf areas near these features have consistently been origins of more frequent ice events observed at HA01 over the six-year period from 2002 to 2007. It was also concluded that the variation of the transmission loss along different acoustic paths from Antarctica should not strongly affect the spatial distribution of ice events detected at the HA01 station.

CHAPTER 7

TEMPORAL VARIATIONS OF THE OCCURRENCE OF ANTARCTIC ICE EVENTS

7.1 Overview of the chapter

Long-term variations in the occurrence of Antarctic ice events detected at the HA01 station are analysed in this chapter along with their correlation with several climate-related meteorological and oceanographic (metocean) characteristics of the Eastern Antarctic coastal zone and the surrounding parts of the Southern Ocean.

Long-term changes in the frequency of occurrence of ice events over the six years of observation are analysed in Section 7.2 in both time and frequency domains using various data processing techniques. Section 7.3 investigates correlation between the variation of the occurrence frequency and seasonal changes in the Eastern Antarctica metocean characteristics, such as the sea surface temperature, air temperature, wind speed in the coastal zone and Antarctic sea ice extent. The long-term variation of the intensity of signals from the ice events observed at HA01 is also analysed in this section and compared with that of the occurrence frequency. Section 7.4 concludes the chapter.

7.2 Variations of occurrence of ice events

The frequency of occurrence of the ice events detected at HA01 was analysed in both time and frequency domains to look for seasonal oscillations and interannual trends.

The number of ice events detected weekly at the HA01 station during the 6-year period from late 2001 to early 2008 is shown in Figure 7.1 as a function of day number since 01/01/2002. Seasonal cycles can be recognised even in this unfiltered series of the occurrence frequency. However, the time series of the ice event occurrence in one week

bins is too noisy to clearly see the seasonal variation and to determine the period of oscillations.

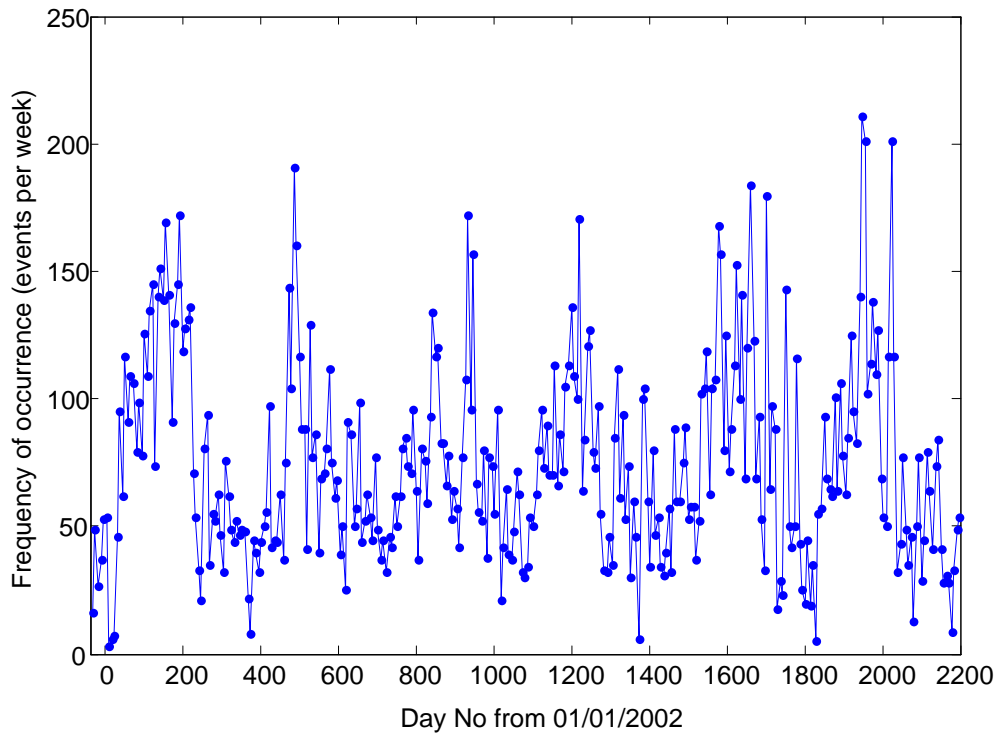


Figure 7.1. Unfiltered variations of the weekly occurrence frequency of ice events detected at the HA01 station over the 6-year period from late 2001 to early 2008.

Long-term variations in the weekly occurrence frequency can be extracted through denoising the unfiltered time series by a low-pass median filter, i.e. by calculating the median value in a sliding time window of a certain length (Pratt, 1991). The selection of the window length is based on the time scale of variations to be examined. Figure 7.2 shows the weekly occurrence frequency median filtered with a time window of 8 weeks. The filtered time series of the weekly occurrence frequency reveals strong seasonal variations, although considerable interannual change is also present in the amplitude of the seasonal cycles.

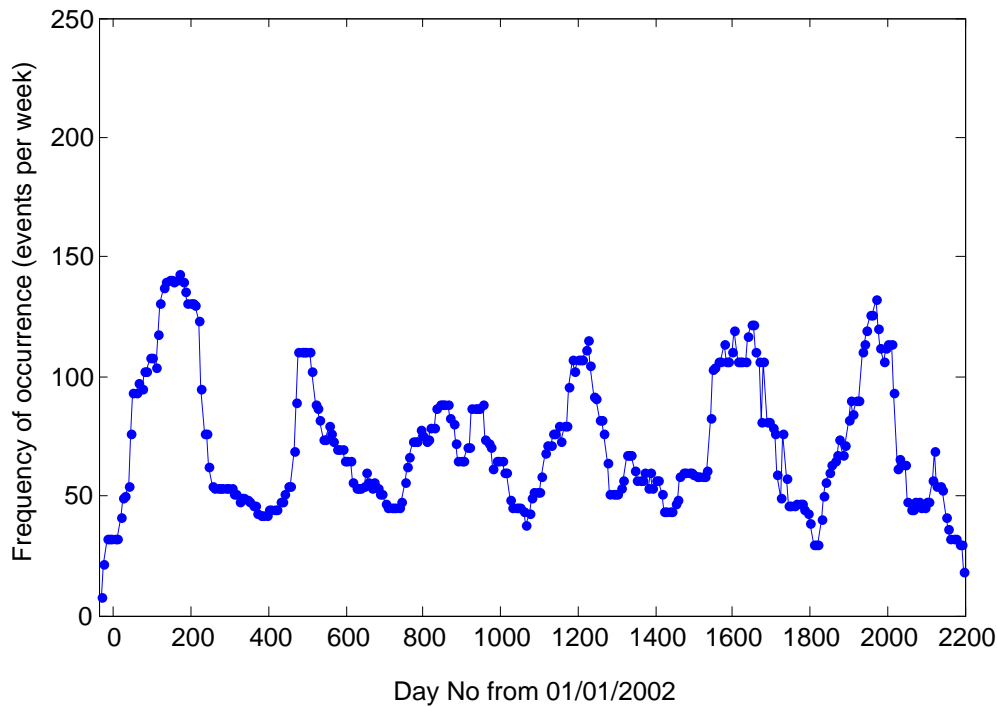


Figure 7.2. Median filtered variation of the weekly occurrence frequency of Antarctic ice events detected at HA01 over the 6-year period from late 2001 to early 2008. The window length of the median filter is 8 weeks.

Hidden periodicities in a relatively short and noisy time series can be found using Periodicity Transforms (PT) (Sethares and Staley, 1999). The PT method searches for a minimum set of periodic nonorthogonal functions (basis) into which the original time series can be decomposed, unlike the Fourier transform and the wavelet transform which use predetermined bases and decompose time series in the frequency and scale domains respectively.

The PT analysis based on the best frequency algorithm (Sethares and Staley, 1999) was applied to the time series of the weekly occurrence frequency centred to zero mean. The periodic basis function of the maximum power, which contributes most to the variation in the time series of the occurrence frequency, is shown in Figure 7.3 after correction for the mean value. This basis function has a period of 53 weeks, i.e. about one year, and corresponds to the seasonal variation in the frequency of occurrence of ice events. The

frequency of occurrence reaches its maximum of about 150 events per week in mid April and drops to its minimum of less than 50 events per week in November. The shape of the seasonal variation derived from the PT analysis is substantially asymmetric and distorted, most likely, by short-term fluctuations in the time series.

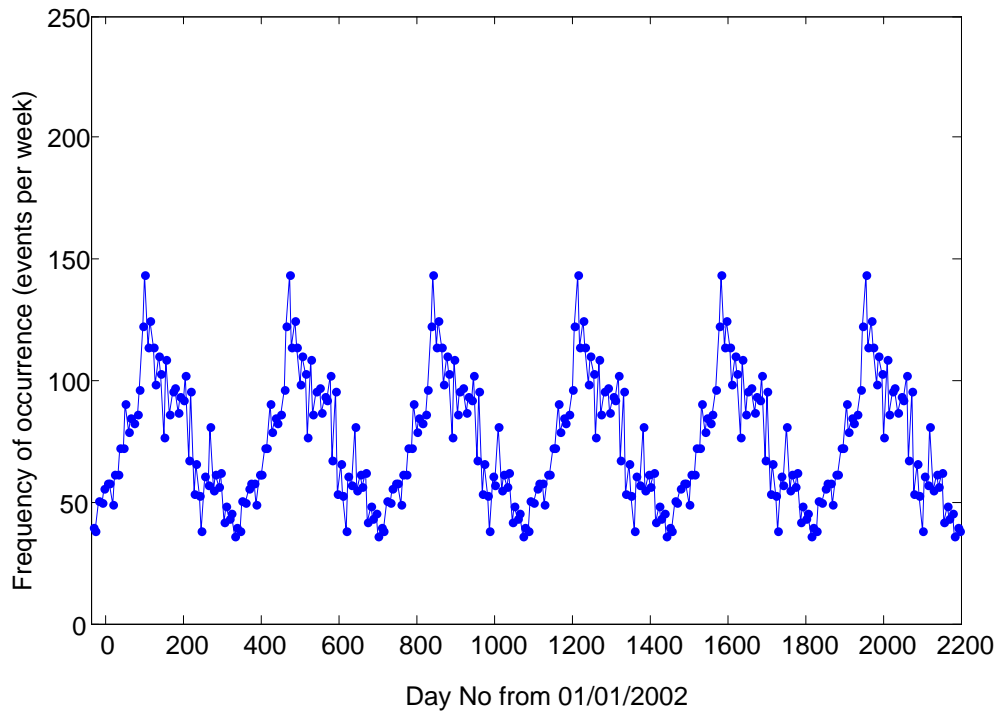


Figure 7.3. The principal basis function of the periodicity transform applied to the occurrence frequency variation shown in Figure 7.1. The mean value of the whole time series is added to the basis function in the plot. The period of this function is 53 weeks.

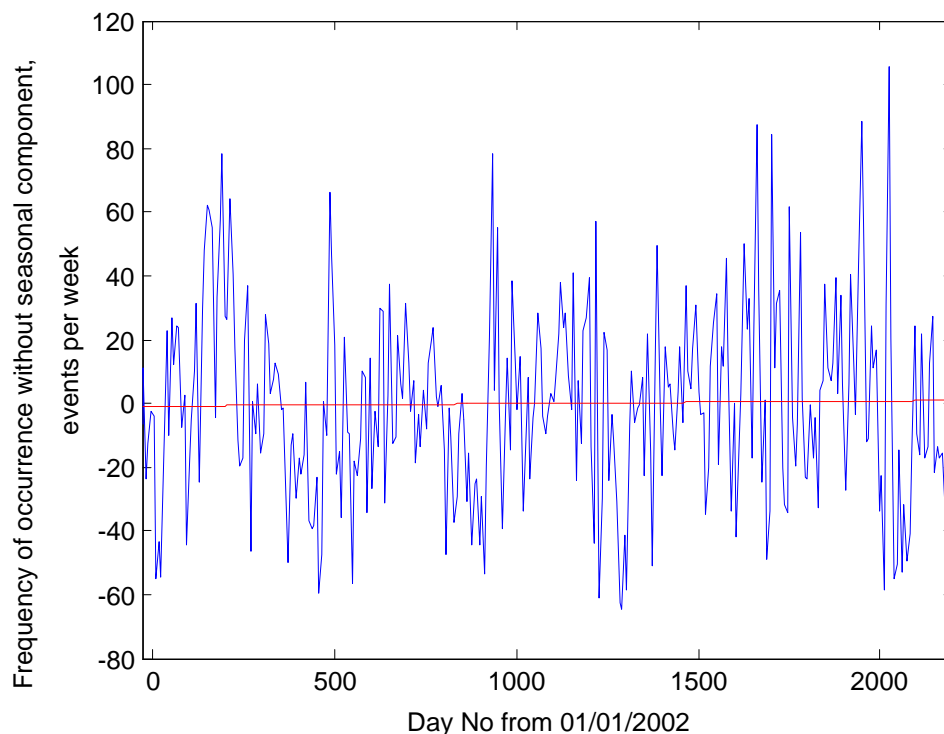


Figure 7.4. The residual variation of the occurrence frequency without the seasonal component (blue line) obtained by subtracting the principal periodic basis of the periodicity transform shown in Figure 7.3 from the original time series shown in Figure 7.1. The red line shows the linear fit to the residual variation.

By subtracting the principal basis function of the periodicity transform from the weekly average occurrence frequency of ice events shown in Figure 7.1, the contribution of the seasonal component to the total variations can be significantly lessened. This residual variation is shown in Figure 7.4. To examine the occurrence frequency for gradual interannual trend, a linear fit to the residual variation was calculated. This fit shown by the red line in Figure 7.4 demonstrates that no interannual trend of significant value is apparent from the 6-year time series of occurrence frequency variations.

The presence of a strong seasonal component in the variation of the occurrence frequency of ice events can also be examined by spectral analysis. Power spectra of the unfiltered time

series of the weekly occurrence frequency were calculated using a conventional periodogram method and a high-resolution eigenvector method (Stoica and Moses, 1997). The resulting spectra are shown in Figure 7.5 normalised to unity peak value. The frequency is represented in cycles per year (365 days) for clarity. Both power spectra have major peaks at a frequency of exactly one cycle per year, which corresponds to the seasonal variation. Another spectral peak of much lower amplitude is seen in both spectra at about 4 cycles per year, which results from an asymmetry of the seasonal cycle

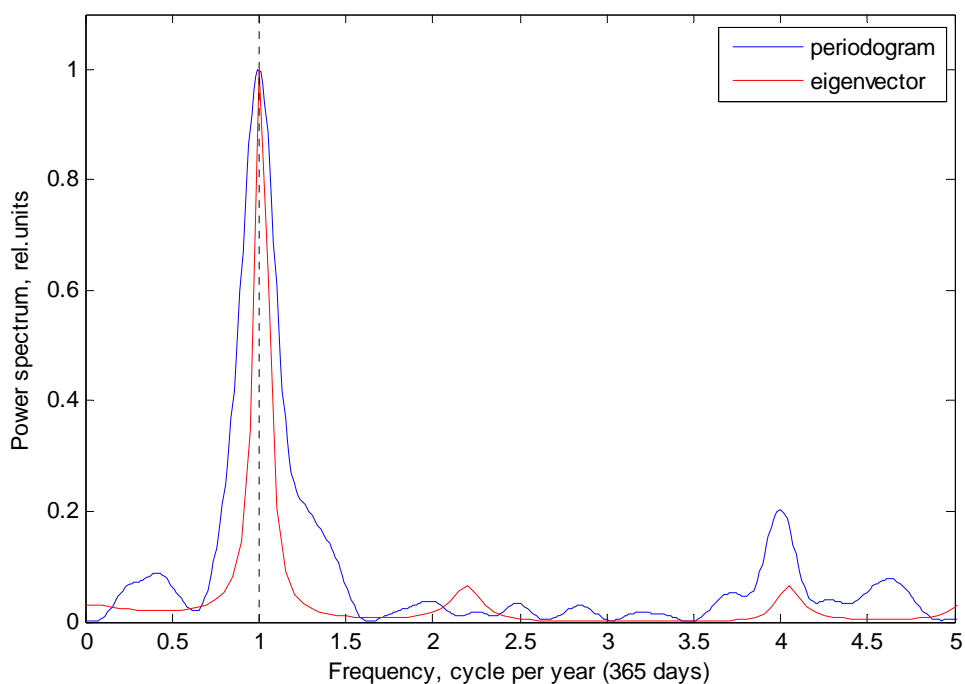


Figure 7.5. Power spectra of the temporal variation in the occurrence frequency of ice events detected at the HA01 station over the 6-year period from late 2001 to early 2008, estimated by periodogram (blue line) and eigenvector (red line) methods.

The observation of regular seasonal cycles means that the long-term variations in the occurrence of Antarctic ice events are most likely driven by the seasonal variations in the climate-related meteorologic and oceanographic characteristics of the Eastern Antarctic coastal zone and the surrounding Southern Ocean. This will be investigated in the next section.

7.3 Correlation between the occurrence frequency of ice events and metocean characteristics of Eastern Antarctica

This section investigates correlation and, in particular, time delay between the variations of the occurrence frequency of ice events and climate-related metocean characteristics in Eastern Antarctica. To reduce the influence of noise from short-period random fluctuations, the correlation was calculated for the time series of the occurrence frequency low-pass filtered with the median filter as shown in Figure 7.2. The temporal variation of the signal level from the ice events measured at HA01 and its correlation with the occurrence frequency and metocean characteristics is also investigated in this section. Physical interpretations of the correlation between the results of remote acoustic observations and metocean characteristics are suggested when possible.

Julian day 1 was used as a reference day to estimate the time delay or phase shift in the seasonal variation of each acoustic and metocean characteristic compared to the reference annual cycle, which was modelled as $\cos(2\pi t[\text{day number}]/365)$, i.e. as a reference harmonic function with the maximum at 00:00 1 January. The leap day in 2004 was ignored in the reference function taken for the whole 6-year period.

The cross-correlation between the occurrence frequency of ice events and the annual cycle is shown in Figure 7.6. It is seen from this plot that the seasonal cycle in the variation of the occurrence frequency is delayed by about 20 weeks (~4.5 months) relative to the annual cycle. In other words, the maximum occurrence frequency occurs in April – May period.

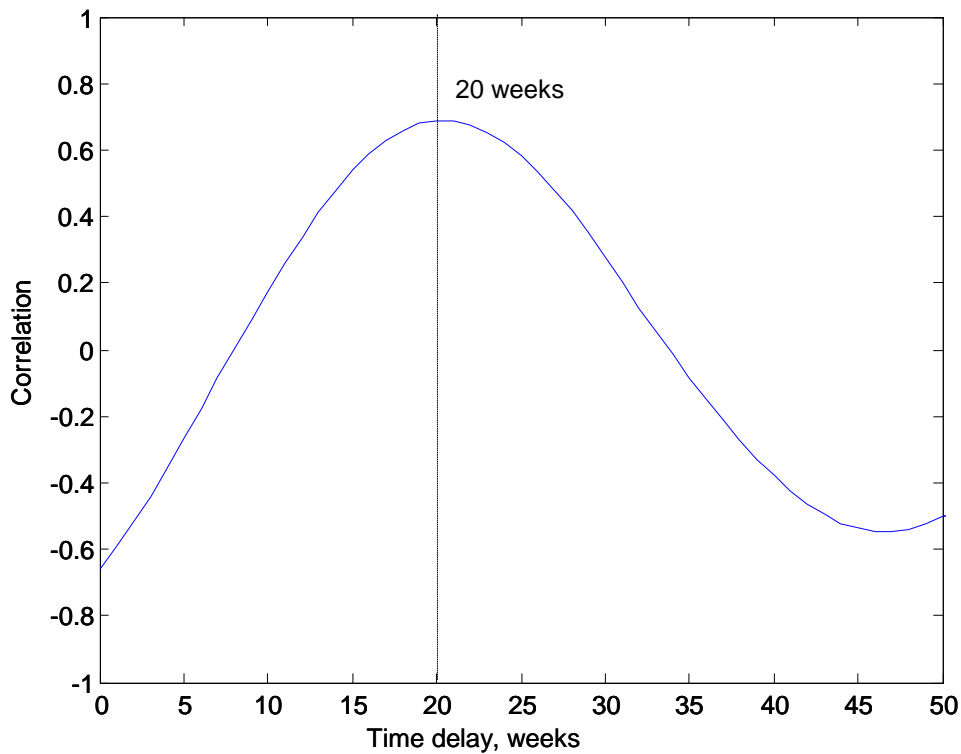


Figure 7.6. Fragment of the cross-correlation between the occurrence frequency of ice events and the annual cycle, taken around its maximum. The cross-correlation plot shows that the occurrence frequency correlates with the annual cycle with a 20-week time lag.

7.3.1 Sea surface temperature

The sea surface temperature (SST) data were taken from the monthly climatology data of the World Ocean Atlas 2005. The area for calculating the average SST and its seasonal variation was the coastal zone from 63°S to 65°S and from 60°E to 160°E in the Southern Ocean south of the Eastern Antarctic coast observed from HA01,. Figure 7.7 shows the monthly SST averaged over the coastal zone. The spatially averaged monthly SST data were interpolated onto a 1-week grid and then replicated to obtain a 6-year time series. Figure 7.8 shows the cross-correlation between the occurrence frequency of ice events and the average SST of the Eastern Antarctic coastal zone. The time delay of the maximum cross-correlation is about 13.5 weeks, which means that the occurrence frequency reaches its maximum 13.5 weeks later than the SST, which is a significantly longer lag than the time delay of one month estimated by Hanson and Bowman (2006) based on a 1-year data

set collected at HA01 in 2003. Accordingly, the seasonal variation of SST has a 6.5-week lag relative to the reference annual cycle.

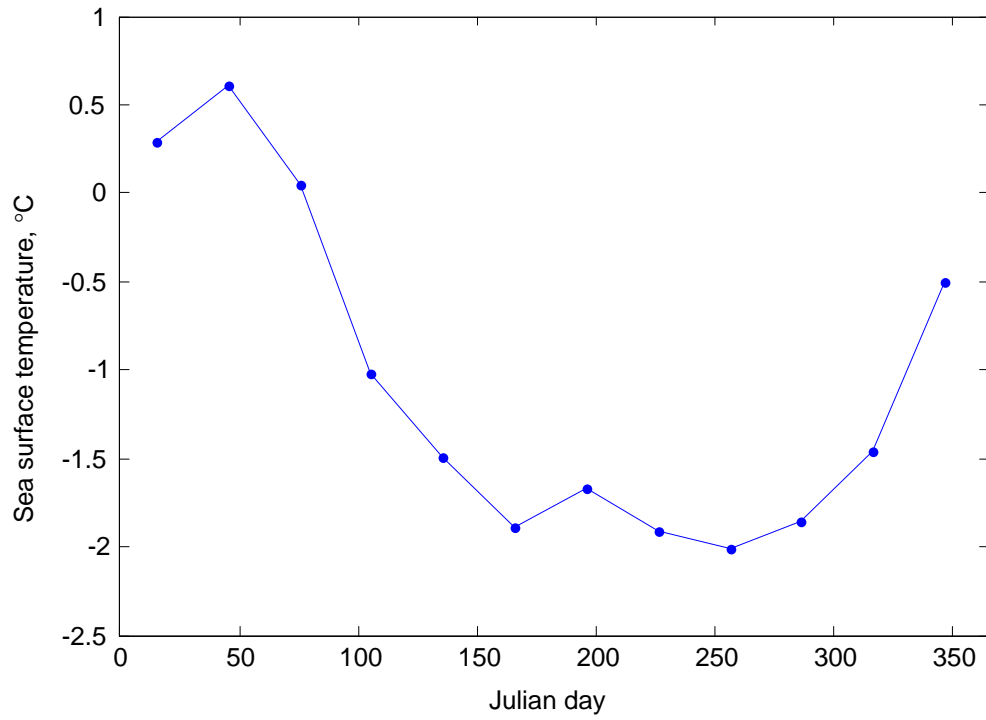


Figure 7.7. Monthly climatology SST averaged over the Eastern Antarctic coastal zone from 63°S to 65°S and 60°E to 160°E.

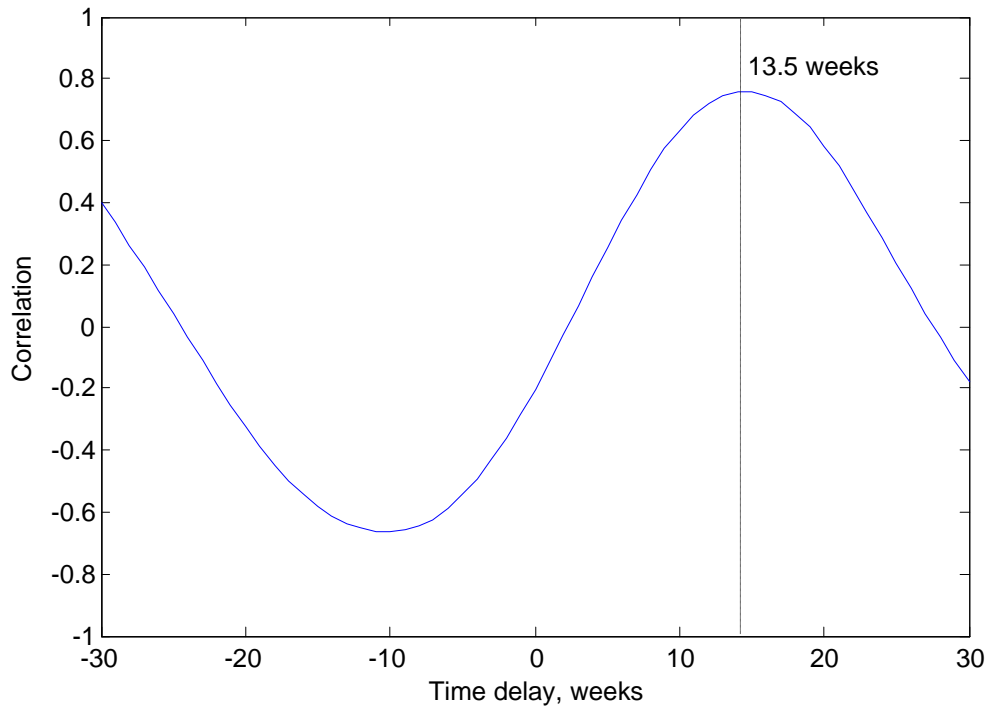


Figure 7.8. Fragment of the cross-correlation function between the occurrence frequency of ice events and the Eastern Antarctica SST, taken around its maximum at 13.5 weeks.

7.3.2 Air temperature

Data of long-term meteorological observations collected at three Australian Antarctic stations, Casey (66.3°S, 110.5°E), Davis (68.4°S, 77.6°E) and Mawson (67.4°S, 62.5°E), were used to analyse the seasonal and interannual variations of the air temperature and wind speed in the Eastern Antarctic coastal region. These data were obtained from the website of the Australian Antarctic Data Centre (<http://data.aad.gov.au/aadc/aws/>). Figure 7.9 shows the weekly average air temperature measured at Casey over the six-year period from 2002 to 2007. The air temperature time series demonstrates very strong seasonal variations, as expected.

The correlation analysis revealed a time lag of about 17 weeks between the occurrence frequency of ice events and the air temperature in the Eastern Antarctic coastal zone, as shown in Figure 7.10. Accordingly, the air temperature variation has a 3-week time lag relative to the reference annual cycle and leads the SST seasonal variation by about 3.5 weeks.

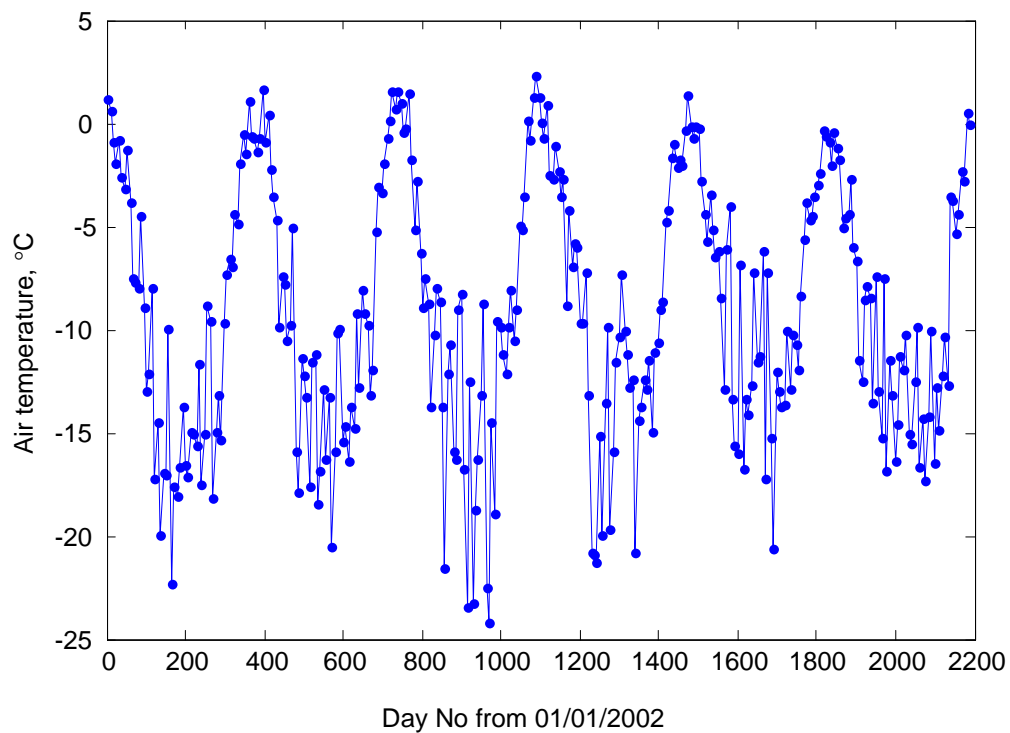


Figure 7.9. Weekly average air temperature measured at Casey station over the six-year period from 2002 to 2007.

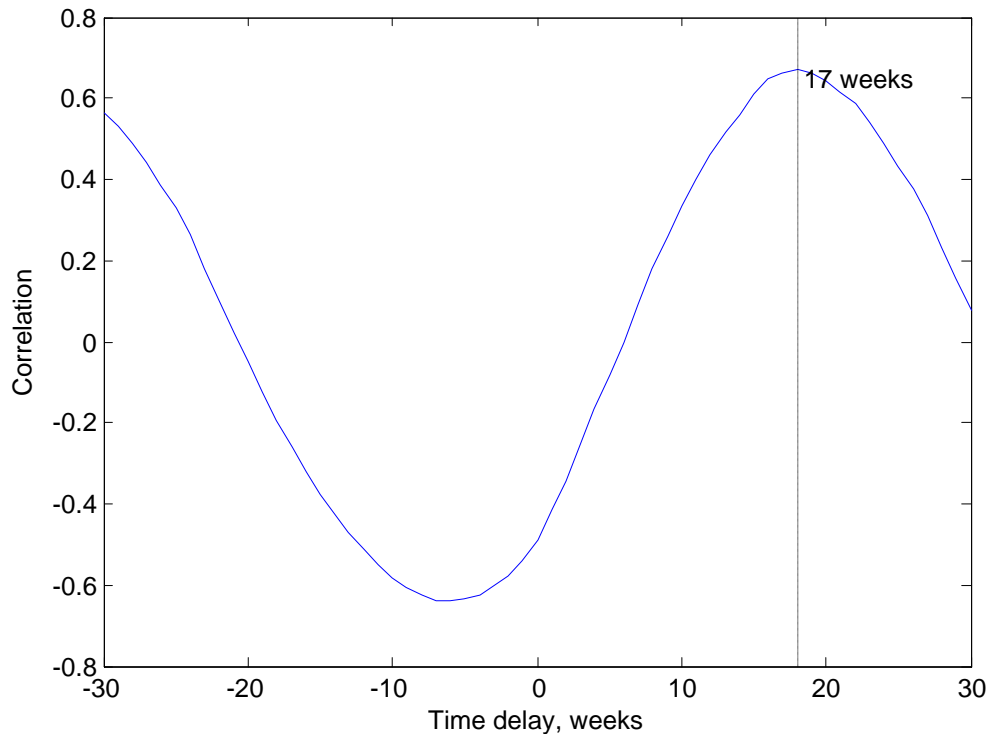


Figure 7.10. Cross-correlation between the occurrence frequency of ice events and the weekly average air temperature at Casey in 2002 - 2007. The correlation has its maximum at about 17-week time delay.

7.3.3 Wind speed

Two horizontal components of the wind speed data collected at the three Australian Antarctic stations were also obtained from the website of the Australian Antarctic Data Centre. The weekly average absolute values of the wind speed measured at Casey station over the six-year period from 2002 to 2007 are shown in Figure 7.11. The local wind is strongly affected by regional weather and topographic conditions and, therefore, its temporal variations contain significant short-period random-like fluctuations superimposed as noise on the seasonal variation, as shown in Figure 7.11. The seasonal variations hidden in a noisy time series of the wind speed can be found through the Periodicity Transform. Figure 7.12 shows the principal periodic basis of the time series in Figure 7.11 corrected for the mean value. The period of this basis function is 53 weeks, i.e. approximately one year.

The seasonal variation represented by this basis function has the maximum wind speed in July and the minimum in January.

Because the wind time series is distorted by noise, the correlation of its principal periodic basis with the occurrence frequency of ice events is relatively low, as seen in Figure 7.13. The seasonal cycle in the wind speed variations lag behind the seasonal cycle of the occurrence frequency by about 9 weeks and, accordingly, has a 29-week lag relative to the reference annual cycle.

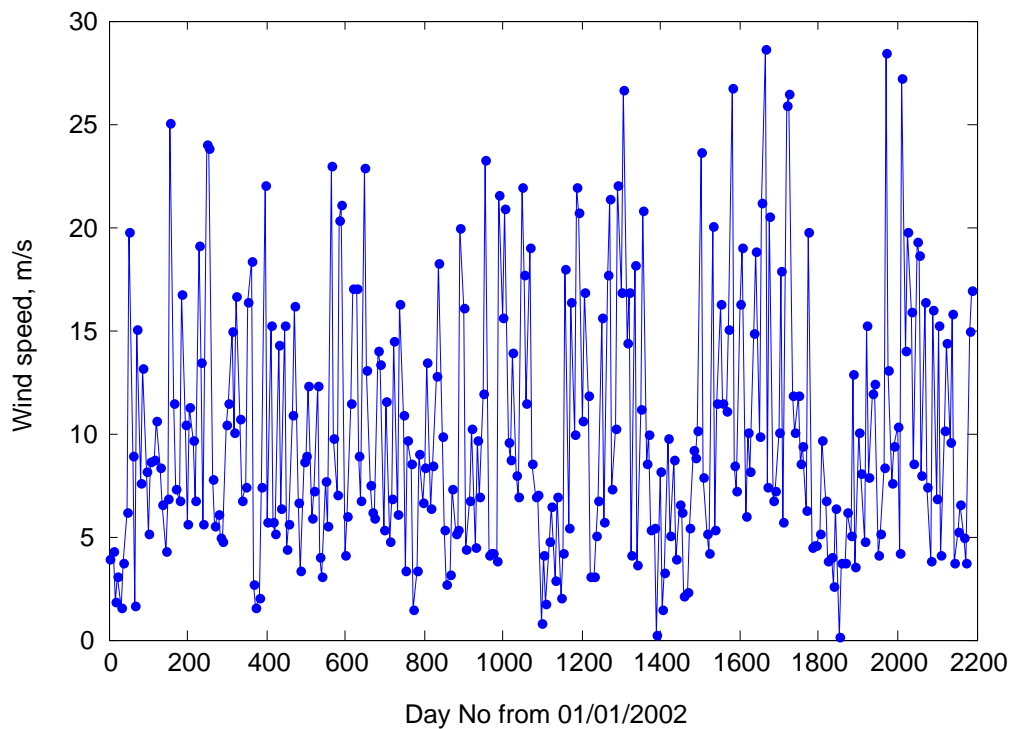


Figure 7.11. Weekly averaged absolute values of the wind speed measured at Casey station over the six-year period from 2002 to 2007.

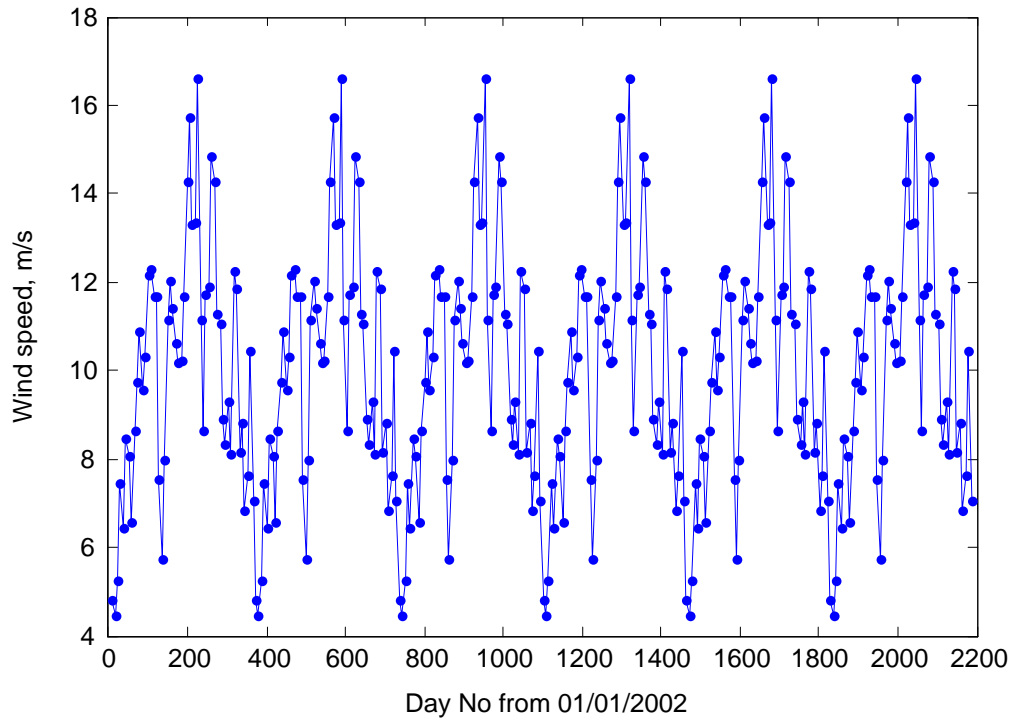


Figure 7.12. Principal periodic basis of the time series shown in Figure 7.11 derived from the periodicity transform and corrected for the mean value. The period of this basis function is 53 weeks.

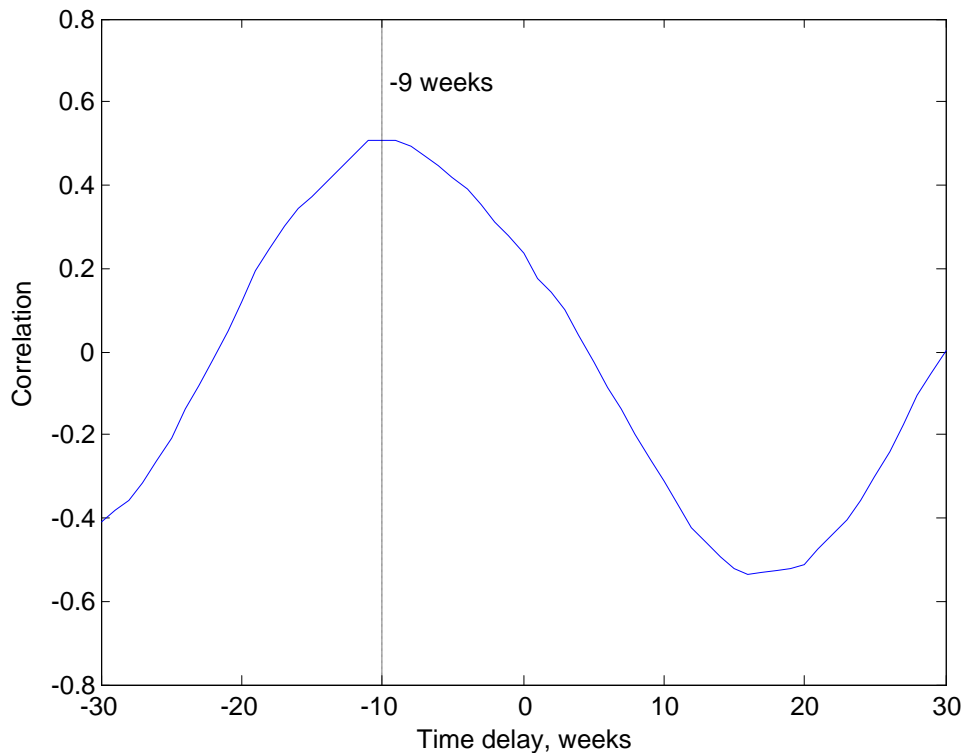


Figure 7.13. The cross-correlation function between the occurrence frequency of ice events and the principal periodic basis of the weekly average wind speed at Casey from 2002 to 2007 as shown in Figure 7.12, taken around its maximum. The wind speed variation correlates with the occurrence frequency with a time lag of 9 weeks.

7.3.4 Antarctic sea ice extent

A dataset of the daily average Antarctic sea ice extent (area in km^2) over the period from 2000 to 2004 was obtained from the National Snow and Ice Data Center (NSIDC) (Long, 2005). The long-term variation of sea ice extent shown in Figure 7.14 is governed primarily by the seasonal change, with the maximum extent in early September and the minimum extent in early March each year. The cross-correlation between the occurrence frequency of ice events and the weekly-averaged Antarctic sea ice extent in 2002 – 2004 is shown in Figure 7.14. The time lag between the maximum occurrence frequency of ice events and the maximum sea ice extent is 14 weeks.

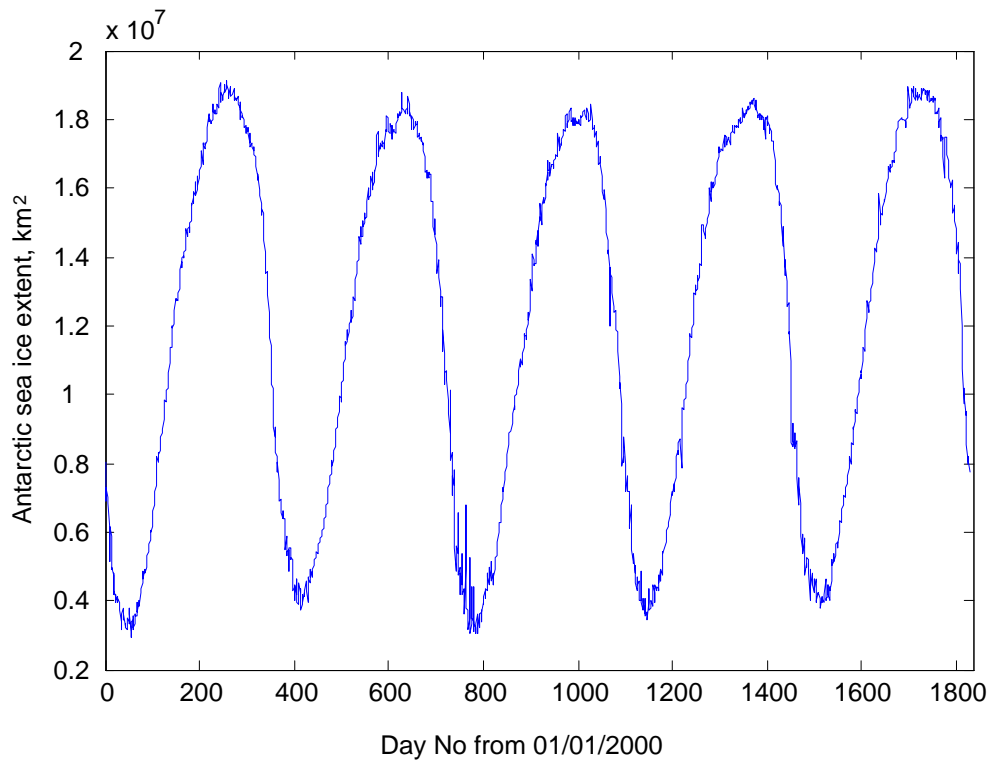


Figure 7.14. Daily Antarctic sea ice extent observed over a 5-year period from 2001 to 2004.

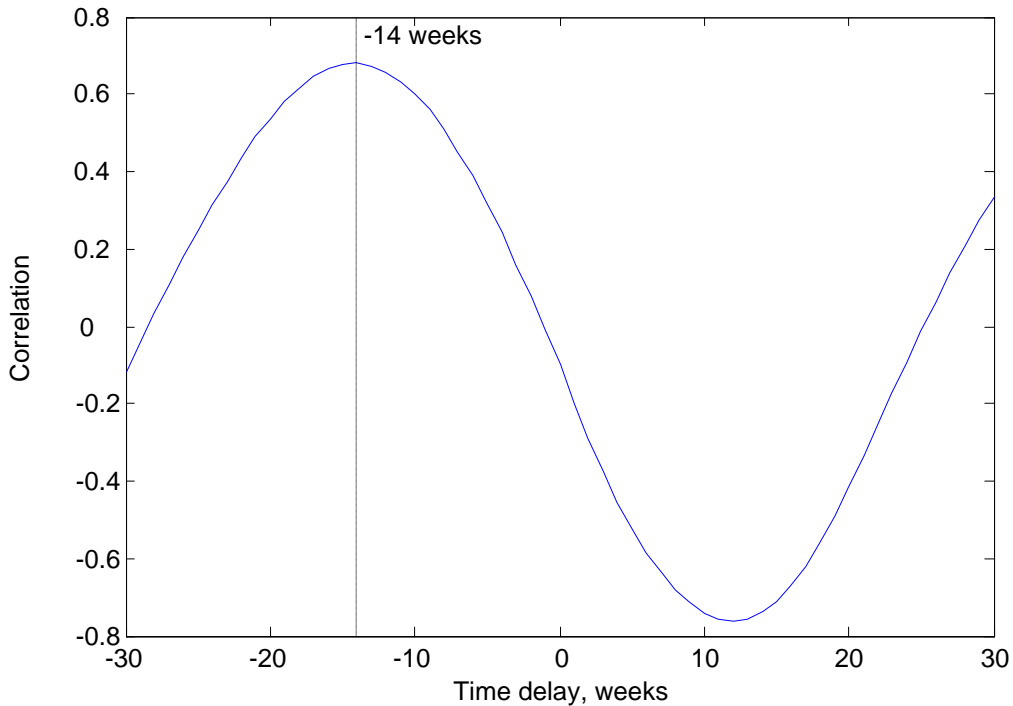


Figure 7.15. The cross-correlation between the occurrence frequency of ice events and the Antarctic sea ice extent, taken around its maximum at a time lag of -14 weeks.

7.3.5 Signal level of ice events observed at HA01

The signal level from ice events measured at HA01 and averaged for each week over the whole observation period from 2002 to 2007 is shown by the blue line with dots in Figure 7.16. The signal level was estimated after correction for the noise contribution, as discussed in Chapter 6. The seasonal variation of the signal level is evident even from the unfiltered time series. The red line in Figure 7.16 shows the principal periodic basis of the 6-year time series of signal level derived through the periodicity transform and corrected for the mean value of the time series. The period of this basis function is 53 week, which corresponds to the seasonal variation. The cross-correlation between the occurrence frequency and the signal level of ice events is shown in Figure 7.17. The temporal variation in the occurrence frequency correlates with that of the signal level with a time lag of approximately 11.5 weeks. The signal level reaches its maximum 8.5 weeks after the New Year, while the

frequency of occurrence is maximum in week 20. It is also evident from a comparison of Figures 7.15 and 7.17 and the time lags estimated from the cross-correlation that the signal level reaches its maximum at about the time when the ice extent has its minimum and drops to minimum values when the sea ice is most extended.

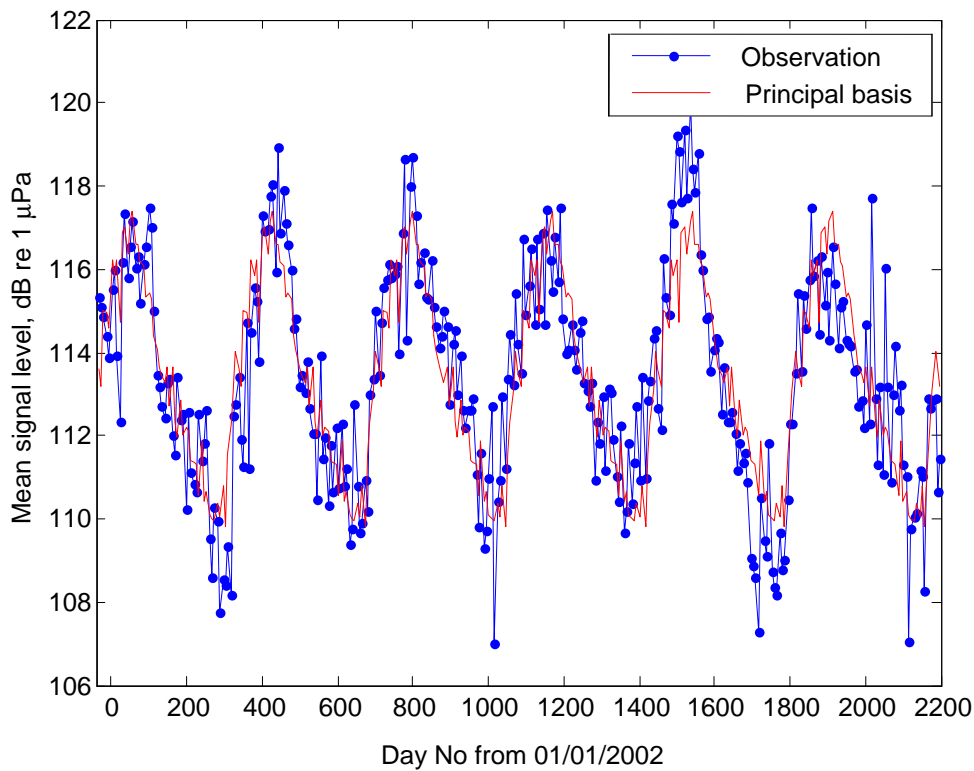


Figure 7.16. Temporal variations of the weekly averaged signal level from the ice events observed at HA01 over the period from 2002 to 2007 (blue line with dots) and the principal periodic basis derived from the periodicity transform and corrected for the mean value of the time series (red line). The period of the basis function is 53 weeks.

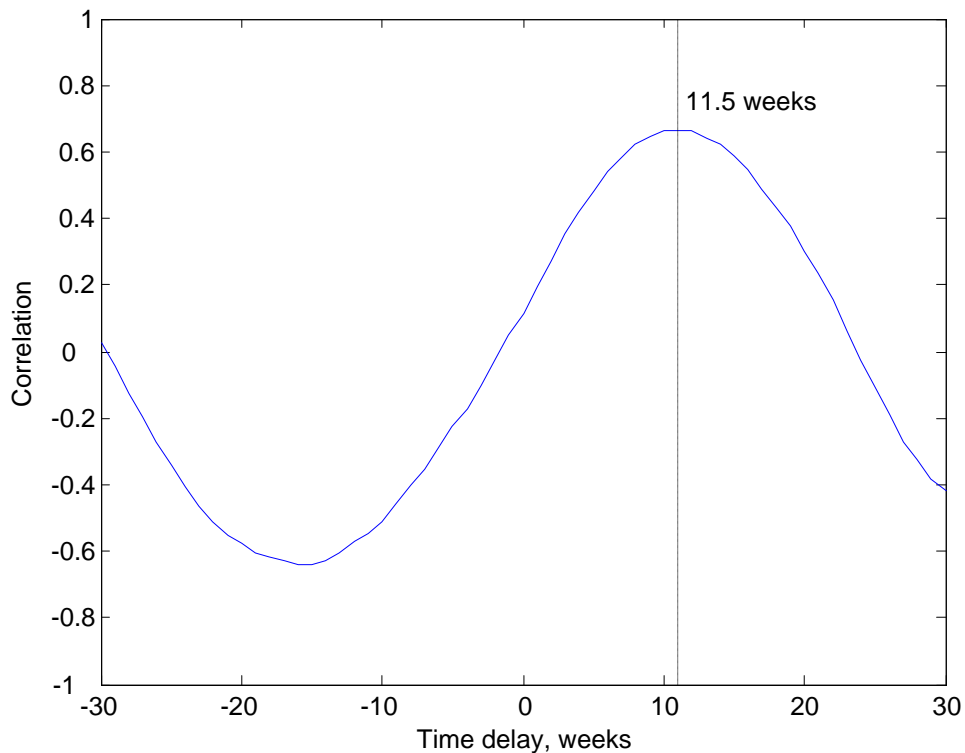


Figure 7.17. The cross-correlation between the occurrence frequency and signal level of ice events observed at HA01 in 2002 – 2007, taken around its maximum. The time lag between the seasonal variations in the signal level and occurrence frequency is about 11.5 weeks.

7.3.6 Discussion

The time lags of the seasonal variations in the acoustic observation and metocean characteristics estimated in the previous sections relative to the reference annual cycle with the maximum on Julian day 1 are shown in Figure 7.18. The day of the maximum solar radiation in the Southern Hemisphere, which is the 21st of December, i.e. about 1.5 weeks before the New Year, is also indicated in this graph.

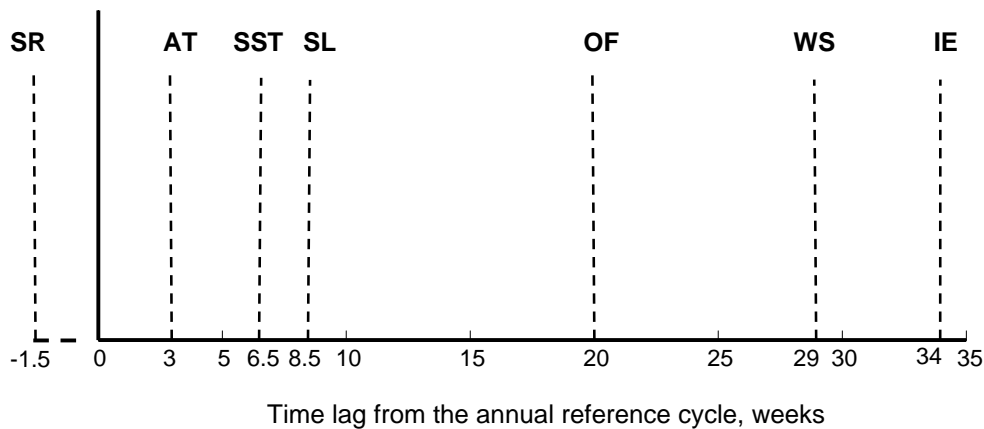


Figure 7.18. Time lags (weeks) from the annual reference cycle estimated for the seasonal variations of the acoustic and metocean parameters which are: solar radiation (**SR**); air temperature in Eastern Antarctic coastal zone (**AT**); sea surface temperature off Eastern Antarctica (**SST**); signal level of ice events received at HA01 (**SL**); occurrence frequency of ice events detected at HA01 (**OF**); wind speed at Casey in the Eastern Antarctica (**WS**); and Antarctic sea ice extent (**IE**).

In a climate system, variations of the climate system components depend not only on changes in the climate forcing, but also on the characteristic responses of different climate components and the coupling between them (Ruddiman, 2000). As clearly seen in Figure 7.18, the variations of the three major climate characteristics in the Eastern Antarctic coastal zone and the surrounding Southern Ocean, which are the air temperature, sea surface temperature and sea ice extent, have increasing time lags from the seasonal variation of climate forcing by the solar radiation. Having relatively low specific heat capacity, the air temperature responds to changes in the solar heat before the other two climate characteristics. The time lag between the maximum solar radiation and the maximum air temperature in Eastern Antarctica is about 4.5 weeks. Sea water has significantly higher heat capacity than air and, moreover, it is isolated from the air and solar radiation by the sea ice canopy of high albedo which grows at high latitudes in the ocean in winter. This explains why the sea surface temperature in the polar environment of the Southern Ocean reaches its summer maximum about one month later than the air temperature. The sea ice extent has the slowest response to climate forcing among the three

characteristics (Lamb, 1972, Ruddiman, 2000). The sea ice canopy starts rapidly melting when the water temperature below ice exceeds the freezing point. Ice melting takes time, so that the ice extent reduces to its minimum after the water temperature reaches the maximum. In the Southern Ocean waters of Eastern Antarctica, the time lag between the maximum SST and minimum sea ice extent is about 1.5 week.

The occurrence frequency of the Antarctic ice events observed at HA01 has a strong seasonal component. However, this seasonal variation does not coincide with seasonal changes in the climate related metocean characteristics. The maximum occurrence frequency of ice breaking events is observed considerably later than the maximum air and water temperatures. Moreover, the seasonal cycle in the variation of the occurrence frequency does not coincide with that of the wind speed in Eastern Antarctica. There is no evident explanation yet for such time lags observed between the seasonal variation in the occurrence of ice events associated with ice rifting and breaking processes and the seasonal variations in the major climate characteristics of the Eastern Antarctic coastal zone. New comprehensive studies of the links between the climate system and glaciological processes in the Antarctic coastal region and new, more representative data in meteorology, oceanography and glaciology are needed to suggest a reasonable explanation for this phenomenon. Such an investigation is beyond the scope of this PhD study.

The almost exactly opposite phases (i.e. one half-year) of the seasonal variations in the signal level from ice events and the sea ice extent indicates that the seasonal changes in the sea ice cover are most likely the main reason for the variation of the acoustic transmission loss and, consequently, the received level of the signals propagated from Antarctica to the Indian Ocean. It is known from several experimental studies in the Arctic Ocean and theoretical modelling that scattering from a ridged sea ice canopy is the major cause of the acoustic transmission loss at low frequencies in the polar ocean environment (DiNapoli and Mellen, 1986, Gavrilov and Mikhalevsky, 2006). The larger the sea ice extent, the longer path the acoustic signals will propagate in the near-surface acoustic channel strongly affected by scattering from the surface roughness and, therefore, more rapidly attenuating. To investigate in more detail the influence of sea ice and other oceanographic

characteristics on the acoustic transmission loss in the Southern Ocean, an experiment on long-range low-frequency acoustic propagation with a calibrated source is required, as well as comprehensive studies of the sea ice roughness and thickness in the Southern Ocean, similar to those conducted in the Arctic (DiNapoli and Mellen, 1986, Gavrilov and Mikhalevsky, 2006).

A considerable time delay of about 11.5 weeks between the maximum signal level and the maximum occurrence frequency of ice events also indicates that the detection rate of ice events at the HA01 station is not significantly affected by seasonal changes in the acoustic transmission loss along the paths from Antarctica to HA01.

7.4 Concluding remarks

In this chapter, the long-term variations of the occurrence frequency of ice events detected at the HA01 station over the 6-year period from 2002 to 2007 were investigated. The correlation of the occurrence frequency with the signal level of ice events and with the Antarctic climate related metocean characteristics, such as the sea surface temperature, air temperature, wind speed in the Eastern Antarctic coastal region, and the Antarctic sea ice extent, was also analysed. The following conclusions can be drawn based on the results of this chapter:

1. The temporal changes in the occurrence frequency of Antarctic ice events reveal strong seasonal variations but no interannual trend.
2. It is believed that the joint effect of the climate system in Eastern Antarctic region, including solar radiation as the climate forcing and other major climate factors such as sea surface temperature, air temperature, wind speed, ocean currents and sea ice extent, causes the seasonal variation of the Antarctic ice occurrence frequency. However, comprehensive studies are needed to explore the links between the climate system and glaciological processes in the Antarctic coastal region.

3. The signal level from ice events observed at the HA01 station varies noticeably with seasons, which is most likely due to the seasonal variation of the Antarctic sea ice extent. However, such variations do not significantly affect the detection rate of ice events at HA01.

CHAPTER 8

CONCLUSIONS AND RECOMMENDATIONS

8.1 Overview

This chapter summarizes this study in Section 8.2 by drawing conclusions based on the investigations of all aspects of the study associated with the original objectives. The recommendations for future work are presented in Section 8.3.

8.2 Conclusions

This project has achieved its aim to demonstrate the feasibility of remote acoustic monitoring of Antarctic ice rifting and breaking events on ice shelves and icebergs using the IMS hydroacoustic listening stations deployed in the Indian Ocean. Investigations of a number of scientific and technical aspects of the project associated with the primary aim were conducted. They are outlined as follows with the achievements and conclusions of the investigations:

- Over six years of hydroacoustic recordings from the HA01 station and four years of recordings from the H08S station of the CTBT IMS hydroacoustic network were collected. A processing algorithm was implemented to automatically divide continuous sea noise recordings into 20-s fragments, to detect all fragments of noise recordings with coherent signal arrivals and to select signals for which the back-azimuths of arrivals can be accurately estimated. The sources of the coherent signal fragments were classified based on characteristics of their waveforms, spectrograms and back-azimuths measured from the receive stations. It was found that Antarctica is one of the major sources of low-frequency underwater noise at the two IMS stations in the Indian Ocean. Short transient signals from the direction of Antarctica, featuring a single dominant arrival with strong negative frequency dispersion, were frequently detected at the two IMS stations. These signals were hypothesized to be produced by ice cracking and

breaking processes on ice shelves or icebergs in the Antarctic coastal zone and the Southern Ocean off Antarctica and were therefore referred to as Antarctic ice events.

- Numerical modelling was conducted to analyse the principal characteristics of sound propagation along the paths from Antarctica to the IMS stations in the Indian Ocean, such as transmission loss, mode coupling, and inter-modal and intra-modal dispersion effects. This aimed to identify the origin of the transient signals with strong frequency dispersion which arrive at the IMS stations from Antarctica. The hypothesis that the Antarctic ice cracking or breaking events are the origin of those signals was supported by a good agreement between the experimental observation and numerical modelling of the arrival structure of transient signals propagated from Antarctica to the IMS stations in the Indian Ocean, as well as by other kinds of observation of ice breaking events in Antarctica conducted in parallel with remote acoustic observation, such as underwater acoustic recordings made in Antarctica and analysis of satellite imagery of the Eastern Antarctica ice shelves.
- The bearing estimation capability of the HA01 and H08S stations was examined by an investigation of various factors that potentially cause bearing estimation errors, which includes: possible errors in the time difference of signal arrival (TDOA) measured on different hydrophones of the IMS stations, random and systematic deviations of hydrophones' positions from the touch-down locations of the hydrophones' moorings determined during installation, and the effect of horizontal refraction along the acoustic propagation paths. The investigation showed that the errors of TDOA measurements, which depend on the signal sampling interval, SNR, signal bandwidth and duration, cause small and negligible bearing errors compared to the other sources of errors. The random component of the bearing error, caused by variable horizontal deviations of the hydrophones deployed on long mooring cables and moving under ocean currents, was investigated using a model suggested for estimating the RMS bearing error as a function of the back-azimuth to the acoustic source and the standard deviation of the receivers' horizontal position. This random bearing error was estimated experimentally based on the variations of back-azimuth measurements for long-lasting low-frequency

hydroacoustic events observed from the stations. The estimates of the random bearing error for both stations are about 0.2° RMS, which corresponds to the differential horizontal deviation of hydrophones in the triplet array of a few meters. The effect of horizontal refraction on the bearing error estimation for the signal arrivals from ice events was numerically investigated and the results showed that the error strongly depends on the angle at which the acoustic path crosses the Australian Convergence Zone and the continental slope. The bearing error at the HA01 and H08S stations, induced by horizontal refraction, could be considerable, up to $\pm 1^\circ$ for sources located in the easternmost and westernmost parts of the Eastern Antarctica coastal zone observed from the IMS stations. The systematic bearing error due to inaccuracy of the touch-down positions of hydrophones' moorings was investigated using a least squares approach to invert the TDOA measurements for a number of underwater explosions of known location. The inversion results showed that the mean error was around 0.8° clockwise for the HA01 station which was also confirmed by measuring the back-azimuth to an Antarctic iceberg collision event of known location. For the H08S station, the systematic error was estimated to be as small as less than 0.2° clockwise, which is comparable to the random errors.

- Three different schemes for Antarctic ice event localization were examined using either two stations HA01 and H08S or only HA01.
 - 1) The localization of several ice events detected at both HA01 and H08S stations was carried out by triangulation, i.e. the intersection of the two geodesics launching from the two receive stations at the measured back-azimuth angles. The accuracy of such localization was verified by comparing modelled and measured arrival time differences of the signals observed at the two stations from the same ice event.
 - 2) Antarctic ice events were also located using back-azimuth measurements of the signal arrivals at one receive station, HA01, and estimation of the range to the sound sources based on the LMS fitting of the measured and modelled frequency dispersion characteristics of mode 1 arrivals at this station. The uncertainty of the localization based on the dispersive arrival structure was comparable to the error of location by triangulation from the two stations. This approach was found to be

applicable only to the signals in which the frequency dispersion characteristics of the mode 1 arrival are not significantly distorted by mode coupling along the path from Antarctica to the HA01 station.

- 3) By measuring the cut-off frequency of mode 1 in the signals from the ice events observed at the HA01 station, the sea depth at the source positions was estimated, and the locations of the ice events were roughly determined by tracing the bathymetry profiles along the acoustic path launched from HA01 at the measured back-azimuth angles. The investigation showed that the majority of these events occurred in relatively shallow water over the Antarctic continental shelf at sea depths of less than 300 m, and therefore the locations of Antarctic ice events can be roughly determined by projecting the back-azimuths of signal arrivals measured at HA01 onto the Antarctic coastline.
- The spatial distribution of Antarctic ice events was analysed based on the measured back-azimuths to the ice events measured at the HA01 station. The azimuth dependence of the acoustic propagation loss from Antarctica to HA01, which might potentially have an effect on the distribution analysis, was also investigated. It was found that the directions to the major glacial features on the Eastern Antarctic coast, such as the Shackleton Ice Shelf, Dibble and Dalton Iceberg Tongues, corresponded to peaks in the spatial distribution. The coastal areas around these major glacial features were consistently active with respect to producing transient underwater noise over the six-year period from 2002 to 2007. The azimuth dependence of the acoustic propagation loss from Antarctica to HA01 is relatively weak and therefore could not significantly distort the spatial distribution of the ice events obtained from the back-azimuth to these events measured at the HA01 station.
 - The long-term variation in the occurrence frequency of the Antarctic ice events detected at the HA01 station over 6 years period from 2002 to 2007 was investigated. Correlation of the occurrence frequency of ice events with the signal level from those events and the long-term changes in the Antarctic climate related metocean factors, such as the sea surface temperature, air temperature, wind speed in the Eastern

Antarctic coastal zone and the Antarctic sea ice extent, was also analysed. Results showed that the occurrence frequency of ice events reveals strong seasonal variations. The climate related metocean characteristics of the Eastern Antarctic coastal region have strong seasonal variations and strongly correlate with the occurrence frequency of ice events, but with significant and different time lags. It is likely that a joint effect of the seasonal changes and coupling of different metocean parameters of the Eastern Antarctic climate system induce such variation of the occurrence frequency of ice events. However, the mechanism of coupling between the major climate characteristics and ice disintegration rate in the Antarctic coastal zone is not obvious yet. The signal level from ice events measured at the IMS stations also undergoes significant seasonal variations, which are most likely due to seasonal change in the acoustic transmission loss in the Southern Ocean correlated with the Antarctic sea ice extent. However, the occurrence frequency of ice events does not directly correlate with the variations in the signal level.

The major findings and conclusions of this project can be briefly summarized as follows:

1. Remote acoustic observations in the ocean are capable of monitoring underwater noise produced by ice breaking events on Antarctic ice shelves and icebergs. Such events can be located and their spatial distribution and temporal variation can be assessed by remote acoustic observations.
2. A strong seasonal variation was observed in the frequency of occurrence of ice noise events. However, this variation is not directly correlated with the seasonal changes in the major metocean characteristics of the Eastern Antarctic climate system.
3. No significant interannual trend driven by climate change has been observed in the 6-year dataset of acoustic observation. A considerably longer time series of acoustic observation is needed to detect potential climate trends in the ice breaking rate in Antarctica.

8.3 Recommendations for future work

Considering the results related to various topics investigated in this study in connection with the main objective outlined in the conclusions, the following recommendations can be given to extend the scope of this study in future work.

First of all, it is strongly recommended to continue the analysis of hydroacoustic data from the IMS stations in the Indian Ocean to monitor long-term interannual changes in the occurrence of ice events in Eastern Antarctica and assess trends associated with the potential effect of climate change. To achieve the long-term hydroacoustic monitoring of ice disintegration processes around the entire Antarctic continent and provide useful data for climate change studies, a continuous analysis of acoustic data from the other three IMS hydroacoustic stations is required in addition to that for the HA01 and HA08 stations. These three stations are deployed off Crozet Islands in the Indian Ocean, off Juan Fernandez Island in the Pacific Ocean and off Ascension Island in the Atlantic Ocean. Acoustic observations from all IMS stations would provide almost full coverage of the Antarctic coast. A robust algorithm needs to be developed for automatic detection of the signals from Antarctic ice events. A pilot version of such an algorithm was developed and examined, as described in Appendix 1, but it still needs further improvement to obtain satisfactory detection and misclassification rates.

The scheme for the bearing error analysis developed in Chapter 4 can be applied to any IMS hydroacoustic stations to enhance their bearing accuracy. In the bearing error analysis scheme, the systematic component of the bearing error estimation was determined by inverting the TDOA measurements for a number of sources of known location using a least squares approach, as presented in Section 4.5. Statistically, the more signals from hydroacoustic events of known location received at one IMS station for its bearing error analysis, the more accurate the estimate of the station's systematic error. Therefore, it is necessary to collect more signals of hydroacoustic events with known position from IMS stations to improve their systematic error estimation. For the H08S station, numerous received air-gun signals from offshore seismic exploration surveys in Australian northwest

shelf can be used for this purpose if the times and positions of those explorations can be sourced.

An algorithm for automatic localization of Antarctic ice events is suggested based on the three localization schemes discussed in Chapter 5. If the ice events can be detected in both HA01 and H08S stations, then the automatic event localization can be implemented by following the scheme that forms automatic event hypotheses based on the hydroacoustic observation of the back-azimuths and arrival times of the detected ice event signals, which was developed in The Prototype International Data Center of the CTBTO [Bowman et al., 2001 and 2006]. If the events can only be detected at one station, programs have to be developed to automatically measure the arrival structures the events signal or their cut-off frequency for the event localization. An automatic routine program also needs to be developed and implemented to select a suitable localization scheme for individual Antarctic ice event.

Finally, it is essential to explore and understand the physical mechanisms that link the occurrence of ice breaking events on Antarctic ice shelves and icebergs with the seasonal and interannual changes in the major metocean characteristics of the Antarctic climate system, such as air temperature, ocean surface temperature, sea ice extent and some others. Based on such an understanding, the remote acoustic observation of ice breaking noise in the Antarctic coastal zone using the IMS hydroacoustic stations can contribute crucial information to the Antarctic climate studies.

REFERENCES

- AMMON, C. J., CHEN, J., THIO, H. K., ROBINSON, D., NI, S., HJORLEIFSDOTTIR, V., KANAMORI, H., LAY, T., DAS, S., HELMBERGER, D., ICHINOSE, G., POLET, J. & WALD, D. 2005. Rupture Process of the 2004 Sumatra-Andaman Earthquake. *Science*, 308, 1133-1139.
- ANTONOV, J. I., LOCARNINI, R. A., BOYER, T. P., MISHONOV, A. V. & GARCIA, H. E. 2006. World Ocean Atlas 2005, Volume 2: Salinity. *In*: S. Levitus, Ed. NOAA Atlas NESDIS 62, U.S. Government Printing Office, Washington, D.C.
- BASSIS, J. N., COLEMAN, R., FRICKER, H. A. & MINSTER, J. B. 2005. Episodic propagation of a rift on the Amery Ice Shelf, East Antarctica. *Geophys. Res. Lett.*, 32.
- BENDAT, J. S. & PIERSON, A. G. 2000. *Random Data: Analysis and Measurement Procedures*, New York, Wiley.
- BLACKMAN, D. K. & GROOT-HEDLIN, C. D. D. 2005. Acoustic propagation through the Antarctic convergence zone-calibration tests for the nuclear test monitoring system. *In*: 27th Seismic Research Review: Ground-Based Nuclear Explosion Monitoring Technologies, 2005 Rancho Mirage, California.
- BLACKMAN, D. K., GROOT-HEDLIN, C. D. D., HARBEN, P., SAUTER, A. & ORCUTT, J. A. 2004. Testing low/very low frequency acoustic sources for basin-wide propagation in the Indian Ocean. *The Journal of the Acoustical Society of America*, 116, 2057-2066.
- BLACKMAN, D. K. & JENKINS, C. S. 2007. NBP0701 Hydroacoustics Project Cruise Report.

- BLACKMAN, D. K., MERCER, J. A., R. ANDREW, GROOT-HEDLIN, C. D. D. & HARBEN, P. E. 2003. INDIAN OCEAN CALIBRATION TESTS: CAPE TOWN-COCOS KEELING 2003. *In: 25th Seismic Research Review - Nuclear Explosion Monitoring: Building the Knowledge Base, September 23-25 2003 Tucson, Arizona.* 517-523.
- BOMFORD, G. 1980. *Geodesy*, Oxford University Press, 885pp.
- BOWMAN, J. R., HANSON, J. A. & JEPSEN, D. 2005. An active-source hydroacoustic experiment in the Indian Ocean. *In: 27th Seismic Research Review: Ground-Based Nuclear Explosion Monitoring Technologies, 2005 Rancho Mirage, California, US.*
- BRATT, S. R. 1996. The CTBT International Data Centre. *EOS Trans. Amer. Geophys. Un.*, 77, F3.
- BREKHOVSKIKH, L. M., GAVRILOV, A. N., GONCHAROV, V. V., PISAREV, S. V., CHEPURIN, A. Y. & MIKHALEVSKY, P. N. 2002. ACOUS Experiment Results. *Izvestiya, Atmospheric and Oceanic Physics*, 38, 642-652.
- BREKHOVSKIKH, L. M. & GODIN, O. A. 1999. *Acoustics of Layered Media II*, Springer.
- BREKHOVSKIKH, L. M. & LYSANOV, Y. P. 1991. *Fundamentals of Ocean Acoustics*, Berlin, Springer-Verlag.
- CANSI, Y. 1995. An Automatic Seismic Event Processing for Detection and Location: The P.M.C.C. Method. *Geophys. Res. Lett.*, 22.
- CHAPP, E., WAYNE, D., BOHNENSTIEHL, R. & TOLSTOY, M. 2005. Sound-channel Observations of Ice-generated Tremor in the Indian Ocean. *Geochemistry, Geophysics and Geosystems*, 6 (Q06003, doi:10.1029/2004GC000889).

- CHIU, C. S., MILLER, J. H. & LYNCH, J. F. 1996. Forward coupled-mode propagation modelling for coastal acoustic tomography. *The Journal of the Acoustical Society of America*, 99, 793-802.
- CUMMINGS, W. C. & THOMPSON, P. O. 1971. Underwater sounds from the blue whale. *The Journal of the Acoustical Society of America*, 50, 1193-1198.
- DINAPOLI, F. & MELLEN, R. 1986. Low frequency attenuation in the Arctic Ocean. *In*: BERKSON, T. A. A. J. M. (ed.) *Ocean Seismo Acoustics*. New York: Plenum.
- DOAKE, C. S. M. & VAUGHAN, D. G. 1991. Rapid disintegration of the Word Ice Shelf in response to atmospheric warming. *Nature*, 350, 328-330.
- DOOLITTLE, R., TOLSTOY, A. & BUCKINGHAM, M. 1988. Experimental confirmation of horizontal refraction of cw acoustic radiation from a point source in a wedge-shaped ocean environment. *The Journal of the Acoustical Society of America*, 83, 2117-2125.
- DUSHAW, B. D., BOLD, G., CHUI, C. S., COLOSI, J., CORNUELLE, B., DESAUBIES, Y., DZIECIUCH, M., FORBES, A., GAILLARD, F., GOULD, J., HOWE, B., LAWRENCE, M., LYNCH, J., MENEMENLIS, D., MERCER, J., MIKHAELVSKY, P., MUNK, W., NAKANO, I., SCHOTT, F., SEND, U., SPINDEL, R., TERRE, T. & WORCESTER, C. 2001. Observing the ocean in the 2000's: A strategy for the role of acoustic tomography in ocean climate observation. *In*: SMITH, C. J. K. A. N. R. (ed.) *Observing the Oceans in the 21st Century*. GODAE Project Office, Bureau of Meteorology: Melbourne.

- DZIAK, R. P., PARK, M., MATSUMOTO, H., BOHNENSTIEHL, D. R., HAXEL, J. H., MELLINGER, D. K., STAFFORD, K. & LEE, W. S. 2007. Hydroacoustic monitoring of the Bransfield Strait and Drake Passage, Antarctica: A first analysis of seafloor seismicity, cryogenic acoustic sources, and cetacean vocalizations, in Antarctica: A Keystone in a Changing World. *In: Online Proceedings of the 10th ISAES X, USGS Open-File Report 2007-1047, Extended Abstract 011, 4 p.*
- EVANS, R. B. 1983. A coupled mode solution for acoustic propagation in a waveguide with stepwise depth variations of a penetrable bottom. *The Journal of the Acoustical Society of America*, 74, 188-195.
- EWING, M. & WORZEL, J. L. 1948. Long-range sound transmission. *Geo. Soc. Am., Memoir 27.*
- FOX, C. G. & DZIAK, R. P. 1998. Hydroacoustic detection of volcanic activity on the Gorda Ridge, February-March 1996. *Deep Sea Research Part II: Topical Studies in Oceanography*, 45, 2513-2530.
- FOX, C. G., RADFORD, W. E., DZIAK, R. P., LAU, T. K., MATSUMOTO, H. & SCHREINER, A. E. 1995. Acoustic Detection of a Seafloor Spreading Episode on the Juan de Fuca Ridge Using Military Hydrophone Arrays. *Geophys. Res. Lett.*, 22.
- GAVRILOV, A. & LI, B. 2007. Antarctica as one of the major sources of noise in the ocean. *Underwater Acoustic Measurements: Technologies & Results, 2nd International Conference and Exhibition.* Heraklion, Crete.
- GAVRILOV, A. N. & MIKHALEVSKY, P. N. 2001. Mode-coupling effects in acoustic thermometry of the Arctic Ocean. *In: G, T. M. A. M. (ed.) Inverse Problems in Underwater Acoustics.* NY: Springer-Verlag.

- GAVRILOV, A. N. & MIKHALEVSKY, P. N. 2002. Recent results of the ACOUS (Arctic Climate Observations using Underwater Sound) Program. *Acta Acustica united with Acustica*, 88, 783-791.
- GAVRILOV, A. N. & MIKHALEVSKY, P. N. 2006. Low-frequency acoustic propagation loss in the Arctic Ocean: Results of the Arctic climate observations using underwater sound experiment. *The Journal of the Acoustical Society of America*, 119, 3694-3706.
- GAVRILOV, A. N., SLAVINSKY, M. M. & SHMELERV, A. Y. 1995. Theoretical and Experimental Investigations of the Feasibility of Acoustic Thermometry of Climatic Changes in the Arctic Ocean. *Physics Uspekhi (Russian Academy of Science)* 38, 797-802.
- GRAEBER, F. M., COYNE, J. & TOMUTA, E. 2006. The Current Status of Hydroacoustic Data Processing at The International Data Centre. *In: The 28th Seismic Research Review: Ground-Based Nuclear Explosion Monitoring Technologies*, 2006 Orlando, Florida, US.
- GRAEBER, F. M. & PISERCHIA, P. F. 2004. Zones of wave excitation in the NE Indian ocean mapped using variations in back-azimuth over time obtained from multi-channel correlation of IMS hydrophone triplet data. *Geophysical Journal International*, 158, 239-256.
- HAGERTY, M. T., SCHWARTZ, S. Y., GARCÉS, M. A. & PROTTI, M. 2000. Analysis of seismic and acoustic observations at Arenal Volcano, Costa Rica, 1995-1997. *Journal of Volcanology and Geothermal Research*, 101, 27-65.
- HANSON, J., BRAS, R. L., DYSART, P., BRUMBAUGH, D., GAULT, A. & GUERN, J. 2001. Operational Processing of Hydroacoustics at the Prototype International Data Center. *Pure and Applied Geophysics*, 158, 425-456.

- HANSON, J. A. & BOWMAN, J. R. 2005. Indian Ocean ridge seismicity observed with a permanent hydroacoustic network. *Geophys. Res. Lett.*, 32.
- HANSON, J. A. & BOWMAN, J. R. 2006. Methods for monitoring hydroacoustic events using direct and reflected T waves in the Indian Ocean. *J. Geophys. Res.*, 111.
- HARBEN, P. E. & RODGERS, A. J. 2000. Calibration of the hydroacoustic station: lessons learned from the Ascension Island experiment. *In: 22nd Seismic Research Symposium, 12 Sep to 15 Sep 2000 New Orleans, US.*
- HEANEY, K. D., KUPERMAN, W. A. & MCDONALD, B. E. 1991. Perth--Bermuda sound propagation (1960): Adiabatic mode interpretation. *The Journal of the Acoustical Society of America*, 90, 2586-2594.
- HOUGHTON, J. T., DING, Y., GRIGGS, D. J., NOGUER, M., VAN DER LINDEN, P. J., DAI, X., MASKELL, K. & JOHNSON, C. A. 2001. *Climate Change 2001: The Scientific Basis*. Contribution of Working Group I to the Third Assessment Report of the Intergovernmental Panel on Climate Change Cambridge, United Kingdom and New York, NY, USA: Cambridge University Press.
- HUYBRECHTS, P. & OERLEMANS, J. 1990. Response of the Antarctic ice sheet to future greenhouse warming. *Climate Dynamics*, 5, 93-102.
- JENSEN, F. B., KUPERMAN, W. A., PORTER, M. B. & SCHMIDT, H. 2000. *Computational Ocean Acoustics*, New York, Springer-Verlag.
- KUPERMAN, W. A. 1975. Coherent component of specular reflection and transmission at a randomly rough two-fluid interface. *The Journal of the Acoustical Society of America*, 58, 365-370.

- KUPERMAN, W. A., D'SPAIN, G. L. & HEANEY, K. D. 2001. Long range source localization from single hydrophone spectrograms. *The Journal of the Acoustical Society of America*, 109, 1935-1943.
- KUPERMAN, W. A. & INGENITO, F. 1977. Attenuation of the coherent component of sound propagating in shallow water with rough boundaries. *The Journal of the Acoustical Society of America*, 61, 1178-1187.
- LAMB, H. H. 1972. *Climate: Present, Past and Future*, Methuen & Co LTD.
- LASHOF, D. A. & AHUJA, D. R. 1990. Relative contributions of greenhouse gas emissions to global warming. *Nature*, 344, 529-531.
- LAWRENCE, M. 2003. Presentation at the CTBT Hydroacoustic Workshop. Hobart, Tasmania, Australia.
- LAWRENCE, M. W. 1999. Overview of the hydroacoustic monitoring system for the Comprehensive Nuclear-Test Ban Treaty. *The Journal of the Acoustical Society of America*, 105, 1037.
- LAY, T., KANAMORI, H., AMMON, C. J., NETTLES, M., WARD, S. N., ASTER, R. C., BECK, S. L., BILEK, S. L., BRUDZINSKI, M. R., BUTLER, R., DESHON, H. R., EKSTROM, G., SATAKE, K. & SIPKIN, S. 2005. The Great Sumatra-Andaman Earthquake of 26 December 2004. *Science*, 308, 1127-1133.
- LEPAGE, K. & SCHMIDT, H. 1994. Modelling of low-frequency transmission loss in the central Arctic. *The Journal of the Acoustical Society of America*, 96, 1783-1795.

- LOCARNINI, R. A., MISHONOV, A. V., ANTONOV, J. I., BOYER, T. P. & GARCIA, H. E. 2006. World Ocean Atlas 2005, Volume 1: Temperature. *In*: S. LEVITU, Ed. NOAA Atlas NESDIS 62, U.S. GOVERNMENT PRINTING OFFICE. (ed.). Washington D.C.: 182 pp.
- LONG, D. G. 2005. *NASA SCP Arctic and Antarctic Ice Extent from QuikSCAT, 1999-2004* Boulder, CO National Snow and Ice Data Center (NSIDC)
- MACAYEAL, D. R., OKAL, E. A., ASTER, R. C. & BASSIS, J. N. 2008. Seismic and hydroacoustic tremor generated by colliding icebergs. *J. Geophys. Res.*, 113.
- MANABE, S., SPELMAN, M. J. & STOUFFER, R. J. 1992. Transient Responses of a Coupled Ocean-Atmosphere Model to Gradual Changes of Atmospheric CO₂. Part II: Seasonal Response. *J. Climate*, 5, 105–126.
- MANABE, S., STOUFFER, R. J. & SPELMAN, M. J. 1994. Response of a Coupled Ocean-Atmosphere Model to Increasing Atmospheric Carbon Dioxide. *Ambio*, 23, 44-49.
- MCCAULEY, R. D., JENNER, C., BANNISTER, J. L., CATO, D. H. & DUNCAN, A. 2000. Blue Whale calling in the Rottnest trench, Western Australia, and low frequency sea noise. *Australian Acoustical Society conference*. Joodalup, Australia.
- MCCAULEY, R. D. & SALGADO, K. C. P. 2005. *Curtin University Underwater Sounds Catalogue*. Centre for Marine Science and Technology (CMST), Curtin University, GPO Box U 1987 Perth 6845, WA.
- MENKE, W. 1984. *Geophysical Data Analysis: Discrete Inverse Theory*, New York, Academic Press.

- MERCER, J. H. 1978. West Antarctic ice sheet and CO₂ greenhouse effect: a threat of disaster. *Nature*, 271, 321-325.
- MIKHALEVSKEY, P. N., GAVRILOV, A. N. & BAGGERORER, A. B. 1999. The Transarctic Acoustic Propagation Experiment and Climate Monitoring in the Arctic. *IEEE of OCEAN ENGINEERING*, 24, 183-201.
- MIKHALEVSKY, P. N., BAGGEROER, A. B., GAVRILOV, A. & SLAVINSKY, M. 1995. Experiment tests use of acoustics to monitor temperature and ice in Arctic Ocean. *EOS, TRANSACTIONS AMERICAN GEOPHYSICAL UNION*, 76, 265.
- MIKHALEVSKY, P. N. & GAVRILOV, A. N. 2001. Acoustic Thermometry in the Arctic Ocean. *Polar Research*, 20, 185-193.
- MILLERO, F. J. & LI, X. 1994. Comments on "On equations for the speed of sound in seawater" [J. Acoust. Soc. Am. 93, 255-275 (1993)]. *The Journal of the Acoustical Society of America*, 5, 2757-2759.
- MUNK, W. & BAGGEROER, A. 1994. The Heard Island papers: A contribution to global acoustics. *The Journal of the Acoustical Society of America*, 96, 2327-2329.
- OGILVY, J. A. 1991. *Theory of Wave Scattering from Random Rough Surfaces*, Bristol, Adam Hilger.
- OPPENHEIM, A. V. & SCHAFER, R. W. (eds.) 1989. *Discrete-Time Signal Processing*, NJ, USA Prentice Hall.
- PERKINS, S. 2001. An armada of ice sets sail for the new millennium. *Science News*.

- PEZZO, E. D. & GIUDICEPIETRO, F. 2002. Plane wave fitting method for a plane, small aperture, short period seismic array: a MATHCAD program. *Computers&Geosciences*, 28, 59-64.
- PORTER, M. B., JENSEN, F. B. & FERLA, C. M. 1991. The problem of energy conservation in one-way models. *The Journal of the Acoustical Society of America*, 89, 1058-1067.
- PORTER, M. B. & REISS, E. L. 1984. A numerical method for ocean-acoustic normal modes. *The Journal of the Acoustical Society of America*, 76, 244-252.
- PRATT, W. K. 1991. *Digital Image Processing*. New York, John Wiley & Sons.
- PRESS, W. H., TEUKOLSKY, S. A., VETTERLING, W. T. & FLANNERY, B. P. 2007. *Numerical Recipes - The art of scientific computing*, New York, Cambridge University Press.
- ROTT, H., RACK, W., SKVARCA, P. & ANGELIS, H. D. 2002. Northern Larsen Ice Shelf, Antarctica: further retreat after collapse. *Annals of glaciology*, 34, 277-282.
- ROTT, H., SKVARCA, P. & NAGLER, T. 1996. Rapid Collapse of Northern Larsen Ice Shelf, Antarctica. *Science*, 271, 788-792.
- RUDDIMAN, W. F. 2000. *Earth's Climate: Past and Future*, New York, W.H.Freeman and Company.
- SANDERS, P. M. & FOFONOFF, N. P. 1976. Conversion of pressure to depth in the ocean. *Deep Sea Research*, 23, 109-111.

- SCAMBOS, T. A., HULBE, C., FAHNESTOCK, M. & BOHLANDER, J. 2000. The link between climate warming and break-up of ice shelves in the Antarctic Peninsula. *Journal of Glaciology*, 46, 516-530.
- SETHARES, W. A. & STALEY, T. W. 1999. Periodicity transforms. *Signal Processing, IEEE Transactions*, 47, 2953-2964.
- SHEPHERD, A., WINGHAM, D., PAYNE, T. & SKVARCA, P. 2003. Larsen Ice Shelf Has Progressively Thinned. *Science*, 302, 856-859.
- SIMON, H., LEWIS, E. O., RANEY, R. K. & JAMES, R. R. 1994. *Remote Sensing of Sea Ice and Icebergs*, New York John Wiley and Sons.
- SMITH, D. K., ESCARTIN, J., CANNAT, M., TOLSTOY, M., FOX, C. G., BOHNENSTIEHL, D. R. & BAZIN, S. 2003. Spatial and temporal distribution of seismicity along the northern Mid-Atlantic Ridge (15-35 degrees N). *J. Geophys. Res.*, 108, 2167-2189.
- SOLOMON, S., QIN, D., MANNING, M., CHEN, Z., MARQUIS, M., AVERYT, K. B., TIGNOR, M. & MILLER, H. L. 2007. Summary for Policymakers. *In: Climate Change 2007: The Physical Science Basis. Contribution of Working Group I to the Fourth Assessment Report of the Intergovernmental Panel on Climate Change.* Cambridge, United Kingdom and New York: Cambridge University Press.
- STOICA, P. & MOSES, R. L. 1997. *Introduction to Spectral Analysis*, Prentice-Hall.
- TALANDIER, J., HYVERNAUD, O., OKAL, E. A. & PISERCHIA, P. F. 2002. Long-range detection of hydroacoustic signals from large icebergs in the Ross Sea, Antarctica. *Earth and Planetary Science Letters*, 203, 519-534.

TALANDIER, J., HYVERNAUD, O., REYMOND, D. & OKAL, E. A. 2006. Hydroacoustic signals generated by parked and drifting icebergs in the Southern Indian and Pacific Oceans. *Geophysical Journal International*, 165, 817-834.

YANG, T. C. 1984a. Dispersion and ranging of transient signals in the Arctic Ocean. *The Journal of the Acoustical Society of America*, 76, 262-273.

YANG, T. C. 1984b. A method for measuring the frequency dispersion for broadband pulses propagated to long ranges. *The Journal of the Acoustical Society of America*, 76, 253-261.

Every reasonable effort has been made to acknowledge the owners of copyright material. I would be pleased to hear from any copyright owner who has been omitted or incorrectly acknowledged.

APPENDIX A

AN ALGORITHM FOR RECOGNISING TRANSIENT SIGNALS RECEIVED FROM ANTARCTICA

Short transient signals received at the IMS hydroacoustic stations from the Antarctic coastal zone are referred to as ice breaking events, or simply ice events, because they are believed to be emitted by ice rifting and breaking processes on the ice shelves and icebergs. The algorithm for detection and recognition of such signals consists of several steps and criteria:

1. As described in Section 2.4, the detection algorithm starts with searching for transient signals in 20-s long fragments of the continuous sea noise recordings, which are correlated in all the three receivers of the IMS station. The minimum correlation of signals is chosen to be 0.5 in at least one pair of hydrophones and one of the four frequency bands of analysis. The time difference of arrivals (TDOA) to different receivers is estimated from the signal cross-correlation. The X- and Y-components of signal propagation slowness is derived from the TDOA estimates and the array geometry using the plane wave fitting method (Pezzo and Giudicepietro, 2002), and then the group velocity and back-azimuth of signal arrivals are found from the slowness components.
2. The initial detection events (20-s fragments of coherent signals) are accepted only when the group velocity estimate lies within the range from 1450 to 1500 m/s, which corresponds to the maximum variation of the group velocity of slowly attenuating low-order modes at frequencies from 3 Hz to 100 Hz in the environmental conditions around the IMS stations. The events of lower or higher values of the group velocity estimate are ignored, because the back-azimuth estimates for such events are erroneous.
3. The Antarctic coast is visible from the HA01 station at azimuth angles from approximately 158° to 210° . In order to include the easternmost and westernmost parts of the observed Antarctic continental shelf, the observation sector is widened

by 2° in both sides, i.e. from 156° to 212° , which allows detection of ice breaking signals from icebergs drifting over those areas of the shelf. Widening the observation sector also allows for possible errors of back-azimuth estimates.

4. The final step is to recognise ice events from other signals which also arrived at the azimuth angles pointing to Antarctica. Sources of such signals include in particular, underwater seismic events, vocalising great whales, man-made noises (e.g. from offshore seismic exploration) and some other events which take place in the Indian or Southern Ocean in the direction to Antarctica. Another source of frequent and intense underwater signals arriving from Antarctica are some large icebergs which produce long-lasting, pseudo-harmonic sounds when colliding with the ice shelf, seafloor or other icebergs. The main feature of the signals from transient ice events is the frequency dispersion effect which is quite distinctive in the signal spectrograms. The typical ice event starts with a relatively broadband noise signal of indefinite spectral structure followed by a distinct arrival pulse of mode 1 which reveals strong waveguide dispersion (Figure A.1).

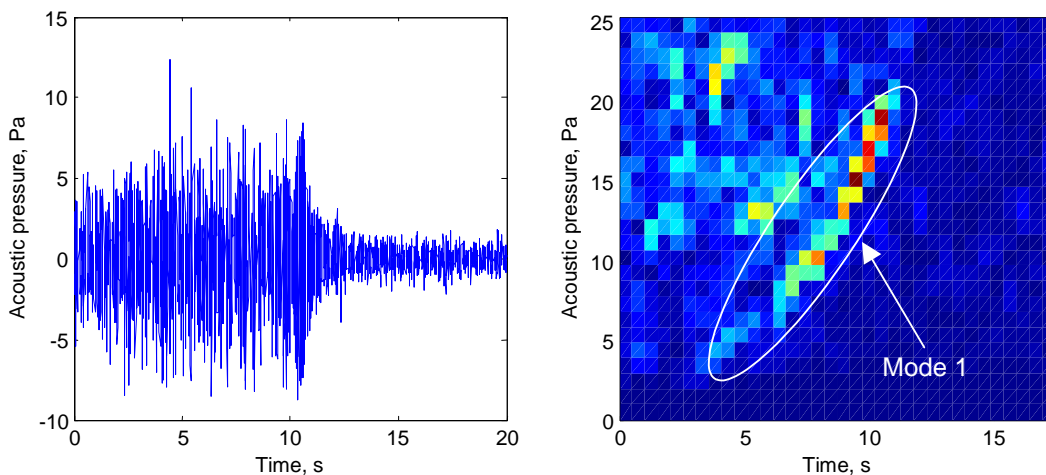


Figure A.1. Waveform (left panel) and spectrogram of a signal received at HA01 from an ice event in summer. The arrival of mode 1 marked out by the oval can be easily recognized.

As discussed in Chapter 3, the shape (slope) of the frequency dispersion curve seen in mode 1 arrival depends on the sound speed profile in the Southern Ocean south of the Antarctic polar front and on the distance that the sound travels in the polar environment.

The noise-like signal preceding the arrival of mode 1 contains higher order modes which usually do not reveal distinct arrivals due to, most likely, strong mode coupling across the polar frontal zone. The contribution of higher-order modes to the signal energy varies much in different events. In about one third of all events, the energy of mode 1 dominates the other modes, so that the dispersive arrival of mode 1 is very distinct in the spectrogram (Figure A.2). This occurs most likely when the sea depth at the noise source (ice event) is too shallow for the higher modes to propagate with little interaction with the seafloor. However, there are many events when the energy of the higher modes, especially at higher frequencies, is higher than that of mode 1. In such cases, the arrival of mode 1 is less distinct in the spectrogram (Figure A.3).

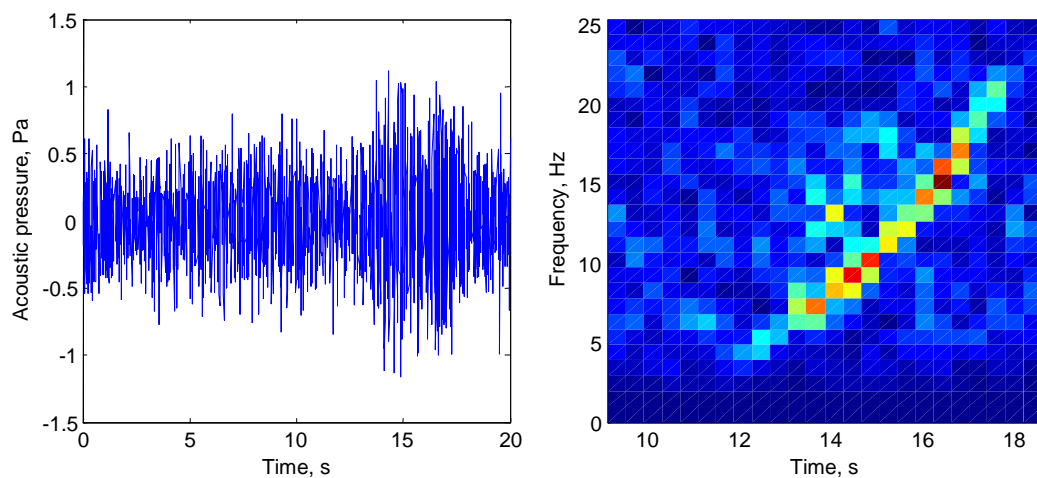


Figure A.2. Waveform (left panel) and spectrogram of an ice event detected in summer. Mode 1 contributes most to the energy of this signal.

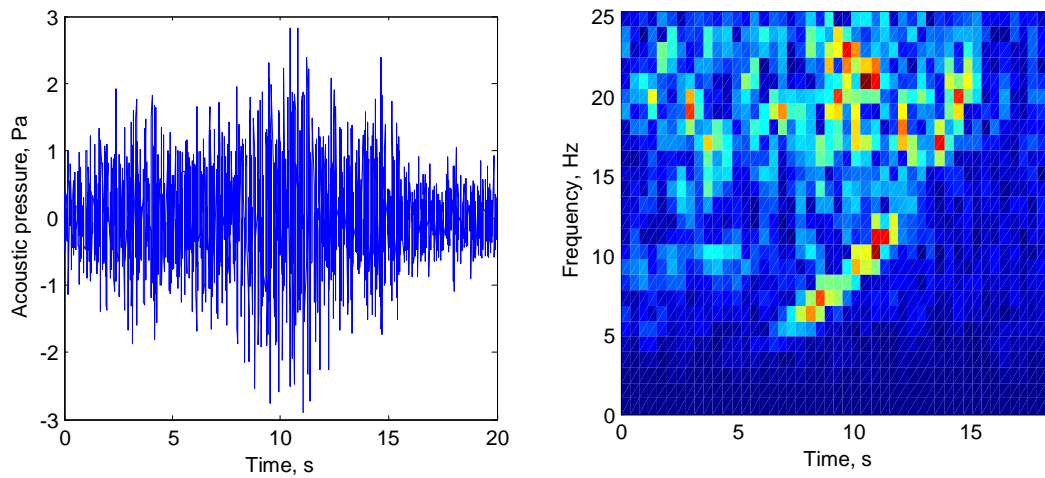


Figure A.3. Waveform (left panel) and spectrogram of an ice event detected in summer. The arrivals of higher modes highly scattered in the frequency-time domain contributes much to the total energy of this signal. The frequency components around 15 Hz almost disappeared in the spectrum of mode 1 arrival.

Another characteristic feature of the Antarctic ice events is the bandwidth of their spectra. It is assumed and also demonstrated by the underwater recordings made in Antarctica (Section 3.4) that the signal spectrum near an ice breaking event is broad. However, the long-range propagation in the ocean acoustic channel plays a role of a pass-band filter. Sound attenuation due to bottom interaction increases rapidly with frequency decreasing below 5 Hz at a sea depth of 300 m, which is typical for some areas of the Antarctic continental shelf. On the other hand, the transmission loss increases with frequency due to the scattering loss primarily at the sea surface roughed by ridged sea ice and surface waves. In Antarctic summer, the sea ice extent is minimum and the average wind speed and wave height are lower than that in winter, so that the signal spectrum of ice events contains significant frequency components up to 25 Hz or even a little higher (Figure A.1 – A.3). In winter, the transmission loss due to surface scattering is noticeably higher, so that the frequencies higher than approximately 15-20 Hz disappear from the signal spectrum (Figure A.4).

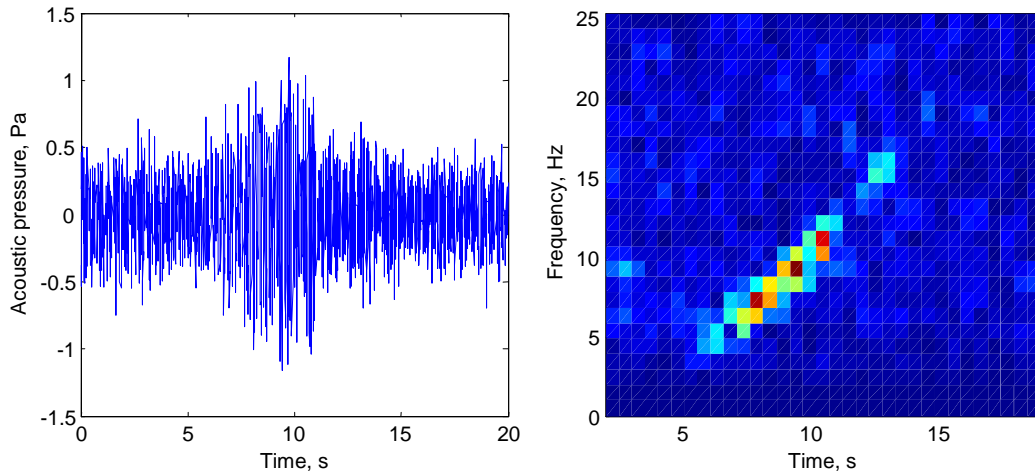


Figure A.4. Waveform (left panel) and spectrogram of a signal received at HA01 from an ice event in winter. The signal bandwidth is noticeably narrower than that of the typical ice events observed in summer, which is a result of higher attenuation at higher frequencies due to stronger scattering by the sea surface roughness in the winter polar conditions.

Despite considerable variations in the appearance of spectrograms of the ice events detected at the IMS station, there is an apparent common feature which can be used for distinguishing such events from other signals. We will consider this feature in terms of the spectrogram matrix. Let \mathbf{A} be a square matrix of the signal spectrogram of which the diagonals correspond to a certain slope dF/dT of the frequency dispersion curve. Such a matrix can be built by choosing appropriate window length and overlap for calculating the spectrogram using FFT algorithm (Figure A.5 and A.6). The slope dF/dT changes with frequency and, moreover, it changes with the propagation path and environmental conditions. According to numerical modelling of acoustic propagation from Antarctica to the IMS stations in Chapter 3, the maximum dispersion (minimum dF/dT) is expected in winter for the longest possible path from the Antarctic coast. The dispersion curve for these conditions is shown in Figure A.5 and A.6 by the upper dashed line, which has the mean slope dF/dT of about 0.19 s^{-2} . The weakest dispersion effect is expected in summer for the shortest propagation paths. For the summer conditions, the slope dF/dT is more rapidly varying with frequency and its mean value is about 0.28 s^{-2} (shown by the lower dashed line in Figure A.5 and A.6). The diagonals of the spectrogram matrices in Figure A.5 and A.6 correspond to the slope dF/dT of 0.22 s^{-2} . If origin of the spectrogram window

coincides with the arrival time of the lowest analysed frequency component of mode 1 (about 4 Hz), then the energy of mode 1 arrival pulse should always be contained in the matrix elements $K, L(K)$, which belong to the area limited by the two dashed lines of the minimum and maximum dispersion. The background noise can be estimated by the energy contained in the reduced upper triangle part of the matrix \mathbf{A} shown by a triangle in Fig A.6. No signal energy is expected to arrive at the corresponding time moments and frequencies, unless another signal from a different source arrives at the same time. So, the first criterion for distinguishing ice events was chosen to be the ration $C_1 = \frac{\sum_{k \in K, l \in L(K)} A_{k,l}}{\sum_{j=M-m+1-i} \sum_{i=1, M-m} A_{i,j}}$, where M is the matrix size and m is the number of off-diagonals omitted in the summation. In other words, the criterion C_1 can be regarded as mode 1 SNR.

The larger the criterion C_1 , the more likely the signal belongs to an ice event. However, the criterion C_1 is essential but insufficient. Some short transient signals received from time to time in the direction to Antarctica have relatively narrow spectra with the dominant frequency components at very low frequencies of 4 – 8 Hz and no frequency dispersion revealed in the spectrogram. The origin of such signals is not definite and, moreover, it is impossible to determine from their spectrograms whether these signals travelled over a long distance from Antarctica or not. Therefore, such signals were suggested not to be regarded as ice events. On the other hand, the value of C_1 for these narrowband signals can be quite high, so that another criterion is needed to distinguish the ice events from those signals. The bandwidth of mode 1 arrival pulse is used as such criterion. The mode 1 bandwidth is estimated only from the spectrogram matrix elements $K, L(K)$. For each frequency bin k , the maximum value \hat{A}_k of $A_{k,l}$ is found and then the number of frequency components which exceed a certain threshold is determined. The threshold is chosen as a fraction of the total maximum of $A_{k,l}$. So, the second criterion characterising the signal bandwidth can be expressed as $C_2 = N_{\hat{A}_k > \gamma \max\{A_{k,l}\}}$, where $\gamma < 1$ is the selected threshold. The greater C_2 , the more certain the observed signal is an arrival of mode 1 travelled from Antarctica.

The signal classification algorithm calculates firstly spectrograms of the whole 20-s signals picked after the previous 3 steps of the detection procedure. A rectangular matrix window of about 12 s long is then slid in the time domain spanning the frequency band from about 4 Hz to 25 Hz and searching for the maximum value of C_1 . Once the maximum C_1 is found, the criterion C_1 is calculated for the corresponding position of the sliding window.

To find the optimum values of C_1 and C_2 , two training sets of 300 selected signals each, classified by visual examination of spectrograms as ice events and other signals, were built and then used to train the classifier with respect to the two criteria using a discriminant analysis. It was found that the variations of the parameters C_1 and C_2 were not correlated and the constant thresholds of $C_1 = 7$ and $C_2 = 3$ (for the FFT window of 256 samples) provided the best performance with respect to the minimum misclassification rate of ice events, which was about 3% for the training sets. The bandwidth threshold parameter γ was chosen to be 0.3.

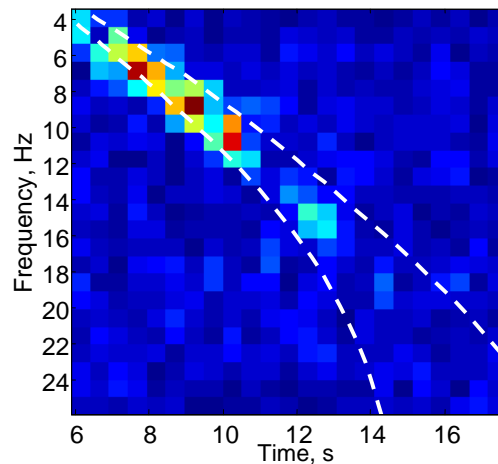


Figure A.5. Rectangular spectrogram matrix used to determine the energy ratio of mode 1 arrival and background noise in the analysis window. The dashed lines show the frequency dispersion curves numerically modelled for the winter environmental conditions along the longest path to the Antarctic coast (upper line) and the summer conditions along the shortest path to Antarctica.

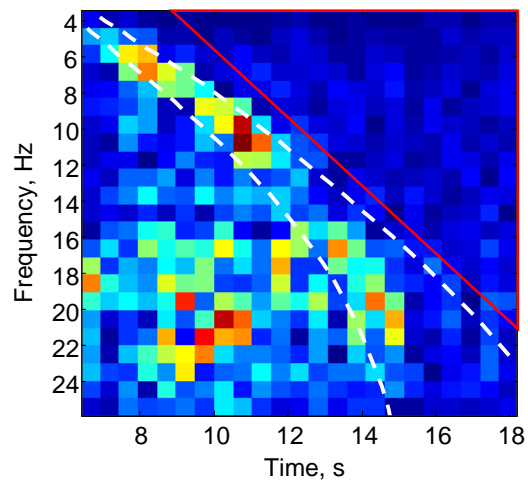


Figure A.6. Same as Figure A.5, but for the signal shown in Figure A.3. The red triangle indicates the upper off-diagonals in which the spectral energy components are summed to estimate the background noise level.